Transport Phenomena in Plasma Expansions Containing Hydrogen: A Laser Spectroscopic Study

Stéphane Mazouffre

Transport Phenomena in Plasma Expansions Containing Hydrogen

A Laser Spectroscopic Study

PROEFSCHRIFT

ter verkrijging van de graad van doctor
aan de Technische Universiteit Eindhoven,
op gezag van de Rector Magnificus, prof.dr. R.A. van Santen,
voor een commissie aangewezen door het College
voor Promoties in het openbaar te verdedigen op
maandag 15 oktober 2001 om 16.00 uur

door

Stéphane Mazouffre

geboren te Limoges, Frankrijk

Dit proefschrift is goedgekeurd door de promotoren:

prof.dr.ir. D.C. Schram

en

prof.dr. H.F. Döbele

Copromotor:

dr. R.A.H Engeln

The work described in this thesis is part of the research program of the Dutch Foundation for Fundamental Research on Matter (FOM) via project 95RG09: *"Thin layer deposition and surface modification. Plasmas in interaction with solid matter"*.
It is financially supported by the Dutch Organization for Scientific Research (NWO) as well as the Euratom Foundation.

Printed and bounded by Universiteitsdrukkerij Technische Universiteit Eindhoven
Cover design by Lies Schopmeijer

CIP-DATA LIBRARY TECHNISCHE UNIVERSITEIT EINDHOVEN

Mazouffre, Stéphane

Transport Phenomena in Plasma Expansions Containing Hydrogen: A Laser Spectroscopic Study / by Stéphane Mazouffre.-
Eindhoven: Eindhoven University of Technology, 2001.-
Thesis.-
ISBN 90-386-1839-5
NUGI 812
Subject headings: plasma expansion / laser spectroscopy / hydrogen atom / gas dynamics / surface chemistry

À mon Père,
À ma Mère,
À Aimée,
À Christian.

Contents

Chapter 1

General introduction

The subject of this thesis is the experimental study of the transport of ground-state hydrogen atoms in thermal plasma expansions. The plasma is generated by a cascaded arc from different gas mixtures: Ar-H_2, He-H_2 and H_2. In all cases, the plasma jet is unmagnetized and weakly ionized. The local properties of H atoms, such as the density, the perpendicular and parallel temperature, and the radial and axial velocity components, are monitored in the course of the plasma expansion by means of Two-photon Absorption Laser Induced Fluorescence (TALIF) spectroscopy. In order to obtain information about the flow of inert neutral particles (Ar, He, H_2), other laser-based diagnostic techniques are available, like cw-Laser Induced Fluorescence and UV-Rayleigh scattering. This work follows the study of the flow of neutrals and charged particles carried out by M.C.M. van de Sanden and R.F.G. Meulenbroeks using Rayleigh-Thomson scattering and Coherent Anti-Stokes Raman Scattering. Here, we focus on the study of the influence of surfaces on the H atom transport mechanisms and on the H atom fluid properties, i.e. coupling between the H fluid and the inert neutral fluid, during the expansion process. We also performed a detailed investigation of the behavior of the atomic velocity distribution function throughout the stationary shock wave of the supersonic plasma jet, to study both the shock wave formation and the invasion of the supersonic domain by the background gas in a rarefied flow regime.

In this introductory chapter, the physical phenomenon of plasma expansion is presented and compared with the expansion of a neutral gas. Furthermore, the experimental facility, including all the different laser-aided diagnostic techniques available, is described, and an outline of this thesis is given.

1.1 Plasma expansion: a general physical phenomenon

The expansion of a plasma from a high temperature and high density region (referred to as the source) where energy is dissipated[1], to a low pressure or vacuum environment, is a very general physical phenomenon. It concerns a large variety of objects and covers a vast range of dimensions. Furthermore, the physical issues addressed are relevant to many subjects in science like astrophysics, fluid dynamics, and surface physics.

At large scale plasma expansions encompass objects like supernovae, solar flares, solar outbursts, and phenomena like solar wind and galactic jets [1, 2, 3, 4, 5]. Those systems represent examples of gigantic jets[2] where the matter ejected out of the source flows into a nearly perfect vacuum until it encounters planets or dense interstellar clouds of gas and dust. Apart from their inconceivable size, such plasma expansions are also characterized by the fact that their structure and properties are also governed by the existence of magnetic fields.

In contrast to huge plasma jets and beams found in the cosmos, one finds at the opposite side of the dimension scale small and even tiny plasma expansions such as laser spots [6, 7, 8, 9] and cathode spots [10, 11]. In the case of a laser spot, the plasma is created by the interaction of a strong electromagnetic field with a target, whose state can be solid, liquid or gas, and subsequently the plasma expands supersonically from a very localized region [12, 13]. Laser plasmas allow for a precise control of the jet parameters like the Mach number and the kinetic energy, and of the jet chemical properties. Such jets are used for instance for thin layer deposition [14], for the fundamental study of collision processes as well as for the generation of VUV and X-ray radiation [15]. Laser produced plasmas are also projected to create modulated plasmas for plasma based accelerators in order to create bunches of relativistic electrons [16, 17]. Tiny plasma expansion can be generated using low current vacuum arcs from a very small cathode spot by evaporation and ionization of a solid target in a low pressure environment. Such plasma flows may be used for thin film deposition by cathode sputtering, as an ion source for ion implantation and for particle accelerator injection for fundamental nuclear physics research [18]. In arc switches and circuit breakers, the conductive properties of the created high density arc plasma are used [19].

Finally, in between macro and microjets, the physical phenomenon of plasma expansion also includes laboratory scale expansions such as jets produced from thermal plasma sources like DC, RF, and microwave torches [20], as well as the divertor[3] region of Toka-

[1] Depending on the kind of source the expansion originates from, the energy that drives the flow process is of different form: electromagnetic (arc, laser spot), nuclear (star), or gravitational (black hole).

[2] The most extreme jets are galactic jets which can have extensions over distances of several thousands of light-years and for which the flow speed can approach the speed of light. Such plasma expansions are likely to be powered by massive black holes.

[3] In a Tokamak reactor a limiter is a solid surface which serves primarily to protect the reactor wall from the plasma (during disruption for instance). A divertor is a special kind of limiter which includes a magnetic field to guide impurities out of the plasma volume.

Tab. 1.1: Physical parameters characterizing a variety of plasma expansions. The given values of the parameters represent standard values. Deviations corresponding to specific cases are possible. Even if all plasma expansions mentioned in this table are very similar from the point of view of the underlying physical processes, as can be seen, they cover a broad range of conditions.

expansion	source properties	flow speed	jet radius	ambient density
solar flare	$T_e \approx 10^4$ eV	10^6 m s^{-1}	$r \approx 10^3$ km	10^6 m^{-3}
	$n_0 \approx 10^{20}$ m^{-3}			
	$n_e \approx 10^{20}$ m^{-3}			
cascaded arc jet	$T_e \approx 1$ eV	5000 m s^{-1}	$r \approx 10$ cm	10^{21} m^{-3}
	$n_0 \approx 10^{23}$ m^{-3}			
	$n_e \approx 10^{22}$ m^{-3}			
laser plasma	$T_e \approx 100$ eV	10^5 m s^{-1}	sphere	10^{18} m^{-3}
(X-ray generation)	$n_0 \approx 10^{24}$ m^{-3}		$r \approx 5$ mm	
	$n_e \approx 10^{26}$ m^{-3}			
cathode spot	$T_e \approx 10$ eV	10^4 m s^{-1}	$r \approx 10$ μm	10^{15} m^{-3}
	$n_0 \approx 10^{24}$ m^{-3}			
	$n_e \approx 10^{24}$ m^{-3}			

mak plasmas [3, 21]. Atmospheric thermal plasma jets are used for instance for plasma cutting, welding, heating (chemical waste treatment), annealing, and for plasma spraying, i.e. deposition of thick coatings [22, 23]. Low pressure thermal plasma jets find applications in surface modifications like fast deposition of thin films [24, 25] and micro-circuit etching [26]. They may serve as ion beam and neutral beam sources for research in the field of controlled nuclear fusion.

All previously mentioned kinds of plasma expansions exhibit similarities in the underlying physical mechanisms. They cover a broad range of conditions, as can be seen in the list of physical parameters given in Tab. 1.1 for several sorts of plasma expansions.

To a large extent, the expansion of a thermal plasma resembles a neutral gas expansion [27], a well-known subject in the field of gas dynamics, meaning that in first order the particles density, temperature, and velocity, behave similarly to a free jet expansion [28, 29, 30].

However, a plasma expansion exhibits specific characteristics which make it a richer and more complex process. First, a plasma is not only composed of particles such as stable atoms and molecules, it also contains ions, electrons, photons and radicals[4]. Under certain circumstances, different kind of particles may have a different temperature in the

[4] A radical is an atom or a molecule with a free bond. As examples one can cite atoms like H, N, or C and molecular fragments like CH, NH, SiH_3. Due to their high reactivity radicals play an important role in chemistry, both in volume and at a surface.

source and/or in the course of the flow. Moreover, large temperature, density and velocity gradients are often present already in the source. Second, a plasma expansion is a non-equilibrium process [31, 32] and, due to recombination effects or due to the action of an electric or magnetic field, a frozen regime in which there is no energy exchange or energy transformation is never achieved. Third, the enlarged heat conductivity and viscosity [22] lead to a non-isentropic supersonic expansion [33]. Three-particle recombination can also disturb the energy transfer mechanisms between charged particles, and can, therefore, create non-adiabatic conditions during the expansion process [34]. Fourth, the plasma nature gives rise to the generation of fields and currents [34, 35], which in turn influence, or even determine, the currents and thus the power dissipation in the hot region. At high power densities, the generated currents and fields may be so strong that the plasma becomes confined by the self-generated magnetic field. Finally, due to plasma-surface interactions, i.e. interactions with dust particles (e.g. in interstellar medium) or with walls (nozzle, reactor), radicals generated from molecules in the plasma source, may decouple from the neutral particles expansion (a two-fluid expansion is then created) and, as a consequence, radicals may exhibit anomalous transport properties [36]. All these specific physical processes and mechanisms make the phenomenon of plasma expansion very rich in view of the possible issues to be studied.

We here restrict ourselves to laboratory scale thermal plasma jets and to the regime where the plasma remains unmagnetized and singly ionized, in which case the main mass is contained in the neutrals and thus the expansion resembles the usual gas expansion. At the same time the study of the intermediate size expansions of thermal plasmas (mm to cm) may serve as a scale model for both the tens of micrometer-sized and the astrophysical size plasma jets as to some extent they are driven by similar physical mechanisms. Furthermore, an important reason to study plasma flow at an intermediate scale is the possibility of application of a variety of diagnostic techniques, both passive and active, and therefore opening the way to acquire extensive sets of data.

1.2 Hydrogen containing plasma jets

The fundamental study of hydrogen containing plasma jets[5] is of particular interest, since it concerns various systems that cover the entire range of plasma expansions.

Atomic hydrogen being the main constituent of both stellar and interstellar matter, all astrophysical scale plasma expansions represent examples of hydrogen plasma jets. In the field of controlled nuclear fusion, hydrogen jets plays a specific role [21]. First, one wants to use H atom sources for neutral beam heating of fusion devices (mainly via the production of negative hydrogen ions H^-). Second, the interaction of neutral H atoms with the reactor wall (in a divertor region for instance) and the resulting formation of new

[5] In order to avoid confusion, we should here emphasize on the difference between a jet and a beam since they are very different media. In a jet, the flow regime is continuum (hydrodynamic) whereas in a beam the flow regime is rarefied (molecular) [28]. If the ambient pressure is low enough, an expansion exhibits a gradual transition from a jet like flow (close to the source) to a beam like flow (far from the source).

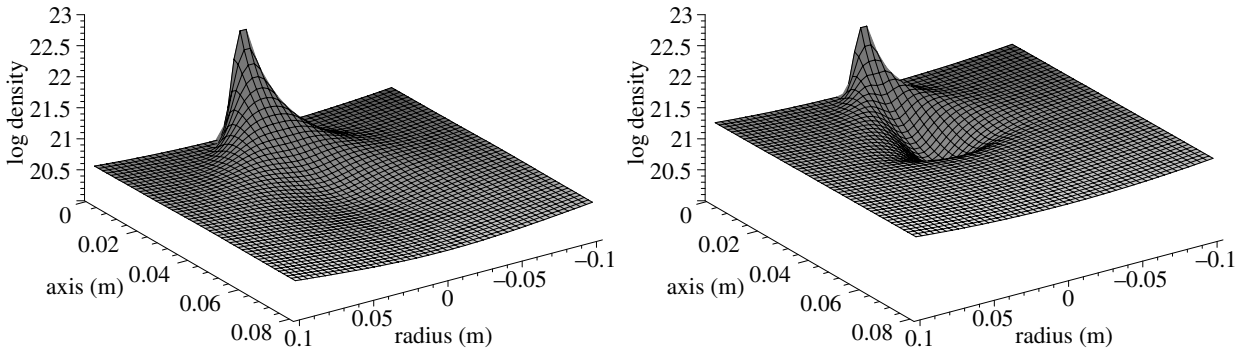

Fig. 1.1: 3D plot of the density (log scale, in m^{-3}) of Ar atoms during the expansion of a cascaded arc generated argon plasma (see section 1.4 for more details) for two different background pressures: 20 Pa (left) and 100 Pa (right). The source conditions are: 3 standard liters per minutes (slm) Ar, pressure = 0.6 atm, temperature = 5000 K, nozzle diameter = 3 mm. These density maps are constructed using simplified 1D hydrodynamic equations (see chapter 2) combined with arbitrary functions that fit the measured radial density profiles. In the subsonic domain, the static pressure is assumed to be constant. A formal calculation using the Navier-Stokes equation would be necessary in order to obtain the exact density behavior. Yet these simple models help the reader to visualize the so-called rarefaction effect (dilution of the fluid into the environment) and the effect of the local pressure on the jet structure (smooth and abrupt jet-background transition at low and high pressure respectively).

products, e.g. H_2 molecules, and the release of impurities due to proton bombardment, have drastic consequences on the stability of the fusion plasma and therefore on device performances in term of energy extraction. Numerous works are nowadays devoted to this so-called hydrogen recycling process [37, 38] and they all require the development of plasma sources capable of generating a high H atom or H ion flux.

From a technological perspective, due to their high reactivity, hydrogen radicals play a key role in many chemical reactions encountered in plasma processes and therefore are of relevance for industrial applications like deposition of thin films and surface modification (etching, passivation). For instance, hydrogen atoms are involved in the plasma-aided fast deposition of thin films of hydrogenated amorphous silicon (a-Si:H) needed for the next solar cell generation. It has been shown recently that hydrogen radicals control the growth process and thus the final film properties [24].

All aforementioned processes that concern intermediate scale expansions, are to a large extent governed by the transport mechanisms of ground-state hydrogen atoms, i.e. H radicals, in an expanding hydrogen containing thermal plasma. In view of the applicability it is therefore of importance to study the H atom flow pattern as well as the influence of plasma-surface interactions on the radical transport properties.

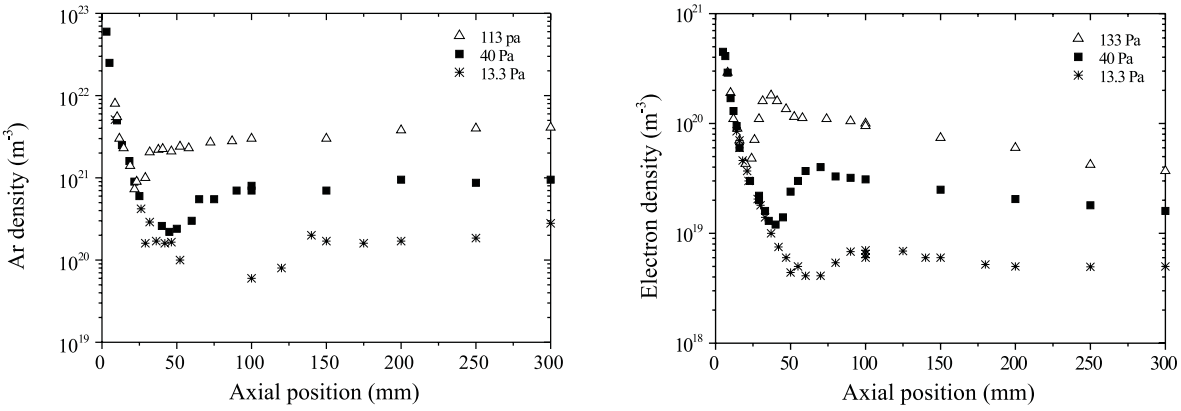

Fig. 1.2: Axial density profiles of the heavy particle density (left) and of the electron density (right) during the expansion of an argon plasma produced by a cascaded arc (see section 1.4) for 3 different background pressures. The data are taken from the work of M.C.M. van de Sanden [34, 39, 40]. The heavy particle density is measured by Rayleigh scattering and the electron density is obtained from Thomson scattering measurements. In the supersonic domain the density decrease is independent of the ambient pressure. On the contrary, the position and the width of the stationary shock wave as well as the compression strength are influenced by the background pressure. Beyond the shock front, the heavy particle density increases as a consequence of the cooling of the plasma flow by heat transfer to the vessel walls, whereas the electron density decreases as the result of 3-particle recombination. Ignoring the e-ion interactions, those profiles are mainly in agreement with the free jet flow theory.

1.3 Transport of particles

Inert neutrals: the classical transport picture

The flow of inert particles, such as Ar or He atoms and H_2 molecules, in a thermal plasma expansion can to a large extent be described with the free jet flow theory developed in the field of gas dynamics [27, 28]. In short, leaving the high pressure region, the gas is accelerated to supersonic velocity due to the conversion of thermal energy gained in the source into kinetic energy and the local particle density decreases due to an increase in the jet cross-section (the so-called rarefaction effect). At some distance from the source the expanding gas collides with the residual ambient gas and a stationary shock wave structure is formed. Behind the shock region, the flow is subsonic and obeys the local pressure conditions. In Fig 1.1, a schematic representation of the inert particle density in an expansion is given. In the case of a plasma, the high temperature leads usually to a quasi-adiabatic expansion. In the work of M.C.M. van de Sanden *et al* [39, 40], it is demonstrated that the flow of Ar atoms in an argon plasma expansion follows the prediction of the free jet flow theory (see Fig. 1.2).

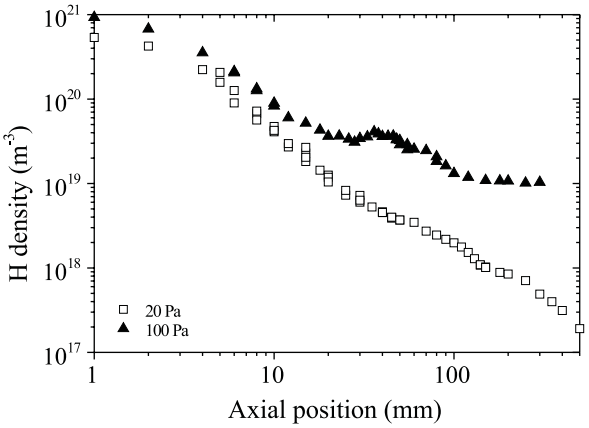

Fig. 1.3: Ground-state hydrogen atom density profile measured along the jet centerline of a Ar-H_2 plasma jet for 2 different background pressures (3 slm Ar, 0.5 slm H_2) [36]. The profile is in disagreement with the free jet flow theory. The density decrease in the supersonic domain is pressure dependent (value at the arc exit and slope), there is no density jump across the normal shock wave and the density drops in the subsonic domain. The departure from the classical expansion picture is a direct consequence of plasma-wall interactions, i.e. recombination of H atom at the reactor wall (stainless steel in that case) to form molecular hydrogen.

Reactive neutrals: anomalous transport

Until recently, physicists thought that the transport of radicals in a plasma expansion would not differ from the transport of neutrals. Therefore, the reader can easily imagine the surprise and the excitation when it was discovered that the measured H atom density development along the jet axis of an Ar-H_2 plasma jet was in contradiction with the expectation, as can be seen in Fig 1.3.

The anomalous transport of H radicals finds its origin in the plasma-surface interactions as it will be shown in this thesis. To please impatient readers, we here give a rapid overview of what is going on. When a H atom reaches a surface it may recombine to form a H_2 molecule (obviously the efficiency of this process depends strongly on the surface properties and on the residence time). If the so-called recombination probability is high, the H atom partial abundance in the background gas is low, that results in the formation of large H density gradients between the plasma jet and its vicinity. Those gradients are responsible for two effects: a decoupling between the H atom fluid and the carrier gas fluid during the expansion and the existence of large H outflow [36]. As a result, only a small fraction of the hydrogen atoms leaving the source is carried towards the downstream region.

The case of charged particles

Even if the charged particles, i.e. ions and electrons, are not directly of interest in this thesis, it is certainly worthwhile to shortly discuss their influence on the plasma flow. In the case of a fully ionized plasma, the expansion process differs from a gas expansion. Several new effects must be considered: the appearance of a charged particles density gradient in the conservation laws, a higher heat conductivity, the existence of fields and currents. In this work we however restrict ourselves to partially ionized plasmas. As pointed out by M.C.M. van de Sanden *et al* [39, 34] a partly ionized plasma flow can be explained as a classic supersonic expansion with slight modifications to account for the presence of charged particles. As an example, the electron axial density profile measured in an expanding argon plasma for several pressures is shown in Fig. 1.2.

Another aspect of the presence of electrons and ions is the emergence of a new chemistry which of course has an impact on the flow properties. This is particularly true when molecular gases like hydrogen are added to an atomic plasma (e.g. argon plasma). Charge exchange between an ion and a molecule, followed by the dissociative recombination of the created molecular ion, is a very effective process to dissociate a molecule at low temperature

$$\begin{aligned} \mathrm{Ar}^+ + \mathrm{H}_2(v=0) &\rightarrow \mathrm{ArH}^+ + \mathrm{H} \qquad k \approx 10^{-15}\ \mathrm{m^3\,s^{-1}} \quad \text{at 1 eV}, \\ e + \mathrm{H}_2(v=0) &\rightarrow e + \mathrm{H} + \mathrm{H} \qquad k \approx 10^{-18}\ \mathrm{m^3\,s^{-1}} \quad \text{at 1 eV}. \end{aligned}$$

Note that the dissocitative recombination of ArH^+, $\mathrm{ArH}^+ + e \rightarrow \mathrm{Ar} + \mathrm{H}^*$ is known to be very fast (rate constant around 10^{-13} $\mathrm{m^3\,s^{-1}}$). Thus the charge exchange process leads to the formation of new molecules and radicals (atomic as well as molecular fragments) which play an important role in the plasma chemistry. Furthermore, this process leads to a loss of ionization (i.e. low ionization degree) which in turn influences the expansion behavior.

1.4 Experimental facility

Plasma source: the cascaded arc

The plasma source used in these experiments is a cascaded arc [42, 43] which is an example of a wall stabilized thermal plasma. It is schematically depicted in Fig. 1.4. The cascaded arc has been first introduced in the 1950s by Maecker [44]. The arc can be operated in a wide range of pressure (10^4 to 10^8 Pa) and currents (5 to 2000 A). In the standard arc conditions (gas flow $\approx$ 3 standard liters per minute (slm), $p_{\mathrm{arc}} \approx 0.5$ atm, $I_{\mathrm{arc}} = 40$ A to 60 A), the generated plasma is characterized by a relatively high electron and heavy particle temperature ($T_e \approx T_h \approx 1$ eV) and a high electron density ($n_e \approx 10^{22}$ $\mathrm{m^{-3}}$). In a cascaded arc, a DC discharge is sustained in a channel between 3 cathodes and a grounded anode to which a nozzle is plugged. The gas is fed through a mass flow controller into the cathode region. The electrically insulated cascaded plates that compose the channel lead to a straight arc. All parts are made of copper, except for the cathode tips (tungsten with 2% lanthanum), the PVC and boron nitride spacers between the plates and the boronnitride

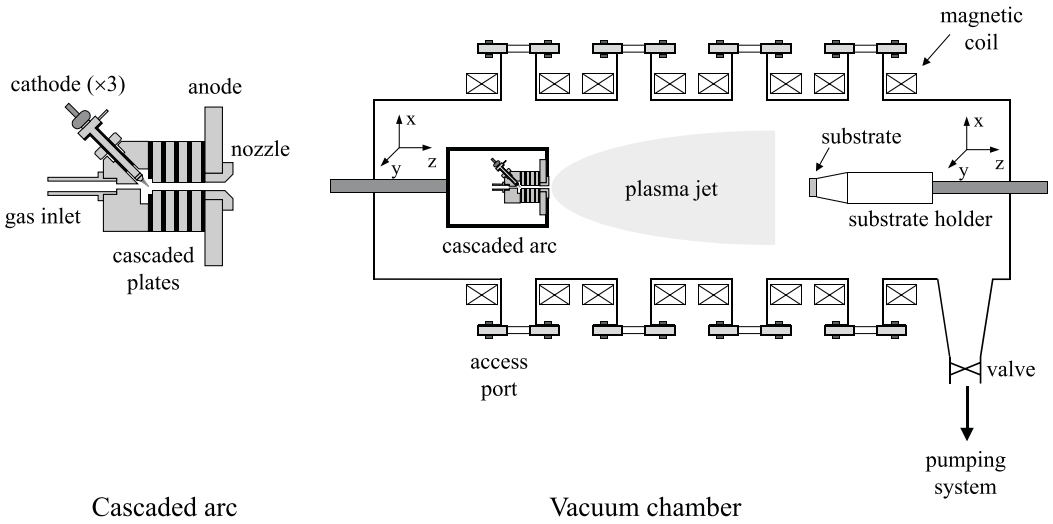

Fig. 1.4: Plasmas under investigation in this work are generated from a flowing gas using a wall-stabilized cascaded arc. Inside the arc channel ($d = 4$ mm) the pressure is sub-atmospheric (≈ 0.5 atm) and the temperature is around 1 eV. The plasma expands freely from the source nozzle, of which geometry can be varied, into a low pressure medium. The vacuum chamber which is made of stainless steel is 4 m long and has a diameter of 0.36 m. The vessel is divided into 4 observation sections surrounded by 8 Helmholtz coils to provide an axially directed magnetic field (0 to 0.5 T). The background pressure can be varied almost independently from the injected gas flow from 10 Pa to 1 atm. Both the cascaded arc and the temperature controlled substrate are mounted on a movable arm that allows for 3D displacement. In this way spatially resolved measurements can be performed while the diagnostic tools remain fixed.

cover of the cathode feedthrough. The arc is vacuum sealed with O-rings; the cathode, the anode and the cascaded plates are water-cooled. The arc that is used in this work is composed of 4 plates; the channel is 30 mm long and has a diameter of 4 mm. The arc nozzle is made of copper and it has a length of 17 mm. Its geometry can be varied. The cascaded arc is mounted on a moveable arm and can therefore be moved in the 3 directions of space.

In the source the plasma is created from a flowing gas by dissipation of (electric) energy [20]. The supplied energy has to be sufficient enough to ionize and heat the gas/plasma. This will lead to a hot and high pressure source and subsequently to expansion of the generated plasma from that source. Moreover, the production of new electrons and ions has to be large enough to compensate for the losses of charged particles by diffusion and convection. The thermal plasma produced in the cascaded arc is in non-equilibrium and it is ionizing [41, 46]. The expanding plasma is also not in equilibrium, however in contrast with the plasma in the source it is recombining and the temperature is relatively low.

The thermal plasma produced inside the arc channel expands freely from the arc nozzle into a low pressure vessel made of stainless steel (see Fig. 1.4). The vessel is 4 m long and has a diameter of 0.36 m; it is divided into 4 segments surrounded by 8 Helmholtz coils to provide an axially directed magnetic field (0 to 0.5 T). The pumping system consists of a large roots blower pump (720 $\mathrm{l\,s^{-1}}$) pumped by a small roots blower pump (140 $\mathrm{l\,s^{-1}}$) which in turn is evacuated by a roughing pump (20 $\mathrm{l\,s^{-1}}$). The pumping capacity of the large roots blower pump can be varied by means of a valve, and in this way the residual pressure can be changed almost independently from the gas flow from 10 Pa to 1 atm. The residence time inside the vacuum chamber is relatively long ($\approx$ 1 s at 20 Pa) and thus recirculation cells, into which the gas is recycled, are formed around the plasma jet [45]. Those cells play an important role in the downstream chemistry.

Laser-aided diagnostics

Several laser-aided diagnostics are used in the experiments mentioned in this thesis to collect valuable information about the particle transport in an expanding thermal plasma[6]. We here briefly introduce them; more information can be found in the rest of the manuscript.

- *Two-Photon Laser Induced Fluorescence*

In order to avoid the experimentally demanding generation of high energy (VUV) photons, ground-state hydrogen atoms are excited to the n=3 level using two 205 nm (UV) photons [47]. The resulting fluorescence radiation is detected at the Balmer-α line (656 nm). Using this spectroscopic technique one obtains spatially resolved information about the H atom density, temperature and velocity. In order to obtain absolute number density, the fluorescence yield has to be calibrated either via a titration reaction or using a two-photon scheme in krypton.

- *cw-Laser Induced Fluorescence*

A continuous wave (cw) laser beam in the near IR is used to probe excited Ar atoms in the 4s multiplet (both resonant and metastable state) via laser induced fluorescence spectroscopy. In that way, the local velocity and temperature of the excited Ar atoms are measured. It can be shown that the properties of excited Ar (but the density) image the properties of ground-state Ar atoms.

- *UV Rayleigh scattering*

The UV laser beam used to excite ground-state H atoms is also used to perform Rayleigh scattering experiments in order to measure the local heavy particle density (i.e. the neutral density, since the ionization degree is below 1 % in our plasmas). The relatively low amount of UV photons available (approximately 10^{15} and 10^{18} photons per pulse at 205 nm

[6] Very often plasma jets properties are monitored using probes such as Langmuir probes, enthalpy probes, and Pitot tubes, which are directly inserted in the jet. However, contrary to laser diagnostics, probes disturb the flow, especially in a supersonic regime. As a consequence, the interpretation of the experimental data is in most cases difficult.

and 532 nm, respectively) is partly compensated by the gain in the scattering cross-section σ^R, since σ^R varies in first approximation like λ^{-4} [48]. The Rayleigh scattering and the two-photon LIF experiments can be performed simultaneously.

Other laser aided diagnostics have been extensively used in the past, like Thomson scattering [49] and Coherent Anti-Stokes Raman Spectroscopy (CARS) [50]. At the present time, the chemistry in the subsonic domain of the expansion is studied by means of Cavity Ring Down Spectroscopy (CRDS) [51]. In the near future, a VUV-LIF setup is projected to be built in order to probe H_2 molecules in a hydrogen expansion [47, 52].

1.5 Aim of this work and outline

Aim: an overall plasma expansion picture

As already suggested in sections 1.2 and 1.3, this thesis deals with the transport phenomena in intermediate scale thermal plasma expansions that contains hydrogen atoms and molecules. Such research is of relevance on a fundamental point of view: detailed dynamic-kinetic study on an intermediate scale plasma expansion with possible extrapolation to expansions at smaller and larger scales. But it also has a large impact on a technological perspective. The field of plasma assisted chemistry, in which radicals and molecules play a key role, is gaining importance. Moreover, researches in the field of controlled nuclear fusion require at present a better understanding in transport and wall-recycling of hydrogen atoms. The thermal plasma jets investigated in this work are generated using a cascaded arc. Such jets are currently used for deposition of thin films: C containing layers [53] and a-Si:H coatings [54] for example. They are also used as particle source for treatment of archeological artefacts [55], and as a light source for spectroscopic applications [56]. Furthermore, a cascaded-arc-produced hydrogen expansion appears to be a good candidate to simulate the H^+ flux impinging onto a divertor, one of the critical components of a Tokamak reactor [21].

The aim of this work is therefore to obtain an overall picture of an unmagnetized and weakly ionized plasma expansion in terms of transport properties. To gain a more profound understanding of the basic processes that govern this kind of plasma expansion with in mind not only the gain in knowledge, but also the optimization of aforementioned applications. This present work is the follow up of the work of M.C.M. van de Sanden [34, 40] and R.F.G. Meulenbroeks [50, 57]. Nevertheless, after several years of research on expanding plasmas using active and passive diagnostics, numerous aspects of the transport phenomena in such a medium still have to be investigated or clarified. In order to make the objective of this work clear to the reader, we present a list of questions we will try to answer in the rest of this thesis.

- Which amount of atomic radicals can the plasma source supply? Which fraction of the H atoms leaving the source reaches the downstream region of the expansion?

- In the case of a pure hydrogen plasma jet, can the low ionization degree and the absence of rovibrationally excited H_2 molecules be explained in view of the H atom content?

- What is the structure of a stationary compression shock wave in a rarefied regime? To which extent does the expanding plasma depart from thermodynamic equilibrium?

- Is the invasion of the supersonic domain of the expansion by the residual background gas significant in a rarefied flow regime? How does the mixing of the ambient gas with the jet affect the downstream chemistry?

- Can the interaction between the background gas and the reactor walls influence the transport properties of radicals in a plasma jet?

Trying to answer those questions, more questions will undoubtedly emerge. In like manner, some conclusions drawn in this work will probably have to be modified later on, as new experimental and computational facts arise. In the general conclusion, we present the current view of the transport phenomena in a plasma expansion and we propose near future investigations which, as we hope, will show that we are on the right route.

Outline of this thesis

The main content of this work consists of seven chapters written in such way that they can be read independently from each other. Apart from the first part in which the main characteristics of an expansion are described, all other parts are organized in such way that this thesis offers a logical trend.

In chapter 2, a detailed description of the continuum free jet flow structure that results from the expansion of a fluid from a high pressure region into a vacuum is given. Moreover, the characteristics of a compression shock wave are presented.

In chapter 3, the transport of argon atoms in an expanding thermal argon plasma seeded with 4 % of hydrogen is studied by means of laser induced fluorescence spectroscopy, and by UV Rayleigh scattering. After demonstrating that the properties of metastable Ar atoms image the properties of ground-state Ar atoms, it is experimentally shown that the Ar atom expansion is understandable in term of a Ar free jet flow with a low isentropic exponent. Non-Maxwellian Ar distribution functions are observed, both at the arc exit (influence of the self-generated E field) and across the stationary shock wave (interaction jet-background).

The Two-photon Absorption Laser Induced Fluorescence (TALIF) spectroscopy of atomic hydrogen is explained in chapter 4. A detailed description of the experimental arrangement is presented. It is shown that from a spectral scan over the two-photon transition several quantities can be extracted: the local H atom velocity distribution function, the mean velocity, the temperature (only at thermodynamic equilibrium) and the relative

density. In order to obtain absolute H atom densities, the LIF setup has to be calibrated. Two calibration methods are presented and compared: titration with NO_2 and comparison with a two-photon excitation of krypton.

In chapter 5 and chapter 6, the transport of ground state atomic hydrogen in the expansion of a thermal plasma generated from an Ar-H_2 mixture (14 % H_2) is studied. The flow of hydrogen atoms is monitored by TALIF, whereas Ar atoms are probed by LIF as well as by UV Rayleigh scattering. Contrary to Ar atoms, H atoms exhibit anomalous transport properties. In the course of the plasma expansion, hydrogen atoms decouple from the argon fluid by a diffusion process as a direct consequence of recombination of H atoms at the vessel walls. It is shown, on the basis of experimental results, how plasma-surface interactions can strongly influence the flow pattern of an atomic radical fluid.

The flow properties of the ground state hydrogen atom fluid in the course of the expansion of a weakly ionized hydrogen plasma are examined and compared with the ones of H_2 molecules in chapter 7. The low dissociation degree measured at the source exit implies that H atoms flow in a H_2 environment. It is clearly proved that as soon as the surface loss probability is high, the losses of radicals by diffusion, and the subsequent decoupling between the inert gas fluid and the reactive gas fluid, cannot be avoided even when the mass of the carrier gas is close to the mass of the radical.

In chapter 8, the evolution of the ground-state hydrogen atom velocity distribution function (VDF) throughout the stationary normal shock wave of a supersonic hydrogen plasma jet is studied. A clear departure from thermodynamic equilibrium is observed. Nevertheless, the H atom VDF can be decomposed into two Maxwellian distributions. One distribution corresponds to the zone of silence conditions and the other one corresponds to the conditions in the shock region. The development of the mean axial velocity is modeled using the Mott-Smith approach. Deviation from the theoretical shock profile is interpreted in terms of the non-conservation of both the H atom forward flux and momentum across the shock wave.

Finally in chapter 9, the general conclusions of this thesis work are presented and some near future perspectives are given.

References

[1] *Beams and Jets in Astrophysics*, edited by P.A. Hugues, Cambridge University, Cambridge, England (1991).

[2] J.M. Shull and C.F. McKee, *Ap. J.* **227**, 131 (1979).

[3] H. Wilhelmsson, *Fusion: A Voyage Through the Plasma Universe*, IOP publishing, Bristol (2000).

[4] *The Cambridge Atlas of Astronomy*, edited by J. Audouze and G. Israël, Cambridge University Press, Cambridge (1988).

[5] L. Golub and J.M. Pasachoff, *The Solar Corona*, Cambridge University Press, Cambridge, United Kingdom (1997).

[6] J.C.Miller, R.F.Haglund, *Laser Ablation and Desorption, Experimental Methods in Physical Sciences*, Academic Press, San Diego, Vol. 30 (1998).

[7] Yu. P. Raizer and D.C. Smith, *J. Opt. Soc. Am.* **70**, 258 (1980).

[8] A. Lebhot and R. Campargue, *Phys. Plasmas* **3**, 2502 (1996).

[9] J.M. Girard, A. Lebhot, and R. Campargue, *J. Phys. D* **26**, 1382 (1993).

[10] E. Hantzsche, *Contr. Plasma Phys.* **30**, 575 (1990).

[11] I.A. Krinberg, *Tech. Phys. Lett.* **20**, 759 (1994).

[12] H.C. Le, D.E. Zeitoun, M. Sentis, and W. Marine, *Phys. Rev. A* **62**, 4152 (2000).

[13] K.R. Chen, T.C. King, J.H. Hes, J.N. Leboeuf, D.B. Geohegan, R.F. Wood, A.A. Puretzky, and J.M. Donato, *Phys. Rev. B* **60**, 8373 (1999).

[14] S.I. Anisimov, D.Bäuerle, and B.S. Luk'yanchuk, *Phys. Rev. B* **48**, 12076 (1993)

[15] A. McPherson, B.D. Thompson, A.B. Borisov, K. Boyer, and C.K. Rhodes, *Nature* **370**, 631 (1994).

[16] T. Katsouleas, *AIP Conf. Proc.* **472**, 19 (1999).

[17] T. Katsouleas, C.E. Clayton, K. Wharton, R. Kinter, T. Peters, S. Heifets, and T. Raubenheimer, *AIP Conf. Proc.* **395**, 75 (1997).

[18] I.G. Brown, *Rev. Sci. Instrum.* **65**, 3061 (1994).

[19] K.T. Hartinger, L. Pierre, and C. Cahen, *J. Phys. D: Appl. Phys.* **31**, 2566 (1998).

[20] D.C. Schram, S. Mazouffre, R. Engeln, and M.C.M. van de Sanden, in *Atomic and Molecular Beams*, edited by R. Campargue, Springer, New York, 209 (2001).

[21] J. Wesson, *Tokamaks*, Clarendon Press, Oxford (1997).

[22] M.I. Boulos, P. Fauchais, and E. Pfender, *Thermal Plasmas, Fundamental and Applications*, Plenum Press, Vol. 1-2 (1994).

[23] S.M. Aithal, V.V. Subramaniam, and V. Babu, *Plasma Chem. Plasma Proc.* **19**, 487 (1999).

[24] W.M.M. Kessels, M.C.M. van de Sanden, and D.C. Schram, *J. Vac. Sci. Technol. A* **18**, 2153 (2000).

[25] J.W.A.M. Gielen, P.R.M. Kleuskens, M.C.M. van de Sanden, L.J. van Ijzendoorn, D.C. Schram, E.H.A. Dekempeneer and J. Meneve, *J. Appl. Phys.* **80**, 5986 (1996).

[26] D.M. Manos and D.L. Flamm, *Plasma Etching*, Academic Press, New York (1989).

[27] H. Askenas and F.S. Sherman, *Proceedings Rarefied Gas Dynamics* **4**, Academic Press, New York, Vol. 2, 84 (1966).

[28] D.R. Miller, in *Atomic and Molecular Beam Methods*, edited by G. Scoles, Oxford University, New York, (1988).

[29] H.C.W. Beijerinck, R.J.F van Gerwen, E.R.T. Kerstel, J.F.M. Martens, E.J.W. van Vliembergen, M.R.Th. Smits, and G.H. Kaashoek, *Chem. Phys.* **96**, 153 (1985).

[30] J.M. Girard, *Étude d'un Jet Supersonique de Plasma Entretenu par Laser*, Ph.D. Thesis, University of Paris-sud, Orsay, (1994).

[31] S.C. Snyder, A.B. Murphy, D.L. Hofeldt, and L.D. Reynolds, *Phys. Rev. E* **52**, 2999 (1995).

[32] A.B. Murphy, *J. Phys. D: Appl. Phys.* **27**, 1492 (1994).

[33] R.B. Fraser, F. Robben, and L. Talbot, *Phys. Fluids* **14**, 2317 (1971).

[34] M.C.M. van de Sanden, R. van den Bercken, and D.C Schram, *Plasma Sources Sci. Technol.* **3**, 511 (1994).

[35] H.J.G. Gielen, *On the Electric and Magnetic Field Generation in Expanding Plasmas*, Ph.D. Thesis, Eindhoven University of Technology, Eindhoven (1989).

[36] S. Mazouffre, M.G.H. Boogaarts, J.A.M. van der Mullen, and D.C. Schram, *Phys. Rev. Lett.* **84**, 2622 (2000).

[37] J. Winter, *Plasma Phys. Control. Fusion* **38**, 1503 (1996).

[38] U. Samm and the TEXTOR-94 Team, *Plasma Phys. Control. Fusion* **41**, B57 (1999).

[39] M.C.M. van de Sanden, J.M. de Regt, and D.C. Schram, *Phys. Rev. E*, **47**, 2792 (1993).

[40] M.C.M. van de Sanden, R. van den Bercken, and D.C Schram, *Plasma Sources Sci. Technol.* **3**, 501 (1994).

[41] V.M. Lelevkin, D.K. Otorbaev, and D.C. Schram, *Physics of Non-Equilibrium Plasmas*, North-Holland, Amsterdam (1992).

[42] G.M.W. Kroesen, D.C. Schram, and J.C.M. de Haas, *Plasma Chem. Plasma Proc.* **10**, 531 (1990).

[43] J.J. Beulens, D. Milojevic, D.C. Schram, and P.M. Vallinga, *Phys. Fluids B* **3**, 2548 (1991).

[44] H. Maecker, *Z. Naturforsch* **11a**, 457 (1956).

[45] W.M.M. Kessels, A. Leroux, M.G.H. Boogaarts, J.P.M. Hoefnagels, M.C.M. van de Sanden, and D.C. Schram, *J. Vac. Sci. Technol. A* **19**, 467 (2001); M. Playez, Von Karman Institute for Fluid Dynamics, Belgium, private communication.

[46] G. Janssen, *Design of a General Plasma Simulation Model*, Ph.D. Thesis, Eindhoven University of Technology, Eindhoven (2000).

[47] H.F. Döbele, *Plasma Sources Sci. Technol.* **9**, 477 (2000).

[48] H. Kempkens and J. Uhlenbusch, *Plasma Sources Sci. Technol.* **9**, 492 (2000).

[49] M.C.M. van de Sanden, J.M. de Regt, G.M. Janssen, D.C. Schram, J.A.M. van der Mullen, and B. van der Sijde, *Rev. Sci. Instrum* **63**, 3369 (1992).

[50] R.F.G. Meulenbroeks, R.A.H. Engeln, J.A.M. van der Mullen, and D.C. Schram, *Phys. Rev. E* **53**, 5207 (1996).

[51] R. Engeln, K.G.Y. Letourneur, M.G.H. Boogaarts, M.C.M. van de Sanden, and D.C. Schram, *Chem. Phys. Lett.* **310**, 405 (1999).

[52] J.D. Buck, D.C. Robie, A.P. Hickman, D.J. Bamford, and W.K. Bischel, *Phys. Rev. A* **39**, 3932 (1989).

[53] W.M.M. Kessels, *Remote Plasma Deposition of Hydrogenated Amorphous Silicon*, Ph.D. Thesis, Eindhoven University of Technology, Eindhoven (2000), and references herein.

[54] A. de Graaf, *Deposition of CNH Materials*, Ph.D. Thesis, Eindhoven University of Technology, Eindhoven (2000), and references herein.

[55] M.J. de Graaf, *A New Hydrogen Particle Source*, Ph.D. Thesis, Eindhoven University of Technology, Eindhoven (1994).

[56] A.T.M. Wilbers, *A Wall Stabilized Arc as a Light Source for Spectroscopic Techniques*, Ph.D. Thesis, Eindhoven University of Technology, Eindhoven (1991).

[57] R.F.G. Meulenbroeks, D.C. Schram, M.C.M. van de Sanden, J.A.M. van der Mullen, *Phys. Rev. Lett.* **76**, 1840 (1996).

Chapter 2

Dynamics of a plasma expansion

Abstract

After presenting the basic hydrodynamic equations that govern the flow of a gas(plasma) in the continuum regime, a set of simplified conservation laws applying to a steady isentropic flow is derived. In first order approximation the expansion of a weakly ionized plasma (ionization degree < 1 %) is similar to the expansion of a hot neutral gas, and can be described using the well established supersonic expansion theory. Therefore a detailed description of the continuum free jet flow structure that results from the free expansion of a fluid from a high pressure region into a vacuum is given. In short, the gas first expands supersonically. After adapting to the local pressure conditions imposed by the residual background gas via the formation of a stationary shock wave system, the gas flows subsonically into the low pressure environment. Departures from the perfect free jet flow picture, when approaching the rarefied(molecular) regime, are also discussed. Finally, the characteristics of a gas shock wave are presented and several theoretical expressions are given for the on-axis density and velocity profile within a shock region.

2.1 Introduction

In this chapter we propose to convey to the non specialist reader the basic features of a plasma expansion. All plasmas studied in this thesis (Ar-H_2, He-H_2, D_2-H_2, H_2) are characterized by a low ionization degree at the source exit (< 1 %). The effects of charged particles on the neutral particle transport properties are therefore neglected. As a consequence, the expansion of a weakly ionized plasma can be treated as the expansion of a hot neutral gas [1]. The transport of charged particles in a partially ionized plasma expansion (ionization degree ≈ 10 %) has been studied in the past [2, 3, 4]. It was shown that the electron(ion) flow can to a large extent be described using the neutral gas expansion theory taking into account recombination processes in the energy balance.

A gas expansion corresponds to a free flow from a high pressure (p_o) region, often referred to as the source region or reservoir, into a low pressure (p_{back}) environment, the so-called background, through an orifice. When the pressure ratio p_o/p_{back} exceeds a critical value (e.g. 2.1 for a monoatomic gas), the gas velocity at the source exit is equal to the local speed of sound (sonic orifice). Then the gas accelerates to supersonic velocity and the flow becomes adiabatic. At some distance from the source, depending on p_{back}, the flowing gas collides with the residual background gas that results in the formation of a stationary shock wave through which the supersonic flow adapts to the local subsonic conditions.

First, the general conservation laws which govern the behavior of a fluid on a macroscopic scale are presented and the specific case of a steady adiabatic flow is discussed as it applies well to the description of a neutral gas expansion. The validity of a macroscopic approach for the treatment of an expansion is discussed. Second, on the basis of the equations of hydrodynamics, we describe in detail the continuum free jet flow structure that results from the expansion of a fluid. Finally, a section is devoted to the shock wave properties as it is an important feature of a gas expansion.

2.2 Governing equations

2.2.1 The Boltzmann transport equation

The Boltzmann transport equation describes the time evolution of the distribution function $f(\vec{\mathbf{r}}, \vec{\mathbf{v}}, t)$ of a given species in the six dimension phase space [5]. It is a nonlinear equation which describes the irreversible evolution of the fluid towards Local Thermodynamic Equilibrium (LTE). The Boltzmann equation reads

$$\frac{\partial f}{\partial t} + \vec{\mathbf{v}} \cdot \vec{\nabla} f + \frac{\vec{\mathbf{F}}}{m} \cdot \vec{\nabla}_v f = \left(\frac{\partial f}{\partial t} \right)_{coll-rad}, \tag{2.1}$$

where $\vec{\mathbf{F}}$ represents forces which act on the system (in a plasma the forces are mainly of electromagnetic origin), m is the mass, and $\vec{\nabla}_v$ is the gradient in the velocity space. The right hand side of Eq. 2.1 describes the changes in the distribution function as a result of elastic and inelastic collisions and as a result of radiative processes.

On a microscopic scale the state of the system, i.e. departure from equilibrium, is entirely defined when the distribution function f is known. If the system is in thermodynamic equilibrium, then the Maxwell distribution function is solution of the Boltzmann transport equation [5]. However it is most of the time difficult to directly access the distribution function and therefore assumptions have to be made about the thermodynamic state of the system. For that reason it is often easier to consider the system on a macroscopic scale and to follow the evolution of quantities like particle density, average velocity, and temperature. The equations describing the evolution in time and space of those thermodynamic quantities, the so-called conservation laws, are deduced from the calculation of the velocity moments of the Boltzmann transport equation. This calculation is based on a decomposition of the velocity $\vec{\mathbf{v}}$ in a random component $\vec{\mathbf{v}}^{\,r}$ and a drift component $\vec{\mathbf{w}}$ using the formalism of Braginskii [6].

2.2.2 Conservation laws and EOS

The conservation laws represent the conservation of mass, momentum and energy in space and time and they form the gas dynamics set of equation [7]. Those equations can only be used in the hydrodynamic regime, i.e. when the fluid can be considered as a continuous medium. The validity of the hydrodynamic approach is discussed in section 2.3.3.

- **Continuity equation**

The conservation of mass is insured by the continuity equation

$$\frac{\partial n}{\partial t} + \vec{\nabla} \cdot (n\vec{\mathbf{w}}) = S, \tag{2.2}$$

where n is the density and $\vec{\mathbf{w}}$ the drift velocity. The right hand side represents the source term, i.e. the particles production and destruction due to radiative and collisional processes.

- **Momentum conservation**

The principle of conservation of momentum is in fact an application of Newton's second law of motion to an element of fluid. The intrinsic momentum equation is given by

$$nm\frac{\partial \vec{\mathbf{w}}}{\partial t} + nm(\vec{\mathbf{w}} \cdot \vec{\nabla}) \cdot \vec{\mathbf{w}} + \vec{\nabla} p + \vec{\nabla} \cdot \vec{\vec{\mathbf{\Pi}}} = qn(\vec{\mathbf{E}} + \vec{\mathbf{w}} \times \vec{\mathbf{B}}) + \vec{\mathbf{R}}, \tag{2.3}$$

where m is the mass of the specie, p is the pressure, $\vec{\vec{\mathbf{\Pi}}}$ is the viscosity tensor, q is the charge of the particle, and $\vec{\mathbf{R}}$ represents the exchange of momentum between different species by means of collisions. Both electric field $\vec{\mathbf{E}}$ and magnetic field $\vec{\mathbf{B}}$ are related to each other via the Maxwell equations [8].

- **Energy conservation**

The principle of conservation of energy amounts to an application of the first law of thermodynamics to a fluid element as it flows. Note that an element of gas has two forms of energy: kinetic energy and internal or thermal energy (molecular gases have additional degrees of freedom of vibration and rotation). The intrinsic energy equation reads

$$\frac{\partial}{\partial t}(n\varepsilon) + \vec{\nabla} \cdot (n\varepsilon \vec{\mathbf{w}}) + p\vec{\nabla} \cdot \vec{\mathbf{w}} + \vec{\vec{\mathbf{\Pi}}} : \vec{\nabla}\vec{\mathbf{w}} + \vec{\nabla} \cdot \vec{\mathbf{q}} = Q, \tag{2.4}$$

where ε is the internal energy, $\varepsilon = \frac{3}{2}k_B T$ with k_B the Boltzmann constant and T the temperature, $\vec{\mathbf{q}}$ the heat flux, and Q the heat transfer term. The latter denotes the energy gain or loss through elastic/inelastic collisions and chemical reactions. For an isotropic fluid the thermal heat flux $\vec{\mathbf{q}}$ is given by

$$\vec{\mathbf{q}} = -\kappa \vec{\nabla} \cdot T. \tag{2.5}$$

This is the Fourier heat conduction law [7], also called general equation of heat transfer. The coefficient κ is the thermal heat conductivity which is usually a function of the temperature [9].

- **Equation of state (EOS)**

The perfect gas law is used as an equation of state. It reads

$$p = nk_B T. \tag{2.6}$$

Dalton's law relates the partial pressures p_i of a species i to the total pressure of a gas mixture

$$p = \sum_i p_i. \tag{2.7}$$

- **Conducting fluid: additional equations**

A plasma can be considered as a conducting fluid since it contains in addition to neutral particles charged particles, i.e. electrons and ions. The transport of charged particles is strongly influenced by electric and magnetic fields, therefore Maxwell equations have to be included in the set of governing equations [8]. Furthermore, quasi-neutrality is usually assumed for the studied plasmas [10], i.e. the electron density approximately equals the ion density.

Seeing that a plasma contains neutral as well as charged particles, several sets of conservation laws are needed, one per kind of particles [11, 3]. If the velocity and temperature of ions and neutral particles are not too different, then they can be treated as one group: the heavy particles. The different fluids are coupled together by means of friction and energy exchange. This coupling is complex, and a detailed analysis of the time scale of

the interactions between the different kinds of particles is needed. The ionization degree of the expanding plasma studied in this thesis is usually low (< 1 %), i.e. the electron(ions) density is low compared to the neutral density, therefore the influence of charged particles on the transport of neutral particles is small and has been ignored.

The knowledge of the conservation laws, the equation of state, and the specific equations applying to a conducting fluid is not enough to wholly describe a plasma dynamical flow. One also needs appropriate boundary conditions to find the appropriate solutions of the equation system.

2.2.3 Steady isentropic flow

The expansion into a vacuum of a neutral gas or a plasma can be considered as a steady expansion contrary for instance to the expansion of a pulsed laser created plasma for which time dependent phenomena are of importance [13, 14].

To a good approximation, the flow which is initially in thermodynamic equilibrium can be assumed to be adiabatic [15], and therefore all dissipative effects, i.e. losses through line and continuum radiation, heat transfer, are absent. If besides the flow is laminar (high Reynolds number), the expansion is isentropic ($dS = 0$ where S is the entropy). Furthermore, in order to go even further in the simplification of the conservation laws, several assumptions are made: the Lorentz force is neglected (we only consider the transport of neutral particle in this work) and viscosity (internal dissipation of energy) is also neglected. The previous remarks lead to a simplification of the conservation laws. We then obtain the set of equation governing a steady isentropic flow.

- The mass balance reads

$$\vec{\nabla} \cdot (n\vec{\mathbf{w}}) = 0. \tag{2.8}$$

- The momentum balance is written as

$$nm(\vec{\mathbf{w}} \cdot \vec{\nabla}) \cdot \vec{\mathbf{w}} = -\vec{\nabla}p. \tag{2.9}$$

If the flow is not rotating (curl $\vec{\mathbf{w}} = \vec{0}$) then we obtain

$$\frac{1}{2}nm\vec{\nabla}w^2 = -\vec{\nabla}p. \tag{2.10}$$

- The energy conservation equation is replaced by the Poisson adiabatic law [7]

$$\left(\frac{n}{n_\mathrm{o}}\right)^{\gamma-1} = \frac{T}{T_\mathrm{o}}, \tag{2.11}$$

where $\gamma = \frac{c_p}{c_V}$ is the specific heat ratio, also called adiabatic exponent or isentropic exponent, which is equal to $\frac{5}{3}$ for monoatomic gases, $\frac{7}{5}$ for rigid diatomic molecules, and $\frac{9}{7}$ for non rigid diatomic molecules.

2.3 Supersonic expansion: the continuum free jet structure

2.3.1 Speed of sound and Mach number

From the hydrodynamic equations one shows that small adiabatic disturbances like small changes in pressure propagate inside a compressible fluid with speed c_s, the so-called speed of sound. The latter is derived from the wave equation which describes the propagation of a density change [12, 16]

$$c_s^2 = \left.\frac{\partial p}{m\partial n}\right|_{dS=0}. \tag{2.12}$$

Note that the speed of sound is a thermodynamic variable. A sound wave is thus an oscillatory motion with small amplitude in a compressible fluid. The propagation of a sound wave is an adiabatic process in which a change in internal energy is caused by expansion or compression of a fluid element. In an ideal gas the local speed of sound reads

$$c_s = \sqrt{\frac{\gamma k_B T}{m}}. \tag{2.13}$$

The sound speed is in the order of the mean thermal speed of the gas. The flow velocity of a fluid can be compared to the speed of sound. For this purpose, a dimensionless number, the Mach number, is introduced. The Mach number M is defined as follows

$$M = \frac{w}{c_s}, \tag{2.14}$$

where w is the drift velocity of the fluid. According to the Mach number, three different flow regimes can be distinguished

- $M > 1$: supersonic flow,
- $M = 1$: sonic flow,
- $M < 1$: subsonic flow.

As we will see, in the case of a gas(plasma) expansion, the flow undergoes a transition from a supersonic regime to a subsonic regime. The transition, which corresponds to the adaptation to the local ambient conditions, is realized via the formation of a shock wave structure.

2.3.2 Free jet flow

The basic phenomena of the expansion of a weakly ionized plasma are to some extent similar to those of the expansion of a hot neutral gas, and can thus be described using the adiabatic supersonic expansion theory [1, 17, 18]. In the expansion of a weakly ionized plasma, because of several heating mechanisms, the temperature remains higher than in

neutral gas adiabatic expansions. The expansion of a plasma can thus be described as a common density rarefaction because of the supersonic expansion, modified to account for disturbances to an isentropic flow.

When a fluid expands freely through an orifice from a high pressure region (source) into a region with a finite pressure rather than perfect vacuum, a well defined free jet shock wave structure is produced [1, 19, 20], as depicted in Fig. 2.1, due to the interaction of the supersonic flow with the residual background gas. In the hydrodynamic flow regime, the gas(plasma) starts to expand from a sonic orifice where the Mach number M equals to 1 and the supersonic flow ends in the formation of a normal stationary shock wave. In the supersonic domain, the density decreases rapidly because of a rarefaction effect (increase in the jet diameter). The gas is accelerated to supersonic velocity over a few source orifice diameter, because of conversion of the thermal energy gained in the source into kinetic energy, i.e. directed motion. As a consequence, the temperature decreases. One has to distinguish between the perpendicular temperature $T_\perp$ and the parallel temperature $T_\parallel$ associated respectively with the velocity distribution perpendicular and parallel to a stream line. If the background pressure is low enough, the collision frequency becomes at one point so low that the flow reaches a steady state [21], in which both the velocity and the parallel temperature are frozen. Behind this limit, $T_\perp$ continues to drop (geometric cooling), and the flow is in non-equilibrium. At the source outlet, the decay in temperature is adiabatic in the case of a neutral gas expansion and the adiabatic exponent γ stays constant. In the case of a plasma, dissipative processes like friction (viscosity) and heat transfer can disturb the cooling mechanism leading to a quasi-adiabatic expansion with a low γ. The isentropic exponent γ depends also on the ionization degree [3, 11, 22]. However, this effect is negligible in view of the very low ion density of all plasmas studied in this thesis.

In radial direction the free jet is limited by the jet boundary and a preceding barrel shock wave. The internal core, the so-called zone of silence, corresponds to the region where the flow is not disturbed by the background gas. In this zone, the particles propagate with a speed higher than the sound speed, and no information can be received from the surroundings.

At the source exit, the flow is underexpanded (jet static pressure > background pressure), but after some distance, it becomes overexpanded (jet static pressure < background pressure) and has to adapt the local ambient gas conditions. As a result, a stationary compression shock wave is formed due to the collision of the moving fluid with the residual background gas. Over the shock wave the flow experiences a transition from a supersonic regime to a subsonic regime. Both the position and the thickness of the normal shock wave depend on the background pressure. Across the shock wave, the flow adapts its pressure to the local pressure, the gas is compressed and the density increases. Since the forward flux is conserved, the velocity drops accordingly. Because of collisions, the kinetic energy is converted back into thermal energy, i.e. random motion, and the temperature increases. Within the shock wave the entropy increases. Moreover, at low pressure, the flow is laminar in the shock region and turbulent mixing does not occur. The dimensionless Reynolds

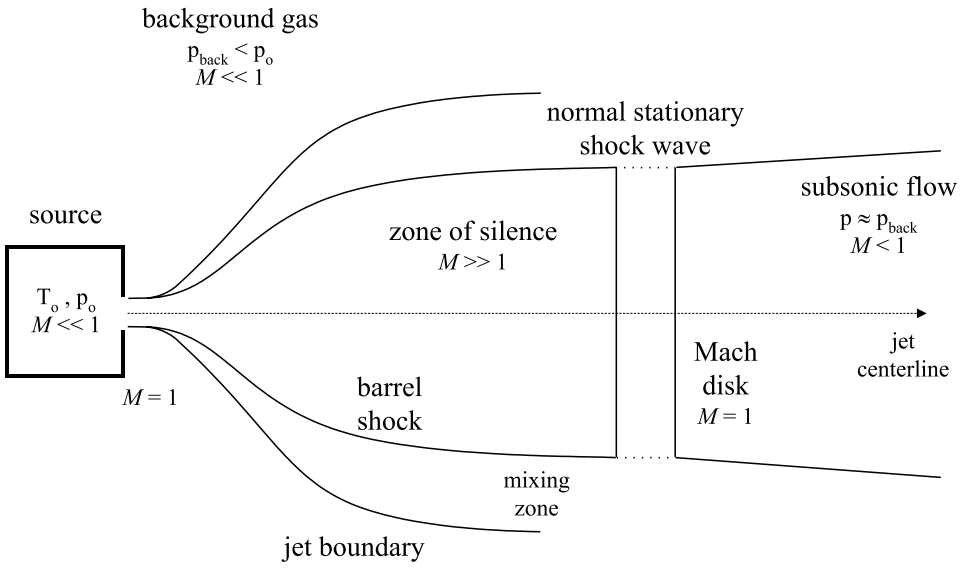

Fig. 2.1: Schematic view of the continuum free jet flow structure created when a fluid expands freely from a high pressure region into a low pressure region.

number Re [7] is defined as

$$Re = \frac{nmwl}{\mu}, \tag{2.15}$$

with l a characteristic length scale of the system and μ the dynamic viscosity. For a free jet flow, if $Re < 10^3$ the flow is laminar, else the flow is turbulent. Inside the shock front of an argon jet ($\mu = 5 \times 10^{-5}$ kg m^{-1} s^{-1}), one finds $Re \approx 30$ at 20 Pa ($l = 10$ cm) and $Re \approx 150$ at 100 Pa ($l = 5$ cm). The features of a shock wave are described in section 2.4.

At the Mach disk location z_M, often referred as the end of the shock wave, $M = 1$ and the flow enters the subsonic regime. The position z_M is given by

$$z_M = Cd\sqrt{\frac{p_{\mathrm{stag}}}{p_{\mathrm{back}}}}, \tag{2.16}$$

where d is the source outlet diameter, p_{stag} is the stagnation pressure in the source and p_{back} is the background pressure. The constant C depends slightly on γ; it equals 0.7 for an atomic gas. The preceding expression can be rewritten in terms of flow and atomic mass number [23]. It has been experimentally discovered by Ashkenas *et al* [17] and later demonstrated theoretically by Young [24].

Behind the Mach disk, the gas expands subsonically and mixes with the background gas. The evolution of the flow is then mainly geometrically determined (general circulation pattern, residence time). The transport of any particle is controlled by diffusion. The flow velocity decreases because of momentum transfer to the ambient gas particles. The temperature decreases because of heat transfer (to the vessel walls for instance). The pressure is constant, therefore the density increases.

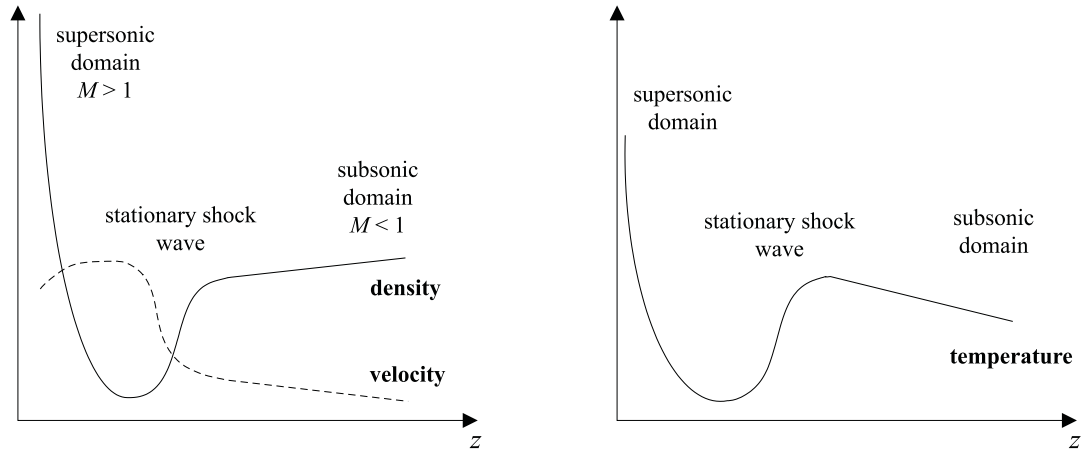

Fig. 2.2: Schematic representation of the fluid particle density and velocity development (left) and temperature development (right) along the jet centerline in the course of the fluid expansion.

A schematic representation of the development of the macroscopic quantities along the jet centerline of a free jet is depicted in Fig. 2.2 in the case of a continuum flow regime. In the supersonic domain, a theoretical expression for the on-axis density, temperature and velocity profile of a neutral gas flow can be derived from the hydrodynamic equations. Such expression are useful to compare the a neutral inert gas expansion to a plasma expansion and will be often used in this thesis.

- **Density development**

Using the conservation laws for a steady isentropic flow (see section 2.2.3), and under the assumption that the particles originate from a virtual point source and flow along straight stream lines, one can obtain the theoretical expression for the density development along the jet centerline

$$n(z) = n_{\mathrm{o}} \frac{z_{\mathrm{ref}}^2}{(z + z_{\mathrm{o}})^2}. \tag{2.17}$$

In Eq. 2.17, n_{o} is the particle density in the source, z_{ref} is a scaling length (determined by the early expansion and by the source orifice geometry), and z_{o} is the position of the virtual point source, i.e. the expansion origin. It means that the free jet flow can be described for $z >> d$ as a source expansion [17, 1, 2]. The expression is valid for an expansion with cylindrical symmetry as well as for an expansion with spherical symmetry [25, 26]. Another expression can be used [23]

$$n(z) = n_{\mathrm{o}} \frac{1}{1 + z^2/z_{\mathrm{o}}^2}. \tag{2.18}$$

This non-standard expression is connected with the plasma character of the source region with its high temperature, sonic exit velocity, and finite temperature gradients. It allows

for a zero first derivative of the density at the source point in order to accommodate for the convective processes in the source, as well as for field generation.

- **Temperature development**

For an adiabatic process, the energy equation can be replaced by the Poisson adiabatic formula (Eq. 2.11). Using Eq. 2.18 to express the density, one obtains for the temperature profile in the supersonic domain

$$T(z) = \frac{T_\mathrm{o}}{(1 + z^2/z_\mathrm{o}^2)^{\gamma-1}}. \tag{2.19}$$

In the case of a plasma expansion, the cooling mechanism is generally not adiabatic and the value of γ is lower than the adiabatic one.

- **Velocity development**

The velocity along the jet axis is obtained from the simplified momentum balance (Eq. 2.10) using the Poisson adiabatic law (Eq. 2.11). Two situations have to be distinguished. When the system is at rest in the source (expansion from a reservoir, $w(0) = 0$) the velocity reads

$$w(z) = \frac{c_{s,\mathrm{o}}}{\sqrt{\gamma-1}}\sqrt{2 - 2\left(\frac{n(z)}{n_\mathrm{o}}\right)^{\gamma-1}}. \tag{2.20}$$

The maximum achievable velocity, that corresponds to the total conversion of the thermal energy into kinetic energy, is

$$w_\mathrm{max} = c_{s,\mathrm{o}}\sqrt{\frac{2}{\gamma-1}}. \tag{2.21}$$

When the fluid is already flowing in the source before it starts expanding (case of thermal arc plasmas under investigation in this thesis) the velocity is given by

$$w(z) = \frac{c_{s,\mathrm{o}}}{\sqrt{\gamma-1}}\sqrt{\gamma + 1 - 2\left(\frac{n(z)}{n_\mathrm{o}}\right)^{\gamma-1}}, \tag{2.22}$$

when the fluid is assumed to flow in the source with the speed of sound ($w(0) = c_{s,\mathrm{o}}$ or $M(0) = 1$). The maximum velocity is

$$w_\mathrm{max} = c_{s,\mathrm{o}}\sqrt{\frac{\gamma+1}{\gamma-1}}. \tag{2.23}$$

2.3.3 Rarefied regime: evanescent shock structure

A measure of the validity of the continuum assumption is given by the calculation of the dimensionless Knudsen number Kn [12]

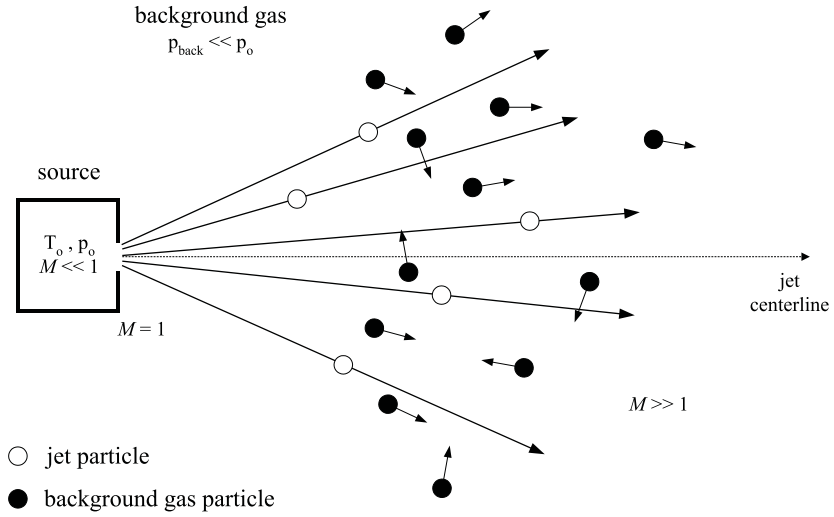

Fig. 2.3: Free jet flow in rarefied (molecular) regime. The shock wave structure becomes evanescent and background gas particles invade the final stage of the supersonic domain of the jet.

$$Kn = \frac{\lambda}{l}, \tag{2.24}$$

where λ is the mean free path for momentum exchange and l is a characteristic length scale of the system. If $Kn < 0.2$ then the flow is said to be in hydrodynamic regime and the continuum model is applicable [27]. As Kn approaches unity, the flow enters the free molecular regime, or rarefied regime, and one has to use the molecular dynamics theory.

The use of hydrodynamics to describe a fluid expansion is only strictly valid in the first few millimeters of the flow. At a relatively high background pressure the flow can always satisfactorily be described using hydrodynamic equations. However at low pressure the flow undergoes a transition between hydrodynamic and free molecular regime and gas kinetic theory is needed.

When the Knudsen number starts to become high, $Kn > 0.2$, the fluid can not be approximated as a continuous medium, and departure from the perfect free jet flow picture occurs [28]. In a transition regime between continuum and rarefied, the shock wave structure is diffuse enough to allow penetration, and the zone of silence is invaded by the residual peripheral gas particles, as depicted in Fig. 2.3. This occurs mainly in the final stage of the free jet expansion, where the barrel shock wave becomes evanescent. The invasion process is strongly mass selective (diffusion process) in favor of the light species. It has been studied as a possible means for aerodynamic separation of mixtures and isotopes [29, 30]. Invasion by the ambient gas particles modifies the shock wave formation mechanisms and influence a priori the distribution function within the normal shock wave. Those effects are discussed in chapter 9 and 10. Deep into the rarefied flow regime, the velocity remains supersonic because of scarce collision events and the shock structure vanishes.

2.4 Shock wave

2.4.1 Properties of a shock wave

A shock wave or shock front is an example of a surface of discontinuity in the field of fluid dynamics [7, 12, 16]. Over a shock wave, the distribution of thermodynamic quantities such as pressure and temperature as well as the distribution of the normal velocity is discontinuous. Certain boundary conditions must be satisfied on a surface of discontinuity: the mass flux, the energy flux as well as the momentum flux must be conserved. This set of conditions forms the so-called shock condition. In the case of an infinitely narrow shock wave it leads to the jump relations for the density, velocity and temperature (see next section). As every thermodynamic variable, entropy is also discontinuous at a shock wave. The entropy increases due to dissipative processes in the shock wave meaning that the gas motion is irreversible. Thus shock waves are a means by which energy can be dissipated in the motion of an ideal fluid.

In general shock waves are classified according to the sign of the pressure jump across the surface: $P = p_2 - p_1$ where the subscript 1 and 2 refer to the quantities ahead of and behind the shock wave respectively. If $P > 0$, respectively $P < 0$, the shock wave is said to be a compression shock, respectively a rarefaction shock [31]. From the entropy balance, and referring to Hugoniot adiabatic, it follows that only compression shocks are possible for the case of a perfect gas with constant specific heats.

For a compression shock wave, the conditions are the following [7]

$$\begin{aligned} & p_1 < p_2, V_1 > V_2, w_1 > w_2 \\ \text{and} \quad & w_1 > c_{s,1}, w_2 < c_{s,2}, \end{aligned}$$

where V is the specific volume. Therefore the upstream flow ahead of the shock wave is supersonic whereas the downstream flow behind the shock wave is subsonic.

2.4.2 Rankine-Hugoniot relations

The so-called Rankine-Hugoniot relations [7, 12] connect the jump in density, velocity and temperature across the shock wave to the Mach number M_1 ahead of the shock front

$$\frac{n_2}{n_1} = \frac{w_1}{w_2} = \frac{(\gamma+1)M_1^2}{(\gamma-1)M_1^2+2}, \tag{2.25}$$

$$\frac{T_2}{T_1} = \frac{\left[2\gamma M_1^2 - (\gamma-1)\right]\left[(\gamma-1)M_1^2+2\right]}{(\gamma+1)^2 M_1^2}. \tag{2.26}$$

The Rankine-Hugoniot relations represent the conservation of flux and energy across a shock front when the latter is infinitely narrow (proper surface of discontinuity). In the case of very strong shock waves, i.e. M_1 tends to infinity, the temperature ratio increases to infinity, whereas the density ratio tends to a constant limit, i.e. $(\gamma+1)/(\gamma-1)$. Therefore for a monoatomic gas ($\gamma = \frac{5}{3}$), the maximum achievable compression ratio is 4.

2.4.3 Shock wave thickness

The treatment of shock waves as discontinuities of zero thickness is an idealization of inviscid gas dynamics. Shock waves in which the discontinuities are small are not geometrical surfaces with zero thickness, but are in reality transition layers with finite thickness. The thickness of a shock front decreases as the magnitude of the discontinuities increases. To determine the structure and the thickness of the transition layer, viscosity and thermal conductivity of the gas, i.e. dissipative effects, have to be taken into account.

The shock thickness L in the z direction is defined as

$$L = \frac{w(-\infty) - w(+\infty)}{|dw/dz|_{\text{mean}}} = (w_1 - w_2) \left.\frac{dz}{dw}\right|_{\text{mean}}, \tag{2.27}$$

according to the Prandtl formalism [32]. In the same manner, the thickness can be defined according to the density jump. Using the continuum theory the shock thickness can also be expressed as a function of the Mach number ahead of the shock front

$$L \approx \frac{8\lambda}{3(M_1 - 1)}, \tag{2.28}$$

where λ is the momentum exchange mean free path of the fluid particles. Thus the thickness of a shock wave is of the same order of magnitude as the mean free path. It follows that the method of gas dynamics, where the gas is treated as a continuous medium, cannot strictly be used to investigate the internal structure of a shock wave (see chapter 9).

When the $Kn < 0.2$ ahead of the stationary shock wave of a free jet (continuum flow regime), the diameter of the jet is constant within the shock region and the Rankine-Hugoniot (RH) relations hold. In the rarefied regime $0.5 < Kn < 0.2$, a departure from the RH relations is possible caused by an increase in the jet diameter but also by the invasion of the jet by the background gas particles.

2.4.4 Shock wave profile

Hydrodynamic approximation

When the continuum approach is valid, and in the low intensity shock wave approximation (low M), the velocity profile across the shock front of a free jet flow can be calculated from the Navier-Stokes equation [12, 33, 34]. This leads to the Taylor shock structure solution for the development of the drift velocity w along the direction z normal to the shock front

$$\frac{\gamma + 1}{2a}(w_1 - w_2)z = \ln\left(\frac{w_1 - w(z)}{w(z) - w_2}\right), \tag{2.29}$$

where $z = 0$ refers to the center of the shock front and a is a coefficient related to acoustic attenuation [12]. In first order approximation, this coefficient can be estimated using the gas kinetic theory to express the viscosity and the thermal conductivity of the gas. One

obtains $a = \lambda c_s$. From the flux conservation, one can derive the density distribution over the shock wave

$$\frac{\gamma+1}{2a} w_1 \left(1 - \frac{n_1}{n_2}\right) z = \ln\left[\frac{n_2\left(n(z) - n_1\right)}{n_1\left(n_2 - n(z)\right)}\right]. \tag{2.30}$$

A more complex approach consists of using the Burnett equations of hydrodynamics as they appear from the Chapman-Enskog solution to the Boltzmann equation [35]. More information about hydrodynamic models can be found in reference [34] and [35].

Solution of the Boltzmann equation

In the case of a strong shock wave or when the continuum assumption is no longer legitimate, the shock structure can only be investigated using the kinetic theory, i.e. by looking directly at the solution of the Boltzmann transport equation. It is a complex problem mainly caused by the nonlinearity of the Boltzmann equation. A possible way of solving the problem is to calculate the numerical solution of the Boltzmann equation by direct Monte-Carlo simulation method [38, 39].

In this thesis we only propose to look at a simple approach that consists of solving the Boltzmann equation assuming that the distribution function within the shock wave can be decomposed into two Maxwellian terms (see chapter 3 and 8). This approach has been first proposed by Mott-Smith [36] about fifty years ago and later extended by several authors [32, 37]. Under the assumption of a bimodal distribution, one obtains an approximate solution to the Boltzmann equation; then using the conservation laws a theoretical density and velocity profile throughout the shock region is determined

$$\frac{n(z)}{n_1} = \frac{w_1}{w(z)} = \frac{1 + \left(\frac{n_2}{n_1}\right)\exp\left(\frac{4z}{L}\right)}{1 + \exp\left(\frac{4z}{L}\right)}. \tag{2.31}$$

Eq. 2.31 is often used to model shock wave profiles at the limit of the continuum flow regime. In the case of inert neutral particle expansion, the theoretical profiles are in good agreement with the measured data [40, 41].

2.5 Conclusions

The set of equations governing the transport of neutral particles in the expansion of a weakly ionized plasma as well as the main characteristics of the free expansion process have been briefly presented. As we will see in the rest of this thesis, apart from the fact that due to the high plasma temperature the flow is not adiabatic, the inert neutral (e.g. Ar atoms or H_2 molecules) flow is in good agreement with the free jet flow theory. On the contrary, the reactive particle (e.g. H or D atoms) flow deviates significantly from the classical picture. It will be demonstrated step by step that surface chemistry, surface recombination of radical to form stable molecules in that case, strongly influences the transport mechanisms of any kind of radicals in plasma expansions.

References

[1] D.R. Miller, in *Atomic and Molecular Beam Methods*, edited by G. Scoles, Oxford University, New York (1988).

[2] R.B. Fraser, F. Robben, and L. Talbot, *Phys. Fluids* **14**, 2317 (1971).

[3] M.C.M. van de Sanden, R. van den Bercken, and D.C. Schram, *Plasma Sources Sci. Technol.* **3**, 511 (1994).

[4] M.C.M. van de Sanden, J.M. de Regt, and D.C. Schram, *Phys. Rev. E* **47**, 2792 (1993).

[5] L.D. Landau and E.M. Lifschitz, *Statistical Physics*, Pergamon, London, (1968).

[6] S.I. Braginskii, *Reviews of Plasma Physics*, ed. M.A. Leontovich, Plenum, New York, (1965).

[7] L.D. Landau and E.M. Lifschitz, *Fluid Mechanics*, Pergamon, London, (1989).

[8] J.D. Jackson, *Classical Electrodynamics*, Wiley, New York, (1975).

[9] M.I. Boulos, P. Fauchais, and E. Pfender, *Thermal Plasmas, Fundamentals and applications*, Vol. 1, Plenum Press, New York, (1994).

[10] J.L. Delcroix, *Plasma Physics*, Wiley, London, (1968).

[11] M.C.M. van de Sanden, *The Expanding Plasma Jet: Experiments and Model*, Ph.D. Thesis, Eindhoven University of Technology, The Netherlands (1991).

[12] P.A. Thompson, *Compressible-fluid dynamics*, McGraw-Hill, New York, (1972).

[13] *Pulsed Laser Deposition of Thin Films*, edited by D.B. Chrisey and G.K. Hubler, Wiley, New York (1994).

[14] K.R. Chen, T.C. King, J.H. Hes, J.N. Leboeuf, D.B. Geohegan, R.F. Wood, A.A. Puretzky, and J.M. Donato, *Phys. Rev. B* **60**, 8373 (1999).

[15] O. Buneman, *Phys. Fluids* **4**, 669 (1961).

[16] Y.B. Zel'dovich and Y.P. Raizer, *Physics of Shock Waves and High Temperature Hydrodynamic Phenomena*, Academic Press, New York (1966).

[17] H. Ashkenas and F.S. Sherman, *Proceedings Rarefied Gasdynamics* **4**, Academic Press, New York, Vol. 2, 84 (1966).

[18] R. Campargue, *J. Chem. Phys.* **88**, 4466 (1984).

[19] H.C.W. Beijerinck, R.J.F. van Gerwen, E.R.T. Kerstel, J.F.M. Martens, E.J.W. van Vliembergen, M.R.Th. Smits, and G.H. Kaashoek, *Chem. Phys.* **96**, 153 (1985).

[20] J.H. Fox, *AIAA Journal* **12**, 105 (1974).

[21] H.C.W. Beijerinck and N.F. Verster, *Physica* **111C**, 327 (1981).

[22] K.T.A.L. Burm, W.J. Goedheer, and D.C. Schram, *Phys. Plasmas* **6**, 2622 (1999).

[23] D.C. Schram, S. Mazouffre, R. Engeln, and M.C.M. van de Sanden, in *Atomic and Molecular beams*, edited by R. Campargue, Springer, New York, 209 (2001).

[24] W.S. Young, *The Physics of Fluids* **18**, 1421 (1975).

[25] B.B. Hamel and D.R. Willis, *Phys. Fluids* **9**, 829 (1966).

[26] J. Goldfinch, *J. Plasma Phys.* **6**, 153 (1971).

[27] G.A. Bird, *Molecular Gas Dynamics and the Direct Simulation of Gas Flows*, Clarendon Press, Oxford (1994).

[28] E.P. Muntz, B.B. Hamel, and B.L. Maguire, *AIAA Journal* **8**, 1651 (1970).

[29] R. Campargue, *J. Chem. Phys.* **52**, 1795 (1970).

[30] J.W. Brook, V.S. Calia, E.P. Muntz, B.B. Hamel, P.B. Scott, and T.L. Deglow, *J. Energy* **4**, 199 (1980).

[31] N.M. Bulgakova, *Phys. Rev. E* **60**, R3498 (1999).

[32] C. Muckenfuss, *Phys. Fluids* **3**, 320 (1960).

[33] G.M. Janssen, J. van Dijk, D.A. Benoy, M.A. Tas, K.T.A.L. Burm, W.J. Goedheer, J.A.M. van der Mullen, and D.C. Schram, *Plasma Sources Sci. Technol.* **8**, 1 (1999).

[34] G.M. Janssen, *Design of a General Plasma Simulation Model*, Ph.D. thesis, Eindhoven University of Technology, The Netherlands (2000).

[35] F.J. Ubribe, R.M. Velasco, L.S. Carcía-Colín, and E. Díaz-Herrera, *Phys. Rev. E* **62**, 6648 (2000).

[36] H.M. Mott-Smith, *Phys. Rev.* **82**, 885 (1951).

[37] P. Glansdorff, *Phys. Fluids* **5**, 371 (1962).

[38] C. Cercignani, A. Frezzotti, and P. Grosfils, *Phys. Fluids* **11**, 2757 (1999).

[39] S. Takata, K. Aoki, and C. Cercignani, *Phys. Fluids* **12**, 2116 (2000).

[40] M.C.M. van de Sanden, J.M. de Regt, and D.C. Schram, *Plasma Sources Sci. Tecnol.* **3**, 501 (1994).

[41] H. Alsmeyer, *J. Fluid. Mech.* **74**, 497 (1976).

Chapter 3

Flow characteristics of a supersonically expanding thermal argon plasma [1]

Abstract

The transport of neutral argon atoms in an expanding thermal argon plasma seeded with 4 % of hydrogen is studied by means of laser induced fluorescence spectroscopy, on the long lived Ar[4s] atoms, and by UV Rayleigh scattering. The results of the latter confirm the inverse quadratic dependence of the argon atom density with distance from the nozzle in the supersonic part of the expansion. The measured atom density jump through the stationary shock wave can be described with the Rankine-Hugoniot relations. From the Doppler-shifted laser induced fluorescence measurements performed on Ar atoms in the metastable $Ar^*(^3P_2)$ and resonant $Ar^*(^3P_1)$ states, it is inferred that the velocity behavior of the supersonically expanding argon gas can be predicted from the momentum balance, and the temperature from the Poisson adiabatic relation. However, the adiabatic constant is found to be smaller than the adiabatic constant of a neutral argon gas expansion. Non-Maxwellian distribution functions are measured along the jet centerline, both at the arc exit and across the stationary shock wave. The results on temperature and velocity in the subsonic region show that the radius of the plasma jet hardly increases after the stationary shock front, indicating that the flow pattern is geometrically determined.

[1] Adapted from:
R. Engeln, S. Mazouffre, P. Vankan, D.C. Schram, N. Sadeghi, accepted for publication in *Plasma Sources Sci. Technol.* (2001).

3.1 Introduction

Expanding thermal plasmas are interesting both from a fundamental point of view as well as from a view of the applicability. From a fundamental point of view, the plasma expansion is the basis for describing phenomena ranging from astrophysical objects and solar flares, the flow into the divertor region of a Tokamak, to laser spots and vacuum arc spots [1, 2, 3, 4]. In view of the applicability, expanding thermal plasmas are used for deposition of thin films, etching and passivation of surfaces, and treatment of archelogical artifacts [5]. Optimal energy conversion from the plasma source, via the expanding plasma, to the gases used for surface treatment or modification, is therefore of eminent importance. The study of the expansion process can substantiate the understanding of the conversion process.

Over the past years, extensive studies have been performed on expanding plasmas. Examples are Thomson-Rayleigh scattering measurements on the expansion properties of pure argon plasmas and argon/hydrogen plasmas, which supplied electron and neutral densities and electron temperatures [6, 7, 8, 9]. Coherent Anti-Stokes Raman scattering experiments on hydrogen plasmas deliver absolute densities of ro-vibrationally excited H_2 showing the importance of wall association and re-circulation of background gas [10]. In a study on the influence of wall recombination processes on the transport of radicals, two-photon laser induced fluorescence measurements on hydrogen atoms in an argon/hydrogen plasma are performed and atomic radical densities, temperatures and velocities are obtained [11, 12]. These studies give better insight in the physics of the expanding plasma, like recombination, excitation, wall association and re-circulation.

Starting from a remote ionizing plasma source, the plasma expands supersonically and becomes recombining. The supersonic flow domain ends in the formation of a stationary shock wave. Behind this shock wave the plasma flows subsonically into the background. In the downstream region of the plasma expansion molecules, e.g. SiH_4, CH_4 or C_2H_2, can be injected into the plasma jet [13]. Here they are fragmented via charge-exchange and dissociative recombination reactions into radicals. These molecular radicals are transported by the plasma flow towards a substrate. At the substrate they can stick to the surface and contribute to film growth, reflect from the surface or recombine at the surface forming 'new' species. Depending on the residence time of the gases in the vessel (about 0.5 s at 20 Pa) the newly formed species can re-circulate and subsequently influence the plasma flow pattern. The understanding of the mixing of the injected monomers and newly formed molecules with the plasma jet is important for optimal use of these species in the processes at hand.

In most of the studies and applications of the expanding plasma jet, argon is used as a carrier gas. Due to its relatively high mass, as compared to the one of injected gases like hydrogen, nitrogen or methane, the velocity with which the plasma expands will be to a large extend determined by the Ar velocity. We here report on laser induced fluorescence measurements on metastable argon atoms in an expanding thermal plasma generated from a mixture of argon with a few percent of hydrogen. From these measurements both the axial and radial velocity components and temperatures of the argon atoms are extracted.

The non-Gaussian velocity distributions in the shock region indicate a departure from thermodynamic equilibrium. It will be shown that the velocity and temperature in the supersonic region of the plasma expansion can be described as a neutral gas expansion with a modified value of the adiabatic exponent γ. Rayleigh scattering measurements are used to determine the total argon atom density and flux in the plasma jet.

3.2 Experimental arrangement

3.2.1 Cascaded arc

The cascaded arc in which a thermal plasma is created ($\hat{T} \approx 1$ eV) has been described in detail elsewhere [14]. The arc operates at subatmospheric pressure (0.6 bar) It consists of 4 insulated plates with a 3 mm diameter channel. Three cathodes are positioned concentrically around the channel. The nozzle, through which the plasma expands into a low pressure chamber, is composed of a straight channel (6 mm diameter, 10 mm length) followed by a diverging opening (45^o, 5 mm length). During the measurements presented here, a current of 40 A is drawn through the arc and an argon flow rate of 3.0 slm (standard liter per minute) is used. A flow of 0.12 slm H_2 is added to the argon flow to decrease the ion density, and thus the metastable density, in order to avoid any significant diminution of the laser intensity due to absorption by metastable atoms present on the laser beam trajectory before reaching the excitation volume. Moreover, H_2 quenches the Ar[$4s$] atoms present outside of the expanding jet and therefore avoids the reabsorption of the LIF photons by these atoms, before reaching the detector. The influence of molecular hydrogen on the very fast ionization loss in an expanding argon/hydrogen plasma has been reported by Meulenbroeks *et al* [15]. The electron and argon ion densities are reduced due to charge-exchange of Ar^+ with molecular hydrogen, followed by dissociative recombination of the ArH^+ ion forming Ar and excited atomic hydrogen. This leads to an ionization degree of less than 1 %.

3.2.2 LIF setup

A schematic view of the Laser Induced Fluorescence setup is depicted in Fig. 3.1. A single-mode cw external cavity diode laser (EOSI LCU 2010M), delivering about 10 mW of radiation, is used to excite Ar^* atoms in the expanding thermal plasma. The laser is tuned to the $1s_5 \rightarrow 2p_9$ transition at 811.53 nm or to the $1s_4 \rightarrow 2p_7$ transition at 810.37 nm [16]. The velocity along the laser beam, w_z, of the group of atoms in the metastable $1s_5$ and resonant $1s_4$ state absorbing the laser photons at frequency ν is deduced from the relation

$$w_z = c \times \frac{\nu - \nu_0}{\nu_0}, \tag{3.1}$$

where ν_0 is the transition frequency for atoms at rest and c the speed of light. In one configuration the laser beam propagates opposite to the flow direction of the plasma jet and

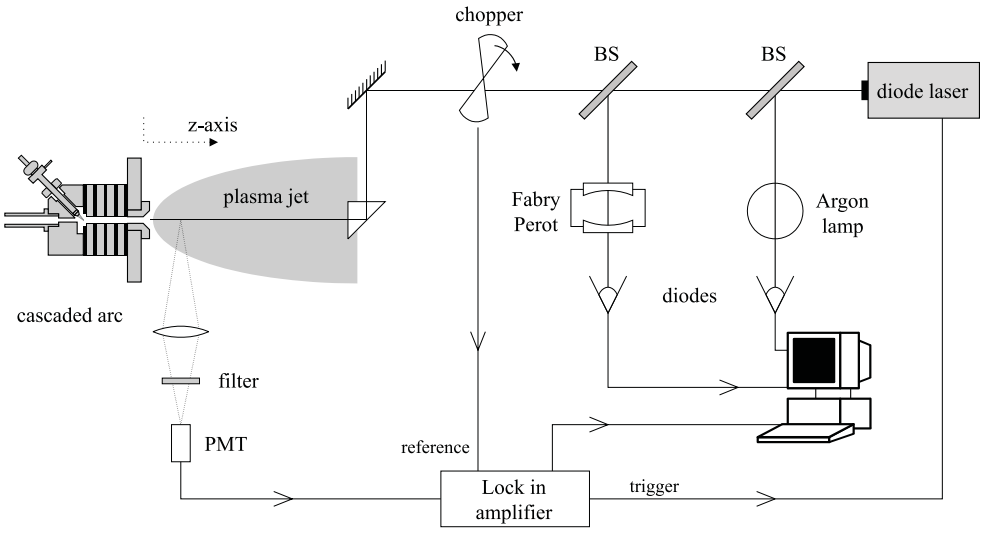

Fig. 3.1: Schematic view of the experimental LIF setup using a cw laser source and synchronic detection. Also shown is the cascaded arc and the expanding thermal plasma. Spatial scans through the plasma jet can be made by moving the arc relative to the intersection of laser beam and detection volume.

excites the atoms on the center z-axis of the expansion. In another configuration the beam is directed perpendicular to the flow direction. In this case the radial velocity of the atoms excited at different radial positions in the jet is monitored. The laser light is chopped at a frequency of about 800 Hz and the laser induced fluorescence signal is detected under 90^o with a photo multiplier tube (PMT). A high pass filter (λ cut-off 780 nm) placed between the plasma and the detector avoids saturation of the detector due to the emission of the plasma. A slit in front of the detector determines the spatial resolution of the measurements to 2 mm in both z and y-direction. The signal from the PMT is analyzed with a lock-in amplifier with an integration time of 500 ms. The signal of the chopper is used as a reference signal for the lock-in amplifier. Part of the laser light is used to measure simultaneously the absorption profile of argon atoms in a low pressure argon lamp ($T \approx 600$ K) and the transmission of a Fabry-Perot etalon. The three signals are recorded simultaneously with a 12 bit 200 kHz analog-to-digital converter (National Instruments PCI-6023E). The tuning of the laser is controlled by the lock-in amplifier via a voltage supplied to the piezo connected to the end mirror of the external cavity of the diode laser. In this way mode hop free scans of a few wavenumbers can be recorded. A typical recording of three traces is shown in Fig. 3.2. The LIF signal in Fig. 3.2 is measured at $z = 10$ mm in the expanding plasma jet after excitation of the $\mathrm{Ar}^*(1s_5) \rightarrow \mathrm{Ar}^*(2p_9)$ transition at 811.53 nm. The linewidth of the laser is in the order of 1 MHz, much narrower than the line width of the recorded Ar transition in the expanding plasma and low pressure argon lamp. The frequency shift between the absorption in the lamp and the LIF signal from the plasma is directly related via Eq. (3.1) to the velocity of the Ar atoms in the expanding plasma. The simultaneously recorded Airy-type transmission of the Fabry-Perot etalon is used to

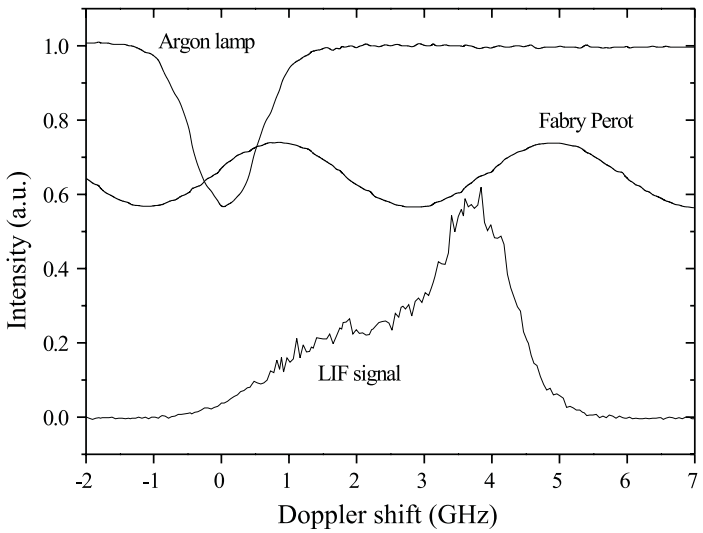

Fig. 3.2: A measurement showing three traces: the LIF signal from the excited Ar metastables in the plasma expansion, the absorption spectrum in a low pressure argon lamp, and the transmission of the Fabry-Perot interferometer.

linearize the frequency axis.

LIF measurements

LIF measurements at different axial positions (z) have been performed in the expanding argon plasma jet for two different background pressures, i.e. 20 and 100 Pa, and on two different Ar[$4s$] $\rightarrow$ Ar[$4p$] transitions, i.e. $1s_5 \rightarrow 2p_9$ and $1s_4 \rightarrow 2p_7$. The recorded spectral profile of the transition is a direct measurement of the Ar atom velocity distribution function (VDF) along the laser beam axis. The local mean Ar atom velocity is deduced from the line profile. If the system is in thermodynamic equilibrium (Gaussian VDF), an Ar atom temperature can be defined (related to the width of the line). The area of the peak provides a direct measure for the local density.

Mainly the results on the $1s_5$ state — the lowest metastable state — will be discussed, since the velocity distributions of the $1s_4$ state — the lowest resonant state — showed no significant difference with the former one. In Fig. 3.3 two velocity distributions are shown, measured at $z = 60$ mm. One is recorded after excitation of the $1s_5 \rightarrow 2p_9$ transition, and one after excitation of the $1s_4 \rightarrow 2p_7$ transition . In both cases the same experimental plasma conditions were applied. The small differences could be attributed to a difference in position at which the two spectra are recorded. The day to day reproducibility of the position of the plasma source in the z direction is in the order of 1 millimeter.

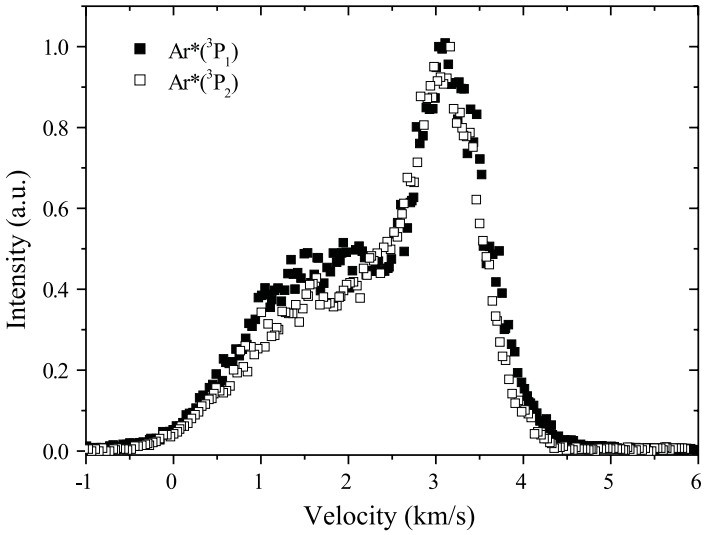

Fig. 3.3: Axial velocity distribution of atoms in the $Ar^*(^3P_2)$ metastable state (open square) and the $Ar^*(^3P_1)$ resonant state (filled square) recorded at $z = 60$ mm. The arc is operated at standard conditions; the background pressure is 20 Pa.

3.2.3 Rayleigh scattering

The Rayleigh scattering [17, 18] measurements are performed with the UV laser beam used to detect atomic hydrogen by means of two photon laser induced fluorescence. The laser setup is described elsewhere [19, 20] (see also chapters 4 and 6). In short, a 20 Hz frequency doubled Nd:YAG laser beam is used to pump a tunable dye laser, which delivers light around 615 nm. This light is then frequency tripled (KDP + BBO crystals). In this way about 2 mJ of tunable radiation around 205 nm can be obtained (5 ns pulse duration, horizontally polarized). The Rayleigh scattering cross-section increases when the radiation wavelength decreases (λ^{-4} dependence) which allows for using a relatively low energy per pulse (compared to the Nd:YAG laser beam for instance). Moreover, the ratio of the scattered light to the stray light increases at low wavelength. The UV radiation is directed into the expansion vessel and the scattered light is detected under 90^o with respect to both the laser beam and the plasma jet with a solar blind photomultiplier tube. The current detection limit for the total density in an Ar-H_2 plasma is 10^{20} m^{-3}. The latter does not permit to measure the Ar density accurately at a background pressure below 40 Pa. The Ar density profiles reported here have been measured under slightly different experimental conditions [11]: 3 slm Ar and 0.5 slm H_2. The small difference in the hydrogen flow is taken into account when the density profiles are used in the data analysis.

3.3 Interpretation of the LIF spectra

In Fig. 3.4 measured axial velocity distribution functions are shown, recorded at 6 different z positions at a pressure of 20 Pa after excitation of the $Ar^*(1s_5) \rightarrow Ar^*(2p_9)$ transition. The laser frequency is converted to the velocity along the laser propagation direction by using Eq. (3.1). Although the measured spectra originate from metastable Ar atoms, it will be demonstrated that the velocity distributions image the velocity distributions of ground-state Ar atoms.

3.3.1 Recombination of Ar ions

Argon atoms in the longlived $4s$ states that are used for the determination of velocity profiles are formed in a three particle recombination process

$$Ar^+ + e + e \rightarrow Ar^* + e. \tag{3.2}$$

It is well established that all Ar^* atoms produced in this three particle recombination cascade down to the $4s$ states [21, 22]. We will first discuss conditions under which the velocity distribution profile of these longlived atoms is identical to that of the ground state argon atoms. We consider a cross section of 2×10^{-19} m^2 for Ar-Ar collisions and a cross section of 1×10^{-18} m^2 for both Ar^+-Ar and Ar[$4s$]-Ar collisions. We also suppose that at any z, the electron density will be about 100 times smaller than the argon density [23]. The argon density is determined from the Rayleigh measurements at 42 and 100 Pa (see Fig. 3.9). The gas temperature T_g and the axial velocity w_z are assumed to be equal to the temperature and mean velocity of the metastable Ar atoms. Shown in Fig. 3.5a for a 20 Pa background pressure and in Fig. 3.5b for 100 Pa, are the mean distances, λ_{00}, λ_{i0} and λ_{m0}, in the laboratory frame, that an Ar, Ar^+ or Ar[$4s$] can travel along the z-axis before colliding with an argon atom. All distances are calculated according to the following relation

$$\lambda = \frac{w_z}{n\sigma v_{\mathrm{th}}}. \tag{3.3}$$

The thermal velocity v_{th} is deduced from T_g according to

$$v_{\mathrm{th}} = \sqrt{\frac{2kT_g}{m}}. \tag{3.4}$$

To consider the kinetics of the four Ar[$4s$] states, we must first remember that the three particle recombination process is instantaneous, and thus the argon atoms in the metastable and resonant states formed in this process image in first instance the velocity distribution of the ions. The cross section for collisions of Ar^+ ions with argon atoms, including both charge transfer and elastic collisions, is about 10^{-18} m^2 [26]. Consequently, as one can see in Fig. 3.5, for $z < 20$ mm, the path length of the ions, λ_{i0}, is smaller than 2 mm. This means that ion-neutral collisions are fast enough to equilibrate the velocity distribution of ions and argon atoms. We therefore assume that in view of the smallness of λ_{i0} compared to the local gradient lengths, the Ar^+ ions and Ar atoms will be in equilibrium at these positions and further downstream.

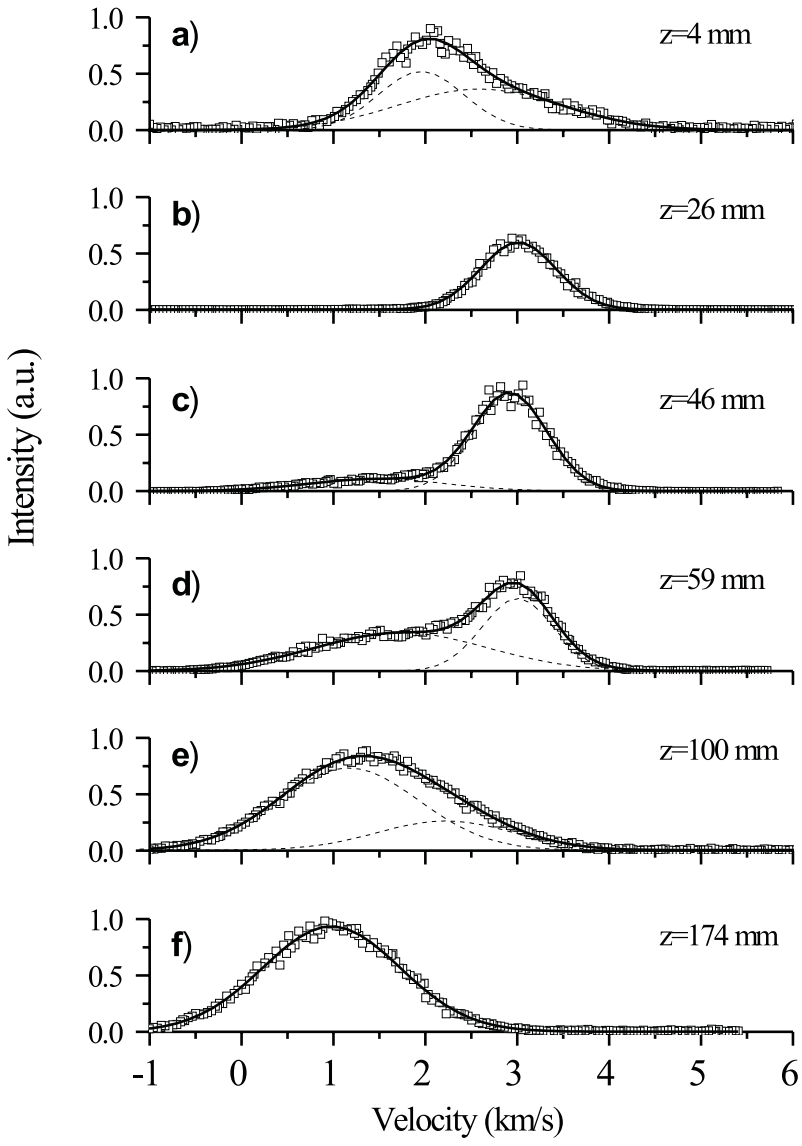

Fig. 3.4: Axial velocity distributions of metastable Ar recorded at 6 different z positions along the jet axis at 20 Pa background pressure. The metastable Ar VDF images the ground-state Ar VDF. The full lines show the result of a fit using a bimodal approximation. The dashed lines show the individual Gaussian VDF. Departure from thermodynamic equilibrium occurs both at the source exit and within the stationary shock wave.

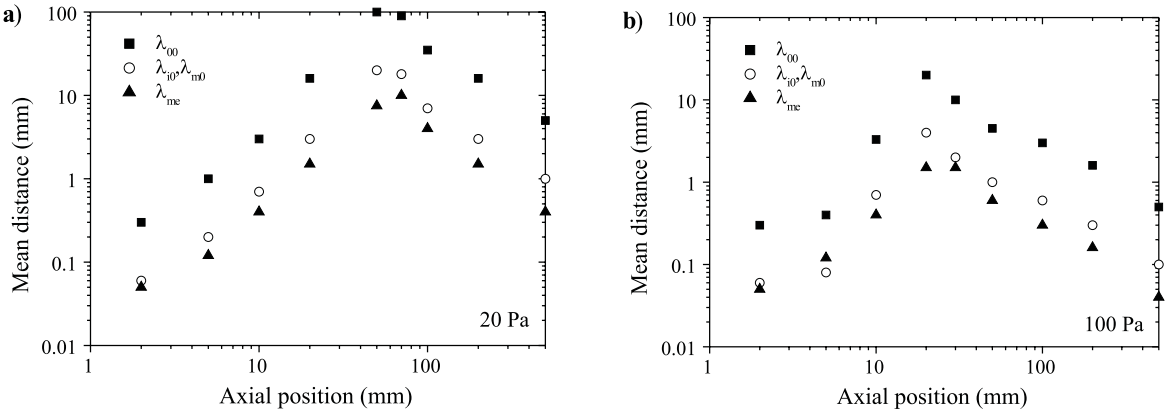

Fig. 3.5: The mean distance an Ar, Ar^+ and Ar^* can travel along the z-axis before colliding with an argon atom at 20 Pa (a) and 100 Pa (b) background pressure. λ_{me} denotes the mean distance an Ar[4s] atom can travel along the z-axis before being transferred to an adjacent Ar[4s] state.

Surprisingly, at short distances from the exit of the nozzle ($z < 16$ mm at 20 Pa and $z < 8$ mm at 100 Pa) we observe a forward peaking of the velocity distribution (see Fig. 3.4a).

Influence of the electric field

The forward peaking of the VDF, i.e. the existence of very fast particles, has already been reported in e.g. time-of-flight measurements in a plasma created from a hollow cathode arc [27]. The fast component of the measured VDF may be attributed to metastable atoms born from recombination of Ar^+ ions accelerated by an electric field generated from the gradient of the charge density in the expanding jet. The amplitude of this field is given by the Boltzmann relation [28]

$$E(z) = \hat{T}_e \frac{\nabla n}{n}. \tag{3.5}$$

Since the decay of n_e is similar to the decay of the neutral density [6], for $z > 4$ mm, $\nabla n/n$ is approximately 2/z and assuming $\hat{T}_e = 0.3$ eV, identical to the gas temperature, the amplitude of the electric field would be about 120 V/m at z=5 mm and 60 V/m at z=10 mm. In the valley and after the shock front the gradient and thus the fields are much smaller and reverse. Consequently the fast component should disappear as it is observed.

3.3.2 Coupling between ground-state Ar and Ar[4s]

Concerning the Ar[4s] atoms, momentum transfer and metastability-exchange collisions with a cross-section of about 10^{-18} m^2 will mix the $Ar^*(^3P_2)$ metastable and ground state

atoms. The collision cross-section σ is determined from a measured diffusion coefficient $D = 1.7 \times 10^{20}$ molecule $\mathrm{m}^{-1}\,\mathrm{s}^{-1}$ at 300 K [29]. The relation between D and σ is [34]

$$D = \frac{3\pi}{16\sqrt{2}} \frac{< w >}{\sigma} \tag{3.6}$$

Here $< w >$ is the mean velocity of argon atoms at 300 K. We can see in Figs. 3.5a and 3.5b that except for $30 < z < 100$ mm at 20 Pa and z around 20 mm at 100 Pa, the mean path length of metastable atoms, λ_{m0}, is comparable to, or smaller than the spatial resolution in our experiments. Similarly, the radiative lifetime of the resonant $\mathrm{Ar}^*(^3\mathrm{P}_1)$ and $\mathrm{Ar}^*(^1\mathrm{P}_1)$ states is in the order of 10 ns. However, under our experimental conditions, due to the radiation trapping [25], the effective lifetimes of these states become a few microseconds. Consequently, due to this effect, resonant and ground-state argon atoms are very efficiently coupled and can therefore be considered as being fully mixed. As an example, at an argon density of 10^{20} m^{-3}, the mean free path of the resonant VUV photons is less than 0.1 mm. This means that the velocity distribution of the resonant $\mathrm{Ar}^*(^3\mathrm{P}_1)$ and ground state atoms are identical. Also, collisions with electrons will transfer Ar[4s] atoms between the resonant $\mathrm{Ar}^*(^3\mathrm{P}_1)$ and metastable $\mathrm{Ar}^*(^3\mathrm{P}_2)$ states, via $\mathrm{Ar}^*(^3\mathrm{P}_2) + \mathrm{e} \leftrightarrow \mathrm{Ar}^*(^3\mathrm{P}_1) + \mathrm{e}$. The mean distance λ_{me} that Ar[4s] atoms can travel along the z-axis before being transferred to the adjacent state is determined by the relation $\lambda_{me} = w_z/(k_e \times n_e)$. For this reaction the rate coefficient k_e is about 2×10^{-13} $\mathrm{m}^3\mathrm{s}^{-1}$ [24]. Assuming an electron density with the same z-dependence as Ar atoms but 100 times smaller, we calculated the mean path length of a metastable atom before suffering a collision with an electron for 20 Pa (see Fig. 3.5a) and 100 Pa (see Fig.3.5b) background pressure. At 20 Pa, for most positions λ_{me} is smaller than the typical gradient length $L_n = n/\nabla n$ (about $z/2$ at these positions); for $30 < z < 100$ mm, the condition is marginally satisfied. At 100 Pa, the condition is fulfilled everywhere. Also, considering the velocity of the expanding jet $w_z \approx 3$ km/s, from the microsecond range lifetime of the resonant states we can conclude that for most positions the argon atoms in the metastable and resonant levels are produced and lost locally [21]. We conclude that for $z > 20(8)$ mm at 20(100) Pa, the velocity distribution function of argon atoms in the 4s states is perfectly similar to that of the ground state atoms. They are created from Ar^+ ions already in equilibrium with argon atoms and they are strongly coupled to the ground state atoms by collisional and radiative processes. Close to the shock wave, located around $z = 70$ mm at 20 Pa and $z = 30$ mm at 100 Pa, the mean free path for the neutral-neutral collisions becomes larger than the gradient length L_n, which means that the velocity distribution of argon atoms can be non-Gaussian in this region.

3.3.3 Ar velocity distribution function

Departure from thermodynamic equilibrium

The velocity distributions shown in Fig. 3.4 can thus be seen as velocity distributions of neutral Ar atoms. As discussed before, the distributions for $z \leq 20$ mm can be distorted due to the existence of an accelerating E-field acting on Ar^+ ions. At 20 Pa, for

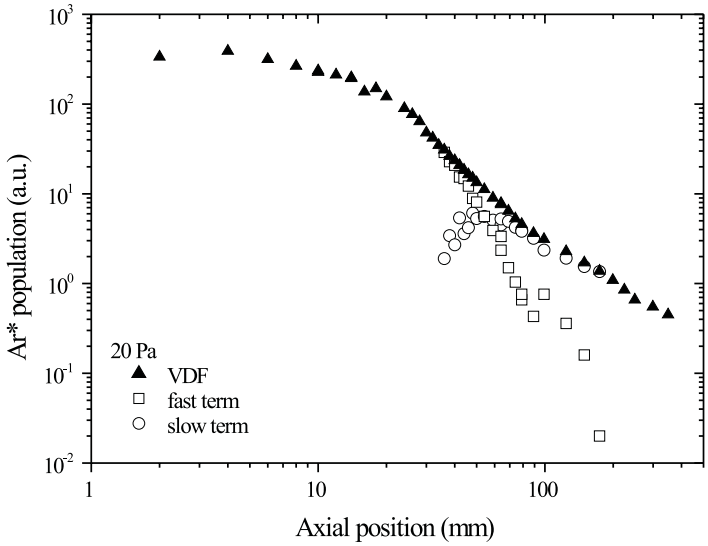

Fig. 3.6: Behavior of the content of the metastable Ar VDF at 20 Pa background pressure along the jet axis. (solid triangle). Also shown is the contents of both the fast (square) and the slow (circle) component across the shock wave.

$20 < z < 30$ mm the measured distribution can be described to a good approximation with a Gaussian profile, i.e. the flow is in thermodynamic equilibrium. As can be seen in Fig. 3.4c, behind $z = 30$ mm, i.e. in the shock region, the VDF measured along the jet centerline starts to deviate from the equilibrium form. Across the stationary shock wave, the Ar VDF can be decomposed into two Gaussian VDF: one corresponds to the conditions upstream of the shock ("fast" component characterized by a high mean velocity and a low temperature), and the other one corresponds to the conditions in the shock wave ("slow" component characterized by a low mean velocity and a high temperature). The bimodal approximation for the VDF within a shock wave has first been proposed by Mott-Smith [30] and latter developed by Glansdorff [31]. However, in the so-called Mott-Smith model, the slow distribution correspond to the condition downstream of the shock front, i.e. its mean velocity and its temperature are constant. Across the shock wave, the population of the fast Gaussian component is gradually transferred to the slow component by means of collisions [32, 33]. More information about shock wave properties can be found in chapter 8. Behind the shock region, $z \geq 150$ mm, i.e. in the subsonic region of the expansion, the velocity profile can be described with a single Gaussian again as shown in Fig. 3.4. In this region the flow is in equilibrium and can be described along the jet axis with one mean velocity and one temperature.

Contents of the VDF

In Fig. 3.6 the contents of the VDF measured along the jet axis at 20 Pa background pressure is shown as well as the contents of the two Gaussian distributions that compose the VDF in the shock region. At the beginning of the expansion, for $z < 20$ mm, the Ar[$4s$] density remains high and changes only by a factor of two. The local metastable production compensates for convective losses due to the rarefaction effect. The production rate of Ar[$4s$] atoms, through electron-ion recombination, is proportional to $n_e^3 \times T_e^{-4.5}$ [35]. The rarefaction of n_e due to the expansion can be compensated by the diminution of T_e in this region of the plasma jet. From $z = 20$ mm up to the shock wave, the density rarefaction effect (see chapter 2) is the main contributor to the decrease of the Ar[$4s$] density. However, the density drops slightly faster than z^{-2} due to the efficient loss of Ar[$4s$] atoms by collisions with electrons and by radiation. The production via three-particle recombination can not compensate for the loss mechanism. Across and behind the shock wave, the Ar[$4s$] density decreases since Ar[$4s$] slowly deexcite (mostly by collision with electrons) to form ground-state Ar atom.

Within the shock region, the population of the fast component of the Ar atom VDF gradually diminishes to finally disappear whereas the population of the slow component gradually increases, due to the population transfer, until it remains the only component.

3.4 Ar atom temperature, velocity, and density

The mean velocity of a distribution is determined from the calculation of the 1$^{\text{st}}$ moment

$$\overline{v} = \frac{\int v f(v) dv}{\int f(v) dv}. \tag{3.7}$$

At thermodynamic equilibrium, i.e. Gaussian VDF, a particle temperature T can be defined that corresponds to the spread in velocity. The 2$^{\text{nd}}$ moment of the distribution, i.e.

$$\overline{v^2} = \frac{\int (v - \overline{v})^2 f(v) dv}{\int f(v) d(v)}, \tag{3.8}$$

is used to calculate T via the relation $k_B T = \frac{1}{2} m \overline{v^2}$, where k_B is the Boltzmann constant and m the mass of the particle. The temperature is in fact directly connected to the width of the Gaussian profile. In a non-equilibrium situation, a temperature can not strictly be defined. However, we proposed to define a mean temperature by the density-weighted temperature of each Gaussian component of the VDF

$$T = \frac{n_1 T_1 + n_2 T_2}{n_1 + n_2}. \tag{3.9}$$

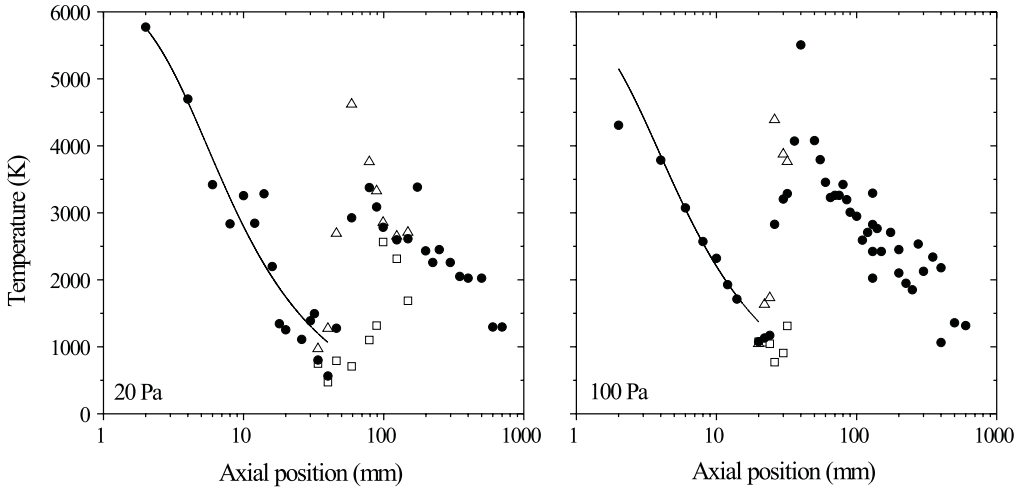

Fig. 3.7: Axial profile of the parallel temperature (circle) for two different background pressures. In the shock region the temperature of the fast (square) and the slow (triangle) component of the VDF is plotted. The solid line is the result of a calculation using the Poisson adiabatic law with $\gamma = 1.4$.

Parallel temperature and mean axial velocity

The development of the parallel temperature $T_{||}$ (associated with the velocity distribution parallel to a stream line) along the jet centerline is shown in Fig. 3.7 for two background pressures. Also shown in Fig. 3.7 is the temperature of the fast (cold) and slow (warm) component of the VDF within the shock region. From a fit to the measured temperature profile in the supersonic domain using the Poisson adiabatic law (Eq. 2.11) one obtains: $\gamma = 1.4 \pm 0.1$, and $T_o = 5600$ K. The speed of sound in the source can be calculated using Eq. 2.13: $c_{s,o} = 1270\ \mathrm{m\,s^{-1}}$. The adiabatic exponent γ proves to be lower than the expected value for a monoatomic gas (5/3). It may arise from the influence of the ionization degree [36]. Another possibility is that a plasma expansion deviates from an adiabatic expansion because of energy transfer from both the source and the hot background gas. The temperature T_o in the nozzle is lower than the source temperature (≈ 1 eV) for two reasons. First, due to the cascaded arc configuration, no energy is supplied to the plasma in the nozzle and therefore the plasma starts to recombine inside the nozzle. Second, due to the nozzle geometry (45° opening angle) the plasma starts to expand, and therefore to cool down, inside the nozzle. In the subsonic domain, the temperature decreases because of heat conduction to the vessel walls.

The measured axial profile of the Ar atom mean velocity is shown in Fig. 3.8 for two different background pressures. Also shown in the graph is the mean velocity of the two components of the VDF across the shock wave. The axial profile of the speed of sound,

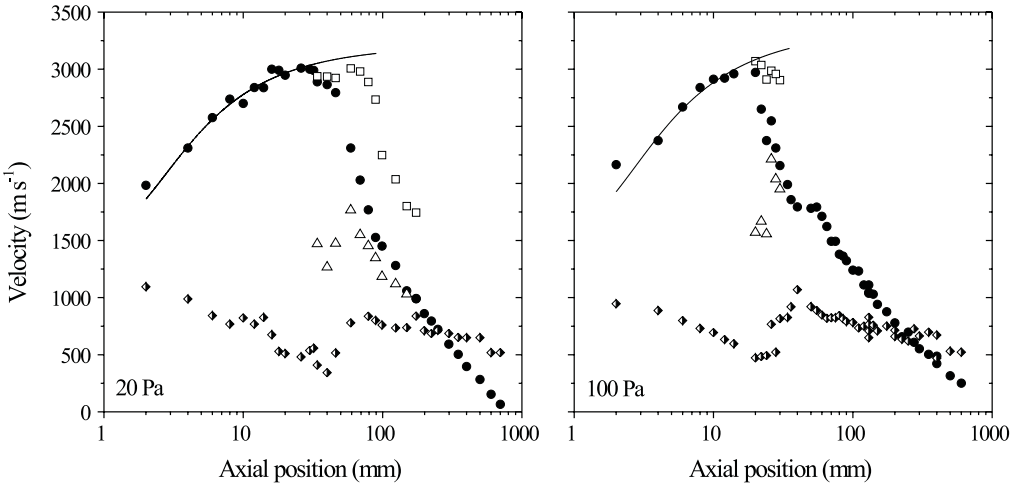

Fig. 3.8: Ar mean axial velocity profile (circle) along the jet axis for two different background pressures. In the shock region the mean velocity of the fast (square) and the slow (triangle) component of the VDF is plotted. Also shown is the speed of sound calculated from the measured parallel temperature (diamond) using Eq. 2.13. The solid line is the result of a calculation using Eq. 2.22.

calculated from the measured $T_{\|}$, is shown in Fig. 3.8. In the supersonic domain, the measured velocity profile is modeled using Eq. 2.22. For the two pressures, the plasma is accelerated up to about six times the sound speed ($M = 6.4$ in front of the shock). Both the position and the width of the shock wave depend on the background pressure as expected. The shock wave being formed in a rarefied flow regime, its thickness is large. At 20 Pa, respectively 100 Pa, the shock wave stretches from $z = 30$ mm to $z = 250$ mm, respectively from $z = 20$ mm to $z = 200$ mm. The end of the shock is defined as the position where $M = 1$. The plateau visible inside the shock region at 100 Pa arises from a second expansion phase due to the step by step adapatation of the Ar static pressure throughout the shock wave. An interesting feature is observed in the 20 Pa case. The mean velocity of the fast component of the VDF drops across the shock wave. In other words, the measured fast component does not exhibit the properties of the supersonic component defined in the Mott-Smith approximation [30, 31]. The MS model is certainly too simple to perfectly describe shock wave properties, however, the deviation from the predicted behavior may be due to the existence at low background pressure of a third equilibrium velocity component, the so-called scattered component [33, 37]. The good agreement of our experimental results on average velocity and temperature with the calculations in which we describe the thermal plasma expansion as if it were a hot neutral gas expansion with a slightly different adiabatic constant, shows the validity of this approach.

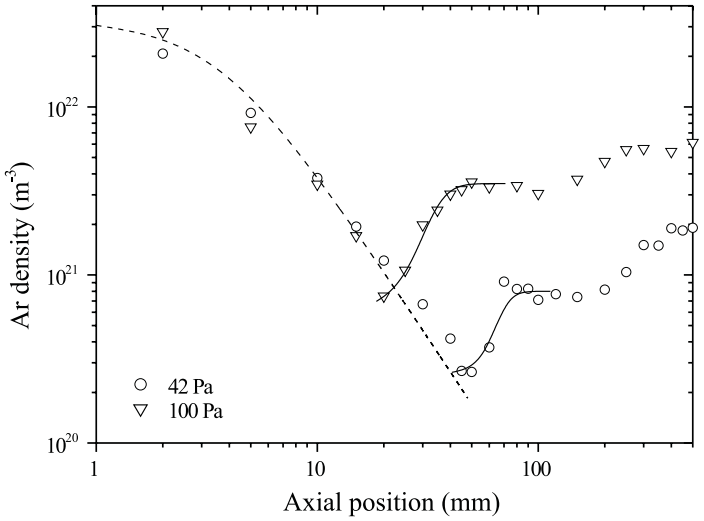

Fig. 3.9: Ar density profile along the jet centerline of an expanding Ar-H_2 plasma (3 slm Ar and 0.5 slm H_2) measured by means of UV Rayleigh scattering at 42 Pa (triangle) and 100 Pa (circle). Also shown is a calculated density profile in the supersonic domain using equation 2.17. The shock wave profiles (first compression stage) are modeled using the Navier-Stokes equation in the two pressure cases.

Density

As shown in Fig. 3.9, the Ar density has been measured by means of UV Rayleigh scattering for a background pressure of 100 Pa and 42 Pa in a plasma generated from an Ar-H_2 mixture ($\sigma^R_{\mathrm{Ar}} = 5\,\sigma^R_{\mathrm{H_2}}$). In the supersonic domain, the decrease in density arises from a rarefaction effect (decay in z^{-2}) and it is pressure independent. The data are fitted using Eq. 2.17 with the following parameters: $n_{\mathrm{o}} = 5 \times 10^{22}$ m^{-3}, $z_{\mathrm{ref}} = 3$ mm, and $z_{\mathrm{o}} = 3.0$ mm meaning that the expansion starts already inside the arc nozzle as expected with our geometry. In the subsonic domain, the density increases because the plasma flows at constant static pressure. The shock wave is formed in a rarefied flow regime since $Kn = 0.2$ at 100 Pa and $Kn = 0.4$ at 42 Pa. The compression ratio equals 4 at 100 Pa, i.e. the maximum compression ratio for an atomic gas, and 3 at 42 Pa. Seemingly the density jump through the shock wave can well be modeled. The Navier-Stokes equation is used in Fig. 3.9 (the Mott-Smith approach would provide the same outcome). However, only the first compression stage is modeled and the good agreement between the calculation and the experimental data is due to the fact that the shock wave thickness L is a free parameter (L is taken to be the dimension of the first stage in that case, i.e. 25 mm). Using the real shock wave thickness, see Fig 3.8, would lead to a very poor agreement. It means that the shock profile models described in chapter 2 do not account for a step by step change in the static pressure of the flowing gas.

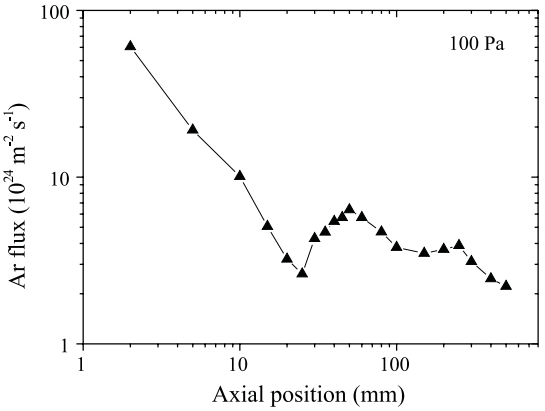

Fig. 3.10: Ar atom on-axis forward flux at 100 Pa determined from Rayleigh scattering measurements.

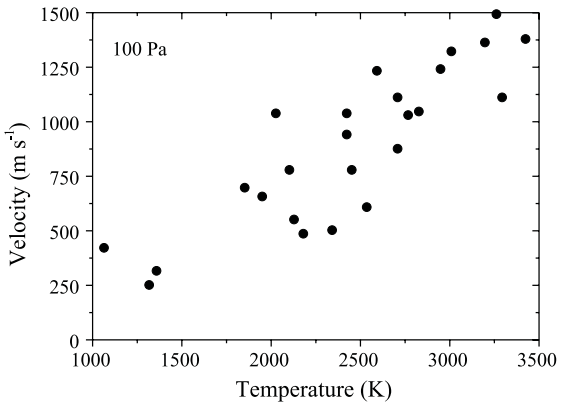

Fig. 3.11: Axial mean velocity as function of the parallel temperature in the subsonic domain at 100 Pa background pressure.

3.5 Ar atom forward flux

Combining the axial velocity measurement with the Ar density measurement, one can obtain the profile of the Ar atom forward flux along the jet axis. The result is shown in Fig. 3.10 at 100 Pa background pressure. In the supersonic flow domain, the flux decreases as z^{-2} because of the density rarefaction effect. The Ar flux entering the shock wave ($\phi \approx 3.2 \times 10^{25}$ m^{-2} s^{-1} at $z = 20$ mm) matches to a good approximation to the Ar flux behind the shock wave ($\phi \approx 3.8 \times 10^{25}$ m^{-2} s^{-1} at $z = 200$ mm). As expected the flux across the shock region is conserved. The trend observed through the shock results from the adaptation of the Ar static pressure to the background static pressure via several successive compression phases. In the subsonic domain the Ar flux decreases since the velocity decreases because of momentum exchange with the residual background gas.

Analysis of the flow pattern in the expansion chamber using a hydrodynamic code (PHOENICS) [38], reveals that in the continuum flow regime behind the stationary shock front the diameter of the jet stays approximately constant. Since the plasma flows at constant static pressure in the subsonic domain, the drift velocity should be proportional to the temperature. This proves to be indeed the case as shown in Fig. 3.11 at a background pressure of 100 Pa. At low background pressure, i.e. in the rarefied regime, the jet opens and the $w \propto T$ relation is not valid.

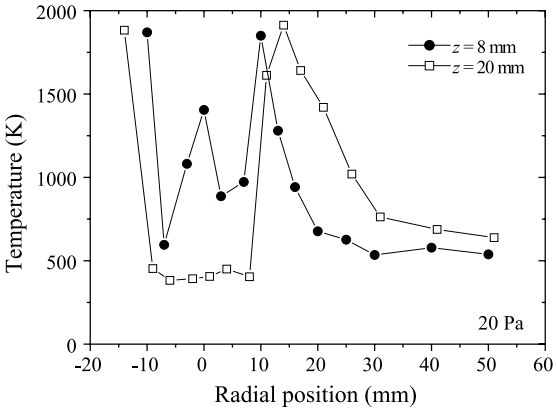

Fig. 3.12: Perpendicular temperature $T_\perp$ versus radial position measured at 20 Pa for two different z positions.

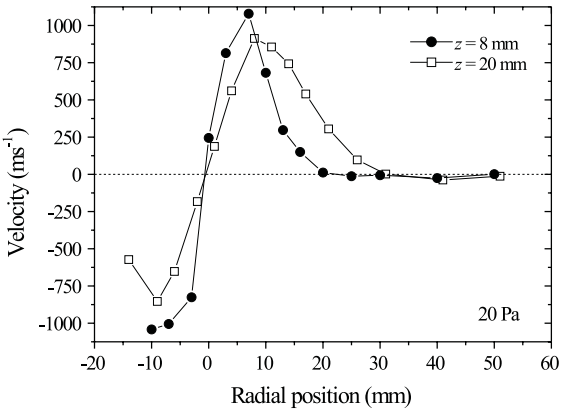

Fig. 3.13: Mean radial velocity component as a function of r measured at 20 Pa for two z positions.

3.6 Radial profiles

3.6.1 Perpendicular temperature

The radial profiles of the perpendicular temperature $T_\perp$ (associated with the velocity distribution perpendicular to a stream line) measured at 20 Pa in the supersonic domain, see Fig. 3.12, show evidence of the quasi adiabatic cooling effect. They also reveal the structure of the barrel shock wave. The structure visible in the core of the jet at $z = 8$ mm results from a geometric effect. The Ar atoms detected on the side have travelled a longer distance in comparison with those moving along the axis, and therefore they have converted a larger part of their thermal energy into kinetic energy. This leads to a lower temperature at the edges of the jet.

At $z = 20$ mm, this geometric effect is not noticeable. The particles can not convert anymore their thermal energy, and the maximum velocity is reached. Furthermore at this location the flow deviates from thermodynamic equilibrium: $T_\perp < T_\parallel$. The pressure is low enough to enable the flow to reach the so-called frozen regime [39].

The rise in $T_\perp$ when going off-axis is due to collisions with Ar atoms in the barrel shock wave. This temperature jump defines the boundary of the plasma jet. Behind the barrel shock wave, $T_\perp$ decreases towards the vessel walls because of heat transfer to the background gas. The gas temperature in the vicinity of the jet is rather low ($T_\perp \approx 600$ K).

3.6.2 Radial velocity component

As can be seen in Fig. 3.13, the radial profiles of the radial velocity reveals the Ar shock wave structure. Because of the expansion process, the radial velocity first increases when

moving away from the jet axis. When flowing Ar atoms collide with Ar atoms in the barrel shock wave, the velocity decreases since it is converted into thermal energy, and the temperature increases accordingly. As expected, the position of the Ar barrel shock as deduced from the radial velocity profile does coincide with the position deduced from the corresponding $T_\perp$ profile.

In the surrounding of the plasma jet, the measured radial velocity is around zero, whereas it is established that in this zone Ar atoms are moving towards the jet due to the existence of vortices (recirculation cells) [38]. In our conditions, their velocity is however too low to be accurately determined ($w_r \approx 20$ m s^{-1}).

3.7 Conclusions

Velocity and temperature measurements using Laser Induced Fluorescence spectroscopy on metastable argon atoms in an expanding thermal argon plasma seeded with 4 % of hydrogen have been presented. We demonstrated that the velocity distribution of metastable or resonant atoms reflects the velocity distribution of ground state argon atoms. At low background pressure it is found that within the stationary shock wave the supersonic component of the VDF is decelerated, in disagreement with the Mott-Smith bimodal approximation. This feature may reveal the existence of a third velocity component linked with the invasion of the jet by the background gas.

The LIF measurements combined with the Rayleigh scattering measurements indicate that the expansion of a thermal plasma can to a large extent be described as a hot neutral gas expansion with a smaller adiabatic constant in the supersonic domain due to energy transfer from both the source and the background.

Acknowledgments

The authors would like to thank Prof. M.C.M. van de Sanden for stimulating discussions The authors greatly appreciate the skillful technical assistance of M.J.F. van de Sande, A.B.M. Hüsken, and H.M.M. de Jong. This work is part of the research program of the Netherlands Foundation for Fundamental Research on Matter (FOM) and is partially founded by Euratom. It is also financially supported by the Netherlands Organization for Scientific Research (NWO).

References

[1] J.C. Miller, R.F. Hagelund, *Experimental Methods in Physical Science*, Vol. **30**, Academic Press, San Diego (1998).

[2] E. Hantzsche, *Contr. Plasma Phys.* **30**, 575 (1990).

[3] R. Campargue, *J. Phys. Chem.* **88**, 4466 (1984).

[4] S.M. Aithal, V.V. Subramaniam, V. Babu, *Plasma Chem. Plasma Proc.* **19**, 487 (1999).

[5] J.W.A.M. Gielen, W.M.M. Kessels, M.C.M. van de Sanden, D.C. Schram, *J. Appl. Phys.* **82**, 2643 (1997).

[6] M.C.M. van de Sanden, M.J. de Regt, D.C. Schram, *Plasma Sources Sci. Technol.* **3**, 501 (1994).

[7] M.C.M. van de Sanden, R. van den Bercken and D.C. Schram, *Plasma Sources Sci. Technol.* **3**, 511 (1994).

[8] M.C.M. van de Sanden, J.M. de Regt, and D.C. Schram, *Phys. Rev. E* **47**, 2792 (1993).

[9] R.F.G. Meulenbroeks, A.J. van Beek, A.J.G. van Helvoort, M.C.M. van de Sanden, D.C. Schram, *Phys. Rev. E* **49**, 4397 (1994).

[10] R.F.G. Meulenbroeks, R.A.H. Engeln, J.A.M. van der Mullen, D.C. Schram, *Phys. Rev. E* **53**, 5207 (1996).

[11] S. Mazouffre, M.G.H. Boogaarts, J.A.M. van der Mullen, D.C. Schram, *Phys. Rev. Lett.* **84**, 2622 (2000).

[12] S. Mazouffre, M.G.H. Boogaarts, J.A.M. van der Mullen, and D.C. Schram, in *Heat and Mass Transfer under Plasma Conditions*, edited by P. Fauchais, J.A.M. van der Mullen, J. Heberlein, ANYAS **891**, 348 (1999).

[13] J.W.A.M. Gielen, M.C.M. van de Sanden, D.C. Schram, *Appl. Phys. Lett.* **69**, 152 (1996).

[14] M.C.M. van de Sanden, J.M. de Regt, G.M. Jansen, J.A.M. van der Mullen, D.C. Schram, and B. van der Sijde, *Rev. Sci. Instrum.* **63**, 3369 (1992).

[15] R.F.G. Meulenbroeks, R.A.H. Engeln, C. Box, I. de Bari, M.C.M. van de Sanden, J.A.M. van der Mullen, D.C. Schram, *Phys. Plasmas* **2**, 1002 (1995).

[16] The Paschen notation is used for the transition (see W.L. Wiese, M.W. Smith, and B.M. Miles, *Atomic Transition Probabilities Vol II*, ed. N.B.S- U.S. Dep. Of Commerce (1969)). The metastable $^3P_2$ and resonant $^3P_1$ levels are also known as the $1s_5$ and $1s_4$ levels in Paschen notation and $4s[3/2]_2$ and $4s[3/2]_1$ in Racah notation.

[17] T.V. George, L. Goldstein, L. Slama, and M. Yokoyama, *Phys. Rev.* **137**, 369 (1965).

[18] S.C. Snyder, L.D. Reynolds, G.D. Lassahn, J.R. Fincke, C.B. Shaw Jr, and R.J. Kearney, *Phys. Rev. E* **47**, 1996 (1993).

[19] H.W.P. van der Heijden, M.G.H. Boogaarts, S. Mazouffre, J.A.M. van der Mullen, and D.C. Schram, *Phys. Rev. E* **61**, 4402 (2000).

[20] S. Mazouffre, M.G.H. Boogaarts, R. Engeln, J.A.M. van der Mullen, and D.C. Schram, *Proceedings of Laser-Aided Plasma Diagnostics* **9**, California, U.S.A., 320 (1999).

[21] A.J.M. Buuron, D.K. Otorbaev, M.C.M. van de Sanden, and D.C. Schram, *Phys. Rev. E* **50**, 1383 (1994).

[22] D.A. Benoy, J.A.M. van der Mullen, M.C.M. van de Sanden, B. van der Sijde, and D.C. Schram, *J. Quant. Spectrosc. Radiat. Transfer*, **49**, 129 (1993).

[23] R.F.G. Meulenbroeks, R.A.H. Engeln , M.N.A. Beurskens, R.M.J. Paffen, M.C.M. van de Sanden, J.A.M. van der Mullen, D.C. Schram, *Plasma Sources Sci. Technol.* **4**, 74 (1995).

[24] D.P. Lymberopoulos and D.J. Economou, *J. Appl. Phys.* **73**, 3668 (1993).

[25] T. Holstein, *Phys. Rev.* **83**, 1159 (1951).

[26] A.V. Phelps, *J. Appl. Phys.* **76**, 747 (1994).

[27] P. Theuws, *Molecular Beam Sampling of a Hollow Cathode Arc*, Ph.D. thesis, Eindhoven University of Technology (1981).

[28] F.F. Chen, *Introduction to Plasma Physics*, Plenum, New York (1985).

[29] J.H. Kolts and D.W. Setser, *J. Chem. Phys.* **68**, 747 (1978).

[30] H.M. Mott-Smith, *Phys. Rev.* **82**, 885 (1951).

[31] P. Glansdorff, *Phys. Fluids* **5**, 371 (1962).

[32] Y.B. Zel'dovich and Y.P Raizer, *Physics of Shock Waves and High Temperature Hydrodynamic Phenomena*, Academic Press, New York, Vol. 1-2 (1966).

[33] A. Ramos, B. Maté, G. Tejeda, J.M. Fernández, and S. Montero, *Phys. Rev. E* **62**, 4940 (2000).

[34] J.D. Hirschfilder, C.F. Curtiss, and R.B. Bird, *Molecular Theory of Gases and Liquids*, ed. John Wiley, New York (1967).

[35] D.R Bates and A.E. Kingston, *Proc. Phys. Soc. London* **83**, 43 (1964).

[36] K.T.A.L. Burm, W.J. Goedheer, D.C. Schram, *Phys. Plasmas* **6**, 2622 (1999).

[37] G. Pham-Van-Diep, D. Erwin, and E.P. Muntz, *Science* **245**, 624 (1989).

[38] W.M.M. Kessels, A. Leroux, M.G.H. Boogaarts, J.P.M. Hoefnagels, M.C.M. van de Sanden, and D.C. Schram, *J. Vac. Sci. Technol. A* **19**, 467 (2001).

[39] H.C.W. Beijerinck and N.F. Verster, *Physica* **111C**, 327 (1981).

Chapter 4

Two-photon laser induced fluorescence spectroscopy of atomic hydrogen

Abstract

Two-photon Absorption Laser Induced Fluorescence (TALIF) spectroscopy is used to monitor ground-state hydrogen atoms (H) properties in an supersonically expanding plasma. Hydrogen atoms are excited with two 205 nm photons from the $1s\,^2S_{1/2}$ ground-state to the n=3 level, and the fluorescence radiation is detected at the Balmer-α line at 656 nm. A detailed description of the experimental arrangement is presented. It includes: the generation of coherent tunable UV radiation, the detection of the fluorescence light, the signal acquisition and treatment, and a list of all parasitic effects that can disturb the fluorescence yield. It is shown that from a spectral scan over the two-photon transition several quantities can be extracted. The spectral profile directly reflects the local H atom velocity distribution function. At thermodynamic equilibrium, the mean velocity is obtained from the Doppler shift of the peak and temperature from the width of the peak (both in the direction defined by the laser beam). The area of the fluorescence line gives the relative local H atom density. In order to obtain absolute H atom densities, the LIF setup has to be calibrated. Two calibration methods are presented and compared: titration with NO_2 in a flow tube reactor and comparison with two-photon excitation of krypton.

4.1 Introduction

The experimental study of the transport mechanisms of ground-state (most populated state in a recombining low temperature plasma) hydrogen atoms in the expansion of a thermal plasma created by a cascaded arc requires the application of a diagnostic technique to locally monitor H atom properties such as velocity, temperature and density. The very sensitive Laser Induced Fluorescence (LIF) technique appears to be a good candidate [1]. It is non-intrusive, making it attractive for in-situ measurements, and state selective with high spectral resolution, and measurements can be spatially as well as temporally resolved. This well established method is often used to measure atomic or molecular densities in chemistry [2], in low temperature plasma physics [3, 4], and in the field of controlled nuclear fusion [5]. However due to the large energy spacing involved the detection of ground-state H requires the use of highly energetic photons (VUV domain of the electromagnetic spectrum) of which generation is experimentally demanding [6]. The problems connected with single-photon excitation can be avoided with the application of a two-photon excitation scheme. In this chapter, a detailed analysis of the Two-Photon Absorption Laser Induced Fluorescence (TALIF) spectroscopy of ground state atomic hydrogen is presented that includes among others a description of the experimental arrangement and accurate explanations about the extraction of information from the measured two-photon spectral profile. This technique is currently used for detection of light atomic radicals in plasmas. Several examples of the use of the TALIF diagnostic tool in H containing plasmas can be found in literature: e.g. concentration measurements [7, 8] and surface loss coefficient determination [9].

The excitation and detection scheme for ground-state atomic hydrogen applied in this work is the one that was first demonstrated by Bokor *et al.* [10]. In this scheme H is excited with two 205.14 nm photons from the 1s $^2S_{1/2}$ ground-state to the n=3 level. The laser induced fluorescence radiation is detected at the Balmer-α line ($2 \leftarrow 3$ transition), thereby largely avoiding self-absorption of the emitted photons. This has direct consequences for the density range in which the detection technique is applicable. Several schemes for 2-photon excitation of H to n=3 and n=4 with detection of non-resonant fluorescence, that differ in the number of laser beams and the wavelength combinations used for excitation, the intensity, polarization, and bandwidth of the laser beams, and the wavelength of the fluorescence light, have been directly compared to each other [11]. This detailed comparison shows that the above described scheme for 2-photon excitation of H with a pulsed, narrowband 205 nm laser beam gives the largest average number of fluorescence photons per incident laser photon.

4.2 Two-photon excitation process

The theoretical calculation of the fluorescence yields that results from a two-photon excitation has already been performed in detail elsewhere [11, 12, 13, 14]. We here only propose a rapid and simplified description of the calculation in the case of an unsaturated two-

photon excitation (low laser intensity), i.e. the ground-state density remains practically unchanged: $n_1(t) \approx n_1(0)$. In that particular case a rate equation description is justified.

The effect of the laser intensity on the ground-state population n_1 can be described by the following differential equation

$$\frac{d}{dt}n_1(t) = -W(t)n_1(t), \tag{4.1}$$

where $W(t)$ is the two-photon excitation rate which is expressed with the aid of the generalized two-photon excitation cross-section $\sigma^{(2)}$

$$W(t) = G^{(2)}\sigma^{(2)}g(\Delta\nu)\left(\frac{\langle\hat{I}(t)\rangle}{h\nu}\right)^2, \tag{4.2}$$

where ν is the photon frequency, h is the Planck constant, $\langle\hat{I}(t)\rangle$ is the mean laser pulse power per unit area (in $\mathrm{W\,m^{-2}}$), $g(\Delta\nu = \nu_{12} - 2\nu)$ describes the normalized profile of the two-photon transition (in s) which is composed of the convolution of the laser line profile and atomic absorption line profile, and $G^{(2)}$ is the two-photon statistical factor [15] ($G^{(2)} = 2$ for a stochastic multimode field, e.g. a dye laser beam).

The population of the excited state n_2 is given by

$$\frac{d}{dt}n_2(t) = W(t)n_1(t) - (A_2 + Q + \Gamma(t))n_2(t), \tag{4.3}$$

where $A_2 = \sum_i A_{2i}$ is the total transition probability of the excited state, Q is the quenching rate, and $\Gamma(t)$ is the photo-ionization rate. The number of generated fluorescence photons per unit volume n_γ is given by

$$n_\gamma = A_{2k}\int_0^\infty n_2(t)dt \tag{4.4}$$

where A_{2k} is the transition probability of the observed fluorescence spectral channel.

If the loss of population due to photo-ionization is neglected ($\Gamma(t) = 0$), the total amount of fluorescence photons N_γ detected at the laser frequency ν is

$$N_\gamma = n_1(0)\frac{A_{2k}}{A_2 + Q}G^{(2)}g(\Delta\nu)\sigma^{(2)}\frac{\langle\hat{I}(t)\rangle^2}{(h\nu)^2}F. \tag{4.5}$$

The factor F is an experimental factor

$$F = V\frac{\Omega}{4\pi}T\eta, \tag{4.6}$$

where V is the detection volume, Ω the detection branch solid angle, T the total transmission of the collection optics, and η is the detector quantum efficiency. The time integrated fluorescence signal is therefore proportional to the initial ground-state population and to the square of the laser pulse energy.

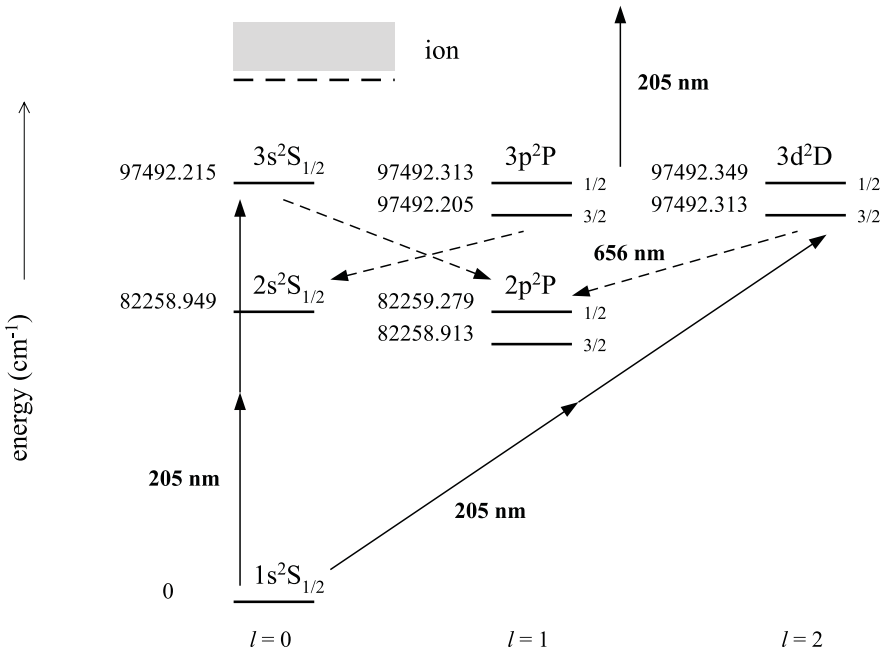

Fig. 4.1: Energy diagram of the hydrogen atom and two-photon excitation scheme. Two 205 nm photons are used to excite H from the ground-state to the $n = 3$ level. The fluorescence radiation is detected at the Balmer-α line. The absorption of a third UV photon from the $n = 3$ level leads to the formation of H^+.

4.3 Excitation and detection of ground-state atomic hydrogen

The excitation and detection scheme for ground-state atomic hydrogen applied in this work is the one that was first demonstrated by Bokor *et al.* in 1981 [10]. In this scheme, depicted in Fig. 4.1, H is excited with two 205.14 nm photons from the 1s $^2S_{1/2}$ ground-state to the n=3 level. The n=3 fine-structure sublevels can not be resolved within the bandwidth of the 205 nm laser radiation (≈ 0.18 cm^{-1}). As a result, in a spectral scan over the 2-photon transition both the 3s $^2S_{1/2}$ and the 3d ^2D_j states will be excited, according to the two-photon electric-dipole selection rules: $\Delta\ell = 0, \pm 2$ for a single electron atom where ℓ is the angular momentum. The case of multi-electron atom is extensively discussed in Ref. [16]. The excitation is monitored by detection of the non-resonant fluorescence on the Balmer-α transition at 656.3 nm from the 3d and 3s states to the 2p ^2P_j states. Usually it is mentioned that the 3d←1s transition dominates over the 3s←1s transition because of the 2-photon absorption cross section ratio [17]

$$\sigma^{(2)}(3\mathrm{d} \leftarrow 1\mathrm{s}) = \quad 17.7\ 10^{-44}\ \mathrm{m}^4,$$
$$\sigma^{(2)}(3\mathrm{s} \leftarrow 1\mathrm{s}) = \quad 2.3\ 10^{-44}\ \mathrm{m}^4.$$

Actually it depends on the degree of saturation of the transition whether the relative population of 3d and 3s is determined by the relative transition strength or rather by the ratio of the statistical weights of the respective quantum states. Moreover, we found evidence for a pure statistical distribution of the population over all the n=3 sublevels from an accurate measurement of the lifetime of the excited state [13]. This can be explained by a complete ℓ-mixing of the quantum states in the electric field associated with the propagating laser beam [18].

A detailed comparison between various 2-photon excitation schemes of H [11] shows that the above described scheme with a pulsed, narrowband 205 nm laser beam gives the largest average number of fluorescence photons per incident laser photon.

4.4 Experimental arrangement

4.4.1 Generation of narrowband coherent tunable UV radiation

A scheme of the experimental laser system used to produce narrowband coherent tunable UV radiation around 205 nm is depicted in Fig. 4.2. The laser system is based on a pulsed Nd:YAG/dye laser combination. The second harmonic output beam (500 mJ pulse energy at 532 nm, 6 ns duration) of an injection-seeded Nd:YAG-laser operating at 20 Hz (Spectra-Physics/Quanta-Ray, GCR-230) is used to pump a tunable dye laser (Spectra-Physics/Quanta-Ray, PDL-3). The dye laser has a bandwidth of 0.07 cm^{-1} and delivers radiation around 615 nm (sulforhodamine 640) with a pulse energy of typically 100 mJ. The dye laser output is frequency doubled in a KD*P crystal (type I). Upon exiting the crystal, the polarization of the generated blue beam is rotated to coincide with the polarization of the fundamental red beam using a low-order waveplate ($\lambda/4$ for the blue beam). Both collinear laser beams are input to a BBO crystal (type I) for sum frequency generation. The two crystals are electronically angle tuned by means of a feed back system to provide a constant output energy while scanning the dye laser wavelength.

The tripled frequency component is separated from the others and directed towards the vacuum vessel using high-power, high-reflective dielectric mirrors for 205 nm (45°) that are at the same time transparent for the other wavelengths. This procedure results in typically 2 mJ of tunable UV light around 205 nm for excitation of ground-state H. The UV laser beam is horizontally polarized and its frequency profile is Gaussian[1] with a measured bandwidth of 0.18 cm^{-1} [19].

The laser wavelength is calibrated by recording simultaneously the molecular iodine (I_2) absorption spectrum, of which the line positions are tabulated to high accuracy [20]. For this, part of the red dye-laser output is directed through a I_2 absorption cell. This glass cell has a 2.5 cm diameter and a 60 cm length and contains only iodine (solid and vapour). The transmitted light intensity is measured behind the cell with a photodiode. The absorption can be optimized by adjusting the I_2 vapour pressure with a heating wire around the cell.

[1] The laser beam profile has been determined using a two-photon excitation of N atom at 207 nm.

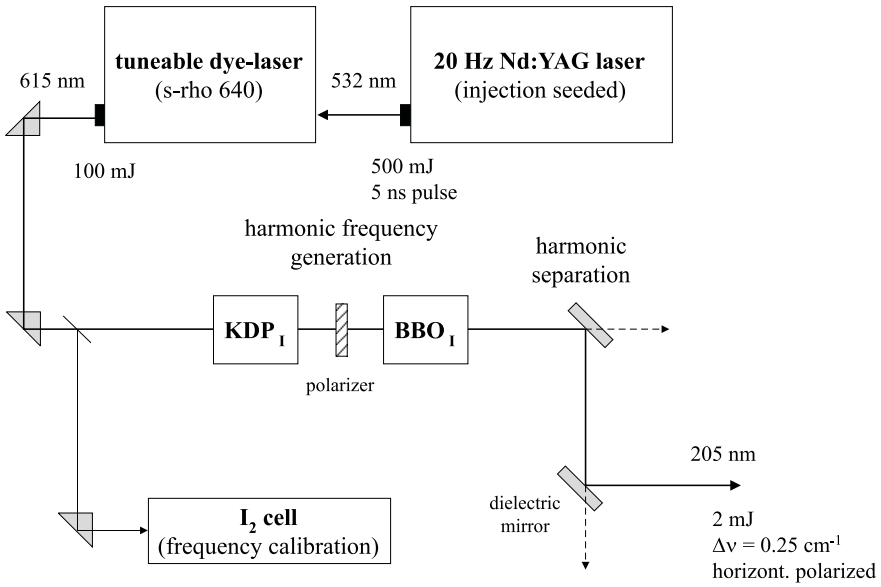

Fig. 4.2: Schematic view of the laser system used to generated narrowband coherent tunable radiation around 205 nm. The output beam of a tunable dye laser is converted into a UV laser beam after indirect third harmonic generation in crystals with nonlinear optical properties. The frequency of the laser beam is calibrated using the absorption spectrum of molecular iodine.

4.4.2 Fluorescence light monitoring

The frequency-tripled laser light is directed into the vessel either perpendicular to the plasma expansion axis or counterpropagating with the expansion, as depicted in Fig. 4.3. In the default perpendicular configuration, where the radial velocity component w_r and the perpendicular temperature $T_\perp$ (associated with the velocity distribution perpendicular to a stream line) can be measured, the UV laser light is focused into the plasma with a 60 cm MgF_2 lens. When the axial velocity component w_z and the parallel temperature $T_\parallel$ are to be measured, a 1 m focusing MgF_2 lens is used in combination with a quartz right-angle prism that directs the light anti-parallel to the plasma beam. In this way only the prism is exposed to the plasma and the combination of its relatively large distance from the plasma source with its mounting in a watercooled protection cylinder ensures a few hours of measurement time before cleaning of the prism is necessary.

The laser induced fluorescence light originating from the focus is imaged onto an adjustable slit mask, in a direction perpendicular to the plane formed by the laser beam and the symmetry axis of the expansion. This is done by two 10 cm diameter plano-convex lenses with focal lengths of 40 cm. The slit mask defines the spatial resolution (typically 1×1 mm^2). The laser induced fluorescence light that passes the slit mask is detected by a gated photo-multiplier (PMT Hamamatsu, R928). The continuous background light emitted by the plasma is strongly reduced by a narrow bandwidth interference filter located in front of the detector (10 nm FWHM, centered at 656 nm).

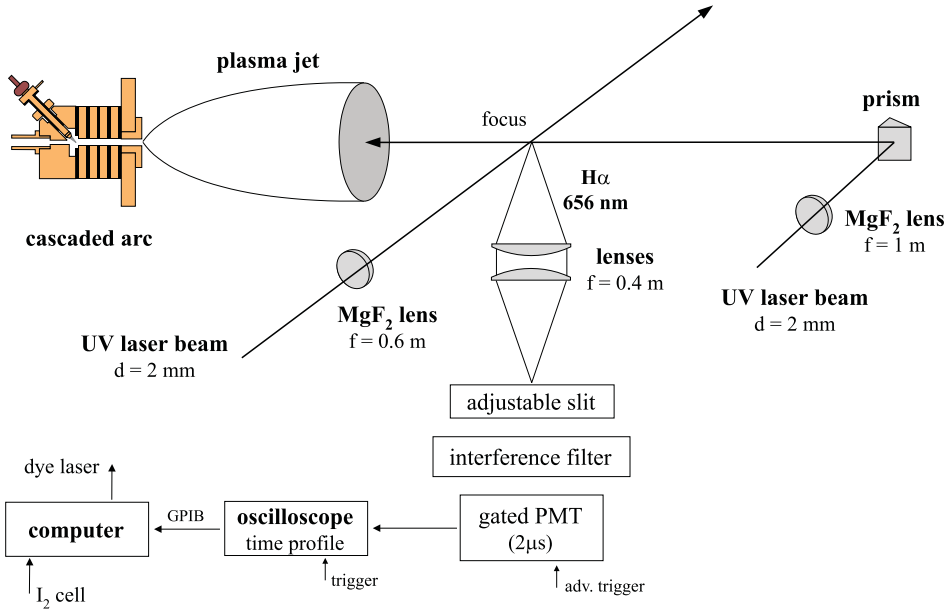

Fig. 4.3: Schematic view of the TALIF detection branch. The UV laser beam can be directed either perpendicular or parallel to the flow direction. Spatial scans through the expanding plasma are performed by moving the cascaded arc relative to the intersection of the laser beam and the detection volume.

However, the suppression of the plasma emission by the optical filter is not always sufficient to allow the PMT to be used with maximum gain. This is a well-known problem in the application of the LIF technique in light emitting media like those encountered in plasma and combustion research, which is usually solved by gating the detection. The Hamamatsu PMT R928 is equipped with a gate unit that enables triggered operation of the PMT during a short time interval (typically 2 μs). This reduces the continuous background further by a factor of 2×10^4, in principle enabling operation of the PMT with maximum gain in all circumstances.

The PMT signal is recorded by a digital sampling oscilloscope (500 $\mathrm{Ms\,s^{-1}}$, 100 MHz bandwidth). The oscilloscope can be used both for time-integrated and for time-resolved measurements. The signal trace is transferred to the PC where it is analyzed. This enables also baseline corrections and a precise time integration of the signal. The PC also controls the wavelength scanning of the dye laser.

The cascaded arc plasma source is mounted on a translation stage. Spatial scans through the expanding plasma are performed by moving the cascaded arc relative to the intersection of the laser beam and the detection volume.

4.4.3 Parasitic effects

Before focusing on the extraction of information from the H atom spectral profile, it is necessary to review the numerous parasitic effects which can disturb the laser induced

fluorescence signal, in order to be able to either avoid them or, when not possible, to quantify and subsequently account for them.

Collisional quenching

The fluorescence quantum yield q_f is given by the Stern-Vollmer factor

$$q_f = \frac{A_{kl}}{A_k + Q} = A_{kl}\tau_k. \tag{4.7}$$

This factor is the ratio between the spontaneous emission rate A_{kl} of level k on the transition to level l where the fluorescence is monitored, and the total depopulation rate of the excited state, which is the sum of the total spontaneous emission rate A_k and the non-radiative depopulation (quenching) rate Q of level k. The total depopulation rate determines the life-time τ_k of this state.

The most common uncontrolled depopulation mechanism is the collisional quenching of the upper state, which occurs when numerous collisions take place during the radiative lifetime of the excited state. This is a well-known problem in the application of LIF in experiments at high density, as for instance encountered in combustion research. However, the importance of fluorescence quenching can be easily underestimated in the field of (low-temperature) plasma research, where the quenching by electrons can be very efficient [13].

The occurrence of quenching can be readily checked in a time-resolved LIF experiment, where the effective life-time τ_k of the upper state k is measured. This lifetime is directly related to the quenching as is indicated by equation 4.7. In fact, a measurement of the lifetime will establish the value of the Stern-Vollmer factor, which potentially allows to correct the density values accordingly. Note that in case the quenching is strong, the fluorescence profile follows in shape the laser pulse and the lifetime can not be extracted from the measured time profile. In a plasma jet generated from an Ar-H_2 mixture or from pure H_2, a decay time of about 10.0 ns has been observed over the entire range of plasma parameters encountered in this plasma, as shown in Fig. 4.4. The longer decay time close to the source outlet is due to the reabsorption of Lyman-β photons (3d$\leftarrow$1s transition) by H atoms within the detection volume ($n_H \approx 10^{21}$ m^{-3}).

Shortly repeating the discussion in reference [13], this is exactly the decay time expected in the case of a statistical distribution of the population over the n=3 sublevels arising from ℓ-mixing induced by the laser E field. Arguments that the 10 ns decay time is the result of quenching of the 15.5 ns $3d \rightarrow 2p$ natural decay time can be discarded, since the same decay time has been found for a large range of ground state H, electron, and Ar(He, H_2) densities. The value of the collisional quenching rate coefficient can be found in Ref. [21, 22] for several collision partners.

3-photon ionization

A characteristic of the applied H excitation scheme is that only one additional laser photon is needed for ionization of the excited atom, as is indicated in figure 4.1. When the laser

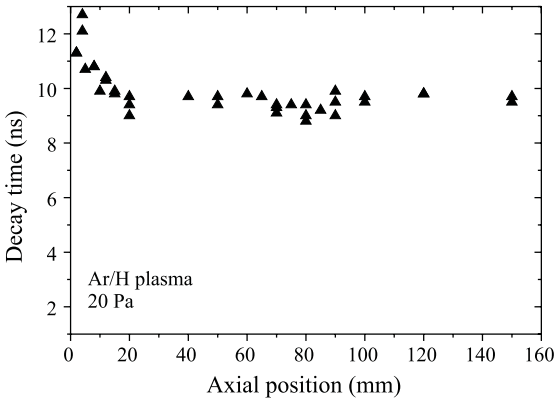

Fig. 4.4: Axial profile of the decay time of the deconvoluted time-resolved fluorescence signal measured in an Ar/H expanding plasma at 20 Pa.

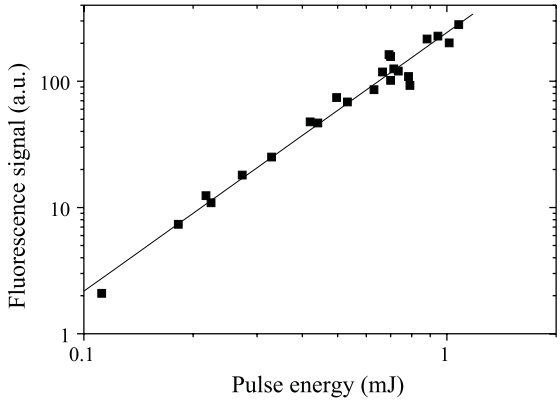

Fig. 4.5: Log-log plot of the fluorescence yield as a function of the laser pulse energy ($n_H = 10^{19}$ m^{-3} and $T_H = 800$ K). The slope is equal to 2.05±0.07.

intensity is increased, this ionization pathway will eventually limit the fluorescence yield, as the rate of depopulation via this process starts to compete with the radiative depopulation rate [11].

Depending on the type of plasma and the ionization degree, the laser-induced excited state, ion, and electron densities can be several orders of magnitude higher than the respective stationary densities. A complete model is then needed to quantitatively assess the effect of the pulsed laser excitation on the local plasma parameters. In a concurrent study presently performed in our group, a time-resolved collisional radiative model (CRM) for H has been developed, that models the response of a system of levels to a temporary disturbance of the level population distribution by for instance pulsed laser excitation of one of the levels [13]. This study shows, among others, that for conditions typically encountered in the expanding cascaded arc plasma, the ion and electron densities can temporarely increase easily by a factor of five due to the applied laser pulse. In such a case, the laser diagnostic method can hardly be qualified as 'non-intrusive' as far as charged particle density and temperature are concerned.

Amplified stimulated emission generation

Another uncontrolled depopulation pathway that might occur is amplified spontaneous emission (ASE) of the laser-excited state [23]. The ASE will propagate within a small solid angle around the laser beam axis, and, consequently, the upper state population lost in this way will not be observed by the LIF detection branch. ASE of Balmer-α radiation at 656 nm in a two-photon LIF experiment for detection of ground-state H has been reported

both for measurements in a flame [24], as well as for measurements in glow discharge plasmas [25, 26]. In these studies, the possibility of explicitly using the ASE signal for the detection of H is investigated.

Dissociation of molecules

A further phenomenon that can disturb the proportionality between ground-state density and observed LIF signal, is the production of the atoms under investigation by the UV laser itself via photo-dissociation of molecules. This is commonly recognized and described in a number of papers [27, 28, 29]. The effect can even be turned into an advantage by using it to identify an impurity and measure its density via an analysis of the spectral profile of the LIF signal [27, 29]. In the expanding cascaded arc plasma generated from a mixture of Ar and H_2, the only species that could produce H atoms from photo-dissociation is molecular hydrogen. We checked the possibility of 205 nm ($\approx$ 6 eV) photo-dissociation of H_2 by filling the vessel with pure molecular hydrogen at room-temperature. For the highest laser-intensity used in our experiments (2 mJ), we did not observe any H LIF signal for pressures up to 200 Pa. This does not exclude that photo-dissociation of H_2 occurs in the plasma. While the effect is negligible for room temperature H_2, it could still be noticeable for hot molecules when the photo-dissociation cross-section is sufficiently enhanced for vibrationally excited molecules. Photo-dissociation of molecules by the UV laser can also seriously disturb the temperature determination. Depending on the excess energy, the atomic fragments end up with more than their thermal share of kinetic energy. This gives rise to a large Doppler width and an apparent high atom temperature. Observations of high atomic hydrogen temperatures in RF, microwave, and DC discharges have been associated with photolysis of NH_3, H_2S, C_2H_2, C_2H_4, and Si_2H_6 [27, 28, 29]. In fact, the photolytically produced atoms exhibit a spectral profile characteristic of their precursor molecule, and the Doppler width can be used to determine the excess translational energy enabling an identification of the precursor molecule [27].

Saturation broadening

A last effect that can significantly disturb the two-photon spectral profile is saturation broadening. The degree of saturation of a transition is given by the saturation parameter, which is basically the ratio between the induced and the spontaneous emission rate of the excited level [30]. Since the induced emission rate is directly proportional to the excitation cross section, the saturation parameter for a two-photon transition will generally be very small, and thus the required energy to saturate will be high.

Apart from collisional quenching that can be determined from time-resolved measurements, probably the best way to check for the existence of parasitic effect is to measure the laser intensity dependence of the H atom two-photon LIF signal from the plasma. For ground-state H atoms a quadratic dependence should be observed for low laser intensities, as shown in Eq. 4.5, saturating to a lower order dependence for higher intensities. When

photo-dissociation by the UV-laser occurs, a higher order dependence will be observed [27]. Fig. 4.5 shows the LIF signal of atomic hydrogen from the expanding Ar-H_2 plasma as a function of the laser intensity. The slope of the data points indeed equals 2 within the experimental accuracy. From this it is concluded that in this plasma there is no contribution to the H atom LIF signal from photo-dissociation by the UV-laser. Moreover, from the figure it can be seen that the H two-photon excitation does not reach saturation in our experiment and that the H two-photon LIF signal remains in the quadratic regime over the entire range of laser pulse energies used in our measurements.

4.5 Density measurements

4.5.1 Integrated spectral profile

The density information gained in a LIF experiment, although in principal absolute, is in practice relative in nature. The relative local H atom density is obtained from the integration of the two-photon spectral profile, see Fig. 4.6. Every measured profile is obtained using 256 shots per data point because of the important pulse to pulse energy fluctuation (sd $\approx$ 25 %) of the UV laser beam.

The usual approach to get quantitative results from a LIF experiment is to calibrate the set-up using an independent source of a well-known amount of the probed species. In the case of stable neutral atoms or molecules this is easily accomplished with e.g. a gas cell containing a fixed pressure of this species. In the case of short-lived species like radicals or ions, calibration is less trivial. For the calibration of the set-up for the atomic hydrogen measurements, two different approaches are used.

4.5.2 Absolute densities: calibration methods

Titration reaction

The first approach uses a 'flow-tube reactor' as a source of ground-state H atoms, in which the exact amount of atomic hydrogen is determined by a titration. This method is based on well-established flow reactor and titration techniques in chemistry [31], and has already been applied more often in LIF measurements of ground-state H radical densities in plasmas [32, 27]. A scheme of the flow-tube reactor, designed to allow implementation in the expansion chamber, is depicted in Fig. 4.7. A small amount of molecular hydrogen that is diluted in helium flows through a quartz tube that is mounted through the centre of a Beenakker-type microwave cavity [33]. Atomic hydrogen is produced in the flow-tube by dissociation of H_2 in the microwave discharge (typical power of 80 W) that is sustained in the cavity. The main flow continues down the quartz tube and a 0.5 m long teflon tube, transporting H atoms to a position 60 cm downstream from the discharge and only 1 or 2 mm away from the scattering volume of the laser, where they are detected with identical excitation and detection geometry as in the expanding cascaded arc plasma. The tube material has been chosen to minimize the H atom loss between the microwave discharge

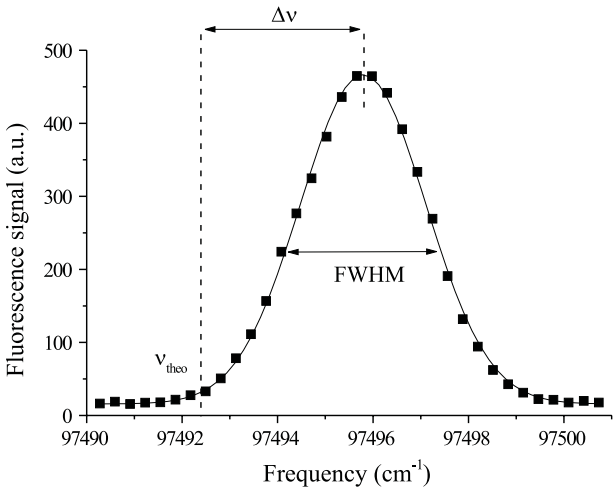

Fig. 4.6: Measured spectral profile of the 3←1 two-photon transition in atomic hydrogen and Gaussian fit. The fluorescence is detected at the Balmer-α line. The area of the peak is a direct measure of the H density (after calibration). The local temperature is deduced from the Doppler broadening of the line after deconvolution with the laser spectral profile. The mean H velocity (in the direction of the laser beam) is determined from the absolute Doppler shift of the line.

and the point where H is detected. The length of the tube ensures that no excited H atoms arrive at the scattering volume of the laser.

The amount of H present in the scattering volume and responsible for the observed signal is determined via a titration with NO_2. The NO_2 comes from a calibrated mixture of 2.11 % NO_2 in He that can be added to the main flow via a small insert that enters the main transport tube near to the end of it. The titration actually determines the H density in the mixing region. To ensure that this density is as close as possible to the H density responsible for the LIF signal in the laser scattering volume, the mixing region should be as close to the exit of the main tube as possible. This distance is small compared to the length of the main tube, and it can therefore be safely assumed that the ground-state H density is constant over the last 3.5 cm of the flow-tube. Upon addition of NO_2, H atoms are lost in the fast reaction

$$H + NO_2 \rightarrow OH + NO, \tag{4.8}$$

with a rate constant k of 1.3×10^{-10} cm^3 s^{-1} [31]. Solving the symmetric set of rate equations

$$\frac{d}{dt} n_H = -k n_H n_{NO_2} = \frac{d}{dt} n_{NO_2} \tag{4.9}$$

for the densities n_H and n_{NO_2} of H and NO_2, respectively, shows that when $t \rightarrow \infty$, i.e. when the reaction is complete, the remaining H density depends linearly on the initial NO_2 density. Fig. 4.8 shows a typical titration curve, i.e. a measurement of the H fluorescence

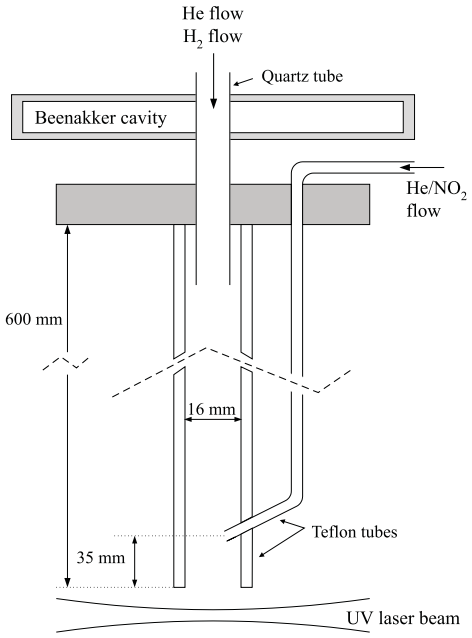

Fig. 4.7: Schematic overview of the flow tube reactor.

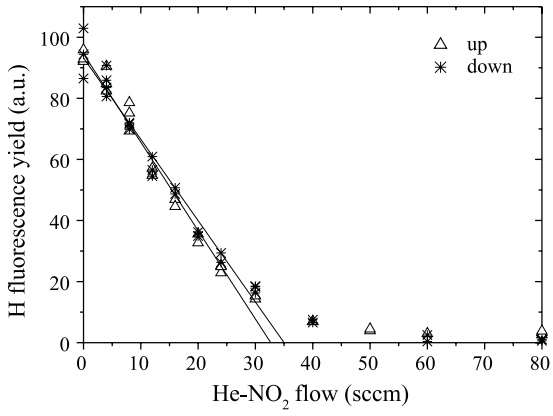

Fig. 4.8: Titration curve (800 sccm He, 8 sccm H_2, 85 W, I_{205} = 0.2 mJ).

signal from the flow-tube reactor as a function of the admixed NO_2 flow. The dependence is recorded both in a series with increasing flow and in one with decreasing flow. The H LIF signal decreases linearly with increasing NO_2 flow until it becomes indistinguishable from the background (end point of titration). Given the 1:1 stochiometric ratio of the titration reaction, the NO_2 density $n_{NO_2}^{(T)}$ at the x intercept in Fig. 4.8, which is necessary to remove all H atoms, equals the original H density n_H at the beginning of the titration that gives rise to the LIF signal at the y intercept

$$n_H = n_{NO_2}^{(T)} = n_{tot}\frac{\Phi_{NO_2}^{(T)}}{\Phi_{tot}} = \frac{p}{kT}\frac{\Phi_{NO_2}^{(T)}}{\Phi_{tot}}, \tag{4.10}$$

with p and T the pressure and temperature in the vessel, respectively, k the Boltzmann constant, $\Phi_{NO_2}^{(T)}$ the NO_2 flow rate. The subscript tot denotes the total density or flow. During the titration, the total flow Φ_{tot} is kept constant in order to keep the pressure p in the vessel constant. The increasing flow of the calibrated NO_2/He mixture is balanced by a decreasing additional pure He flow in the small titration tube.

The first equality in equation 4.10 only holds under certain conditions. First of all, the titration reaction should be complete. This condition can be quantified by evaluating the solution of the set of equations 4.9 for the case that the initial NO_2 density $n_{NO_2,0}$ approaches the initial H density $n_{H,0}$, i.e. near the end point of titration. This yields

$$n_H(t) = \frac{n_{H,0}}{1 + kn_{H,0}t}. \tag{4.11}$$

The end point of titration ($n_{NO_2,0} = n_{H,0}$) is only sharply determined if $kn_{H,0}t \gg 1$. This is the condition for linearity and complete titration. In addition, the $[NO_2]/[H]$ stoichiometry should be 1:1. Other reactions that could change the stoichiometry should only play a minor role. The secondary reactions OH + OH $\rightarrow$ H_2O + O and O + OH $\rightarrow$ O_2 + H are significantly reduced at the low H concentrations in the flow-tube reactor [34, 35], and other interfering reactions such as O + NO_2 $\rightarrow$ O_2 + NO and OH + H_2 $\rightarrow$ H_2O + H are made negligible by diluting both NO_2 and H_2 in He [34]. The second equality in equation 4.10 implies the assumption of efficient mixing between the NO_2/He flow from the titration tube and the main flow. A proper density calibration furthermore avoids a 'self-generated signal'. The occurrence of UV-photolysis of H containing impurities from the flow-tube reactor can be easily checked by examining the Doppler-width of the H LIF signal. This should yield a temperature close to room temperature. The Doppler width of the H LIF signal from our flow-tube reactor corresponds to a temperature close to 400 K.

In the titration shown in Fig. 4.8 the end point of titration is not very sharply determined, and is therefore derived from a linear fit, yielding $\Phi_{NO_2}^{(T)} = 0.71 \pm 0.04$ sccm. The corresponding initial H density can now be derived from equation 4.10 using the settings $p = 240$ Pa, $T = 300$ K, and $\Phi_{tot} = 908$ sccm, resulting in $n_H = (8.2 \pm 0.4) \times 10^{19}$ m^{-3}. The real inaccuracy in n_H is however larger (around 25 %) since it is determined by the uncertainty in the value of all parameters (pressure, temperature, flows) and by the uncertainty in the exact state of the chemical reactions involved. The condition for linearity and complete titration can now be evaluated. The reaction time t is determined by the 3.5 cm distance between the end of the titration tube and the exit of the main tube and by the flow velocity. Using the above values yields $t = 2.1$ ms and $kn_{H,0}t = 22$. This shows that the condition for linearity and complete titration is only just fulfilled.

It is of upmost importance to change as little as possible when switching between the recording of the H LIF signal from the flow-tube reactor and that from the expanding thermal plasma. In practice this means that the two measurements should be performed directly after each other. Finally, when converting H LIF signal values from the plasma jet to H densities one should take into account that the H atom temperature in the two recordings will generally be different. This demands to compare only spectrally integrated signal values.

Two-photon excitation of Kr

The second approach avoids the cumbersome generation of a well-known amount of atomic hydrogen radicals from an independent source. Instead, a LIF signal is generated from a fixed pressure of a different stable species by a comparable two-photon excitation scheme. The H density in the plasma beam can then be determined from the ratio of the LIF signals when the ratio of the two-photon cross sections is known. This method has recently been demonstrated for the calibration of ground-state atomic hydrogen densities [22] as well as of ground-state atomic nitrogen densities [19, 22] by using a two-photon transition in krypton. The method has also been applied to calibrate the fluorescence yield of oxygen atoms via a two-photon transition in xenon [12]. This method is more elegant and experimentally

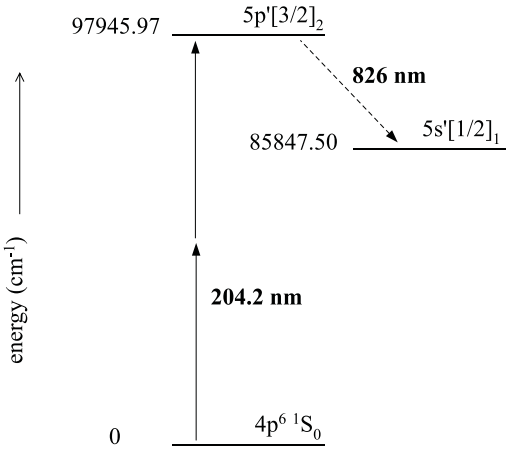

Fig. 4.9: Simplified energy diagram of krypton. Also depicted is the two-photon excitation scheme used to calibrate H densities (to be compared with Fig. 4.1).

easier than the first one, but it relies on critical cross section data.

The basic idea behind a radical density calibration using a known density of a stable species, is to find and use an excitation and detection scheme in a stable species as similar as possible to that of the radical. This warrants a comparable response to the laser excitation, especially when the excitation wavelengths are close to each other, which allows the excitation conditions (laser spectral, temporal, and beam profile, intensity, and focusing) to be the same in the two LIF measurements. The excitation and detection scheme for krypton that is used in the atomic hydrogen density calibration is depicted in figure 4.9. In this scheme Kr is excited with two 204.2 nm photons from the $4p^6\ {}^1S_0$ ground-state to the $5p'[3/2]_2$ state. The resulting non-resonant fluorescence from this state to the $5s'[1/2]_1$ state is detected at 826 nm. In both schemes the excitation concerns a two-photon transition, which gives a quadratic response to the laser intensity in the small signal limit (low laser intensity). The wavelengths used for excitation are in addition nearly equal and can actually be generated from the same dye solution in the tunable dye laser. This means in practice that we can switch between H and Kr measurements within an instant; the laser is tuned to the other wavelength and only the fluorescence filter in front of the PMT has to be replaced.

In the quadratic regime and under equal excitation conditions, the ratio S_{Kr}/S_H of the spectrally integrated fluorescence signals of krypton and hydrogen according to equation 4.5, reduces to [12, 19, 22]

$$\frac{S_{Kr}}{S_H} = \frac{n_{Kr}}{n_H}\frac{\sigma^{(2)}_{Kr}}{\sigma^{(2)}_H}\left(\frac{\nu_H I_{Kr}}{\nu_{Kr} I_H}\right)^2 \frac{A_{Kr}\tau_{Kr}}{A_H\tau_H}\frac{T_{Kr}}{T_H}\frac{\eta_{Kr}}{\eta_H}. \tag{4.12}$$

Here, n refers to the ground-state density, I is the corresponding laser beam energy, ν is the photon frequency, A is the Einstein transition probability for the detected spontaneous emission, τ is the lifetime of the excited state, T is the transmission of the optical

Tab. 4.1: Values of the parameters involved in the H density calibration via krypton, using equation 4.12. For the meaning of the symbols, see the text. The transmission T of the optical filters in the detection branch for the respective fluorescence wavelengths has been measured with a FT spectrometer. The PMT quantum efficiency η for the Kr fluorescence wavelength (826 nm) has been measured relative to the one for the H Balmer-α fluorescence (656.3 nm) with a ribbon lamp.

	Kr	H
I_{laser} (mJ)	0.12	0.39
ν (cm^{-1})	48972.985	48746.15
A (s^{-1})	2.7×10^7	4.4×10^7
τ (ns)	35.4	10.0
T	0.95	0.447
η (relative)	0.088	1.0

detection branch for the detected fluorescence, and η is the detector quantum efficiency at the corresponding wavelength. The solid angle that is captured by the detection optics, the detection volume, and the gain of the photon detector are the same in the two LIF measurements. The ratio of the two-photon excitation cross sections has recently been measured to be $\sigma^{(2)}_{Kr}/\sigma^{(2)}_{H} = 0.62$ [22].

For the Kr LIF measurements the vacuum chamber is filled with 10 Pa Kr at room temperature which corresponds to a Kr density of 2.4×10^{21} m^{-3}. The two-photon transition in Kr, that is induced here for the H density calibration, is easily saturated. The transition is for instance known to readily generate ASE, enhanced by its small Doppler width [36]. Since equation 4.12 only holds in the quadratic regime, special care is taken to avoid saturation of the transition. A longpass filter, T = 0.95 above 700 nm, is used to reduce the laser stray light impinging onto the PMT. The fluorescence decay times τ of Kr and H have been measured with a fast PMT (Hamamatsu R5600P-01; 1 ns FWHM single photon response time [13]). As already mentioned, the lifetime of the H n=3 excited state has been measured to be 10.0 ns. The lifetime τ_{Kr} of the Kr 5p'$[3/2]_2$ state is found to be 35.4±2.7 ns, in agreement with a value recently measured by Niemi *et al* [22]. The measured radiative lifetime of krypton is longer than the one usually found in literature (τ_{Kr} = 26.9 ns) [37]. In the calibration procedure reported here, a branching ratio of 0.95 is used for krypton. Table 4.1 summarizes the values of all parameters involved in the H density calibration via krypton, using equation 4.12.

Figure 4.10 shows two axial profiles of the absolute atomic hydrogen density in the supersonic domain of a thermal Ar-H_2 plasma expansion. One density profile is calibrated via a NO_2 titration in a flow-tube reactor, the other via a two-photon LIF measurement of krypton. The H density values determined by the two different methods agree well with each other. This comparison therefore validates the H density calibration via a two-photon LIF measurement of Kr, which is experimentally easier than the calibration with

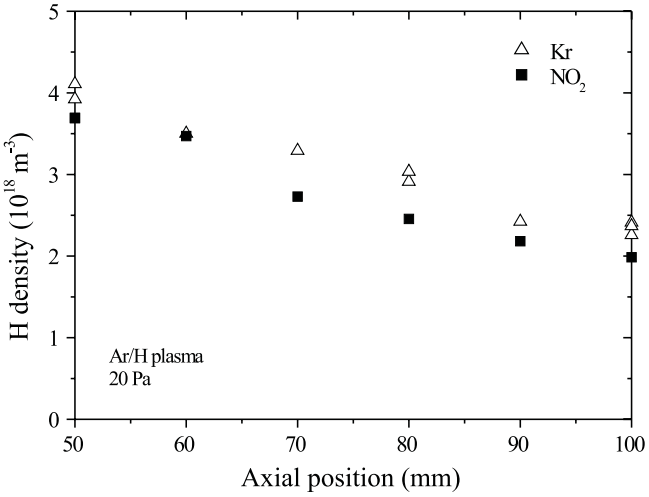

Fig. 4.10: Comparison between absolute atomic hydrogen density profile along the axis of an Ar/H plasma jet (20 Pa) that are calibrated via 2-photon excitation in Kr (triangle) and via a titration in a flow tube reactor with NO_2 (square). Using the latter, a 2-photon cross-section ratio $\sigma^{(2)}_{Kr}/\sigma^{(2)}_{H}$ of 0.56 is obtained.

the flow-tube reactor, once the values of the parameters in equation 4.12 are accurately determined.

Using the H densities determined with the titration method, a two-photon cross-section ratio $\sigma^{(2)}_{Kr}/\sigma^{(2)}_{H}$ equals 0.56 is obtained, in good agreement with the value 0.62 measured by Niemi *et al* [22].

To conclude this section, the H atom density detection limit that can be achieved under our experimental conditions, has to be given. In an expanding Ar(H_2, He)/H plasma it is found to be $10^{15}\,m^{-3}$, which is certainly sufficient to obtain valuable information about the amount of H atoms that are carried away by a plasma jet.

4.6 Temperature measurements

In case of thermodynamic equilibrium (TE), the local atom temperature is derived from the width of the spectral profile of the two-photon transition[2]. The experimentally observed linewidth is the result of the convolution of all contributions to the width. Under our experimental conditions, the main contribution comes from the Doppler broadening

[2] In TE, the temperature is related to the second moment of the velocity distribution function (VDF) via the relation $kT = \frac{1}{2}m\overline{v^2}$; a detailed calculation shows however that the temperature can simply be determined from the width of the spectral profile. Note that when the system departs from TE, the temperature is not defined anymore and one has to refer directly to the VDF.

that results from the velocity distribution of the ground-state atoms. Collisions (pressure broadening) do not contribute significantly to the broadening of the line within our pressure range ($p < 1$ torr). Another effect that should be seriously considered when determining temperatures from LIF measurements in plasmas, is Stark broadening [38]. In the plasmas investigated in this work, it will not significantly contribute to the experimentally observed linewidth, since the Stark broadening of the two-photon transition in atomic hydrogen, which is mainly determined by the Stark coefficients of the n=3 level, is negligible for the range of electron densities and temperatures encountered in the expanding plasma ($n_e \leq 10^{19}$ m^{-3}, $T_e \approx 0.3$ eV [39]).

The general expression for the Doppler width $\Delta\nu_D$ (FWHM) of a two-photon transition, induced by the absorption of one photon with frequency ν_1 and one photon with frequency ν_2 with an angle θ between their k-vectors, is [15]

$$\Delta\nu_D = 2(\nu_1^2 + \nu_2^2 + 2\nu_1\nu_2\cos\theta)^{1/2}\,\bar{v}/c, \tag{4.13}$$

where $\bar{v}$ is the average velocity of the atom or molecule, and c is the speed of light in vacuum. In the case of absorption of two photons from one single laser beam with a frequency of half the transition frequency ν_0 ($\nu_1 = \nu_2 = \nu_0/2$, $\theta = 0$), and with a Maxwellian distribution function ($\bar{v} = \sqrt{2\ln 2 \cdot kT/m}$), this expression reduces to the well-known relation between the Doppler width and the temperature T

$$\Delta\nu_D = \nu_0/c\sqrt{8\ln 2 \cdot kT/m} = 7.16 \times 10^{-7}\nu_0\sqrt{T/M} \quad \text{(in cm}^{-1}\text{)}, \tag{4.14}$$

with k the Boltzmann constant, m the mass of the atom or molecule, and M its molecular weight in amu. The Doppler width $\Delta\nu_D$ is convoluted twice with the linewidth $\Delta\nu_L$ of the UV laser radiation (= 0.18 cm^{-1} [19]). Assuming a Gaussian spectral profile for the latter, the experimentally observed linewidth $\Delta\nu$ is simply given by: $\Delta\nu^2 = \Delta\nu_D^2 + 2\Delta\nu_L^2$. In the case of atomic hydrogen, the error in $\Delta\nu_D$ — and thus in the temperature — introduced by this squared summation when the laser spectral profile is non-Gaussian, is expected to be small since the observed linewidths are typically one order of magnitude larger than the laser linewidth.

4.7 Velocity measurements

Besides determining the velocity spread — and from that the temperature — of the particles in the plasma jet from the Doppler width, in thermodynamic equilibrium the Doppler shift of the center frequency ν_0 of the transition can be used to determine the mean velocity of these particles[3]. The velocity w in the direction of the laser beam of a group of atoms absorbing the laser photons at frequency ν is given by [40]

$$w = c\frac{\nu - \nu_0}{\nu_0}. \tag{4.15}$$

[3] The mean particle velocity is obtained directly from the first moment of the velocity distribution function (VDF). In TE the mean velocity can simply be determined from the shift of the spectral profile.

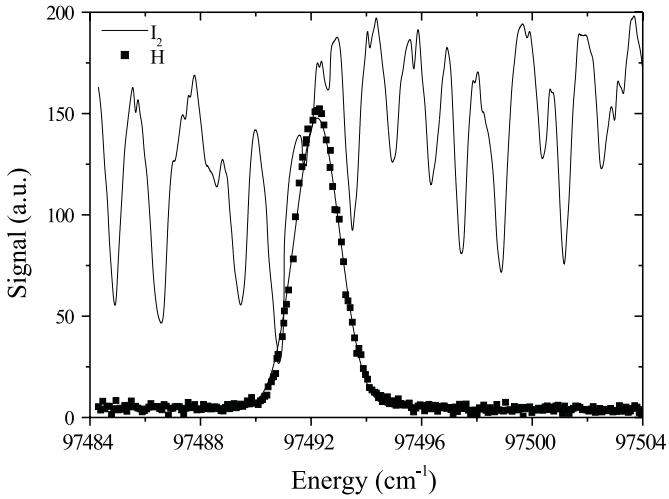

Fig. 4.11: Example of a spectral scan with simultaneous recording of the H atom 2-photon LIF signal (solid square) and the I_2 absorption signal (solid line). The scan is recorded on the jet centerline of an Ar-H_2 plasma jet. The horizontal axis is two times the energy of the UV photon used to excite H atoms. This axis is calibrated by the position of the I_2 absorption lines.

Previous equation is used to convert the measured spectral profile into the local velocity distribution function (VDF) in the direction defined by the laser beam. The energy distribution function (EDF) can be obtained from the VDF using the kinetic energy formula $E = \frac{1}{2}mw^2$. At thermodynamic equilibrium, the VDF is Gaussian and the EDF is Maxwellian.

To determine the Doppler shift, a Doppler shifted signal must be compared with a non shifted signal, which usually requires two laser beams. An absolute determination of the Doppler shift 'only' requires an absolute frequency scale — and then the shift is obtained from a comparison of the center frequency with the literature value — but obviously in that case the laser frequency needs to be accurately calibrated. This is accomplished by using a small fraction of the red dye laser output beam for the simultaneous recording of the absorption spectrum of molecular iodine, as is described in the experimental section 4.4. An example of such a simultaneous recording is given in Fig. 4.11. In the region of the fundamental dye-laser frequency, the I_2 spectrum shows many absorption lines that are tabulated in frequency to an accuracy of 0.015 cm^{-1} [20]. The width of the I_2 absorption lines, which is at room temperature mainly determined by the underlying hyperfine structure, amounts to ≈ 0.03 cm^{-1}. The medium is therefore very well suited for the frequency calibration of pulsed dye-lasers of which the bandwidth is usually in the same order of magnitude (in our case 0.07 cm^{-1}), and the method is widely used in spectroscopy.

Since the Doppler shift method determines velocities relative to the velocity of light,

accurate results are not to be expected *a priori*, and it is worthwhile to address the topic of accuracy into somewhat more detail. In the applied method, the error in the velocity has several sources. The error in the calibrated frequency scale depends on the signal to noise (S/N) ratio in the I_2 absorption spectrum, and is ultimately limited by the bandwidth of the laser. The attainable minimum error in the (fundamental) frequency scale is ≈ 0.01 cm^{-1}. A further error comes from the determination of the center frequency of the two-photon spectral line from the Gaussian fit. The error in the observed center frequency depends again on the stepsize in the spectral scan and on the S/N ratio of the H LIF signal. In practice, the overall error in the velocity is mainly determined by this contribution.

A last uncertainty concerns the literature value for the transition frequency. Accurate values for the energies of the individual n=3 sublevels can for instance be found in [41], but since the maximum energy separation between these levels is smaller than the bandwidth of the 205 nm laser radiation, these levels are not resolved and the resulting center frequency will be at an averaged value. This leaves some room for the exact reference value to take for the velocity determination. The one used in this work is obtained from the experiment itself. In a measurement of the radial velocity in a radial cross section through the expanding plasma jet, symmetry arguments are used to put the radial velocity on the symmetry axis of the expansion to zero. This leads to the value $\nu_0 = 97492.315$ cm^{-1}. This value[4] is very close to the averaged literature value that accounts for a pure statistical distribution of the population over all the n=3 sublevels, which is consistent with the lifetime of the excited state that is observed in this work.

The resulting maximum accuracy that can be attained in the determination of the velocity of atomic hydrogen from the Doppler shift of the transition frequency in the two-photon LIF measurements in the expanding plasma is ≈ 200 m s^{-1}, which is a fraction of less than 10^{-6} of the speed of light. This value is consistent with the S/N ratio that we experimentally observe in our velocity measurements. This accuracy is certainly sufficient to gain valuable information about the flow pattern in the expanding plasma, where H atom velocities in the range $0 - 8000$ m s^{-1} are observed.

4.8 Conclusions

The TALIF spectroscopic method at 205 nm is perfectly suited for the study of the transport mechanisms of ground-state H(D) atoms in a plasma expansion. From the spectral scan over the two-photon transition, several parameters can be extracted that are of crucial relevance for the understanding of the plasma flow properties. First, the measured spectral profile can be easily transformed into the local H atom velocity distribution function that allows for discussion about the thermodynamic state of the plasma. Second, a mean H atom velocity as well as a temperature when the system is at thermodynamic equilibrium (both are defined in the direction of the laser beam) are obtained. Third, the local absolute

[4] The transport of deuterium atoms (D) in a plasma expansion is also investigated in this thesis. The energy diagram of D of H are linked via the isotopic mass shift relation [42]: $E_D = (\mu_D/\mu_H)E_H$, where μ is the reduced mass. One obtains $\mu_D/\mu_H = 1.000272099$ and $\nu_0 = 97518.843$ cm^{-1}.

H atom density is determined from the area of the fluorescence line after calibration of the LIF setup.

Therefore the TALIF diagnostic technique enable to accurately measure the plasma jet density, velocity and temperature map. From the large dataset that is obtained, the expansion of H atoms can be compared with the classical inert neutral gas expansion picture. This led among others to the discovery of anomalies in the transport of atomic radicals in a plasma expansion. But more than that the application of the TALIF tool to H containing plasma allowed to identify the reason of those anomalies: plasma-wall interactions.

Acknowledgments

The author would like to thank Dr M.G.H. Boogaarts for his valuable contribution in the fulfillment of this chapter. Professor H.F. Döbele (institute for Laser and Plasma Physics, Essen University, Germany) is gratefully acknowledged for his vital contribution in the initial phase of the TALIF experiment. The author greatly appreciates the skillful technical assistance of M.J.F. van de Sande, A.B.M. Hüsken, and H.M.M. de Jong.

References

[1] J. Amorim, G. Baravian, and J. Jolly, *J. Phys. D: Appl. Phys.* **33**, R51 (2000).

[2] Y-C. Hsu, Y-J. Shiu, and C-M. Lin, *J. Chem. Phys.* **103**, 5919 (1995).

[3] M. Hertl, N. Dorval, O. Leroy, J. Jolly, and M. Péalat, *Plasma Sources Sci. Technol.* **7**, 130 (1998).

[4] N. Sadeghi, M. van de Grift, D. Vender, G.M.W. Kroesen, and F.J. de Hoog, *Appl. Phys. Lett.* **70**, 835 (1997).

[5] K. Muraoka and M. Maeda, *Plasma Phys. Control. Fusion* **35**, 633 (1993).

[6] H.F. Döbele, *Plasma Sources Sci. Technol.* **4**, 224 (1995) and references herein.

[7] J. Larjo, J. Waalewski, R. Hernberg *Appl. Phys. B* **72**, 455 (2001).

[8] B.L. Preppernau and T.A. Miller *J. Vac. Sci. Technol. A* **8**, 1673 (1990).

[9] A.D. Tserepi and T.A. Miller, *J. Appl. Phys.* **75**, 7231 (1994).

[10] J. Bokor, R.R. Freeman, J.C. White, and R.H. Storz, *Phys. Rev. A* **24**, 612 (1981).

[11] U. Czarnetzki, K. Miyazaki, T. Kajiwara, K. Muraoka, M. Maeda, and H.F. Döbele, *J. Opt. Soc. Am. B* **11**, 2155 (1994).

[12] A. Goehlich, T. Kawetzki, and H.F. Döbele, *J. Chem. Phys.* **108**, 9362 (1998).

[13] H.W.P. van der Heijden, M.G.H. Boogaarts, S. Mazouffre, J.A.M. van der Mullen, and D.C. Schram, *Phys. Rev. E* **61**, 4402 (2000).

[14] D. Voslamber, *Rev. Sci. Instrum.* **71**, 2334 (2000).

[15] R. Loudon, *The Quantum Theory of Light*, Clarendon Press, Oxford (1983).

[16] K.D. Bonin and T.J. McIlrath, *J. Opt. Soc. Am. B* **1**, 52 (1984).

[17] J.H. Tung, A.Z. Tang, G.J. Salamo, and F.T. Chan, *J. Opt. Soc. Am. B* **3**, 837 (1986).

[18] B.L. Preppernau, K. Pearce, A. Tserepi, E. Wurzberg, and T.A. Miller, *Chem. Phys.* **196**, 371 (1995).

[19] S. Mazouffre, C. Foissac, P. Supiot, P. Vankan, R. Engeln, D.C. Schram, , and N. Sadeghi, *Plasma Sources Sci. Technol.* **10**, 168 (2001).

[20] S. Gerstenkorn and P. Luc, *Atlas de spectroscopie d'absorption de la molécule d'iode*, CNRS, Paris (1975); S. Gerstenkorn and P. Luc, *Rev. Phys. Appl.* **14**, 791 (1979).

[21] J. Bittner, K. Kohse-Höinghaus, U. Meier, and Th. Just, *Chem. Phys. Lett.* **143**, 571 (1988).

[22] K. Niemi, V. Schultz von der Gathen, and H.F. Döbele, *Proceedings of Hakone* **7**, Greifswald, Germany, Vol. 1, 199 (2000).

[23] L. Allen and G.I. Peters, *Phys. Rev. A* **8**, 2031 (1973).

[24] J.M. Goldsmith, *J. Opt. Soc. Am. B.* **6**, 1979 (1989).

[25] G. Hancock and M. Toogood, *Appl. Phys. Lett.* **60**, 35 (1992).

[26] J. Amorim, G. Baravian, M. Touzeau, J. Jolly, *J. Appl. Phys.* **76**, 1487 (1994).

[27] J.R. Dunlop, A.D. Tserepi, B.L. Preppernau, and T.A. Miller, *Plasma Chem. Plasma Process.* **12**, 89 (1992).

[28] K. Miyazaki, T. Kajiwara, K. Uchino, K. Muraoka, T. Okada, and M. Maeda, *J. Vac. Sci. Technol. A* **14**, 125 (1996).

[29] J. Amorim, G. Baravian, and G. Sultan, *Appl. Phys. Lett* **68**, 1915 (1996).

[30] W. Demtröder, *Laser Spectroscopy*, Springer series in chemical physics, Vol. 5, Springer-Verlag, Berlin (1988).

[31] see for instance *Reactive Intermediate in the Gas Phase*, ed. D.W. Setser, Academic Press, New York (1979).

[32] U. Meier, K. Kohse-Höinghaus, L. Schafer, and C.P. Klages, *Appl. Opt.* **29**, 4993 (1993).

[33] C.I.M. Beenakker, *Spectrochem. Acta.* **31B**, 483 (1976).

[34] A.D. Tserepi, J.R. Dunlop, B.L. Preppernau, and T.A. Miller, *J. Appl. Phys.* **72**, 2638 (1992).

[35] A. McKenzie, M.F.R. Malcahy, and J.R. Steven, *J. Chem. Soc. Faraday Trans. I* **70**, 549 (1974).

[36] J.C. Miller, *Phys. Rev. A* **40**, 6969 (1989).

[37] R.S.F. Chang, H. Horiguchi, and D.W. Setser,*J. Chem. Phys.* **73**, 778(1980).

[38] W.L. Wiese, in *Plasma Diagnostic Techniques*, edited by R.H. Huddlestone and S.L. Leonard, Academic Press, New York, 265 (1965).

[39] R.F.G. Meulenbroeks, R.A.H. Engeln, M.N.A. Beurskens, R.M.J. Paffen, M.C.M. van de Sanden, J.A.M. van der Mullen, and D.C. Schram, *Plasma Sources Sci. Technol* **4**, 74 (1995).

[40] J.G. Liebeskind, R.K. Hanson, and M. Cappelli, *Appl. Opt.* **32**, 6117 (1993).

[41] S. Bashkin and J.O. Stoner Jr., *Atomic Energy Levels and Grotrian Diagrams*, North-Holland, Amsterdam (1975).

[42] G.T. Emery, in *Atomic, Molecular and Optical Physics Handbook*, edited by G.W.F. Drake, AIP Press, 198 (1996).

Chapter 5

Anomalous atomic hydrogen shock pattern in a supersonic plasma jet [1]

Abstract

A two-photon LIF study on the transport of ground-state atomic hydrogen in a supersonic plasma jet, generated from an Ar-H_2 mixture, reveals an unexpected shock pattern. Spatially resolved hydrogen atom densities, temperatures, and velocities are measured in the expansion of a thermal plasma source. Whereas both the axial velocity profile and the temperature profile of hydrogen atoms along the jet centerline can be interpreted in terms of a supersonic expansion of an Ar-H gas mixture, the H atom density profiles do not satisfy the well established Rankine-Hugoniot relation leading to a non-conservation of the forward flux. The experimental results show that H atoms escape from the supersonic expansion by a diffusion process due to strong density gradients between the core of the jet and its vicinity.

[1] Adapted from:
S. Mazouffre, M.G.H. Boogaarts, J.A.M. van der Mullen, D.C. Schram, *Phys. Rev. Lett.* **84**, 2622 (2000).

5.1 Introduction

Plasma expansion from a high pressure source region into a low pressure region is a general physical phenomenon [1, 2, 3] that covers a broad range of physical systems such as solar flares, remote plasma systems, and vacuum arc spots. Apart from the large differences in scale, those phenomena exhibit numerous similarities. For instance, they are all governed by the same set of equations, and after being accelerated the plasma flow undergoes a transition from a supersonic to a subsonic regime resulting in the formation of a shock wave structure.

From a practical view point it is advantageous to study the physics of expanding plasmas on the intermediate scale as then the system is well suited for diagnostics. In this letter we report on the study of the dynamics of a supersonic plasma jet generated by a cascaded arc [4] from a mixture of Ar and H_2, where Ar is used as a carrier gas. We aim at an understanding of the transport of ground-state atomic hydrogen (H) from a reservoir, i.e. the plasma source, to a processed surface. From a fundamental perspective, such an investigation is unique because, contrary to commonly studied supersonic expansions, one of the components of the jet is almost absent in the background gas beyond the barrel shock. Indeed, hydrogen atoms can recombine at the wall to form molecular hydrogen, and, due to the large available surface, the vessel walls act as a huge sink for such a reactive light component.

The study of the transport of atomic hydrogen has also a strong technological relevance because H plays a key role as a chemical agent in many plasma processing applications like plasma enhanced chemical vapor deposition [5, 6]. In addition, remote plasma sources can be used to produce beams of neutral atomic hydrogen, and they may serve for volume production of hydrogen negative ions, both species being of importance in the field of nuclear fusion.

In spite of specific properties such as the presence of charged particles, high viscosity, high thermal conductivity, and large temperature gradients over the radius, so far plasma expansion has been described using the adiabatic supersonic expansion theory [7] developed for the expansion of a neutral gas. This theory describes the continuum free jet shock wave structure [8, 9] that results from the interaction of a supersonic flow with the ambient gas when a gas or a gas mixture expands from a reservoir into a region with a finite pressure rather than a perfect vacuum.

In the case of an expanding argon plasma, it has been demonstrated experimentally [10, 11] that the expansion of the neutrals can be well described in terms of the adiabatic supersonic expansion of an ideal gas. Likewise, supersonic plasma flow created by a cascaded arc from a Ar-H_2 mixture should be understandable in terms of the adiabatic supersonic expansion of a Ar-H gas mixture leading to the formation of a well defined free jet shock structure in the continuum regime. Only a segregation effect, the so-called mass focusing effect [9], where the heavier species is relatively more concentrated in the center of the jet, is expected in view of the mass difference between H (1 amu) and Ar (40 amu) atoms. Indeed, both the axial and radial profiles of the hydrogen atom velocity as well as the axial temperature profile are characteristic for a free jet shock structure as we will see.

5.2 Experimental arrangement

Two-photon LIF

In the experiments reported here, ground-state hydrogen atoms are spatially probed using a two-photon excitation laser induced fluorescence (LIF) technique [12, 13]. A 20 Hz Nd:YAG-pumped tunable dye laser is operated around 615 nm. The output of the dye laser is frequency-tripled resulting in 5 ns pulses of tunable UV light around 205 nm with a pulse energy of 2 mJ and a bandwidth of 0.18 cm^{-1}. The frequency-tripled laser light is directed into the vessel either perpendicular to the plasma expansion axis or counterpropagating with the expansion. It should be noticed that the dimensions of the detection volume that can be achieved (<1 mm^3) are smaller than the gradient sizes. Hydrogen atoms are excited with two 205 nm photons from the $1s^2S$ ground state to the $3d^2D$ and $3s^2S$ states. The excitation is then monitored by detection of the resulting fluorescence yield on the Balmer-α line at 656 nm. From a spectral scan with the frequency calibrated laser over the two-photon transition the local H atom density, temperature, and velocity along the laser beam are obtained. By applying this method for different positions in the expansion, the H distribution in the plasma beam in terms of density, temperature, and velocity has been completely mapped.

Cascaded arc operating conditions

The cascaded arc is operated at a 40 A DC current and with a cathode-anode voltage of 100 V. A gas flow of 3.0 standard liters per minute (slm) Ar and 0.5 slm H_2 is used. The diameter of the arc channel is 3 mm, the stagnation pressure is 0.6 bar, and the opening angle of the arc nozzle is 45°. Using a 6:1 Ar-H_2 mixture, at the arc outlet the plasma jet turns into almost a gas jet composed of Ar and H atoms and of residual H_2 molecules, the electrons being consumed immediately at the outlet of the arc channel [14]. Both the amounts of H and H_2 depend on the dissociation degree of the source which is around 30% at the arc outlet with these operating conditions.

5.3 On-axis velocity profile

The development of the H drift velocity along the jet centerline, shown in Fig. 5.1, gives proof of an incomplete momentum coupling between H and Ar atoms inside the jet. First the gas is accelerated over a few arc nozzle diameters to a maximum speed of about 4000 ms^{-1}, due to conversion of thermal energy gained in the arc into kinetic energy by means of collisions. This value is not in agreement with a theoretical value of 3500 ms^{-1} found for the terminal velocity of a 3:1 Ar-H mixture, at a temperature in the nozzle of 5000 K, that expands into vacuum [9]. This indicates that H atoms are not perfectly coupled with Ar atoms. From a comparison with the sound velocity profile (Fig. 5.1), determined from the measured parallel temperature $T_{||}$ associated with the velocity distribution parallel to a stream line (see Fig. 5.2), the Mach number M can be estimated. At

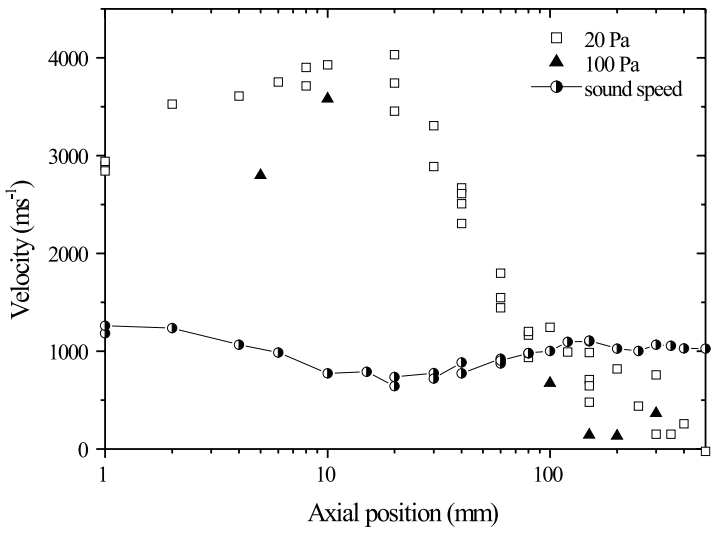

Fig. 5.1: Profile of the H atom axial velocity component along the jet centerline at 20 Pa (open square) and 100 Pa (solid triangle) background pressure. Also indicated is the local speed of sound for an Ar-H_2 mixture at $p_{\mathrm{back}} = 20$ Pa (circle), as it is determined from the measured parallel temperature $T_{||}$.

a background pressure (p_{back}) of 20 Pa, $M = 2.4$ at the arc nozzle exit and $M = 6$ in front of the stationary shock wave. A Mach number higher than 1 at the source exit ($M = 1$ correspond to a sonic orifice) is expected in view of the nozzle geometry. Then the velocity drops because of collisions between jet particles and background particles which results in the formation of a stationary shock front whose thickness is in the order of one local mean free path for H-Ar and Ar-Ar collisions. At $p_{\mathrm{back}} = 20$ Pa the Mach disk (end of the shock wave) is located around 100 mm from the arc nozzle in agreement with the result given by a theoretical expression for the Mach disk location [9, 15]. As can be seen from Fig. 5.1, the deceleration of the flow in the subsonic domain depends on the background pressure, because particles from the jet will lose their forward momentum more efficiently at higher pressure. The shape of the hydrogen drift velocity profile is somewhat quite similar to that of argon measured in the same conditions (see Fig. 3.8). It implies that the flow characteristics of the plasma jet are to a large extend determined by the argon atoms. However the fact that the H velocity is larger than the Ar velocity reveals that H and Ar are not perfectly coupled during the plasma expansion.

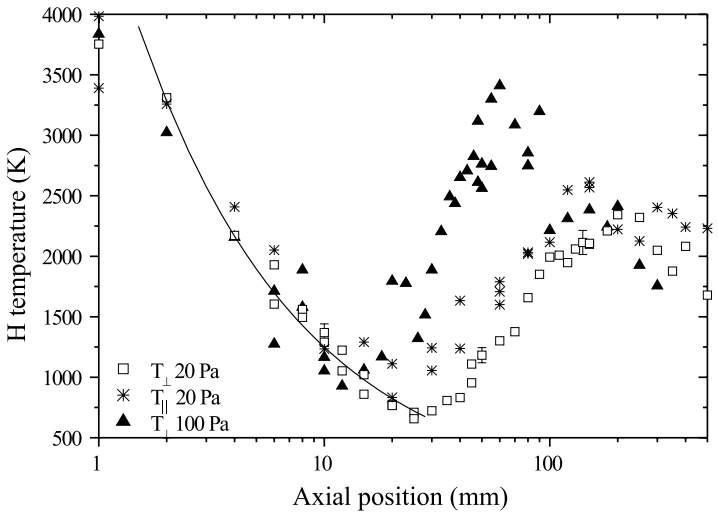

Fig. 5.2: Perpendicular temperature $T_\perp$ of H atoms as a function of the distance from the nozzle exit at 20 Pa (open square) and 100 Pa (solid triangle) background pressure. Also shown is the axial profile of the parallel temperature $T_\parallel$ at 20 Pa. The theoretical temperature profile in the supersonic domain is calculated from the Poisson adiabatic law with $\gamma = 1.3$ (solid line).

5.4 Perpendicular and parallel temperature

The axial profiles of the perpendicular temperature $T_\perp$ associated with the velocity distribution perpendicular to a stream line of atomic hydrogen, depicted in Fig. 5.2, clearly reveal the presence of a stationary shock front. The shape of the axial temperature profiles complies with the theory which predicts a strong cooling effect in the supersonic domain and a dependence of both the position and the thickness of the shock front on p_{back} [16]. Nevertheless, using Rankine-Hugoniot (R-H) relations [17] and taking a value of 5/3 for the adiabatic exponent γ, a Mach number ahead of the normal shock front of 2.6 is deduced from the temperature jump over the shock in the 20 Pa case, in disagreement with the value of 6 deduced from the axial velocity profile. This discrepancy might be explained by heat transfer from both the source and the hot background gas into the supersonic region which partly disturbs the effect of cooling in the core of the jet. This disturbance leads to an apparent smaller γ, meaning that the expansion is not adiabatic. By taking a value of 1.3 for γ, a Mach number ahead of the shock front of 5 is found and the calculated temperature development in the supersonic domain using the Poisson adiabatic law [16], agrees well with the measurements as can be seen in Fig. 5.2. In the background the gas temperature depends both on the thermal conductivity of the gas mixture and on the power input. The profile along the jet centerline of the parallel temperature $T_\parallel$ associated

with the velocity distribution parallel to a stream line measured at 20 Pa is also shown in Fig. 5.2. In the supersonic domain, the two temperature components match each other, i.e. the collision frequency is sufficiently high to maintain equilibrium and the continuum flow conditions hold. Just ahead of the stationary shock wave, we observe a departure from equilibrium: $T_{\parallel} > T_{\perp}$. In this region, the local mean free path becomes in the order of the jet radius, i.e. collisions become scarce, and equilibrium can not be preserved. The jet enters the so-called frozen regime: the parallel temperature "freezes" whereas the perpendicular temperature continues to decrease geometrically [9, 18]. Surprisingly, throughout the stationary shock front the deviation from equilibrium subsists whereas the collision frequency increases. This can be a direct consequence of an outward diffusion of H atoms. In order to explain the difference between $T_{\perp}$ and $T_{\parallel}$ within the shock wave, we here anticipate on the results discussed in the next section and in the following chapter. In the shock region, due to the numerous collisions with the background the temperature rises, which simply images an increase in disorder. A large H atom outflow however can be seen as an organized motion of particles in the radial direction which therefore leads to a lower spread of the radial velocity component in comparison with the spread in the axial velocity component. In other words, radial losses of H atoms act as a cooling mechanism and as a consequence $T_{\perp} < T_{\parallel}$. Behind the stationary shock wave, i.e. in the subsonic domain, the flow returns to equilibrium, $T_{\perp} \approx T_{\parallel}$, because of mixing with the background gas.

5.5 Anomalous H atom transport

5.5.1 Density profile along the jet axis

In contrast to the previously mentioned results, the measured H atom density profiles along the axis of the jet, depicted in Fig. 5.3, are in conflict with the theory. Throughout the stationary shock front no discontinuity (or jump) in density is observed in contrast to the Ar profile [10]. In the 20 Pa case the density even decreases over the shock front (Fig. 5.3) whereas the drop in drift velocity should be accompanied by a density jump with a factor of 3.7 according to the R-H relation (and as shown by the calculated profile). At 100 Pa the density is almost constant over the shock. The theoretical H atom density profile $n_H(z)$ along the jet centerline can be calculated from the measured H axial velocity profile $w_H(z)$, see Fig. 5.1, using a simple model for $n_H(z)$ derived from the conservation of the forward H flux. Under the assumption that the particles originates from a point source and flow along straight stream lines, the flux conservation in the supersonic domain reads in the case of a 45° expansion [16]

$$n_H w_H \pi (z + z_o)^2 = \phi_H^o, \tag{5.1}$$

where z_o is the position of the origin of the expansion ($z_o = 3$ mm, see chapter 6) and ϕ_H^o is the H flux in the plasma source. Throughout the stationary shock front, the diameter of the plasma jet is constant. In the subsonic domain the gas flows at a constant pressure and no recombination effects at the wall are taken into account. The expansion of a pure

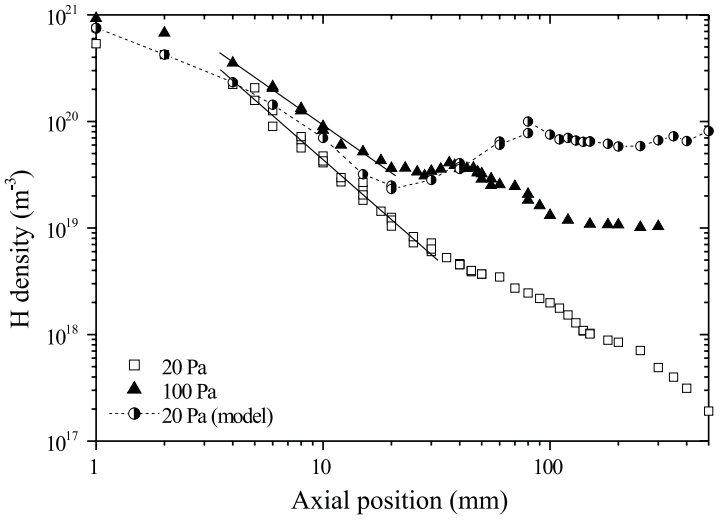

Fig. 5.3: Axial density profile of H atom at 20 Pa (open square) and at 100 Pa (solid triangle) background pressure. The lines are drawn to guide the eye. Also shown is the model density profile at 20 Pa (circle) based on the axial velocity data of Fig. 5.1.

Ar plasma can be satisfactorily described by this simple model [10]. The result of the calculation for $p_{\mathrm{back}} = 20$ Pa is also depicted in Fig. 5.3. The observed density profile leads to a non-conservation of the forward flux of atomic hydrogen. Such effects can not be explained by volume recombination of atomic hydrogen because of the too low reaction rates [19]. Therefore the only explanation to this anomalous shock pattern is to consider the fact that H atoms radially escape the supersonic expansion.

5.5.2 H atom flux in the shock region

From measured radial profiles of H atom density, temperature and velocity components at $z = 8$, 20, 50, 80, and 100 mm, several fluxes can be estimated in order to clarify the situation. From an integration of the product $n_H \times w_H$ over the shock front radius, we determined the forward flux of H atoms entering the shock front ϕ_H^{in} as well as the flux behind the shock front ϕ_H^{out}. We found that $\phi_H^{\mathrm{in}} = 3.3 \times 10^{19}$ s^{-1} and $\phi_H^{\mathrm{out}} = 3.9 \times 10^{18}$ s^{-1} which means a one order of magnitude radial loss of H flux.

The mass focusing effect[9] can not explain this H outflow. The key of the problem is the following: there is a significant density gradient between the interior of the plasma jet and the surroundings, caused by the quasi absence of H in the ambient gas, that drives a radial diffusion of atomic hydrogen. In contrast, when the plasma jet turns from underexpanded into overexpanded, this gradient for Ar is opposite (non reactive species). From radial profiles, an averaged H atom radial flux ϕ_H^{rad} over the shock front can be estimated.

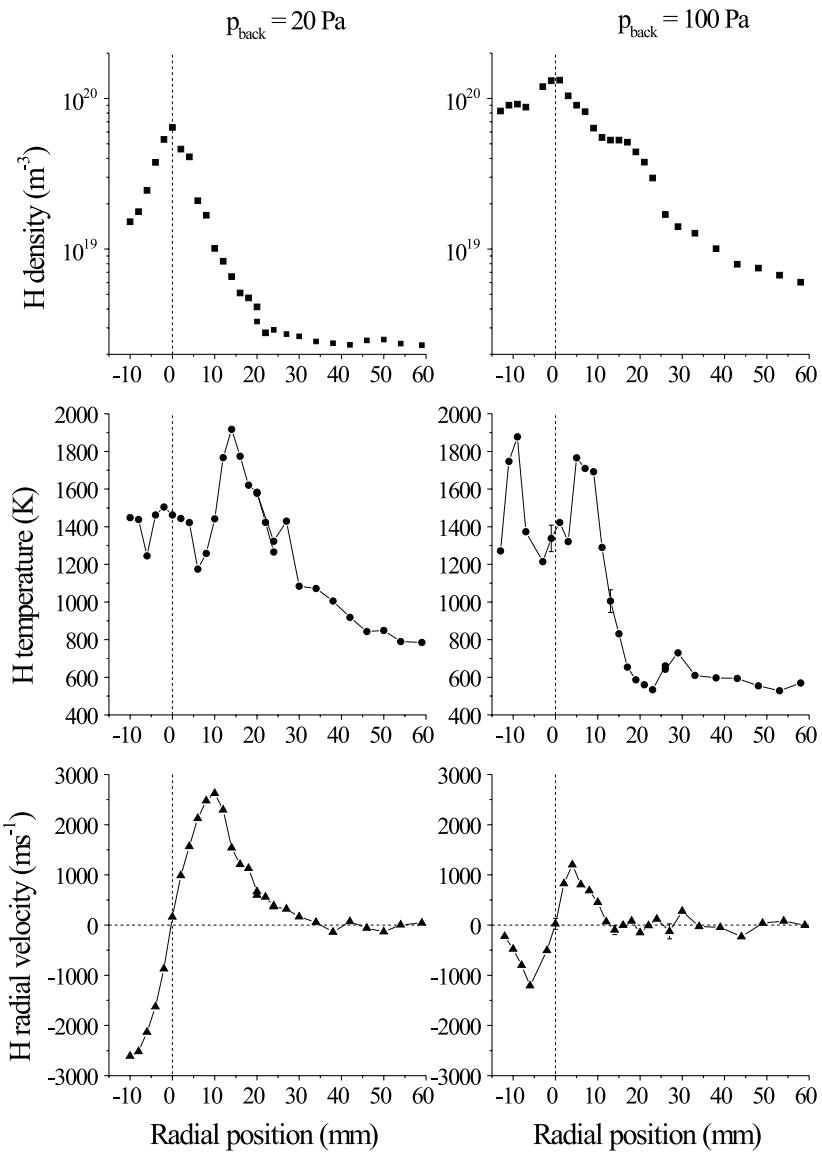

Fig. 5.4: Radial profile of the density (square), perpendicular temperature (circle), and radial velocity (triangle) of H atoms at $z = 8$ mm for a background pressure of 20 Pa (left) and for 100 Pa (right).

We found $\phi_H^{\text{rad}} = 3.4 \times 10^{19}$ s^{-1} which is in quite good agreement with the loss of forward flux inside the stationary shock front. In addition, an estimate of the same flux can be obtained using Fick's diffusion law. This gives 1.1×10^{19} s^{-1} which strongly encourages the idea of radial outflow induced by a density gradient. The determination of both fluxes is not straightforward and it is explained in detail in chapter 6.

5.5.3 Confinement in the jet core

Within the supersonic domain of the jet the density decays slightly faster than predicted by the model which means that it is not only geometrically determined [9, 16]. Moreover, the steepness of the density decay depends on p_{back} in contrast with the prediction by the expansion theory. Again these effects can be explained by H atoms radially escaping the expansion by a diffusion process.

A study of the beam cross-section at a distance z = 8 mm from the arc outlet, of which the results are shown in Fig. 5.4, reveals that the hydrogen diffusion phenomenon is strong and that it occurs already at the beginning of the mixture expansion. The radial profile of both the radial velocity component and the perpendicular temperature reveal the barrel shock structure of the expansion and they show the influence of the background pressure on both the dimension of the jet and on the shock wave structure. The lower absolute H density in the 20 Pa case compared to the 100 Pa case, visible in both Fig. 5.3 and Fig. 5.4, can only mean that in between the nozzle and the measurement position already more H is lost from the plasma jet than in the 100 Pa case.

At low pressure the outward diffusion phenomenon is strong because of the large local mean free path for momentum exchange which creates a diffuse shock structure [20]. The higher density in the wings of the 100 Pa profile (Fig. 5.4) as well as the plateau in the axial density profile at 100 Pa (Fig. 5.3) can then be explained by a slower outward diffusion of H. It just takes more collisions for H to pass the barrel shock in the 100 Pa case than in the 20 Pa case. This means that H atoms are poorly confined within the supersonic domain of the plasma beam, the efficiency of the confinement depending on p_{back}, i.e. on the permeability of the shock structure.

5.5.4 Subsonic domain

In the subsonic domain, the H density is still decreasing. After diffusing out of the jet, H atoms travel towards the vessel wall where they can recombine to form molecular hydrogen. The large available wall area combined with the high recombination probability for H on a steel surface causes H to almost vanish from the residual gas. This is confirmed by the measurement of the dissociation degree at 300 mm from the arc outlet (i.e. in the background) which equals to 0,2 % for $p_{\text{back}} = 20$ Pa and to 1 % at 100 Pa. This creates very specific boundary conditions for the H density and results in the formation of large radial H density gradients all over the expansion which are responsible for the diffusion process of H out of the beam.

5.6 Conclusions

To conclude, we experimentally demonstrated that the expansion of atomic hydrogen when seeded in Ar can not be entirely described in terms of the adiabatic supersonic expansion theory. On the first hand, heat transfer leads to an apparent smaller adiabatic exponent. On the other hand, the striking absence of a H atom density jump across the shock front arises from a strong outward diffusion of H atoms. This process is driven by large radial density gradients induced by the loss of H atoms from the background gas by wall recombination. The Ar shock structure is partially transparent to H leading to a poor confinement of H atoms even at high pressure and therefore to a non efficient transport mechanism. This leads to a less than optimal use of the chemical potential of the plasma source. The loss of H atoms at the vessel wall should therefore be taken into account in the design of reactors using remote plasmas as an atomic hydrogen source.

Acknowledgments

The authors gratefully acknowledge Prof. H. F. Döbele for his vital contribution in the initial phase of the two-photon LIF experiments in Eindhoven. This work is part of the research program of the Netherlands Foundation for Fundamental Research on Matter (FOM) and it is also financially supported by the Netherlands Technology Foundation (STW).

References

[1] *Beams and Jets in Astrophysics*, edited by P.A. Hugues, Cambridge University Press, (1991).

[2] E. Gidalevich, R.L. Boxman, and S. Goldsmith, *J. Phys. D: Appl. Phys.* **31**, 304 (1998).

[3] A. Lebhot and R. Campargue, *Phys. Plasmas* **3**, 2502 (1996).

[4] G.M.W. Kroesen, D.C. Schram, and J.C.M. de Haas, *Plasma Chem. Plasma Proc.* **10**, 551 (1990).

[5] M. Weiler, S. Sattel, T. Giessen, K. Jung, H. Ehrhardt, V.S. Veerasamy, and J. Robertson, *Phys. Rev. B* **53**, 1594 (1996).

[6] M.C.M. van de Sanden, R.J. Severens, W.M.M. Kessels, R.F.G. Meulenbroeks, and D.C. Schram, *J. Appl. Phys.* **84**, 2426 (1998).

[7] H. Ashkenas and F.S. Sherman, *Proceedings of Rarefied Gasdynamics* **4**, Academic press, New York, Vol. 2, 84 (1966).

[8] R. Campargue, *J. Chem. Phys.* **52**, 1795 (1970).

[9] *Atomic and Molecular Beam Methods*, edited by G. Scoles, Oxford University press, (1988).

[10] M.C.M. van de Sanden, J.M. de Regt, and D.C. Schram, *Plasma Sources Sci. Technol.* **3**, 501 (1994).

[11] M.C.M. van de Sanden, R. van den Bercken, and D.C. Schram, *Plasma Sources Sci. Technol.* **3**, 511 (1994).

[12] J.C. White, J. Bokor, R.R. Freeman, and R.H. Storz, *Phys. Rev. A* **24**, 612 (1981).

[13] U. Czarnetzki, K. Miyazaki, T. Kajiwara, K. Muraoka, M. Maeda, and H.F. Döbele, *J. Opt. Soc. Am. B* **11**, 2155 (1994).

[14] R.F.G. Meulenbroeks, R.A.H. Engeln, J.A.M. van der Mullen, and D.C. Schram, *Phys. Rev. E* **53**, 5207 (1996).

[15] W. S. Young, *Phys. Fluids* **18**, 1421 (1975).

[16] H.C.W. Beijerinck, R.J.F. van Gerwen, E.R.T. Kerstel, J.F.M. Martens, E.J.W. van Vliembergen, M.R.Th. Smits, and G.H. Kaashoek, *Chem. Phys.* **96**, 153 (1985).

[17] L. Landau and E. Liftshitz, *Fluid Mechanics*, Pergamon, London (1989).

[18] H.C.W. Beijerinck and N.F. Verster, *Physica* **111C**, 327 (1981).

[19] H. Tahara, K. Minami, A. Murai, T. Yasuri, and T. Yoshikawa, *Jap. J. Appl. Phys* **34**, 1972 (1995); L.E. Kline, W.D. Partlow, and W.E. Bies, *J. Appl. Phys.* **65**, 70 (1989).

[20] E.P Muntz, B.B. Hamel, and B.L. Maguire, *AIAA Journal* **8**, 1651 (1970).

Chapter 6

Transport of ground-state hydrogen atoms in an Ar-H_2 plasma expansion [1]

Abstract

The transport of ground state atomic hydrogen in the expansion of a thermal plasma generated from an Ar-H_2 mixture is studied by means of laser-based diagnostic techniques. The flow of hydrogen atoms is investigated by two-photon excitation Laser Induced Fluorescence (LIF), whereas Ar atoms are probed by LIF as well as by UV Rayleigh scattering. The transport of Ar atoms can be fully understood in terms of a free jet flow; H atoms on the contrary exhibit an anomalous behaviour. In the course of the plasma expansion, hydrogen atoms decouple from the argon fluid by a diffusion process as a direct consequence of recombination of H atoms at the vessel walls. It is shown, on the basis of experimental results, how plasma-surface interactions can strongly influence the flow pattern of an atomic radical fluid.

[1] Adapted from:
S. Mazouffre, M.G.H. Boogaarts, I.S.J. Bakker, P. Vankan, R. Engeln, and D.C. Schram, *Phys. Rev E* **64**, 016401 (2001).

6.1 Introduction

Understanding the transport of atomic radicals in a plasma expansion, i.e. the flow pattern and the interactions with the surrounding gas, is of interest from several aspects. From a fundamental point of view, a plasma expansion is a very general physical phenomenon which covers a broad range of dimensions, ranging from astrophysical objects [1] to small laser spots [2]. In comparison with the expansion of a neutral gas, plasma expansion is a more complex phenomenon. For instance, different kinds of particles are present (neutral, ion, electron, photon), current and electric fields can be generated, and the flow is often not isentropic. From a technological perspective, due to their high reactivity, atomic radicals play a major role in plasma chemistry and therefore are of relevance for industrial applications like deposition of thin films [3, 4, 5] and surface modification [6].

From a practical point of view it is advantageous to study the physics of expanding plasmas on the intermediate scale, as then the system is well suited for diagnostics. In this contribution, we focus on the transport of ground-state hydrogen atoms in the expansion of a thermal plasma generated from an Ar-H_2 mixture by a DC wall stabilized arc plasma source. Such a plasma jet can serve as an example, and the results obtained may be generalized to other kind of localized plasma expansion, like solar outbursts and laser spots. Atomic hydrogen is of particular interest. Such a light radical plays an important role in the field of nuclear fusion, e.g. Tokamak plasmas [7], as well as in numerous manufacturing techniques employing processing plasmas. Furthermore, H is one of the main components of both stellar and interstellar matter.

In order to clearly understand the dynamics of such a plasma jet, both neutral Ar atoms and H radicals have to be probed in such a way that the plasma flow is not disturbed. The local argon atom density is monitored by means of UV Rayleigh scattering, whereas the Ar velocity and temperature are measured by means of Laser Induced Fluorescence (LIF). The detection of ground-state hydrogen atoms is more cumbersome due to the large energy gap between the electronic ground state and the first excited states. Hydrogen atoms are spatially probed by means of Two-Photon Absorption Laser Induced Fluorescence (TALIF). By applying this method for different positions in the expansion, the H distribution in the plasma jet in terms of density, temperature, and velocity has been completely mapped.

In a foregoing paper [8], we have shown that the transport of H radicals, contrary to that of argon neutrals, can not be entirely described in terms of the well-established free jet flow picture. Hydrogen atoms exhibit a very specific behaviour. Whereas the occurrence of a stationary shock wave can clearly be identified on both the temperature profile and the velocity profile along the jet centerline, there is no density discontinuity throughout the shock front. This leads to a non-conservation of the H atom forward flux. It was stated that H radicals can escape the core of the plasma jet by a diffusion process induced by the presence of large density gradients between the jet and its periphery. The latter arise from the recombination of H at the vessel walls which leads to the formation of H_2 molecules. The H radical anomalous shock wave pattern is analyzed on the basis of detailed measurements, and it will be demonstrated that the hypothesis of outward diffusion controlled by density gradients can fully explain the measurements.

6.2 Plasma jet and experimental arrangement

The cascaded arc [9] is operated at a 40 A DC current, and with a cathode-anode voltage of 100 V. In normal condition a gas flow of 3.0 standard liters per minute (slm) Ar and 0.5 slm H_2 is used. The diameter of the arc channel is 3 mm, the stagnation pressure inside the arc is 0.6 atm, and the opening angle of the arc nozzle is 45°. The cascaded arc thermal plasma expands supersonically into a vacuum vessel (length 3 m, diameter 0.36 m) where the background pressure (p_{back}) can be varied almost independently from the gas flow from 10 Pa to 1 atm. Because the plasma expands from the orifice of the arc into a region with a finite pressure, a well defined free jet shock wave structure [10, 11, 12] is produced due to the interaction of the supersonic flow with the ambient gas.

In the case of an Ar-H_2 mixture, a fast lowering in the electron density appears soon after the onset of the expansion [13]. At an electron temperature of 1 eV this ionization loss is due to the production of hydrogen atoms by the associative charge exchange reaction

$$\mathrm{Ar^+ + H_2 \rightarrow ArH^+ + H} \qquad k = 1.2 \times 10^{-15}\ \mathrm{m^3\,s^{-1}}, \tag{6.1}$$

followed by the dissociative recombination reaction [14, 15, 16]

$$\mathrm{ArH^+ + e^- \rightarrow Ar + H^*} \qquad k \approx 10^{-13}\ \mathrm{m^3\,s^{-1}}. \tag{6.2}$$

Thus, using a 6:1 Ar-H_2 mixture, at the arc outlet the plasma jet turns into almost a gas jet composed of Ar and H atoms and of H_2 molecules. Both the amounts of H and H_2 depend on the dissociation degree of the source which is very likely to be close to 1 [17]. Beyond the Mach disk, the gas expands subsonically and mixes with the residual background gas. Then the evolution of the flow is determined by the circulation pattern in the vessel, which is a direct consequence of the large residence time ($\tau_{\mathrm{res}} \approx 1$ s at 20 Pa). Furthermore, as the diffusion time is much shorter than the residence time ($\tau_{\mathrm{diff,H}} \approx 1$ ms at 20 Pa), there is ample time for plasma-wall interactions.

In this experiment ground-state hydrogen atoms are spatially probed by using two-photon absorption laser-induced fluorescence (TALIF) [18, 19, 20]. The experimental method is described elsewhere [20, 21], and only a short overview is presented here. A simplified scheme of the setup is depicted in Fig. 6.1. A tunable 20 Hz Nd:YAG pumped dye laser delivers radiation around 615 nm. The output of the dye laser is frequency-tripled using non-linear optical crystals resulting in 2 mJ of tunable UV light around 205 nm with a measured bandwidth of 0.18 $\mathrm{cm^{-1}}$. The UV laser beam is focused either perpendicular or parallel to the plasma expansion axis. Hydrogen atoms are excited with two 205 nm photons from the $1s^2S$ ground state to the $3d^2D$ and $3s^2S$ states. The excitation is monitored by detection of the resulting fluorescence yield on the Balmer-α (H_α) line at 656 nm using a gated photo-multiplier tube. A narrow bandwidth interference filter is used to isolate the H_α line from the plasma emission. A slit mask is used to define the detection volume which dimensions are smaller than any gradient scale length. The dye laser frequency is calibrated by the simultaneous recording of the absorption spectrum of molecular iodine.

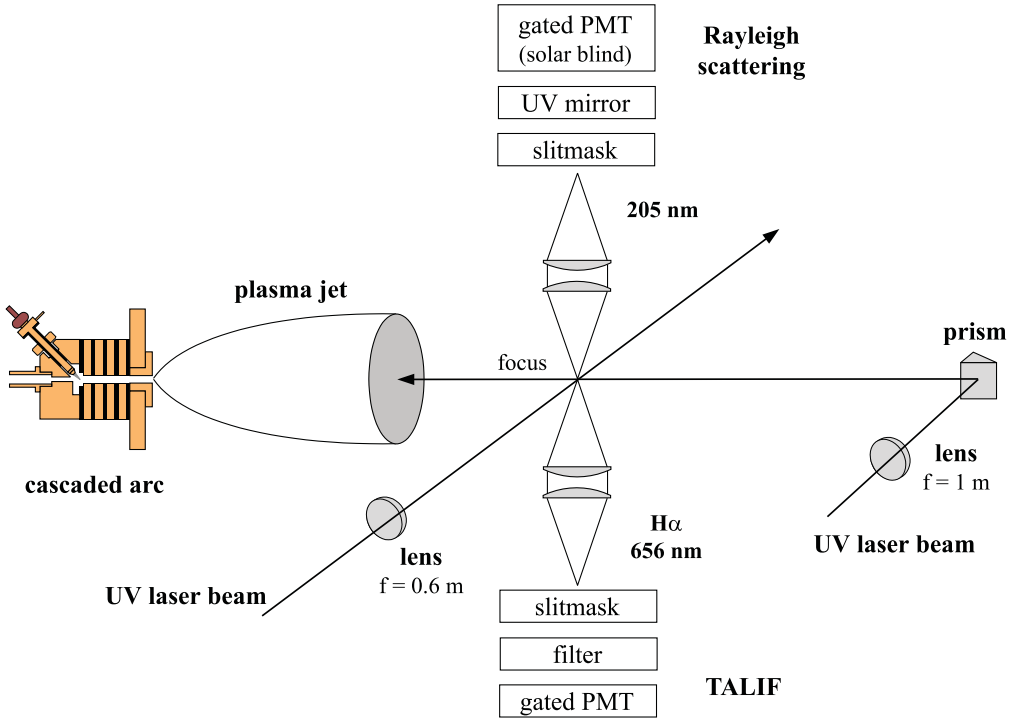

Fig. 6.1: Schematic view of the experimental arrangement. The UV laser beam is used to perform both TALIF and Rayleigh scattering measurements. It can be directed either perpendicular or parallel to the jet axis which allows for the measurement of ($T_\perp$, w_r) and ($T_\parallel$, w_z) respectively.

From a spectral scan over the two-photon transition, the local H atom density, temperature, and velocity along the laser beam are measured. Note that the measurements are performed in succession. Absolute number densities are obtained by calibrating the TALIF setup by means of a titration reaction with NO_2 in a flow tube reactor [21, 22].

The UV laser beam at 205 nm is also employed to measure the argon heavy particle density by means of Rayleigh scattering [23, 24]. The polarized, scattered radiation at 205 nm is detected at an angle of 90° using a gated solar blind PMT, as shown in Fig. 6.1. A dielectric UV mirror centered on 205 nm ($\Delta\lambda = 10$ nm) is used to filter out the plasma background light. The amount of stray light is reduced by means of a set of diaphragms and by using windows at Brewster's angle. Although the amount of photons at 205 nm is much smaller than the amount of photons that can be generated at for instance 532 nm with our Nd:YAG laser, the number of scattered photons is similar. The enhanced scattering result from a much higher argon differential scattering cross-section at 205 nm; it is about 60 times larger than at 532 nm [25]: $\sigma = 3.6 \times 10^{-30}$ m^2 at 205 nm and $\sigma = 5.6 \times 10^{-32}$ m^2 at 532 nm. The current detection limit in an Ar-H_2 plasma is around 10^{20} m^{-3}: it does not permit to accurately measure the Ar density in the shock region at a background pressure below 40 Pa.

6.3 Transport of atoms along the jet centerline

6.3.1 Argon atoms

In the case of an expanding argon plasma, it has been demonstrated experimentally [26] that the expansion of neutral atoms can be well understood in terms of an adiabatic supersonic expansion of an ideal gas [10]. Furthermore, the entire axial density profile can be described by a quasi-one dimensional model based on hydrodynamic equations [26], despite the fact that the Knudsen number Kn inside the supersonic domain is rather high. For instance, at a 40 Pa background pressure, $Kn = 0.1$ ahead of the stationary shock wave. Later, this model has been extended to study the case of an expanding argon plasma seeded with a small amount of molecular hydrogen [13].

The development along the jet centerline of the Ar heavy particle density, measured by means of UV Rayleigh scattering for a 6:1 Ar-H_2 mixture, is shown in Fig. 6.2 for two different background pressures. Our data are in agreement with foregoing measurements obtained in the case of a pure Ar plasma [13]. It implies that the Ar flow is not disturbed by the presence of H and H_2. From the conservation laws in stationary state, and under the assumption that the particles originate from a point source and flow along straight stream lines, one can obtain the theoretical expression for the density development along the jet centerline

$$n(z) = n_{\mathrm{o}} \frac{z_{\mathrm{ref}}^2}{(z + z_{\mathrm{o}})^2}. \tag{6.3}$$

In Eq. 6.3, n_{o} is the density in the source, z_{ref} is a scaling length equal to the source nozzle radius in the case of a 45 degrees expansion, and z_{o} is the position of the virtual point source. This formula is similar to the one used to describe the supersonic expansion of an inviscid gas through a sonic orifice in the field of gas dynamics [10, 27]. The axial density decay starts at some position z_{o} depending on the source nozzle geometry, e.g. several nozzle diameters in the case of a straight orifice. This decrease in density describes a rarefaction effect due to the increase in the jet cross-section.

The measured Ar density profiles in Fig. 6.2, are fitted according to Eq. 6.3. As can be seen, the experimental data are well described by the theoretical expression. Up to the stationary shock front the density decrease is not affected by a change in p_{back}, meaning that the supersonic domain of the expansion can be considered as a closed domain surrounded by a shock wave structure [11, 26]. From the fit, both length parameters can be estimated. We find that $z_{\mathrm{ref}} = 3.0 \pm 0.2$ mm and that $z_{\mathrm{o}} = 3.0 \pm 0.2$ mm. This means that the virtual point source, i.e. the start of the expansion, is located 3 mm inside the nozzle. This is a direct consequence of the use of a diverging nozzle. The density jump across the normal shock wave, which results from the conservation of the forward flux, can clearly be seen in Fig. 6.2. From the Rankine-Hugoniot relation [28] the compression ratio is found to be 3 at 40 Pa and 4, i.e. the maximum compression ratio, at 100 Pa. In the subsonic region, a slow increase in the Ar density is observed which is due to a cooling of the gas by heat transfer, the static pressure being constant. The velocity of Ar atoms in an expanding

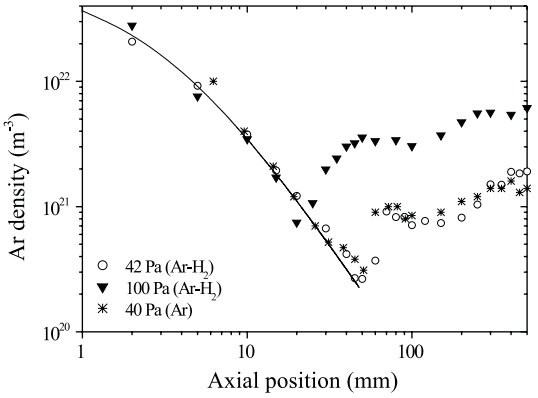

Fig. 6.2: Axial density profile of Ar neutrals at 42 Pa (open circles) and 100 Pa (solid triangles) in an Ar-H_2 mixture, and at 40 Pa in pure Ar (star).

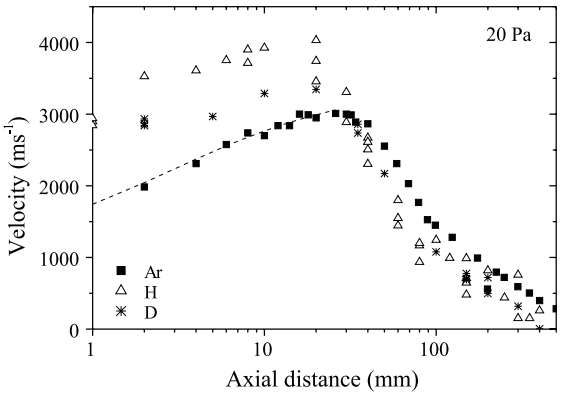

Fig. 6.3: Axial velocity component profile along the jet centerline for Ar, H, and D atoms at a 20 Pa background pressure. The decoupling between H(D) and Ar inside the supersonic domain is clearly visible.

Ar-H_2 thermal plasma jet created by a cascaded arc, has recently been determined by measuring the Doppler shift in a LIF experiment on metastable Ar [29]. The development of the Ar axial velocity component along the plasma jet axis at $p_{\mathrm{back}} = 20$ Pa is shown in Fig. 6.3 as well as a theoretical profile in the supersonic domain (see also chapter 3).

6.3.2 Hydrogen atoms

Anomalous density profile

Contrary to the argon case, hydrogen atom axial density profiles do not exhibit any jump throughout the stationary shock front, as can be seen in Fig. 6.4, while the drift velocity drops, as can be observed in Fig. 6.3. This means that the forward flux of H atoms is not conserved in the shock region. This striking demonstration of an anomalous H atom shock pattern has been reported in a foregoing paper [8]. It is postulated that strong density gradients between the core of the jet and its surroundings, due to a low H concentration in the background gas, are responsible for an outward diffusion of H atoms. The efficient destruction of hydrogen ground-state atoms at the wall of the vessel [30], where they recombine to form molecular hydrogen [31, 32, 33], is responsible for the very low H background density. In neutral gas mixture expansions migration of the light species towards the edges of the jet has been observed within the first millimeters of the flow [12]. In this region this so-called mass focusing effect arises from a mass dependent kinetic energy.

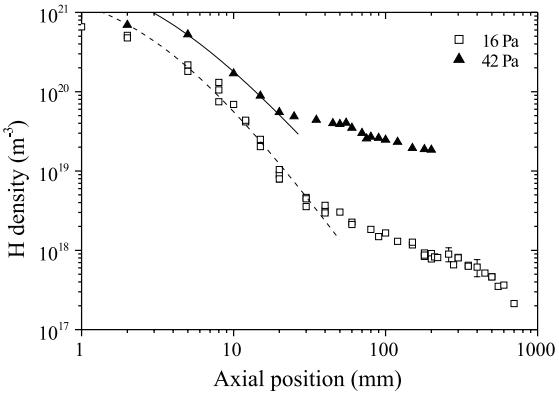

Fig. 6.4: Axial H atom density profile at 16 Pa (square) and 42 Pa (triangle).

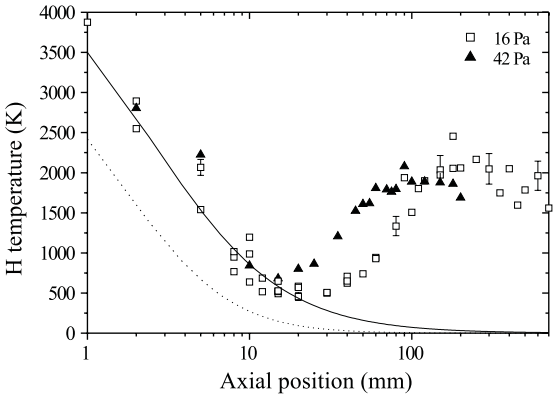

Fig. 6.5: Axial H atom $T_\perp$ profile at 16 Pa (square) and 42 Pa (triangle). The lines represent a fit with $\gamma = 1.45$ (solid) and $\gamma = 5/3$ (dotted).

One can exclude under our experimental conditions that H atoms recombine in volume during the expansion process to form molecular hydrogen, which would also lead to a non-conservation of the axial H flux. The chemical reactions that have to be considered are the three-body reactions [34, 35]

$$\begin{aligned} \mathrm{H + H + Ar} &\rightarrow \mathrm{H_2 + Ar} \quad & k &= 9.8 \times 10^{-42} \quad & \mathrm{m^6\,s^{-1}}, \\ \mathrm{H + H + H_2} &\rightarrow \mathrm{H_2 + H_2} \quad & k &\approx 2 \times 10^{-42} \quad & \mathrm{m^6\,s^{-1}}, \\ \mathrm{H + H + H} &\rightarrow \mathrm{H_2 + H} \quad & k &= 4.5 \times 10^{-44} \quad & \mathrm{m^6\,s^{-1}}. \end{aligned} \tag{6.4}$$

Under our experimental conditions, these reaction rates are too small to lead to any significant recombination of hydrogen atoms during the residence time.

Furthermore, as already mentioned in [8], the steepness of the density decay within the supersonic domain depends on p_{back}, which means that H atoms which come from the source receive information about the standing ambient gas. This proves that a shock wave structure does not form a totally closed system. As shown in Fig. 6.4, the H axial density profile ahead of the shock wave can be well described by a modified point source expansion law of the form

$$n(z) = n_{\mathrm{o}} \frac{z_{\mathrm{ref}}^{\beta}}{(z + z_{\mathrm{o}})^{\beta}}, \tag{6.5}$$

where the exponent β is larger than two, because an outward diffusion effect is superimposed on the normal rarefaction effect. The length parameters z_{ref} and z_{o} are taken to be the ones determined from the Ar measurements. The values of n_o and β depend on p_{back} and are listed in Table 6.1. It can clearly be seen that β gets closer to 2 as the pressure increases, meaning that H atoms get better confined inside the supersonic jet. In other

Tab. 6.1: Parameters governing the H atom expansion at different background pressures. The subscript o refers to the source region. The variable β is linked to the on-axis H atom density decrease, see Eq. 6.5, and γ is the quasi-adiabatic exponent.

p_{back} (Pa)	16	20	42	100
n_{o} (m^{-3})	$(5.6 \pm 1.0) \times 10^{21}$	$(2.2 \pm 0.2) \times 10^{21}$	$(5.6 \pm 1.0) \times 10^{21}$	$(2.2 \pm 0.2) \times 10^{21}$
β	2.65 ± 0.10	2.35 ± 0.05	2.20 ± 0.05	2.10 ± 0.05
γ	1.40 ± 0.10	1.40 ± 0.04	1.50 ± 0.15	1.45 ± 0.05
T_{o} (K)	9000 ± 3000	4800 ± 600	8100 ± 3500	5600 ± 800

words, it becomes more difficult for H to cross the barrel shock wave at high p_{back}, since the local mean free path decreases. This also explains why the H density in the ambient gas depends on p_{back}, as can be seen in Fig. 6.4.

Perpendicular temperature

The axial profile of the atomic hydrogen perpendicular temperature $T_{\perp}$ (associated with the velocity distribution perpendicular to a stream line) is depicted in Fig. 6.5 for two different background pressures[1]. The temperature profiles clearly reveal the presence of a stationary shock front across which $T_{\perp}$ rises due to the conversion of the jet particle kinetic energy into random thermal motion. As predicted by the theory, both the position and the width of the shock front depend on p_{back} [12]. In the supersonic region of the expansion a strong cooling effect occurs because the thermal energy gained by the particles in the plasma source is converted into kinetic energy by means of collisions. For an adiabatic process, the energy equation can be replaced by the Poisson adiabatic law [28]

$$\left(\frac{n}{n_{\mathrm{o}}}\right)^{\gamma-1} = \frac{T}{T_{\mathrm{o}}}, \tag{6.6}$$

where γ is the adiabatic exponent which is equal to $\frac{5}{3}$ for a monoatomic gas. By plotting the H atom temperature as a function of the density, the isentropic exponent can be evaluated. The value of γ for various values of p_{back} is listed in Table 6.1. As can be seen, γ for H radicals has the almost constant value 1.4. The fact that the measured γ is smaller than the theoretical γ for a monoatomic gas means that, contrary to a neutral gas expansion, the supersonic expansion of a plasma is non-adiabatic [36]. As can be seen in Fig. 6.5, the measured temperature is well above the theoretical isentropic temperature. In the case of a plasma expansion the cooling of neutrals in the supersonic domain can be disturbed by heat transfer from both the source and the hot background gas behind the shock front. Re-entry of background gas into the supersonic domain through the barrel shock wave can also disturb the flow, especially at low pressure [29]. In Fig. 6.5, a fit to the measured data is shown using the adiabatic law with measured β and γ. The source temperature T_{o},

[1] The comparison between $T_{\perp}$ and $T_{\parallel}$ profiles is discussed in chapter 5.

that corresponds to the temperature inside the arc nozzle, is found to be close to 0.5 eV, independent of p_{back} as it should.

Axial velocity component

The measured axial profiles of the axial velocity components of H and D atoms are shown in Fig. 6.3 for a background pressure of 20 Pa. Also the Ar velocity profile is shown. The shape of the H and D velocity profile along the jet centerline is very similar to the Ar one. This means that the mechanisms responsible for the H and D axial velocity development are connected to those which determine the Ar profile. Throughout the supersonic domain, the H(D) velocity is higher than the Ar velocity. The decoupling between the Ar fluid and the radical fluid, which is already present at the source exit, is a direct consequence of losses of H atoms at the walls. A possible way of describing the hydrogen drift velocity is to consider this velocity as the sum of the argon drift velocity and a diffusion term[2]. The diffusion velocity, which contains implicitly the H density gradients, would control the H flow relative to the Ar flow. More theoretical and computational work is needed to validate this idea. Nonetheless, primary work using an hydrodynamic approach to model the Ar-H flow, seems to confirm this view. Behind the shock wave, all velocities are about the same, meaning that all particles are well coupled. This is a consequence of the much higher collision frequency in the subsonic domain. However, across the stationary shock front, the velocities differ substantially, the atomic hydrogen velocity being lower than the argon velocity. Because of collisions in the shock, we can expect the difference in velocity to slowly diminish. It can also be seen that the H(D) velocity starts to decrease earlier than the Ar velocity. This effect is not yet well understood.

6.4 Influence of the mass on the transport of radicals

6.4.1 Use of a light carrier gas

In order to study the influence of the mass on the radical transport mechanism, the carrier gas has been changed: argon ($m_{Ar} = 40$ amu) has been replaced by helium ($m_{He} = 4$ amu). The parameters are the following: the arc current is 50 A, the cathode-anode voltage is 140 V, the He flow is 2 slm, the H_2 flow is 0.5 slm and the background pressure is 20 Pa. The source geometry is identical to the one used in the Ar-H_2 mixture case. An admixture of less than 2 % Ar gas is used to prevent a too fast degradation of the cascaded arc cathode tips. Thus the average mass of the mixture is equal to 4.3 amu, using the fact that the plasma source delivers mainly H_2 in view of the low measured H density, see Fig. 6.6.

The results of the measurements are given in Fig. 6.6. The H density at the source exit is much less, by nearly 2 orders of magnitude at $p_{\text{back}} = 20$ Pa, than when Ar is used

[2] Starting from the relation $\vec{w}_H = \vec{w}_{Ar} + \vec{w}_H^{\text{diff}}$, a calculation based on two simplified momentum balances (H and Ar) coupled via a friction term and using the fact that $m_H \ll m_{Ar}$ shows that $\vec{w}_H^{\text{diff}}$ is the diffusion velocity as given by the Fick's diffusion law multiplied by the isentropic exponent γ.

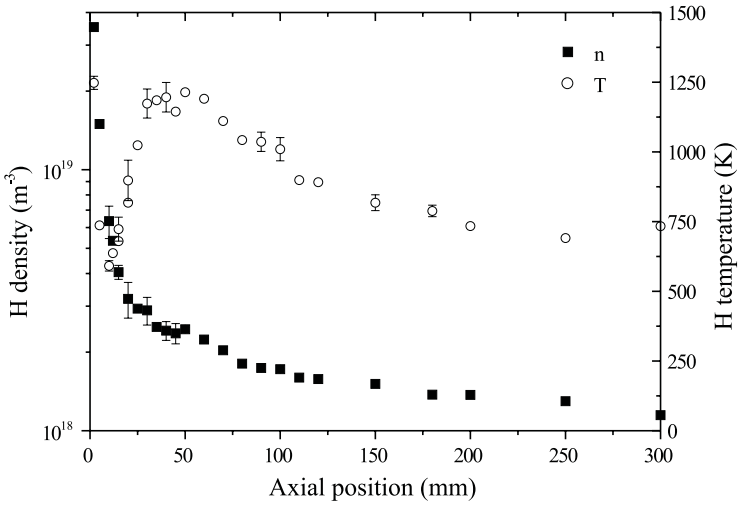

Fig. 6.6: Axial profiles of the H density and H perpendicular temperature $T_\perp$ when He is used as a carrier gas instead of Ar. The shock front structure is visible in the temperature profile. However, no discontinuity is observed in the H density profile.

as a carrier gas [8]. The relatively low delivered amount of H arises directly from the way H atoms are created in a He-H_2 mixture [37, 38, 39]. The low H temperature at the arc outlet is due to the high thermal conductivity of the He-H_2 mixture. The sharp rise in the temperature, which occurs behind the arc exit as depicted in Fig. 6.6, reveals the occurrence of a stationary shock front. In comparison with the results obtained at the same p_{back} for an Ar-H_2 mixture, two remarks can be made. First, the shock wave is located very close to the arc exit since the shock position varies with the stagnation pressure, which at constant flow decreases when the atomic mass decreases [12]. Second, the shock front, whose thickness is always in the order of one local mean free path for momentum exchange, is narrow despite a relatively small neutral-neutral momentum exchange cross section for He. This originates from the fact that the shock wave occurs close to the nozzle exit, where the He density is still high. According to the temperature jump, the Mach number M is found to be equal to 2.3 in front of the shock when using the Rankine-Hugoniot relation with a value of 1.5 for the isentropic exponent γ. With this value for M, the amplitude of the density jump should be 2.8. However, no significant density jump is observed across the shock wave. This again indicates an outward diffusion of H atoms. Despite the small mass ratio between He and H, H atoms leave the core of the plasma jet and recombine at the vessel wall. This result points out the importance of the density gradients in the H atom loss process.

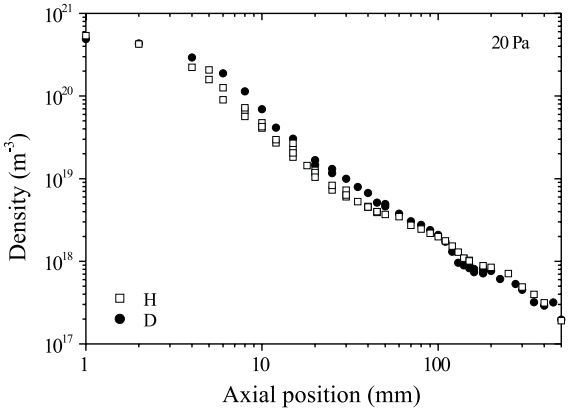

Fig. 6.7: Axial H (square) and D (circle) density profile at 20 Pa with Ar as a carrier gas.

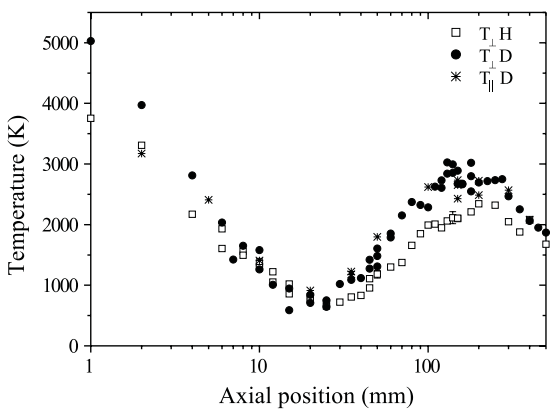

Fig. 6.8: Axial H (square) and D (circle) $T_\perp$ profile at 20 Pa. Also shown is the axial D $T_{||}$ profile (star) at 20 Pa.

In the subsonic domain of the flow, the temperature decays fast because of the large thermal conductivity of the mixture, and the density remains relatively constant. Despite the low H density at the source outlet, it is slightly higher behind the stationary shock wave ($z > 100$ mm) than in the case where Ar is used as a carrier gas. This means that H is better transported when the mass of the carrier gas is small. The gain in confinement when the mass of the carrier gas is closer to that of the transported species is known for multicomponent neutral beam expansions [12]. But we demonstrated that despite a better confinement, the atomic hydrogen anomalous shock wave pattern does not vanish. A better transport is of relevance for the downstream chemistry since the amount of ground state radicals can be one of the limiting factors when an expanding plasma jet is used for thin film deposition [5] or surface modification. Then a good compromise has to be found between the quantity of radicals available in front of the surface and the momentum of the carrier gas which is also used to transport other particles like molecules of the precursor gas.

6.4.2 Isotopic effect

Another way to study the influence of the mass is to replace H by one of its isotopes, e.g. deuterium (D). The arc parameters are kept the same as in the case of H_2 seeding. To obtain absolute D density we assume that the two-photon absorption cross sections of H and D are identical. In Fig. 6.7, the axial H and D density profiles are shown for $p_{\text{back}} = 20$ Pa, and in Fig. 6.8 the axial H and D perpendicular temperature profiles are compared at 20 Pa. In the supersonic domain, after approximately one nozzle diameter, D is better confined inside the jet (higher density) because of its larger mass that results

in a lower diffusion velocity ($T_D \approx T_H$) as can be seen in Fig. 6.8.

As expected, no density jump is visible in the D density profile across the stationary shock wave, whereas the velocity decreases by a factor 3. The apparent difference between the H atom and the D atom perpendicular temperature may arise from the important radial losses of H atoms that act as a cooling mechanism (see chapter 3). Note that the two D atom temperature component remain in equilibrium over the course of the expansion, see Fig. 6.8, contrary to the H ones. In the subsonic domain, the higher H density is a consequence of the lower H temperature.

6.5 Confinement of radicals inside the jet core

In order to have a better insight in the lack of confinement of atomic hydrogen inside the core of the plasma jet generated from an Ar-H_2 mixture, it is of interest to study beam cross-sections at several axial positions. Also the permeability of the Ar barrel shock wave needs to be discussed. In Figs. 6.9, 6.10, and 6.11, radial profiles of the H atom density, perpendicular temperature, and radial velocity component are given for $p_{\text{back}} = 16$ Pa at $z = 2$, 8, 20, 50, 80, and 100 mm behind the arc outlet.

6.5.1 Radial profiles of the H density

From the radial density profiles, we observe that the density of atomic hydrogen decreases fast as we move away from the source exit. This is a direct consequence of the rarefaction effect due to the increase of the beam diameter. However, this effect is enlarged by the outward diffusion phenomenon. Contrary to argon, the H jet is never overexpanded i.e. the H atom density inside the jet is never lower than outside the jet. Across the stationary shock front, from $z = 50$ mm to 100 mm, the radial H density profile is flat because the diffusion process levels out the density profile.

The shape of the density profile in the core of the plasma beam can be theoretically described. Such a shape corresponds to a situation in which the jet is underexpanded. We propose the following function

$$n(r, z) = n(z) \cos^a(\varphi), \tag{6.7}$$

with the angle φ given by

$$\varphi = \arctan\left(\frac{r}{z + z_o}\right), \tag{6.8}$$

where r is the radial distance and z_o is the position of the virtual point source. In the field of gas dynamics, some more complex functions have been proposed based on experimental data [10, 40]. The results of fits using Eq. 6.7 are depicted in Fig. 6.9 at $z = 2$ and 8 mm. As can be seen in the graph, the function reasonably represents the experimental data inside the jet. However, to obtain such an agreement, the exponent a in Eq. 6.7 has to be modified when changing the axial position z: $a = 2.4$ at $z = 2$ mm and $a = 5.5$ at $z = 8$ mm. In the classic supersonic expansion picture, the value of this exponent only

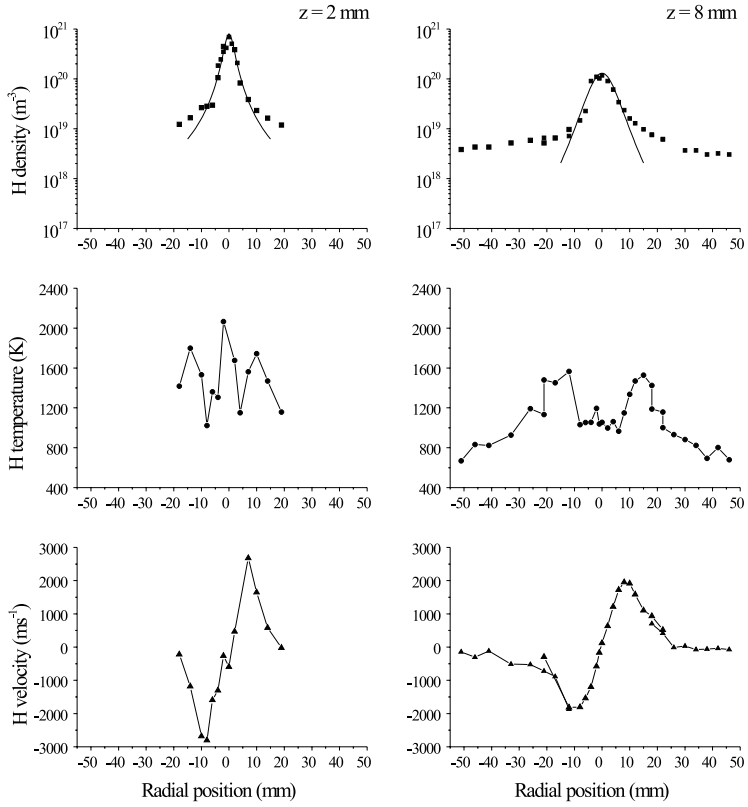

Fig. 6.9: Radial profiles of the density (top), perpendicular temperature $T_\perp$ (middle), and radial velocity w_r (bottom) of H atoms for a background pressure of 16 Pa at $z = 2$ mm (left) and $z = 8$ mm (right). The H density profile in the core of the jet is modeled using Eq. 6.7 (solid line) with $a = 2.4$ and 5.5 at $z = 2$ mm and 8 mm respectively.

depends on the source conditions and geometry and on γ, but it is a constant in the course of the expansion. Once more the increase in a is connected to an outward loss of H radicals in particular in the outward regions of the jet.

6.5.2 Temperature and radial velocity

The radial profiles of the H atom perpendicular temperature $T_\perp$ clearly show evidence of the quasi-adiabatic cooling effect. They also reveal the structure of the barrel shock wave. It can be seen in Fig. 6.9 that at $z = 2$ mm in the core of the jet $T_\perp$ is not constant. The temperature is higher on axis than on the sides. This is purely a geometrical effect: the H atoms detected on the sides have travelled more in comparison with those on the jet axis. Then, since the former have undergone more collisions they converted a larger part of their thermal energy into kinetic energy which leads to a lower temperature. At $z = 8$ mm, this

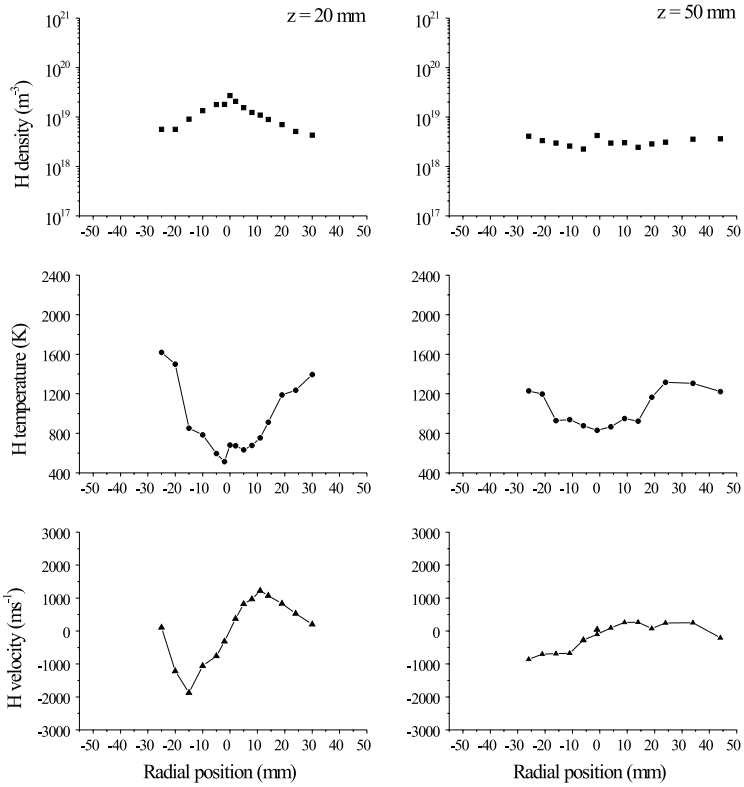

Fig. 6.10: Radial profiles of the density (top), perpendicular temperature $T_\perp$ (middle), and radial velocity w_r (bottom) of H atoms for a background pressure of 16 Pa at z = 20 mm (left) and z = 50 mm (right).

geometrical effect is almost not noticeable anymore. The rise in $T_\perp$ when going off-axis is due to collisions with Ar atoms in the barrel shock wave [12]. This temperature jump defines the boundary of the plasma jet. Then, behind the barrel shock wave, $T_\perp$ decreases towards the vessel walls because of heat transfer to the background gas. As can be seen in Fig. 6.9, the background gas temperature is rather low, around 500 K. In the subsonic domain, the temperature of flowing H atoms is homogeneous over the jet radius, as can be seen in Fig 6.11, and relatively high. This shows that the heat gained in the source is transported mainly forward with some radial losses due to thermal conduction.

The radial profiles of the H atom radial velocity component also reveal the Ar shock wave structure. Because of the expansion process, the radial velocity first increases when moving away from the jet axis. Then when H atoms collide with Ar atoms in the barrel shock wave, the velocity decreases since it is converted into thermal energy, and the temperature increases accordingly. As expected, the position of the Ar barrel shock as deduced from the H radial velocity profile does coincide with the position deduced from the corresponding $T_\perp$ profile.

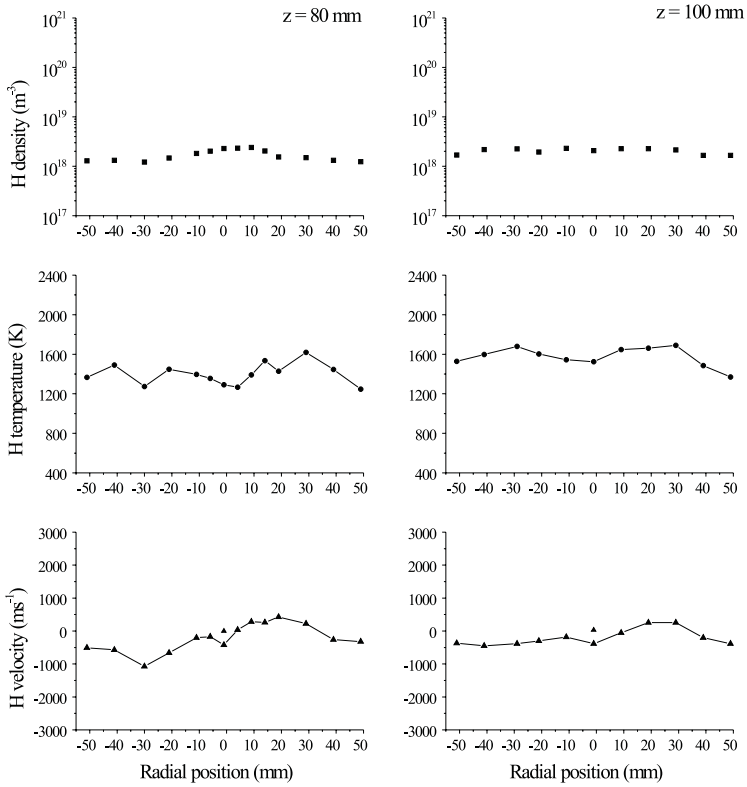

Fig. 6.11: Radial profiles of the density (top), perpendicular temperature $T_\perp$ (middle), and radial velocity w_r (bottom) of H atoms for a background pressure of 16 Pa at z = 80 mm (left) and z = 100 mm (right).

As can be seen in Figs. 6.9 and 6.10, the maximum value of the H radial velocity w_r^{max} decreases as z increases. This is not predicted in the classical expansion picture. Assuming that the total velocity does not vary with the radial position, the magnitude of the radial velocity component as a function of the radial position for a given axial position can be written in the classical picture as follows

$$w_r = w_{z,0} \sin(\varphi), \tag{6.9}$$

where $w_{z,0}$ is the axial speed at $r = 0$ and φ is the expansion angle given by Eq. 6.8. In the case of a free jet, the maximum radial velocity is always reached at roughly the same angle φ for a given p_{back}, independent of z. Since up to the stationary shock wave the axial velocity increases slightly, as can be seen in Fig. 6.3, w_r^{max} should then also increase a bit. However, it decreases by approximately a factor 3 between z = 2 and 20 mm. By using the measured argon axial drift velocity, shown in Fig. 6.3, it is possible to estimate with Eq. 6.9 the maximum value of the H radial velocity component in case of a perfect coupling between H radicals and Ar atoms. The velocity is calculated at the boundary of

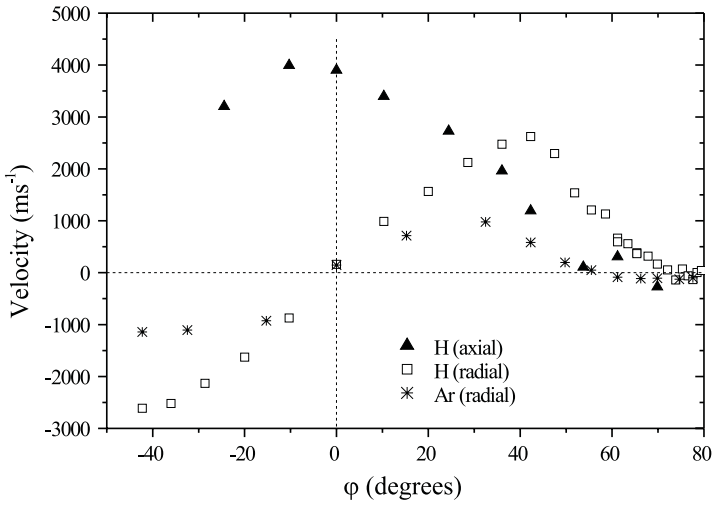

Fig. 6.12: Profiles of the axial and radial component of the H velocity as well as the radial component of the Ar velocity as a function of the angle with the jet axis, recorded at z=8 mm behind the arc nozzle.

the plasma jet of which the location is taken from the $T_\perp$ profile. The maximum speed is found to be equal to 1000, 900, and 900 m s^{-1} at z = 2, 8, and 20 mm, respectively. At any z, the highest H radial velocity is always larger than the calculated value, which points out the importance of the radial escape of H radicals. This radial escape process is certainly most important at the beginning of the plasma expansion where the atomic hydrogen radial velocity component is highest. The discrepancy between the expected H radial velocity and the measured one not only confirms the idea of a decoupling between H and Ar atoms, but it also suggests that the H velocity is connected to the H density gradients which are the largest at the beginning of the expansion and which decrease with increasing z.

6.5.3 Permeable Ar barrel shock wave

The picture of a strong decoupling between H and Ar is substantiated by comparing the radial profile of the axial and radial velocity of the H atoms and the radial velocity components of the Ar atoms [29]. This is done in Fig. 6.12 for a position of 8 mm behind the arc outlet and at p_{back} = 20 Pa. The data points are plotted as a function of the angle φ with the expansion axis given by Eq. 6.8.

This figure confirms the picture of an outward diffusion of H. Moreover, it can be fully understood by considering that the H density gradient is the driving mechanism of the diffusion process. First, the graph clearly shows the decoupling between H and Ar atoms.

On the expansion axis, both radial velocity components are zero. As r increases, i.e. further from the axis, the gap between the two velocities also increases, the maximum H radial speed being approximately 3 times higher than the maximum Ar speed. Second, H atoms penetrate and even cross the Ar barrel shock. The decay in Ar radial velocity, due to friction with the standing gas, indicates the position of the barrel shock. It follows from the picture that at $z = 8$ mm, the expansion angle is about 30°. But the H atom radial velocity only starts to decrease beyond the beginning of the Ar barrel shock wave. Moreover, when the Ar velocity is zero, the H velocity is still high, indicating that H atoms are still moving radially into the background gas, where Ar atoms are motionless. Finally, the H velocity becomes zero because of increasing friction with the neutral background gas. Then the directed motion is replaced by a random thermal motion. Third, even if H atoms penetrate the Ar barrel shock wave with still a significant axial velocity component, H mainly escapes the plasma jet radially. Indeed, the axial velocity component becomes zero whereas the radial component is still high. This is a direct consequence of the steep radial density gradients between the core of the plasma beam and its vicinity.

Another effect which has to be mentioned is the fact that beyond the plasma jet boundary the H atom radial velocity component is zero (see Figs 5.4 and 6.9 for clearness) whereas hydrodynamic calculations predict a negative velocity [42]. This proves that H atoms do not recirculate inside the vacuum chamber, i.e. H atoms are not trapped into recirculation vortices that surround the jet. In other words, H atoms diffuse out of the jet directly to the vessel walls where they stick or recombine.

6.6 Atomic hydrogen diffusion flux

To confirm the fact that hydrogen atoms escape the core of the plasma jet by a diffusion process we estimate, at a background pressure of 16 Pa, the losses of H radicals over the normal shock wave, i.e. from $z = 20$ mm to $z = 100$ mm, and compare them with a calculated diffusion flux[3].

The loss of atomic radicals in the shock region can be estimated by determining the difference between the forward flux of H atoms entering the shock front, ϕ_H^{in}, and the flux behind the shock, ϕ_H^{out}.

[3] Since H atom do not recombine in volume, the total H atom flux has to be conserved at any z position throughout the plasma flow. The experimental verification of the flux conservation would however necessitate a extremely large dataset. Nevertheless, using our somewhat restricted dataset, the H flux conservation has been verified along the plasma jet axis. In cylindrical coordinates, and with cylindrical symmetry, the flux conservation reads $\frac{1}{r}\frac{\partial}{\partial r}(nrw_r) + \frac{\partial}{\partial z}(nw_z) = 0$. On the jet axis, i.e. at $r = 0$, and for every value of z, previous equation becomes $2n\frac{w_r}{r} = -\frac{\partial}{\partial z}(nw_z)$. The right hand side and the left hand side flux values are found to be in reasonable agreement meaning that the H atom flux evaluated on the jet centerline is conserved at a given z position. Moreover we observe that both flux components decrease in magnitude in the course of the plasma expansion as a consequence of losses of H radicals on the jet axis.

At a given z, the forward flux (in s^{-1}) is given by

$$\phi^{\text{forward}} = \iint_S nwdS = \int_0^R n_z(r)w_z(r)2\pi r dr, \tag{6.10}$$

where R represents the position of the boundary of the jet which is taken to be the radial position at which the H atom radial velocity is maximum. In order to calculate the forward flux, the radial profile of the H axial velocity component is needed. We will assume that the profile is identical to the one measured at $z = 8$ mm, which, in the core of the jet, can be well approximated by

$$w_z(r) = w_z(0)\cos^2(\varphi), \tag{6.11}$$

where the expansion angle φ is given by Eq. 6.8. We find that $\phi_H^{\text{in}} = 3.3 \times 10^{19}$ s^{-1} and $\phi_H^{\text{out}} = 3.9 \times 10^{18}$ s^{-1}, which means one order of magnitude loss of H flux.

Now this loss of H radicals has to be compared with the H radial flux across the shock front. At a specific axial position z, the differential radial flux of H atoms at the jet boundary R is given by

$$\frac{\partial}{\partial z}\phi_H^{\text{rad}} = 2\pi R n(z,R)w_r(z,R). \tag{6.12}$$

With our data set, only an averaged H atom radial flux $\overline{\phi_H^{\text{rad}}}$ can be calculated over the shock front. The latter is obtained by multiplying the averaged differential flux[4] by the shock thickness L, which is equal to 80 mm at 16 Pa. We find that $\overline{\phi_H^{\text{rad}}} = 3.4 \times 10^{19}$ s^{-1}, which is in good agreement with the decrease in forward flux. Thus we find that the total H atom flux is conserved throughout the shock front.

Finally, the radial flux can be compared with a diffusion flux. An estimate of the thermal flux can be obtained by using Fick's diffusion law. The radial diffusion flux of H atoms through the stationary shock wave is given by

$$\phi_H^{\text{th}} = -\frac{1}{3}\lambda^{H-Ar}v_{th}\frac{\partial n_H}{\partial r}S = \frac{v_{th}}{n_{Ar}\sigma_{Ar-H}}\frac{\partial n_H}{\partial r}S, \tag{6.13}$$

where σ_{Ar-H} is the momentum transfer cross section [41], v_{th} is the H atom thermal speed, and $S = 2\pi RL$ is the surface around the stationary shock wave. The H atom density gradient between the jet and the vessel wall can be estimated in first order from

$$\frac{\partial n_H}{\partial r} = \frac{n_H(R) - n_H(wall)}{R - r_{\text{vessel}}} \approx \frac{n_H(R)}{R - r_{\text{vessel}}}, \tag{6.14}$$

where $r_{\text{vessel}} = 180$ mm is the radius of the vacuum chamber. From Rayleigh scattering measurements [13, 26], the average Ar density at the jet boundary is found to be equal to 6×10^{20} m^{-3}. The H diffusion flux is then equal to 1.1×10^{19} s^{-1}. This value is lower than those calculated previously. The difference may arise from a too simple model for the diffusion coefficient of H atoms into an Ar-H_2 mixture. Moreover, the estimate of the H atom density gradient between the jet boundary and the vessel wall is also certainly too rough. A complete solution of the diffusion equation would therefore be necessary to confirm the picture of radial outflow induced by a density gradient.

[4] The differential flux is calculated at $z = 20$, 50, 80 and 100 mm and the mean value is used in the estimation of the diffusion flux. The corresponding value of R are: 15, 20, 20 and 20 mm.

6.7 Conclusions

Before giving the concluding remarks, it is worthwhile to provide the reader with a list of the most striking effects that support the idea of an outward diffusion of H atoms driven by plasma-wall interactions in the course of the expansion process

- ▷ pressure dependent H density decrease in the supersonic domain,
- ▷ no H density jump within the stationary shock wave,
- ▷ extremely low H concentration in the background gas,
- ▷ mass dependent decoupling between $\vec{w}_H$ and $\vec{w}_{Ar}$,
- ▷ H atom flow through the Ar barrel shock wave,
- ▷ zero H radial velocity component beyond the jet boundary.

In the expansion of a plasma generated from an Ar-H_2 mixture, hydrogen atoms are decoupled from argon atoms. As a consequence a peculiar situation is created where the plasma flow is composed of two fluids with their own macroscopic features. The Ar flow pattern can be entirely described using the well-established inert gas supersonic expansion theory. On the contrary the H flow pattern exhibits a significant departure from the classical expansion theory. The anomalous H atom flow characteristic is a direct consequence of the interaction between the plasma and the vessel walls where H atoms recombine to form molecular hydrogen.

The decoupling effect, of which the strength depends on the background pressure and on the reduced mass, is a general physical phenomenon which applies to most of atomic radicals as soon as the plasma expansion is surrounded by surfaces where the radicals can recombine with a high probability. In that case the surfaces, e.g. a reactor wall or dust particles, act as a sink for the radical. This in turn creates density gradients which are the driving force for this effect.

Acknowledgments

The authors would like to acknowledge fruitful discussion with Prof. M.C.M. van de Sanden and Dr. J.A.M van der Mullen. The authors greatly appreciate the skillful technical assistance of M.J.F. van de Sande, A.B.M. Hüsken, and H.M.M. de Jong. This work is part of the research program of the Netherlands Foundation for Fundamental Research on Matter (FOM) and is partially founded by Euratom. It is also financially supported by the Netherlands Organization for Scientific Research (NWO).

References

[1] *Beams and Jets in Astrophysics*, edited by P.A. Hugues, Cambridge University, Cambridge, (1991).

[2] A. Lebéhot and R. Campargue, *Phys. Plasmas* **3**, 2502 (1996).

[3] M. Veiler, S. Sattel, T. Giessen, K. Jung, H. Ehrhardt, V.S. Veerasamy, and J. Robertson, *Phys. Rev. B* **53**, 1594 (1996).

[4] M.C.M. van de Sanden, R.J. Severens, W.M.M. Kessels, R.F.G. Meulenbroeks, and D.C. Schram, *J. Appl. Phys.* **84**, 2426 (1998).

[5] W.M.M. Kessels, J.P.M. Hoefnagels, M.G.H. Boogaarts, D.C. Schram, and M.C.M. van de Sanden, *J. Appl. Phys.* **89**, 2065 (2001).

[6] S. Vepřek, J. Patscheider, and J.Th. Elmer, *Plasma Chem. Plasma Process.* **8**, 445 (1988).

[7] J. Wesson, *Tokamak*, Clarendon Press, Oxford, (1997).

[8] S. Mazouffre, M.G.H. Boogaarts, J.A.M. van der Mullen, and D.C. Schram, *Phys. Rev. Lett.* **84**, 2622 (2000).

[9] G.M.W. Kroesen, D.C. Schram, and J.C.M. de Haas, *Plasma Chem. Plasma Process.* **10**, 551 (1990).

[10] H. Ashkenas and F.S. Sherman, *Proceedings of Rarefied Gas Dynamics*, Academic Press, New York, Vol. 4, 84 (1966).

[11] E.P. Muntz, B.B. Hamel, and B.L. Maguire, *AIAA J.* **8**, 1651 (1970).

[12] *Atomic and Molecular Beam Methods*, edited by G. Scoles, Oxford University, New York, (1988).

[13] R.F.G. Meulenbroeks, R.A.H. Engeln, M.N.A. Beurskens, R.M.J. Paffen, M.C.M. van de Sanden, J.A.M. van der Mullen, and D.C. Schram, *Plasma Sources Sci. Technol.* **4**, 74 (1995).

[14] R.F.G. Meulenbroeks, A.J. van Beek, A.J.G. van Helvoort, M.C.M. van de Sanden, and D.C. Schram, *Phys. Rev. E* **49**, 4397 (1994).

[15] P. Gaucherel and B. Rowe, *Int. J. Mass Spectrom. Ion. Phys.* **25**, 211 (1977).

[16] P. Tosi, O. Dmitrijev, Y. Soldo, D. Bassi, D. Cappelletti, F. Pirani, and V. Aquilanti, *J. Chem. Phys.* **99**, 985 (1993).

[17] R.F.G. Meulenbroeks, R.A.H. Engeln, J.A.M. van der Mullen, and D.C. Schram, *Phys. Rev. E* **53**, 5207 (1996).

[18] J. Bokor, R.R. Freeman, and R.H. Storz, *Phys. Rev. A* **24**, 612 (1981).

[19] U. Czarnetzki, K. Miyazaki, T. Kajiwara, K. Muraoka, M. Maeda, and H.F. Döbele, *J. Opt. Soc. Am. B.* **11**, 2155 (1994).

[20] H.W.P. van der Heijden, M.G.H. Boogaarts, S. Mazouffre, J.A.M. van der Mullen, and D.C. Schram, *Phys. Rev. E* **61**, 4402 (2000).

[21] S. Mazouffre, M.G.H. Boogaarts, R. Engeln, J.A.M. van der Mullen, and D.C. Schram, *Proceedings of Laser-Aided Plasma Diagnostics* **9**, California, U.S.A., 320 (1999).

[22] A.D. Tserepi, J.R. Dunlop, B.L. Preppernau, and T.A. Miller, *J. Vac. Sci. Technol. A* **10**, 1188 (1992).

[23] T.V. George, L. Goldstein, L. Slama, and M. Yokoyama, *Phys. Rev.* **137**, 369 (1965).

[24] S.C. Snyder, L.D. Reynolds, G.D. Lassahn, J.R. Fincke, C.B. Shaw Jr, and R.J. Kearney, *Phys. Rev. E* **47**, 1996 (1993).

[25] G.I. Chashchina, V.I. Gladushchak, and E. Ya. Shreider, *Opt. Spectrosc.* **24**, 1008 (1968).

[26] M.C.M. van de Sanden, J.M. de Regt, and D.C. Schram, *Plasma Sources Sci. Technol.* **3**, 501 (1994).

[27] H.C.W Beijerinck, R.J.F van Gerwen, E.R.T. Kerstel, J.F.M. Martens, E.J.W. van Vliembergen, M.R.Th. Smits, and G.H. Kaashoek, *Chem. Phys.* **96**, 153 (1985).

[28] L. Landau and E. Liftshitz, *Fluid Mechanics*, Pergamon, London, (1989).

[29] R. Engeln, S. Mazouffre, P. Vankan, D.C. Schram, and N. Sadeghi, submitted for publication in *Plasma Sources Sci. Technol.*

[30] P. Kae-Nune, J. Perrin, J. Jolly, and J. Guillon, *Surf. Sci. Lett.* **360**, L495 (1996).

[31] R.I. Hall, I. Cadez, M. Landau, F. Pichou, and C. Shermann, *Phys. Rev. Lett.* **60**, 337 (1988).

[32] P.J. Eenshuistra, J.H.M. Bonnie, J. Los, and H.J. Hopman, *Phys. Rev. Lett.* **60**, 341 (1988).

[33] M. Persson and B. Jackson, *J. Chem. Phys.* **102**, 8 (1998).

[34] N. Cohen and K.R. Westberg, *J. Phys. Chem. Ref. Data* **2**, 531 (1983).

[35] L.E. Kline, W.D. Partlow, and W.E. Bies, *J. Appl. Phys.* **65**, 70 (1989).

[36] R.B. Fraser, F. Robben, and L. Talbot, *Phys. Fluids* **14**, 2317 (1971).

[37] E. Grant Jones, R.L.C. Wu, B. Mason Hughes, T.O. Tiernan, and D.G. Hopper, *J. Chem. Phys.* **73**, 5631 (1980).

[38] R. Johnsen, A. Chen, and M.A. Biondi, *J. Chem. Phys.* **72**, 3085 (1980).

[39] H. Tawara, *J. Phys. Chem. Ref. Data* **19**, 617 (1990).

[40] A.H.M Habets, Ph.D. thesis, Eindhoven University of Technology, The Netherlands (1977).

[41] A.V. Phelps, *J. Phys. Chem. Ref. Data* **21**, 883 (1992).

[42] M. Playez, Von Karman Institute for Fluid Dynamics, Belgium, private communication.

Appendix 6A

Dissociation degree

The dissociation degree α of the plasma source which characterized the strength of the source, i.e. the capability to generate radicals, is defined as

$$\alpha = \frac{\phi_H}{2\phi^o_{H_2}}$$

where ϕ_H is the ground state atomic hydrogen flux and $\phi^o_{H_2}$ is the gas flow of molecular hydrogen at the arc inlet. In our experimental conditions we have: $\phi^o_{H_2} = 0.5$ slm $= 2.2 \times 10^{20}$ s^{-1}. The knowledge of α in the source would necessitate the measurement of the H atom flux inside the arc channel, which is a difficult task. However, we will see that the knowledge of α in the core of the plasma jet can deliver information about α inside the source.

If there is no radial flux and no volume recombination, which is the case in the expansion of a neutral gas, then α can be estimated inside the plasma jet when knowing the forward flux. At a given z, the forward flux (in s^{-1}) is given by

$$\phi^{\text{forward}} = \iint_S nwdS = \int_0^R n_z(r)w_z(r)2\pi r dr,$$

where R represents the position of the boundary of the jet, i.e. the beginning of the barrel shock wave. In this case, α is conserved throughout the supersonic domain (in the absence of mass-focusing effects). Therefore by measuring α in this part of the jet, one obtains its value at the source exit.

Since the radial dependence of the H axial velocity has been measured at $z = 8$ mm, see Fig. 6.12, it is possible to determine α at this location by using the density profile of Fig. 6.9. The boundary position, which is needed to calculate the forward flux, is taken from the Ar radial velocity profile shown in Fig. 6.12. We find that at 8 mm behind the arc outlet $\phi_H^{\text{forward}} = 8 \times 10^{19}$ s^{-1} and thus $\alpha = 18$ %. It is likely that the dissociation degree inside the channel of the plasma source is close to unity when using such an Ar-H_2 mixture. Therefore, the low value of α measured at 8 mm behind the arc exit is an indication of the importance of the losses of H atoms in the arc nozzle as well as in the first few millimeters of the expansion.

Appendix 6B

Influence of the nozzle geometry

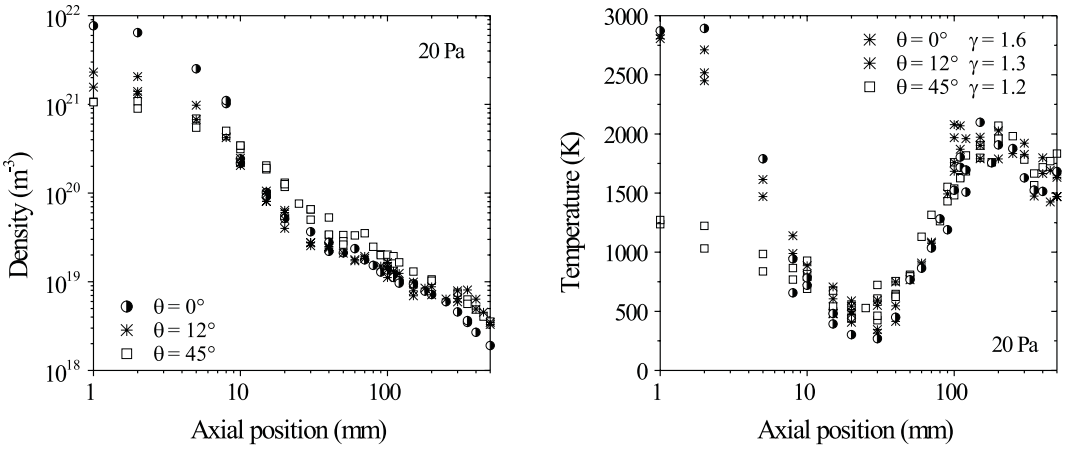

Fig. 6.13: Axial H density profile (left) and perpendicular temperature profile (right) measured at 20 Pa for 3 different arc nozzle opening angles: 0 degrees (circle), 12 degrees (star), and 45 degrees (square).

The cascaded arc is often used as a H atom source for surface treatment or modification. In that case the amount of H atom transported towards the downstream region of the flow is of relevance. In this appendix the influence of the cascaded arc nozzle geometry, i.e. the opening angle, on the H atom density is investigated. The arc is operated in standard conditions: 40 A, 100 V, 3 slm Ar, and 0.5 slm H_2. Three different opening angles are compared: 0 degrees (straight), 12 degrees, and 45 degrees (without pre-expansion zone).

At the arc exit, the difference in density between the 3 nozzles arises from a geometrical effect, i.e. a difference in the jet diameter. The smaller the angle, the smaller the diameter over the first few millimeters; since the forward flux is approximately constant, the density increases. At large angle (45°), the plasma expands already inside the nozzle and therefore cools down already inside the nozzle that explains the lower temperature at the outlet. In view of the aforementioned applications, the difference in density has to be compared in the subsonic domain (in this zone the temperature is independent of the geometry). The H atom density appears to be higher when using a large opening angle. The confinement inside the jet is not enhanced; the higher H density results from lower H losses in the source nozzle. Indeed a large opening angle do not favor (nozzle)wall-recombination: the gas temperature is lower and the available area is less since the plasma starts to flow ahead of the source exit.

Chapter 7

H atom fluid properties in a hydrogen plasma expansion [1]

Abstract

The flow properties of the ground state hydrogen atom fluid in the course of the expansion of a weakly ionized hydrogen plasma created by a cascaded arc are studied by means of Two-photon Absorption Laser Induced Fluorescence (TALIF). The transport of H_2 molecules is investigated using Rayleigh scattering. In view of the low ionization degree (< 1 % as measured by Thomson scattering), the hydrogen plasma resembles a hot neutral gas. Furthermore the low dissociation degree measured at the source exit implies that H atoms flow in a H_2 environment. It is shown that the H atom expansion pattern is in disagreement with the neutral gas supersonic expansion theory. Indeed the transport of H atoms in the plasma jet is strongly influenced by surface-recombination processes. Because of the large density gradients between the core of the jet and its surroundings induced by the recombination of H atoms at the reactor walls, hydrogen atoms diffuse out of the plasma jet during the expansion process. When the surface loss probability is high, e.g. combination of a large wall-recombination probability with a long residence time, the losses of radicals by diffusion, and the subsequent decoupling between the inert gas fluid and the reactive gas fluid, can not be avoided even when the mass of the carrier gas is close to the mass of the radical.

[1] Adapted from:
S. Mazouffre, P. Vankan, R. Engeln, and D.C. Schram, *Phys. Plasmas* **8**, 3824 (2001).

7.1 Introduction

The study of hydrogen plasma expansions is in the first place of particular interest since it concerns many different systems that cover a broad range of dimensions. Hydrogen being the most abundant form of matter in the universe, an object like solar outburst and a phenomenon like solar wind represent examples of astrophysical scale expanding hydrogen plasma [1]. At intermediate scale, hydrogen expansions are found in systems like the divertor region of a Tokamak plasma [2] and the remote plasma jets used for surface modifications.

In the second place, hydrogen plasma expansions contain light and highly reactive hydrogen atoms which play a key role in many chemical reactions encountered in plasma processes. To clearly demonstrate the importance of H atom chemistry, two examples will be given that are associated with energy and environmental problems humanity has to face in the next century. Hydrogen atoms are involved in the plasma-aided fast deposition of thin films of hydrogenated amorphous silicon (a-Si:H) needed for the next solar cell generation [3]. Atomic hydrogen radicals control the growth process ($SiH_4 + H \rightarrow SiH_3 + H_2$, SiH_3 being the main growth precursor) and thus the final film properties. In the field of controlled nuclear fusion, atomic hydrogen plays a specific role. First, one wants to use H atom sources for neutral beam heating of fusion devices (mainly via the production of negative hydrogen ions H^- [4]). Second, the interaction of neutral H atoms with the reactor surfaces and the resulting reaction products, i.e. H_2 molecules, have drastic consequences on the stability of the plasma and therefore on device performances [5, 6]. Numerous works are nowadays devoted to this so-called hydrogen recycling process and they all require the development of plasma sources capable of generating a high H atom flux.

All aforementioned processes are to a large extend governed by the transport mechanisms of H atoms in an expanding hydrogen plasma. In view of the applicability it is therefore of importance to study the H atom flow pattern as well as the influence of plasma-wall interactions on the transport properties. Moreover, the study of a plasma expansion at a specific scale may serve as an example, and the results obtained can be generalized to other kinds of localized plasma expansions with larger and smaller scales. On a more fundamental point of view, this study serves as a test case to find new evidences in order to confirm the fact that a radical expansion can differ strongly from a neutral gas expansion. The anomalous transport of radicals in a supersonic plasma jet induced by wall-recombination phenomena, i.e. the existence of a weak coupling between the inert gas fluid and the reactive gas fluid, has been reported recently in the case of an Ar-H_2 and He-H_2 mixture [7, 8]. In a hydrogen expansion, the mass of the carrier gas is close to that of the radical, and the resulting enhancement of confinement especially is of interest.

In the experiments reported here, ground-state hydrogen atoms are spatially probed using a two-photon excitation laser induced fluorescence technique in an expanding weakly ionized hydrogen plasma produced by a cascaded arc. The determination of the atomic hydrogen density, temperature, and velocity profiles enable to investigate in detail the transport mechanisms of H atoms in the supersonic plasma jet. The molecular hydrogen density profiles are measured by means of UV Rayleigh scattering that allows for discussions

about the coupling between the H fluid and the H_2 fluid over the expansion process.

7.2 Hydrogen plasma jet and optical system

Plasma source and plasma jet

The hydrogen plasma is created by a cascaded arc [9]. The arc channel is composed of 4 insulated plates and has a diameter of 4 mm. The operating standard conditions are: a 55 A DC current, a cathode-anode voltage of 150 V and a H_2 gas flow of 3.5 standard liters per minute (slm). The stagnation pressure inside the arc is 0.14 bar. The thermal hydrogen plasma expands from a straight nozzle with a diameter of 4 mm into a roots-blower pumped vacuum vessel where the background pressure (p_{back}) can be varied, almost independently from the gas flow, from 10 Pa to 1 atm. The cascaded arc plasma source is mounted on a translation arm. Spatial scans through the expanding plasma can be performed by moving the arc relative to the intersection of laser beam and detection volume.

Since in this contribution we focus on the transport of H atoms, it is of interest to briefly present the ways H atoms can be produced in the plasma source where the electron temperature T_e is around 1 eV. Ground-state atomic hydrogen can be generated by direct dissociation of H_2 molecule by electron impact

$$e + \mathrm{H_2} \rightarrow \mathrm{H} + \mathrm{H} + \mathrm{e}. \tag{7.1}$$

Yet the rate coefficient is relatively low at 1 eV [10, 11, 12]. A more favorable process at low temperature is the dissociative recombination of molecular ions

$$e + \mathrm{H_2^+} \rightarrow \mathrm{H^*} + \mathrm{H} \qquad \text{and} \qquad e + \mathrm{H_3^+} \rightarrow \mathrm{H} + \mathrm{H} + \mathrm{H}. \tag{7.2}$$

Both reactions are fast at low T_e [12]. Note that H_2^+ can easily form H_3^+ when reacting with H_2 and this again leads to the formation of H atom

$$\mathrm{H_2^+} + \mathrm{H_2} \rightarrow \mathrm{H_3^+} + \mathrm{H}. \tag{7.3}$$

Another mechanism of interest for H atom production is the charge transfer between a proton and a rovibrationally excited hydrogen molecule [13, 14]

$$\mathrm{H_2}^{v,J} + \mathrm{H^+} \rightarrow \mathrm{H_2^+} + \mathrm{H}. \tag{7.4}$$

The excited molecules are necessary to make the reaction exothermic. The energy deficit is around 2 eV, thus the charge exchange process is strongly favored for $H_2(v \geq 4)$. Note that the dissociation by impact with a proton of the H_2 molecule to form two H atoms is also possible at high v number [13]. The foregoing reactions have been proposed to explain the anomalous ion recombination, i.e. the fast ionization loss, in the expansion of an hydrogen plasma created by a cascaded arc [14]. Indeed without any influence of the arc parameters the plasma emerging from a cascaded arc with a straight nozzle is dark, which means that it contains mainly neutral particles, i.e. H atoms and H_2 molecules in our case. As measured by Thomson scattering, the ionization degree at the arc exit is less than 1 % [15].

Laser-aided diagnostics

H atom detection: TALIF

In the experiment reported in this contribution, ground-state hydrogen atoms are spatially probed by using a two-photon absorption laser-induced fluorescence (TALIF) technique [16, 17]. Only a short overview of the experimental method is presented here. A tunable 20 Hz Nd:YAG pumped dye laser delivers radiation around 615 nm. The output of the dye laser is frequency-tripled using non-linear optical crystals resulting in 2 mJ of tunable UV light around 205 nm with a measured bandwidth of 0.18 cm^{-1}. The UV laser beam is focused into the vacuum chamber either perpendicular or parallel to the plasma expansion axis. Hydrogen atoms are excited with two 205 nm photons from the $1s^2S$ ground state to the $3d^2D$ and $3s^2S$ states. The excitation is monitored by detection of the resulting fluorescence yield on the Balmer-α line at 656 nm using a gated photo-multiplier tube. A narrow bandwidth interference filter is used to isolate the H_α line from the plasma emission. A slitmask is used to define the detection volume of which the dimensions are smaller than any gradient scale length. The dye laser frequency is calibrated by the simultaneous recording of the absorption spectrum of molecular iodine. From a spectral scan over the two-photon transition, the local H atom density, temperature (perpendicular and parallel to a stream line), and velocity (radial and axial component) are determined.

Absolute number densities are obtained from the ratio of the H LIF signal in the plasma to the LIF signal of a well defined amount of krypton [18, 19]. Krypton atom has a two-photon excitation scheme very similar to that of hydrogen atom. Furthermore, the ratio of the two-photon absorption cross section of Kr to H has been recently accurately measured (see chapter 4).

H_2 molecule detection: Rayleigh scattering

The heavy particle density is measured by means of Rayleigh scattering using the UV laser beam. The polarized, scattered radiation at 205 nm is detected at an angle of 90° using a gated solar blind PMT. A dielectric UV mirror centered on 205 nm is used to filter out the plasma background light. The amount of stray light is reduced by a set of diaphragms and by using windows at Brewster's angle. The current detection limit in a H_2 plasma is 10^{21} m^{-3}. The H and H_2 Rayleigh cross-sections are almost identical [20]. The local H_2 density is therefore determined by subtracting from the measured density the contribution of the H density measured by TALIF under the same conditions. A possible way to directly obtain the molecular species concentration by Rayleigh scattering is to use the depolarization effect [21].

7.3 H_2 density behavior along the jet axis

Because the hydrogen plasma created in the cascaded arc expands from a high pressure region into a low pressure region, a well defined free jet shock wave structure is produced [22]. Indeed, the H_2 density profile measured at $p_{\mathrm{back}} = 100$ Pa along the jet axis, see Fig. 7.1,

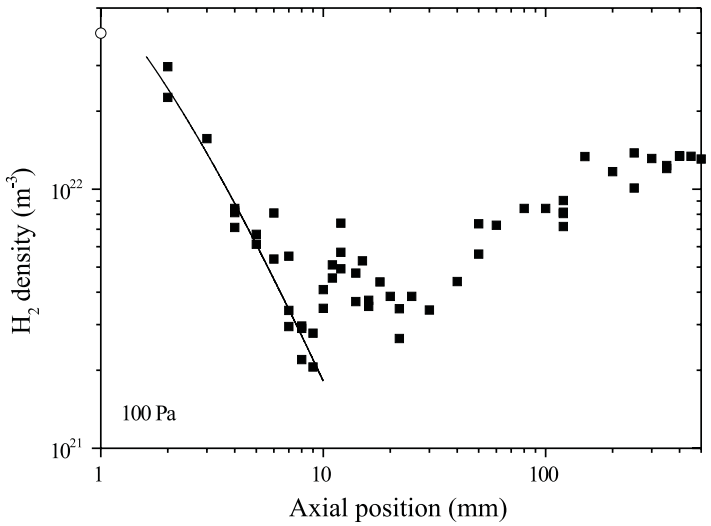

Fig. 7.1: Axial H_2 density profile measured at 100 Pa by Rayleigh scattering (full square). The solid line is the result of a fit using Eq. 7.5 with $\beta = 2$ and $z_0 = 1$ mm. The first point (open circle) is obtained under two assumptions: the injected H_2 flux is conserved and H_2 molecules flow at the local speed of sound.

is characteristic for such a structure[1]. In the supersonic domain, the pronounced density decrease results from the rarefaction effect. Within the stationary shock wave, the H_2 density increases as a consequence of the forward flux conservation. In the shock region, two compression stages are visible (from 8 to 13 mm and from 20 to approximately 50 mm) which arise from the step by step adaptation of the jet static pressure to the background gas static pressure [24]. In between the H_2 fluid re-expands, and the density drops. A compression ratio, which gives indication about the strength of the shock, of 3, respectively 1.7, is found for the first, respectively the second, compression stage. Those numbers simply show that the pressure difference is higher before the first compression step. A Mach number in front of the shock wave $M = 3$ is deduced from the Rankine-Hugoniot relation [24] using the magnitude of the density jump over the entire shock wave. Behind the shock wave, the plasma flows at constant static pressure. Since the temperature drops because of heat transfer to the vessel walls, the H_2 density increases accordingly as can be seen in Fig. 7.1. Using the measured H atom temperature, the static pressure in the subsonic domain is around 100 Pa. The H_2 axial density behavior, especially in the shock region, is well predicted by a calculation using a hydrodynamic code based on the Navier-Stokes equation [25]. The H_2 density profile is also in good agreement with the H atom

[1] In previous works, the H_2 density has been measured by CARS [23]; however the laser beam configuration did not allow to accurately resolve the plasma jet structure in the first millimeters.

temperature and velocity profile measured at 100 Pa as we will see.

In the supersonic domain, a theoretical expression for the density behavior is obtained from the flux conservation law in stationary state, and under the assumption that the particles originate from a point source and flow along straight stream lines (see chapter 2). The general expression for the particle density as a function of the distance to the source exit $n(z)$ reads

$$n(z) = n_{\mathrm{o}} \frac{z_{\mathrm{ref}}^{\beta}}{(z + z_{\mathrm{o}})^{\beta}}. \tag{7.5}$$

In Eq. 7.5, n_{o} is the density at the origin of the expansion, z_{ref} is a scaling length and z_{o} is the position of the virtual point source, i.e. the expansion origin. The exponent β defines the steepness of the density decrease. In the case of a supersonic expansion of an inviscid gas through a sonic orifice, it is shown that the exponent β is equal to 2, which corresponds to the classical rarefaction effect [22, 26]. The same value of 2 also applies in the case of the transport of neutral atoms in a plasma expansion [27]. From a fit of the supersonic H_2 density profile using Eq. 7.5 we find that $\beta = 2.0 \pm 0.1$ and $z_{\mathrm{o}} = +(1.0 \pm 0.5)$ mm. The exponent β correspond as expected to the case of an expansion of an inert gas; according to the value of z_{o}, the expansion starts close to the arc exit, as expected with a straight nozzle. According to the supersonic expansion theory, those two parameters are pressure independent. Setting z_{ref} to the nozzle radius (2 mm), one obtains $n_{\mathrm{o}} = (5 \pm 2) \times 10^{22}$ m^{-3} which is in good agreement with the value of 4×10^{22} m^{-3} obtained at $z = 1$ mm under the assumptions that the injected H_2 flux is conserved and that H_2 molecules flow at the local speed of sound.

7.4 Axial H atom density and temperature profiles

7.4.1 Loss of H atoms by diffusion

As mentioned in the introduction, the flow pattern of H atoms is expected to be governed by wall-recombination processes. As a consequence, it should significantly deviate from the classical expansion behavior, i.e. from the free jet flow picture. The measured ground-state H atom density profile along the plasma jet centerline is shown in Fig. 7.2 for two different background pressures. The H atom density profile is indeed in disagreement with the H_2 molecule density profile shown in Fig. 7.1. At $p_{\mathrm{back}} = 20$ Pa, there is no evidence of any density jump throughout the stationary shock wave. At $p_{\mathrm{back}} = 100$ Pa, a density jump with an amplitude of 1.4 is visible but this is in disagreement with the magnitude of the H_2 density jump. Moreover, only the first compression stage is apparent: the H density solely drops behind $z = 10$ mm. The two H density profiles reveal a non-conservation of the H atom forward flux throughout the stationary shock wave in contradiction with the well established Rankine-Hugoniot relations. Behind the shock wave, the H density decreases as shown in Fig. 7.2, and since also the temperature decreases, hydrogen atoms do not flow at constant static pressure which is a sign for losses of H atoms.

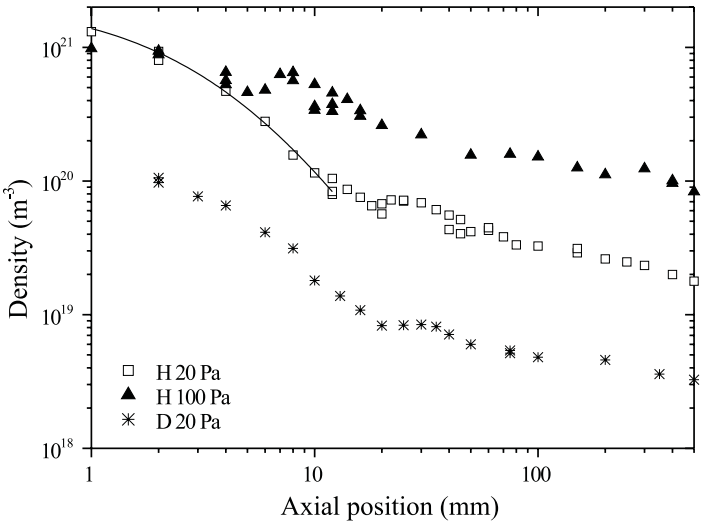

Fig. 7.2: Ground-state H atom density profile along the jet centerline at $p_{\mathrm{back}} = 20$ Pa (open square) and $p_{\mathrm{back}} = 100$ Pa (solid triangle) in standard conditions. Also shown is the ground-state D atom axial density profile at 20 Pa background pressure (star) in the case of a H_2-D_2 mixture (3.1 slm H_2 and 0.4 slm D_2). The solid line represents a fit using equation 7.5 with $\beta = 2.4$ and $z_{\mathrm{o}} = 4$ mm.

From a fit of the H density profile ahead of the shock wave using Eq. 7.5, see Fig. 7.2, we find that $z_{\mathrm{o}} = +(4 \pm 1)$ mm and $\beta = 2.4 \pm 0.2$ at $p_{\mathrm{back}} = 20$ Pa. First, the expansion of H atoms starts already inside the plasma source nozzle, contrary to that of H_2 molecules. Second, the H density drop is faster than the expected one, meaning that a loss mechanism is superimposed onto the rarefaction effect. Note that in previous works devoted to the study of the transport of H atoms in an Ar-H_2 plasma, β is also found to be larger than 2 as well as pressure dependent, and it approaches 2 at high background pressure [8]. Both effects support the idea of a decoupling between the H atom fluid and the H_2 molecule fluid which starts already in the source nozzle. Moreover, fixing z_{ref} to the nozzle radius, that allows for comparison with the H_2 profiles, we find that $n_{\mathrm{o}} = (2.5 \pm 1.5) \times 10^{21}$ m^{-3}.

Even if ground-state hydrogen atoms can recombine in volume due to the following three-body reactions

$$\mathrm{H + H + H_2 \rightarrow H_2 + H_2} \qquad \text{and} \qquad \mathrm{H + H + H \rightarrow H_2 + H}, \tag{7.6}$$

the reaction rates [28] however are too low to lead to any significant loss of H atoms under our experimental conditions. Therefore the observed anomalous transport of H atoms arises from the fact that H escapes the plasma jet in the course of the expansion. As shown in previous papers [7, 8], the loss of H atoms is a direct consequence of the existence of large density gradients between the core of the plasma jet and its surroundings. The low H atom concentration in the background gas, which is responsible for a H radical

outward diffusion, results from the very efficient destruction of H atoms at the reactor walls when a high wall-recombination probability (Γ) is combined with a long residence time (τ). The wall-recombination probability on stainless steel for H atoms is known to be large: $\Gamma_{ss} = 0.1$ - 0.2 [34, 35] at temperatures close to room temperature. The coefficient Γ depends on the surface temperature [30], on the state of the surface (roughness, presence of impurities, coverage by H) and on the energy of the incident H atom. That indicates how difficult it is to have an accurate estimate of Γ. However, the residence time inside our vacuum vessel is relatively long: $\tau \approx 0.8$ s at 20 Pa and $\tau \approx 4$ s at 100 Pa. That makes high losses of H radicals at the vessel walls, and thus a low H atom density in the background, very probable.

7.4.2 Perpendicular temperature development

The H atom perpendicular temperature ($T_\perp$) profile along the jet centerline is plotted in Fig. 7.3 for two different background pressures. Due to conversion of thermal energy into kinetic energy, i.e. directed motion, the H temperature drops quickly in the supersonic domain. The temperature profiles clearly reveal the occurrence of a stationary shock wave across which the temperature rises because of collisions with the background gas particles. As can be seen in Fig. 7.3 both the position and the thickness of the shock wave depend on p_{back}. In the subsonic part of the expansion, the temperature decreases due to heat transfer to the vessel walls. Behind the shock region, the measured H atom temperature is in good agreement with the rotational temperature of H_2 molecules measured by means of CARS [23]. The numerous collisions in the subsonic domain enable to maintain thermal equilibrium between H and H_2.

Using the Poisson adiabatic law, the temperature at the origin of the H atom expansion T_o as well as the isentropic exponent γ can be determined from a plot of the H temperature as a function of the H density in the supersonic domain. It is found that $\gamma = 1.55 \pm 0.05$ at $p_{\text{back}} = 20$ Pa and $\gamma \approx 1.7$ at $p_{\text{back}} = 100$ Pa. At 20 Pa background pressure the plasma expansion is found to be non adiabatic since γ is smaller than its adiabatic value $\frac{5}{3}$, as shown in Fig. 7.3. The fact that the supersonic expansion is not an adiabatic process may be explained by heat transfer from both the plasma source and the hot gas located behind the shock region. Another possibility is the entry in the jet of hot H_2 molecules, coming from the surrounding gas, in the last part of the supersonic domain where the mean free path for momentum exchange is large. The fact that the measured γ does not contain any molecular effects, especially at high pressure, whereas the jet is mainly composed of H_2 ($\gamma_{mixture} \approx 1.3$) is again an indication in favor of a decoupling between H atoms and H_2 molecules during the expansion process. The temperature T_o is equal to 2500 ± 500 K. This temperature correspond to the H temperature inside the arc nozzle, since $z_o = +4$ mm with this geometry. Therefore, the temperature inside the nozzle is different from the temperature inside the arc channel, which is about 1.2 eV [31]. In fact the plasma starts to cool down already in the arc nozzle and this drop in temperature may have a non negligible influence on plasma processes like ion-recombination for instance.

In the shock region, the H atom temperature profile measured at 100 Pa images the

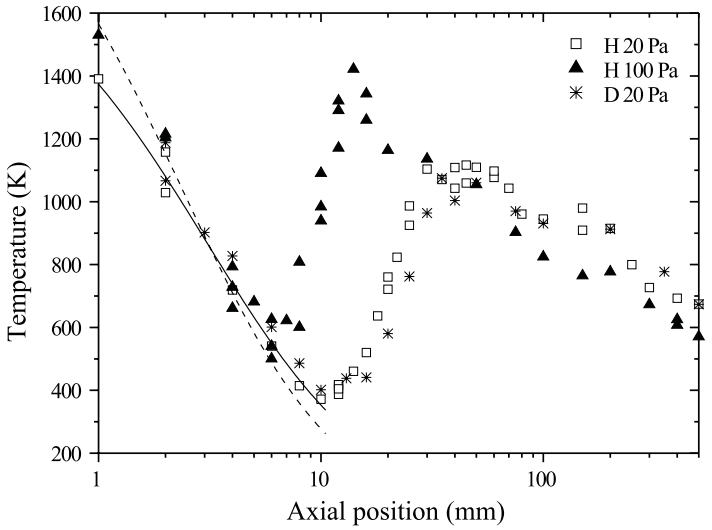

Fig. 7.3: Ground-state H atom perpendicular temperature ($T_\perp$) profile along the jet centerline at $p_{\text{back}} = 20$ Pa (open square) and $p_{\text{back}} = 100$ Pa (solid triangle). Also shown is the atomic deuterium axial $T_\perp$ profile at 20 Pa background pressure (star) for a H_2-D_2 mixture (3.1 slm H_2 and 0.4 slm D_2). The theoretical H temperature profile in the supersonic domain is shown at 20 Pa using the Poisson adiabatic law with $\gamma = 1.55$ (solid line) and $\gamma = \frac{5}{3}$ (dashed line).

H_2 density profile. For instance the second compression stage is noticeable: first the gas re-expands and then cools down (from $z = 13$ to $z \approx 20$ mm); secondly the expanding gas collide again with the background gas and the temperature rises or remains constant if the process is not too strong (from $z \approx 20$ to $z \approx 50$ mm). Note that a qualitative agreement between the H_2 density profile and the H atom temperature profile does not necessarily imply that $T_H = T_{H_2}$ during the expansion.

7.4.3 Injection of molecular deuterium in the arc

In order to study the influence of the mass on the transport of radicals and particularly on the confinement of radicals inside the jet, deuterium is added to the hydrogen flow and the created D atoms are monitored in the H_2-D_2 expanding plasma. The flow mixture is composed of 3.1 slm H_2 and 0.4 slm D_2. The cascaded arc parameters stay unchanged.

The deuterium atom perpendicular temperature profile along the jet axis, measured at $p_{\text{back}} = 20$ Pa, is shown in Fig. 7.3, together with the H atom $T_\perp$ profile. Both profiles indicate the same shock wave location and width. In the supersonic domain as well as in the subsonic domain, H and D temperature profiles overlap reasonably. Throughout the stationary shock wave, the D atom $T_\perp$ is slightly lower than the H atom $T_\perp$ by approxi-

mately 20 %. This departure from thermal equilibrium in the shock region is not yet well understood. It may be caused by a difference in energy exchange in a D-H_2 collision as compared to an H-H_2 collision, H_2 molecules being the main collision partner.

The deuterium atom density profile for an H_2-D_2 plasma at a pressure of 20 Pa is compared to the hydrogen atom density profile for a pure H_2 plasma in Fig. 7.2. At the plasma source outlet, the ratio of the H density to the D density is approximately equal to the injected gas flow ratio. This supports the idea of a high dissociation degree and an efficient mixing inside the arc channel where the plasma is created. In the supersonic domain, we obtain $\beta = 2.0 \pm 0.1$ and $z_{\text{source}} = +(4 \pm 1)$ mm when using Eq. 7.5 to describe the density drop. The value of the exponent β is equal to the value characteristic for a neutral gas supersonic expansion. Deuterium atoms are well coupled to H_2 molecules, as expected in view of the equal mass of the two particles, and thus they are relatively well confined inside the plasma jet, as indicated by the value of β. Nevertheless when the jet is underexpanded, losses of D atoms can occur in the barrel shock, i.e at the sides of the jet, where the mean free path is large and the radial velocity high. Across the stationary shock wave, the forward D atom flux is not conserved. In the shock region D atoms can escape the plasma jet because of the large mean free path. In the subsonic region, even if the confinement of D is better than that of H, D atoms are lost. The mass of the particle plays a role in the transport mechanism, since the loss of radicals arises from a diffusion process. It is shown however that when the mass of the carrier gas is close to that of the radicals the confinement inside the jet is improved but the losses by diffusion can not be avoided if the wall-recombination probability is high.

7.5 Recombination in the arc nozzle

From the measured H atom density and axial velocity it is possible to estimate the plasma source dissociation degree α. This parameter characterizes the source strength, i.e. the capability of producing H radicals. The dissociation degree can be expressed as follows

$$\alpha = \frac{\phi_H}{2\phi^{\circ}_{H_2}} = \frac{n_H}{n_H + 2n_{H_2}}, \tag{7.7}$$

where ϕ_H is the ground-state atomic hydrogen flux and $\phi^{\circ}_{H_2}$ the gas flow of molecular hydrogen at the arc inlet. Under our experimental conditions, $\phi^{\circ}_{H_2} = 1.56 \times 10^{21}$ s^{-1}. At the origin $z_{\circ}$ of the H atom expansion, i.e. inside the arc nozzle, $\alpha \approx 0.1$, if the plasma is assumed to flow with the local speed of sound $c_{s,\circ}$. Just behind the source exit ($z = 1$ mm), using the H and H_2 density profiles, one finds $\alpha \approx 0.02$. In our conditions, the low value of α does not arise from volume recombination of H atoms in view of the low three-body reaction rates [28]. For comparison, the dissociation degree in the background is found to be less than 1%. The low value of α in the downstream part of the flow is a direct consequence of the loss of H by diffusion during the expansion process. However, such a low dissociation degree in the source is not expected at an electron temperature of around 1 eV.

To a large extend, the low dissociation degree at the arc exit can be connected with the low electron density observed in the case of an expansion of a hydrogen plasma [14]. As already mentioned, the emerging plasma is dark. It thus appears that the expanding plasma jet is mainly composed of H_2 molecules. The low local value of α as well as the ionization loss need further clarification. A possible way to explain this experimental fact is to consider the production of vibrationally excited hydrogen molecules (in the electronic ground-state) on a surface. Neutral hydrogen atoms can indeed recombine on a surface to form excited H_2 molecules

$$H_{gas} + H_{ad} \rightarrow {H_2}^{v,J}_{gas}. \tag{7.8}$$

This chemical reaction has been extensively studied both experimentally and theoretically (see for instance [32, 33] and [34]). Because the probability for recombinative desorption of H atoms on a Cu surface is close to unity [34, 35], H atoms can easily be lost via the previous reaction in the arc nozzle, which is made of Cu. Accordingly, a large amount of $H_2^{v,J}$ molecules can be generated. Atomic hydrogen ions H^+, the most abundant ion, can easily exchange their charge with vibrationally excited H_2 molecule leading to H_2^+ ions (see section 7.2). The dissociative recombination of H_2^+ molecular ions is the main source of visible light at low electron density (production of H_α radiation if $H_2^+(v > 5)$ or $T_e \approx 1$ eV).

Inside the arc nozzle, recombination processes are favored. In the standard cascaded arc configuration, the nozzle acts as the anode. The arc root however attaches at the nozzle inlet (nozzle length = 17 mm) and thus no energy is supplied in the largest part of the nozzle. Therefore surface-recombination of H atoms and the subsequent $H_2^{v,J}$ formation can explain the low value of both the dissociation degree and the ionization degree at the arc exit: H atoms are lost at the nozzle wall and the created H_2^+ ions recombine before they escape the source.

CARS measurements performed on a pure hydrogen plasma [23] reveal a low density of excited H_2 molecules in the jet. At $z = 20$ mm, the density of $H_2(v{=}0)$ is equal to 1.4×10^{21} m^{-3}, the density of $H_2(v{=}2)$ is approximately equal to 10^{18} m^{-3} and the density of $H_2(v{=}4)$ is less than 10^{17} m^{-3}. This may denote that all $H_2^{v,J}$ molecules produced in the arc nozzle by wall-recombination of H atom are quickly lost either via the formation of H_2^+ ions (that explains the absence of visible light) or via the formation of negative hydrogen ions H^- by dissociative attachment of low energy (≈ 1 eV) electrons [36]

$$H_2^{v,J} + e \rightarrow H + H^-. \tag{7.9}$$

There are indications for the production of H^- ions in a cascaded arc, e.g. the existence of blue radiation around 300 nm at the plasma jet periphery at high pressure [37] that may originate from the recombination of H^- [38]. The CARS measurements unfortunately could not be performed at the arc exit because of the crossed laser beam geometry and thus information concerning the energy distribution of H_2 molecules leaving the arc is still lacking. As it appears, the process of surface-recombination in the arc nozzle is complex, but it certainly needs further investigation since it plays a decisive role when the plasma jet is to be used as an efficient H ion or H radical source.

7.6 Axial velocity component and sound speed

Another important parameter to be determined in order to characterize the atomic radical transport mechanism is the flow velocity. The measured H atom axial velocity component profile along the jet centerline is shown in Fig. 7.4 and Fig. 7.5 at 20 Pa and 100 Pa background pressure respectively. Throughout the stationary shock wave, the distribution function is found to be non-Maxwellian. The departure from thermodynamic equilibrium in the shock region of an expanding plasma is studied in chapter 8. In this section we only consider the mean axial velocity in the shock region, i.e. the velocity calculated from the first moment of the distribution function. To clearly discern the three different flow regimes (supersonic, shock, subsonic), the flow velocity has to be compared with the local speed of sound in order to obtain the Mach number M. The speed of sound is given by

$$c_s = \sqrt{\frac{\gamma k_B T}{m}}, \tag{7.10}$$

where γ is the adiabatic exponent and k_B the Boltzmann constant, and m the mass. The on-axis development of the speed of sound is plotted in Fig. 7.4 and Fig. 7.5 for two different background pressures using the measured H atom parallel temperature ($T_{\|}$), the temperature associated with the velocity distribution parallel to a stream line, and using as mass number $m = 2$ amu and $\gamma = 1.3$ since H_2 is the major component of the jet. The sound speed at the expansion origin z_o inside the arc nozzle can be calculated using T_o: with $\gamma = 1.3$, $c_{s,o} \approx 4000$ m s^{-1}. At the plasma source exit the Mach number is already high, $M = 2$. A theoretical expression describing the evolution of the axial velocity along a stream line in the supersonic domain can be obtained from the Bernoulli equation and the Poisson adiabatic law [37]. If we consider that the plasma starts to expand with $c_{s,o}$, one finds for the velocity

$$w(z) = \frac{c_{s,o}}{\sqrt{\gamma - 1}} \sqrt{\gamma + 1 - 2\left(\frac{z_{ref}}{z + z_o}\right)^{\beta(\gamma-1)}}. \tag{7.11}$$

Since the previous expression contains β it accounts automatically for the outward diffusion effect when $\beta > 2$. In Fig. 7.4 the measured H atom axial velocity profile in the supersonic domain at 20 Pa is compared with a calculation using Eq. 7.11. The agreement is satisfactory with $\gamma = 1.55$. This again supports the idea of a H atom fluid partly decoupled from the H_2 molecule fluid in the course of the plasma expansion [8]. At this point however, we suffer from a lack of information about the transport properties of H_2 molecules. It is now clear that the problem concerning the coupling between H and H_2 in the jet can only be untangled by measuring the H_2 velocity and temperature profile along the jet axis.

As can be seen from Eq. 7.11 the maximum flow velocity depends on T_o and accordingly on the source temperature. In our conditions, $w_{max} = 8600$ m s^{-1} for H atoms. However, before the hydrogen atoms can reach the maximum velocity they start colliding with the residual background gas meaning that the expansion never enters the so-called frozen regime [22]. The existence of a stationary shock wave is clearly revealed in Fig. 7.4 and

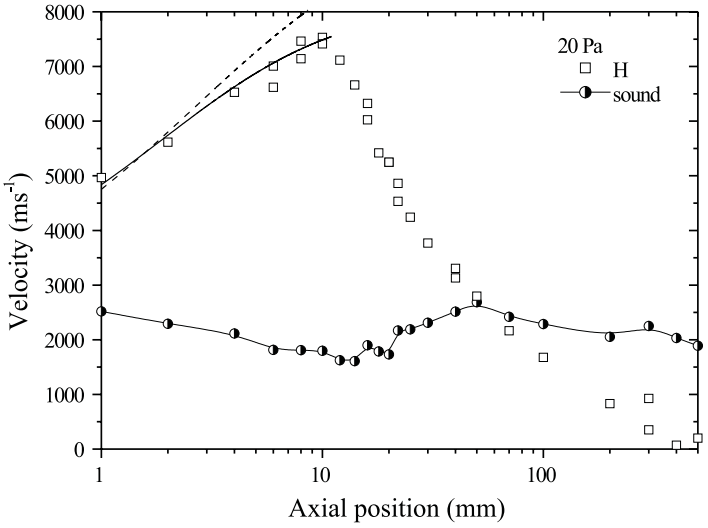

Fig. 7.4: Development of the atomic hydrogen axial velocity component w_z along the jet axis at $p_{\text{back}} = 20$ Pa (open square) and speed of sound c_s calculated from the measured parallel temperature ($T_{||}$) with $m = 2$ amu and $\gamma = 1.3$ (circle). $M = 4.2$ ahead of the stationary shock wave. The lines represent the outcome of a model describing the H axial velocity in the supersonic domain, see Eq. 7.11, with $\gamma = 1.55$ (solid) and with $\gamma = 1.3$ (dashed).

Fig. 7.5. In the two figures, the effect of the background pressure on both the shock wave position and the shock wave thickness is visible. The Mach disk location z_{M} is found to be equal to 50 mm at 20 Pa and approximately 40 mm at 100 Pa. At $p_{\text{back}} = 20$ Pa, the measured shock thickness is equal to 40 mm. It can be compared with the H-H_2 collision mean free path ahead of the shock region since H atoms mainly collide with H_2 molecules. The mean free path is given by

$$\lambda_{H-H_2}^{mfp} = \frac{1}{n_{H_2}\sigma_{H-H_2}}, \tag{7.12}$$

where n_{H_2} is the molecular hydrogen density and σ_{H-H_2} the momentum exchange cross-section. The H_2 density has been measured by CARS [23]: $n_{H_2} = 4 \times 10^{20}$ m^{-3} at 20 Pa. The value for the cross-section can be found in literature [39]; at 500 K $\sigma_{H-H_2} \approx 2{\times}10^{-19}$ m^2. At 20 Pa a mean free path for momentum exchange ahead of the shock wave of 12 mm is found. Thus the shock wave thickness is in the order of few $\lambda_{H-H_2}^{mfp}$. At this pressure the mean free path becomes in the order of the jet dimension (10 mm radius at $z = 10$ mm if a 45° expansion is assumed). Therefore at this point the flow can not be satisfactorily described using the hydrodynamic theory and one must turn to the more complex gas kinetic theory.

The Mach number ahead of the stationary shock wave can be deduced from our mea-

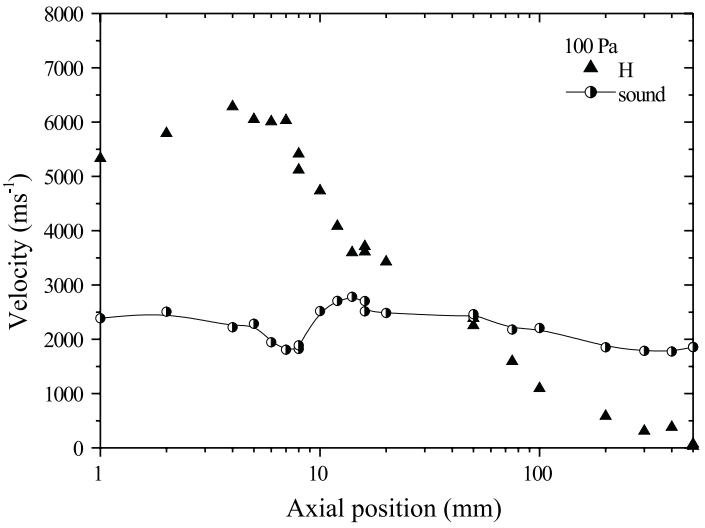

Fig. 7.5: Development of the atomic hydrogen axial velocity component w_z along the jet axis at $p_{\mathrm{back}} = 100$ Pa (solid triangle) and speed of sound c_s calculated from the measured parallel temperature ($T_{\|}$) with $m = 2$ amu (circle). $M = 3.3$ in front of the shock wave.

surements: $M = 4.2$ at 20 Pa and $M = 3.3$ at 100 Pa. Using the Rankine-Hugoniot relations both the theoretical density and temperature jump across the shock wave can be calculated using these Mach numbers. With an adiabatic exponent of 1.55, the expected density jump is equal to 3.6 at 20 Pa and 3.2 at 100 Pa in complete disagreement with the measured values of 1.3 and 0.5 respectively (see Fig. 7.2). The observed discrepancy is a direct consequence of the losses of H atoms by diffusion combined with a weakening of the shock structure. The calculated temperature jump is equal to 5.9 at 20 Pa and 3.4 at 100 Pa, whereas the measured jump is equal to 3.3 and 2.7 at 20 Pa and 100 Pa respectively. A too small temperature jump across the shock wave confirms the idea of the invasion of the shock region by the surrounding background gas. The resulting energy transfer modifies the temperature. Behind the stationary shock wave, the velocity decreases because of momentum transfer to the background gas particles.

7.7 Plasma jet vicinity

In order to evaluate the difference in the H atom concentration and temperature between the core of the jet and the surrounding background gas, it is of interest to study jet cross-sections. The radial profile of the H atom density as well as the corresponding temperature profile have been measured at $p_{\mathrm{back}} = 20$ Pa at an axial position z of 30 mm from the arc

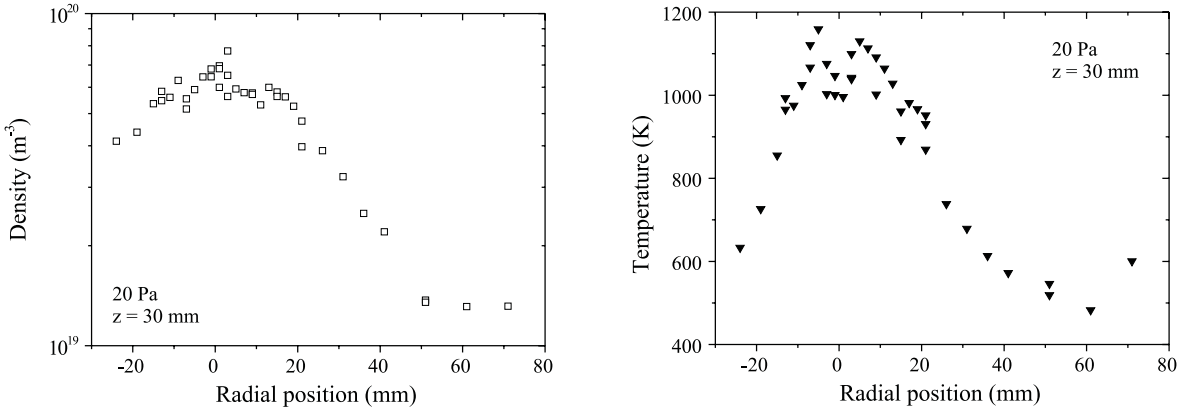

Fig. 7.6: Radial profile of the H atom density (left) and perpendicular temperature (right) at 20 Pa background pressure measured at 30 mm behind the arc outlet. The H density outside the jet is relatively low due to wall-recombination processes. For comparison, the H_2 density around the plasma jet is approximately 3×10^{21} m^{-3} at 20 Pa. The H_2 rotational temperature in the background is found to be 600 K [23], in good agreement with the H temperature at large r position.

outlet, i.e. in the shock region.

The density profile is shown in Fig. 7.6. In the core of the jet the H density is high, $n_H = 6 \times 10^{19}$ m^{-3} whereas it is relatively low in the jet vicinity, $n_H \approx 10^{19}$ m^{-3}. Therefore, in the shock wave zone the H radical expansion is not overexpanded, contrary to that of non-reacting neutrals. As mentioned previously, the low H density in the background is a consequence of the recombination of H atoms at the walls of the vacuum chamber. For comparison, the background molecular hydrogen density at 20 Pa is about 3×10^{21} m^{-3} as measured by CARS [23]. The existence of strong density gradients at the jet boundary supports the idea of an outward diffusion process.

The radial profile of the H atom perpendicular temperature is also shown in Fig. 7.6. The temperature is on the average relatively high in the core of the jet, approximately 1100 K, however it is slightly lower around the jet axis. Indeed at $r \approx 0$, a dip is visible in the temperature profile in Fig. 7.6. The temperature is higher at the jet boundary because of collisions with the background gas. The temperature gradually decreases in the vicinity of the plasma jet to about 500 K due to heat transfer to the vessel wall. The measured H atom background gas temperature is in good agreement with the H_2 rotational temperature measured outside the jet by CARS [23].

7.8 Conclusions

The study of the transport of ground-state hydrogen atoms in the expansion of a thermal hydrogen plasma reveals that surfaces can have a great influence on the chemistry and

on the dynamics of a system containing reactive particles. The low dissociation degree as well as the quasi-absence of charged particles at the plasma source exit, can be explained by the recombination of H atoms on the arc nozzle wall and the subsequent formation of vibrationally excited hydrogen molecules. As expected the transport of H atoms is also strongly influenced by surface-recombination processes. The efficient loss of H atoms at the vessel walls creates large density gradients between the jet and the surroundings which in turn force H to diffuse out of the plasma jet. It is shown that when the surface loss probability is high, e.g. combination of a large wall-recombination probability with a long residence time, the losses of radicals by diffusion can not be avoided even when the mass of the carrier gas is close to the mass of the radical. A full understanding of the decoupling between the H fluid and the H_2 fluid, that results from the outward diffusion of H atoms, during the expansion would however necessitate to also investigate the H_2 molecules transport properties. In other words, the "coupling problem" will not be solved without the measurement of the H_2 velocity and temperature profiles under the same experimental conditions.

This work stresses the importance of plasma-wall interactions in the manufacture of a plasma source with specific requirements but also in the design of reactors devoted to plasma-assisted chemistry. Nowadays the transport of radicals in a plasma expansion starts to be better understood, and technological solutions can be proposed in order to enhance the confinement inside the plasma jet (e.g. by using a vessel wall material with a low surface-recombination probability). Nevertheless further investigations have to be performed on plasma-wall interactions and the related generation of molecules. To better understand the dynamics of the process and to investigate the possibility of using a surface as a catalyst to favor the production of a desired molecule for instance. This may open in the near future a new field in plasma-aided chemistry.

Acknowledgments

The authors would like to acknowledge fruitful discussion with Prof. M.C.M. van de Sanden. The authors greatly appreciate the skillful technical assistance of M.J.F. van de Sande, A.B.M. Hüsken, and H.M.M. de Jong. This work is part of the research program of the Netherlands Foundation for Fundamental Research on Matter (FOM). It is financially supported by the Netherlands Organization for Scientific Research (NWO) as well as the Euratom foundation.

References

[1] *Beams and Jets in Astrophysics*, edited by P.A. Hugues, Cambridge University, Cambridge (1991).

[2] J. Wesson, *Tokamak*, Clarendon Press, Oxford, (1997).

[3] W.M.M. Kessels, M.C.M. van de Sanden, and D.C. Schram, *J. Vac. Sci. Technol. A* **18**, 2153 (2000).

[4] A.J.T. Holmes, *Plasma Phys. Control. Fusion* **34**, 653 (1992).

[5] J. Winter, *Plasma Phys. Control. Fusion* **38**, 1503 (1996).

[6] U. Samm and the TEXTOR-94 Team, *Plasma Phys. Control. Fusion* **41**, B57 (1999).

[7] S. Mazouffre, M.G.H. Boogaarts, J.A.M. van der Mullen, and D.C. Schram, *Phys. Rev. Lett.* **84**, 2622 (2000).

[8] S. Mazouffre, M.G.H. Boogaarts, I.S.J. Bakker, P.J.W. Vankan, R. Engeln, and D.C. Schram, accepted for publication in *Phys. Rev. E.*

[9] G.M.W. Kroesen, D.C. Schram, and J.C.M. de Haas, *Plasma Chem. Plasma Process.* **10**, 551 (1990).

[10] M. Capitelli, M. Dilonardo, and E. Molinari, *Chem. Phys.* **20**, 417 (1977).

[11] M.A. Cacciatore, M. Capitelli, and R. Celiberto, Atomic and Plasma-Material Interaction Data for Fusion, Sup. to *Nuclear Fusion* **2**, 65 (1992).

[12] H. Tawara, Y. Itikawa, N. Nishimura, and M. Yoshino, *J. Phys. Chem. Ref. Data* **19**, 617 (1990).

[13] A. Ichihara, O. Iwamoto, and R.K. Janev, *J. Phys. B: At. Mol. Opt. Phys.* **33**, 4747 (2000).

[14] M.J. de Graaf, R. Severens, R.P. Dahiya, M.C.M. van de Sanden, and D.C. Schram, *Phys. Rev. E* **48**, 2098 (1993).

[15] R.F.G. Meulenbroeks, R.A.H. Engeln, M.N.A. Beurskens, R.M.J. Paffen, M.C.M. van de Sanden, J.A.M. van der Mullen, and D.C. Schram, *Plasma Sources Sci. Technol.* **4**, 74 (1995).

[16] U. Czarnetzki, K. Miyazaki, T. Kajiwara, K. Muraoka, M. Maeda, and H.F. Döbele, *J. Opt. Soc. Am. B.* **11**, 2155 (1994).

[17] H.W.P. van der Heijden, M.G.H. Boogaarts, S. Mazouffre, J.A.M. van der Mullen, and D.C. Schram, *Phys. Rev. E* **61**, 4402 (2000).

[18] K. Niemi, V. Schultz von der Gathen, and H.F. Döbele, *Proceedings of Hakone* **7**, Greifswald, Germany, Vol. 1, 199 (2000).

[19] S. Mazouffre, C. Foissac, P. Supiot, P. Vankan, R. Engeln, D.C. Schram, and N. Sadeghi, *Plasma Sources Sci. Technol.* **10**, 168 (2001).

[20] see U. Hohm and K. Kerl, *Mol. Phys.* **69**, 803 (1990) for the H_2 Rayleigh cross-section; see W.A. Bowers, *Am. J. Phys.* **54**, 347 (1986) for the H Rayleigh cross-section.

[21] R.F.G. Meulenbroeks, D.C. Schram, L.J.M. Jaegers, and M.C.M. van de Sanden, *Phys. Rev. Lett.* **69**, 1376 (1992).

[22] D.R. Miller, in *Atomic and Molecular Beam Methods*, edited by G. Scoles, Oxford University, New York (1988).

[23] R.F.G. Meulenbroeks, R.A.H. Engeln, J.A.M. van der Mullen, and D.C. Schram, *Phys. Rev. E* **53**, 5207 (1996).

[24] P.A. Thomson, *Compressible-fluid Dynamics*, McGraw-Hill, New York (1972).

[25] M. Playez, von Karman Institute for Fluid Dynamics, Brussel, Belgium, private communication.

[26] H.C.W. Beijerinck, R.J.F. van Gerwen, E.R.T. Kerstel, J.F.M. Martens, E.J.W. van Vliembergen, M.R.Th. Smits, and G.H. Kaashoek, *Chem. Phys.* **96**, 153 (1985).

[27] M.C.M van de Sanden, J.M. de Regt, and D.C. Schram, *Plasma Sources Sci. Technol.* **3**, 501 (1994).

[28] N. Cohen and K.R. Westberg, *J. Phys. Chem. Ref. Data* **2**, 531 (1983).

[29] M. Mozetič, M. Drobnič, and A. Zalar, *Appl. Surf. Sci.* **144-145**, 399 (1999); P. Kae-Nume, J. Perrin, J. Jolly, and J. Guillon, *Surf. Sci.* **360**, L495 (1996).

[30] L. St-Onge and M. Moisan, *Plasma Chem. Plasma Process* **14**, 87 (1994).

[31] G. Janssen, *Design of a General Plasma Simulation Model*, Ph.D. Thesis, Eindhoven University of technology, The Netherlands (2000).

[32] R.I. Hall, I. Čadež, M. Landau, F. Pichou, and C. Shermann, *Phys. Rev. Lett.* **60**, 337 (1988); P.J. Eenshuistra, J.H.M. Bonnie, J. Los, and H.J. Hopman, *Phys. Rev. Lett.* **60**, 341 (1988).

[33] D. Kolovos-Vellianitis, Th. Kammler, J. Küppers, *Surf. Sci.* **454-456**, 316 (2000).

[34] B. Jackson and M. Persson, *J. Chem. Phys* **96**, 2378 (1992).

[35] B. Freiesleben Hansen and G.D. Billing, *Surf. Sci.* **373**, L333 (1997).

[36] T. Mosbach, H.-M. Katsch, and H.F. Döbele, *Phys. Rev. Lett.* **85**, 3420 (2000) and references herein.

[37] D.C. Schram, S. Mazouffre, R. Engeln, and M.C.M. van de Sanden, in *Atomic and Molecular Beams*, edited by R. Campargue, Springer, New York, 209 (2001).

[38] M.C.M. van de Sanden, Z. Qing, D.K. Otorbaev, M.J. de Graaf, J.C.A. Wevers, and D.C. Schram, *Proceedings of European Workshop on the Prod. and Appl. of Light Negative Ions* **5**, Dublin (1994).

[39] A. Phelps, *J. Phys. Chem. Ref. Data* **19**, 653 (1996).

Chapter 8

Behavior of the H atom velocity distribution function within the shock wave of a hydrogen plasma jet [1]

Abstract

The evolution of the ground-state hydrogen atom velocity distribution function throughout the stationary shock wave of a supersonic hydrogen plasma jet (3 < Mach number < 4) is studied using laser induced fluorescence spectroscopy. A clear departure from thermodynamic equilibrium is observed. The H atom velocity distribution function can be decomposed into two Maxwellian distributions. The fast component of the distribution corresponds to the conditions upstream of the shock region. The slow component corresponds to the conditions in the shock region, i.e. within the shock front the mean velocity and the temperature of this atom group vary.T Across the shock wave, the H atom population is gradually tranferred from the fast to the slow component by means of collisions. The development of the mean axial velocity is modeled using the Mott-Smith approach. Deviation from the theoretical shock profile is interpreted in terms of the non-conservation of both the H atom forward flux and momentum across the shock wave.

[1] Adapted from:
S. Mazouffre, P. Vankan, R. Engeln, and D.C. Schram, accepted for publication in *Phys. Rev. E* (2001).

8.1 Introduction

The study of physical systems under non-equilibrium conditions has been the subject of numerous researches for a long period of time. An example of a system characterized by a departure from thermodynamic equilibrium is the interior of a shock wave [1]. Across a shock wave, a flowing medium exhibits a rapid change in its macroscopic properties, i.e. density, velocity, and temperature, over a short distance (merely a few mean free paths). Shock waves are nowadays relatively easy to produce and to control using several kinds of experimental facilities like wind tunnels, shock tubes, and free jets. Moreover laboratory shock waves offer the possibility to cover a vast ensemble of physical conditions: a broad range of Mach numbers (M) is accessible, the flow regime can be varied from continuum to rarefied, the shock wave can be created in an atomic gas, a molecular gas or a plasma, to only name a few.

As recently pointed out by Ramos *et al* [2], scientists are confronted with a paradox. Although the general properties of a shock wave are at present well established, there still exist numerous issues concerning the evolution of the distribution function within such a disturbed region. This peculiar situation is a direct consequence of the relative lack of detailed experimental studies in comparison with the large amount of theoretical works (see for instance [3, 4, 5] and references herein).

Most of experimental investigations of a gas(plasma) shock wave are devoted to the measurement of the development of macroscopic parameters. Several diagnostic techniques have been employed: electron-beam absorption [6] and electron beam induced fluorescence [7], Rayleigh scattering [8], laser-Doppler technique [9] and Thomson scattering in the case of charged particles [10]. Despite the fact that those studies furnish a large amount of data which can be compared with the prediction of different theories, i.e. hydrodynamic approach (Navier-Stokes equation) or kinetic theory (Boltzmann equation), they only provide indirect information concerning the distribution function. Up until now only a few works have been directly devoted to the study of the distribution function across a shock wave. In the work of Ramos *et al* [2] the rotational state distribution function of N_2 molecules is studied in a nitrogen free jet by means of Raman scattering, and in the work of Pham-Van-Diep *et al* [11] the velocity distribution function in a helium jet is measured by means of electron beam induced fluorescence (see also Ref. [12] for measurements in an argon jet). Those works confirm the main conclusions of Mott-Smith [13] and Glansdorff [14] about a bimodal distribution function in a shock region, even though the discovery of a third component, related with the invasion of the jet, is reported.

In the present contribution, the behavior of the velocity distribution function (VDF) of ground-state hydrogen atom is directly studied within the stationary shock wave of a weakly ionized expanding hydrogen plasma ($3 < M < 4$, depending on the background pressure) by means of two-photon absorption laser induced fluorescence (TALIF) spectroscopy. From the VDF, the local H atom density, mean velocity and temperature are also deduced. The large Doppler broadening of H atoms, combined with the relatively high temperature of the plasma medium, allows to obtain accurate data on the VDF. In this plasma environment, we are confronted with a very particular situation: neither the H atom forward flux nor

the H atom momentum is conserved within the shock wave [15]. Recombination of H atoms at the vessel walls induces large density gradients between the core of the plasma jet and its surrounding, which in turn force H to diffuse out of the jet [16]. This effect is very pronounced in the shock region where the mean free path is large. Because of recombination processes in the arc nozzle, the expanding plasma is mainly composed of H_2 molecules to which H atoms transfer most of their momentum. As a consequence the Rankine-Hugoniot relations are not valid for the H atom fluid, not even at high background pressure.

8.2 Experimental determination of the H atom VDF

Ground-state hydrogen atoms are spatially probed by using a two-photon absorption laser-induced fluorescence (TALIF) technique [17, 18, 19]. Only a short overview is presented here (see chapter 4 for more information). A tunable 20 Hz Nd:YAG pumped dye laser delivers radiation around 615 nm. The output of the dye laser is frequency-tripled resulting in 2 mJ of tunable UV light around 205 nm. The UV laser beam is focused parallel to the plasma expansion axis. Hydrogen atoms are excited with two 205 nm photons from the $1s^2S$ ground state to the $3d^2D$ and $3s^2S$ states. The excitation is monitored by detection of the resulting fluorescence yield on the Balmer-α line at 656 nm using a gated photo-multiplier tube. An interference filter is used to isolate the H_α line from the plasma emission. A slitmask is used to define the detection volume which dimensions are much smaller than any gradient length. The dye-laser frequency is accurately calibrated by the simultaneous recording of the absorption spectrum of molecular iodine. A spectral scan over the two-photon transition provides a direct access to the local H atom velocity distribution function (VDF), which allows for discussion on the state of equilibrium of the plasma flow. From the measured line profile the H density and mean velocity are obtained. In the case of a Maxwellian distribution a H atom temperature can also be defined. The influence of the laser line profile (FWHM ≈ 0.18 cm^{-1}) on the shape of measured spectral profile is neglected. This is legitimate in view of the low mass of H atoms and the relative high plasma temperature.

The experimental determination of the velocity distribution function of a particle group is based on the Doppler effect. The broadening of a spectral line results from the Doppler shift of the optical transition induced by the spread in velocity within a group of particles. A particle moving with velocity v_z towards a probing light source absorbs a photon at a frequency ν given by[1]

$$\nu = \nu_o \left(1 - \frac{v_z}{c}\right), \tag{8.1}$$

where ν_o is the absorption frequency of the particle at rest, c is the speed of light in vacuum.

[1] In view of the low particle velocity in comparison with the speed of light, relativistic effects are not taken into account. For information, the longitudinal Doppler effect in relativity reads $\nu = \nu_o \sqrt{\frac{c+v}{c-v}}$ when the source and the observer move towards one another [20]. A transverse Doppler effect, that is purely a relativistic effect, is also predicted by the theory [20].

If the Doppler effect is the main broadening mechanism, the measured absorption profile is essentially the distribution of the velocity component v_z. Indeed one can not directly probe the three-dimensional velocity distribution $F_{\mathbf{v}}$, i.e. the density in velocity space, only the one-dimensional distribution $f_v(v_z)$ of the velocity component in the direction z of propagation of the laser beam is measured. The 1D and 3D velocity distribution functions are related by

$$f_v(v_z) = \int\int F_{\mathbf{v}}\, dv_x\, dv_y, \tag{8.2}$$

which corresponds to a projection in velocity space[2]. The energy distribution function $f_E(E)$ follows from a transformation of velocity into translational energy via $E = \frac{1}{2}mv^2$.

The hydrogen plasma is created by a cascaded arc [21]. The arc channel is composed of 4 insulated plates and has a diameter of 4 mm. The operating standard conditions are: a 55 A DC current, a cathode-anode voltage of 150 V and a H_2 gas flow of 3.5 standard liters per minute. The stagnation pressure inside the arc is 0.14 bar. The thermal hydrogen plasma expands from a straight nozzle with a diameter of 4 mm into a low background pressure (p_{back}) chamber. At the arc outlet the plasma turns into almost a hot gas, most electrons being consumed in the nozzle (ionization degree $< 1\%$). Furthermore the generation of H_2 molecules by surface-recombination of H atoms is favored inside the arc nozzle which leads to a relatively low dissociation degree at the source exit. Thus H atoms flow in an environment mostly composed of H_2 molecules [15].

The flow pattern of H atoms in supersonic plasma jets generated from H_2 and from an Ar-H_2 mixture has been recently investigated by studying the H atom density, temperature and velocity development during the expansion process [15, 16, 22]. Here, we focus on the study of the plasma shock region with two main objectives: to examine the evolution of the H atom VDF in this region and to understand the related shock wave characteristics.

8.3 Non-Gaussian VDF within the stationary shock wave

The behavior of the ground-state H atom VDF is examined throughout the normal shock wave of the expanding hydrogen plasma. The system being in stationary state, the VDF only depends on spatial coordinates. The VDF is measured along the jet centerline, namely the velocity distribution is observed parallel to a stream line. Therefore only the axial component of the H atom velocity is determined. The departure from thermodynamic equilibrium is directly reflected in the shape of the velocity distribution function, which markedly deviates from the Gaussian form, i.e. the equilibrium form, within the shock wave, as we will see.

[2] If $F_{\mathbf{v}}$ is isotropic then it can be reconstructed from $f_v(v_z)$.

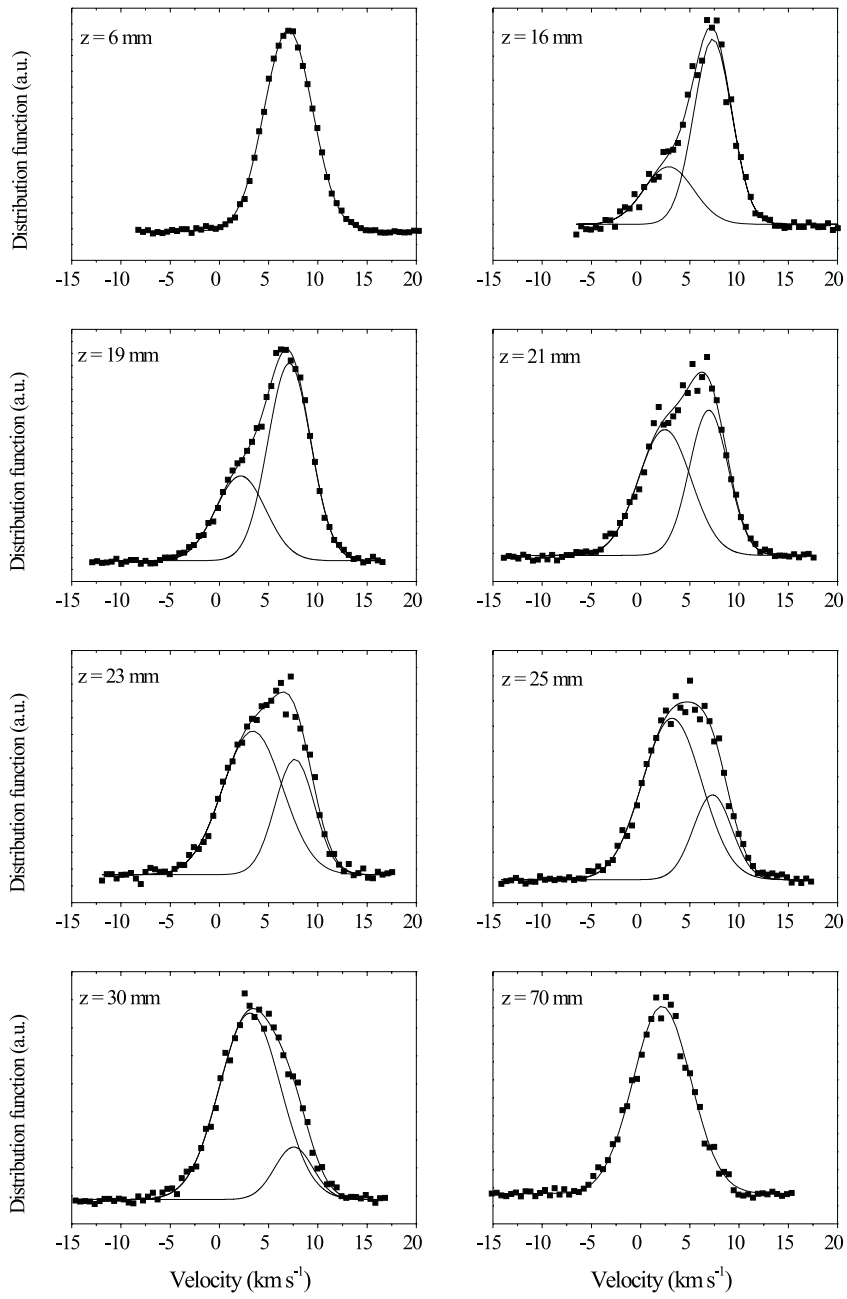

Fig. 8.1: Ground-state hydrogen atom velocity distribution function (VDF) measured at 20 Pa background pressure within the stationary shock wave of an expanding hydrogen plasma. In the shock region (10 to 50 mm), where departure from thermodynamic equilibrium is observed, the VDF consists of the sum of two Gaussian terms corresponding to the conditions upstream and downstream of the zone of silence.

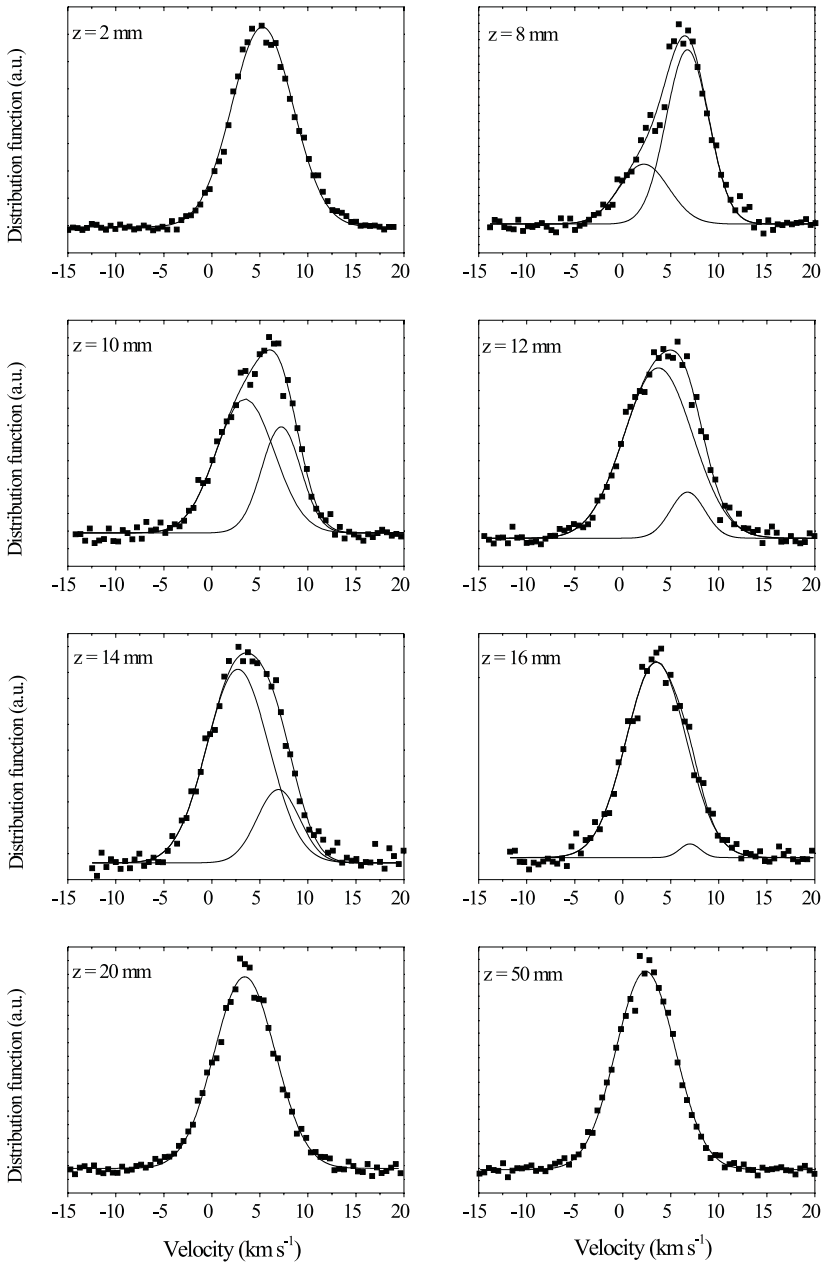

Fig. 8.2: Ground-state hydrogen atom velocity distribution function (VDF) measured at 100 Pa background pressure within the stationary shock wave of an expanding hydrogen plasma. In the shock region (6 to 30 mm), where departure from thermodynamic equilibrium is observed, the VDF consists of the sum of two Gaussian terms corresponding to the conditions upstream and downstream of the zone of silence. It can be seen that all H atoms are thermalized (Gaussian VDF) in front of the shock wave.

Eight H atom velocity distribution functions recorded at different locations in the shock wave region are shown in Fig. 8.1 for a background pressure of 20 Pa. The local VDF is obtained from the measured spectral profile using the Doppler shift relation (see Eq. 8.1) to switch from frequency space to velocity space. At $p_{\mathrm{back}} = 20$ Pa, the normal shock wave stretches from $z = 10$ mm to $z = 50$ mm. The Mach number prior to the shock equals 4. The end of the shock is defined as the position where $M = 1$.

Ahead of and behind the shock wave, the VDF is Gaussian. The corresponding energy distribution function is therefore Maxwellian, meaning that the H atom flow is in thermodynamic equilibrium. Throughout the stationary shock wave, there is a clear departure from thermodynamic equilibrium, since the VDF becomes non-Gaussian, as can be seen in Fig. 8.1. However, the H atom VDF can be decomposed into two Gaussian VDF, i.e. into two equilibrium components, corresponding to the conditions upstream of the zone of silence and in the shock wave. This so-called bimodal approximation of the distribution function is not arbitrary, but it arises directly from the definition of a shock wave which is a transition zone where a supersonic flow has to adapt to the ambient subsonic conditions. It was first proposed about half a century ago by Mott-Smith [13] and Glansdorff [14] in order to be able to solve the Boltzmann transport equation in a gas shock wave. The first component corresponds to the supersonically flowing particles that have not yet experienced any collisions with particles from the shock region: we name it the *fast* component. The second component reassembles particles which have experienced at least one collision and thus have become partly thermalized: we name it the *slow* component.

The bimodal approximation for the H atom VDF across the shock wave is found to be also valid at a background pressure of 100 Pa, as shown in Fig. 8.2. At this pressure the normal shock wave stretches from $z = 6$ mm to $z = 30$ mm, and $M = 3$ prior to the shock. Across the shock wave of the expanding plasma, the H atom population is gradually transferred from one group (the fast component of the VDF) to the other group (the slow component of the VDF) by means of collisions with the background particles, i.e. H_2 molecules under our experimental conditions. This transfer of population, and the subsequent emergence of a bimodal VDF, is clearly visible in Fig. 8.1 and Fig. 8.2. In Fig. 8.3 we plotted the contents of the two Gaussian components as well as the total H atom density across the shock wave for a background pressure of 20 Pa. The emergence of the slow component and the disappearance of the fast component can easily be seen. Note that, due to plasma-wall interactions, the total H atom density does not increase across the shock wave [15, 16, 22]. At the end of the shock wave, all H atoms have changed from an initial supersonic Gaussian VDF to a final subsonic Gaussian VDF and the system returns to equilibrium. Note that all H atoms are thermalized (Gaussian VDF) in front of the shock, i.e. they all have at least undergone one collision before the flow becomes subsonic. The fast component of the VDF contains only particles with a positive axial velocity whereas the slow component contains both particles with a positive and a negative axial velocity, and the dispersion in velocity (given by the width of the Gaussian VDF) is larger. This corresponds to an increase in disorder, i.e. an increase in the entropy of the H atom fluid throughout the shock wave.

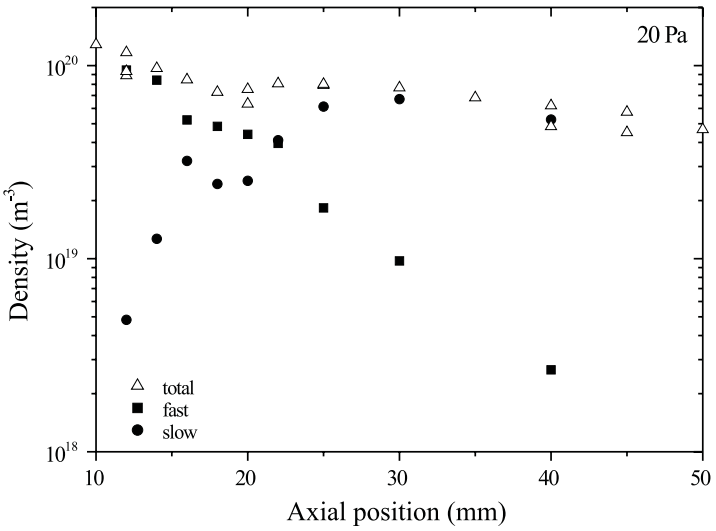

Fig. 8.3: On-axis profile of the total H atom density, i.e. the contents of the VDF, across the stationary shock wave at 20 Pa background pressure (open triangle). The population of the fast component (solid square) decreases to finally vanish whereas the population of the slow component (solid circle) increases. At the end of the shock wave, only remain subsonically flowing H atoms.

The H atom VDF within the shock region is well described by a bimodal approximation, as can be seen from the fit in Fig. 8.1 and Fig. 8.2. No evidence for the existence of a third component, the so-called scattered fraction, is experimentally found, contrary to what is reported in previous studies [2, 11, 12]. In References [11] and [12], one-dimensional VDF measured in He and Ar shock waves are compared with predictions from Monte Carlo Direct Simulation (MCDS) method based on realistic interatomic potential. An excellent agreement is found between experimental data and data calculated using MCDS. In particular, the MCDS method is able to predict the existence of a third group of particles. In other words, in those gas shock wave the Mott-Smith approach fails to represent the distribution function (Mott-Smith and MCDS predictions are compared in Ref. [11]).

In our case, the validity of a bimodal model may arise from the fact that, contrary to the Mott-Smith approach, the slow VDF does not correspond to the conditions dowstream of the zone of silence but it corresponds to the conditions in the shock wave. In other words, as we will see in the next section, the mean velocity and the temperature of the slow Gaussian component vary through the shock region, and therfore this component accounts for mixing effects [11, 12].

The scattered component may also originate from gas particles which penetrate the shock region from the jet boundary and from the Mach disk. This invasion can lead to the appearance of a third fraction since the initial VDF of these particles (as measured along

a stream line) is neither the fast one nor the slow one. Under our experimental conditions, due to wall-association processes H atom are almost absent in the background gas. As a consequence, the shock wave is invaded mainly by H_2 molecules, and no H atom scattered distribution is formed. The appearance of a third fraction in the VDF would in that case merely be visible in the H_2 molecule VDF. Note that this effect should be more pronounced at low background pressure where the invasion of the shock region by the background gas is favored [23, 24].

8.4 Velocity and temperature profiles along the jet axis

From the measured H atom velocity distribution function, a mean axial velocity as well as a parallel temperature, which represents the spread in velocity along a stream line, can be calculated for each Gaussian component. The velocity is determined from the Doppler shift of the peak. The temperature is determined from the Doppler broadening of the peak, which is the dominant broadening mechanism in our case, taking into account the bandwidth of the laser profile which is assumed to be Gaussian.

Throughout the stationary shock wave the average H atom axial velocity is obtained from the first moment of the VDF. In this region the H atom parallel temperature can not be strictly defined since the flowing medium is not in thermodynamic equilibrium. We define an average local parallel temperature $\hat{T}_{\parallel}$ by weighting the temperatures of the two Gaussian components with their corresponding densities

$$\hat{T}_{\parallel} = \frac{n_{\mathrm{fast}} T_{\parallel\,\mathrm{fast}} + n_{\mathrm{slow}} T_{\parallel\,\mathrm{slow}}}{n_{\mathrm{fast}} + n_{\mathrm{slow}}}. \tag{8.3}$$

The subscripts *fast* and *slow* refer to the two components of the distribution function. $\hat{T}_{\parallel}$ can be seen as the temperature which would be given by a hypothetical thermometer plunged into the shock region (ignoring the perpendicular temperature). The H atom velocity profile along the plasma jet centerline is shown in Fig. 8.4 for $p_{\mathrm{back}} = 20$ Pa and for $p_{\mathrm{back}} = 100$ Pa. On both graphs, the measured velocity is compared with the local speed of sound calculated from the measured H atom parallel temperature ($\hat{T}_{\parallel}$ across the shock wave) and using $m = 2$ amu and $\gamma = 1.3$ since the jet is mainly composed of H_2 molecules. The corresponding on-axis development of the H atom parallel temperature is shown in Fig. 8.5 for $p_{\mathrm{back}} = 20$ Pa and for $p_{\mathrm{back}} = 100$ Pa. The general shape of both the velocity and the temperature profile in the course of the plasma expansion has already been explained in preceding articles [15, 16]. In this contribution we only focus on the shock region.

As already mentioned, the *fast* component of the H atom VDF, i.e. the component which corresponds to the conditions upstream of the zone of silence, represents the fraction of hydrogen atoms that have not yet collided with the particles of the shock wave region, namely H_2 molecules. This component thus exhibits the flow properties of a supersonic beam [25]. The mean H atom axial velocity of the fast component remains high. At

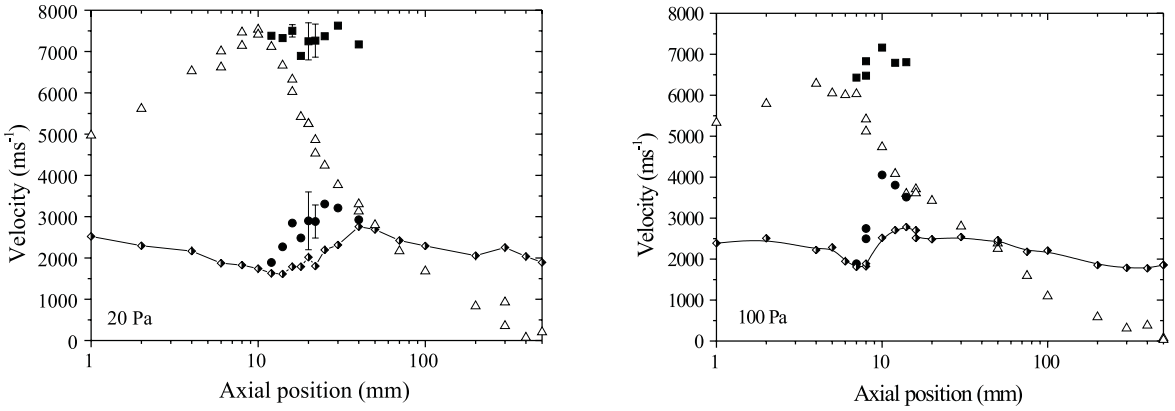

Fig. 8.4: Profile of the H atom axial velocity (open triangle) along the jet centerline measured at 20 Pa (left) and 100 Pa (right). Throughout the shock wave the average H atom velocity is calculated from the first moment of the distribution function. The mean velocity of both the fast (solid square) and the slow (solid circle) component of the VDF are shown in the shock region. Also shown is the axial profile of the speed of sound (diamond) determined from the measured H atom parallel temperature with $m = 2$ and $\gamma = 1.3$.

20 Pa background pressure the velocity is frozen at about 7500 m s^{-1}, whereas at 100 Pa the velocity still increases across the shock wave meaning that H atom can still convert part of the thermal energy they gained in the plasma source into kinetic energy. The corresponding parallel temperature decreases down to 300-200 K, meaning that the spread in velocity decreases. The fast component of the VDF is thus often referred to as the cold component.

The *slow* component of VDF, i.e. the component which corresponds to the conditions in the shock wave, contains H atoms that have experienced at least one collision with the particles located in the stationary shock wave. The mean axial velocity of the slow component is low at the beginning of the shock region, around 2000 m s^{-1}. It increases across the shock wave due to collisions slow H atoms undergo with remaining supersonically flowing particles. The rise of the mean velocity of the VDF slow component is faster at the beginning of the shock region, as can be seen in Fig. 8.4. It arises from the fact that collisions of slow H atoms with fast H_2 molecules (the main collision partner) become quickly scarce because the population of the fast H_2 VDF component drops also fast across the shock wave to finally disappear. The temperature of the slow component is relatively high. It increases because kinetic energy is converted into thermal motion in a collision involving a fast H atom. In other words, directed motion is transformed into random motion within a shock wave. The slow component of the VDF is also often called the warm component.

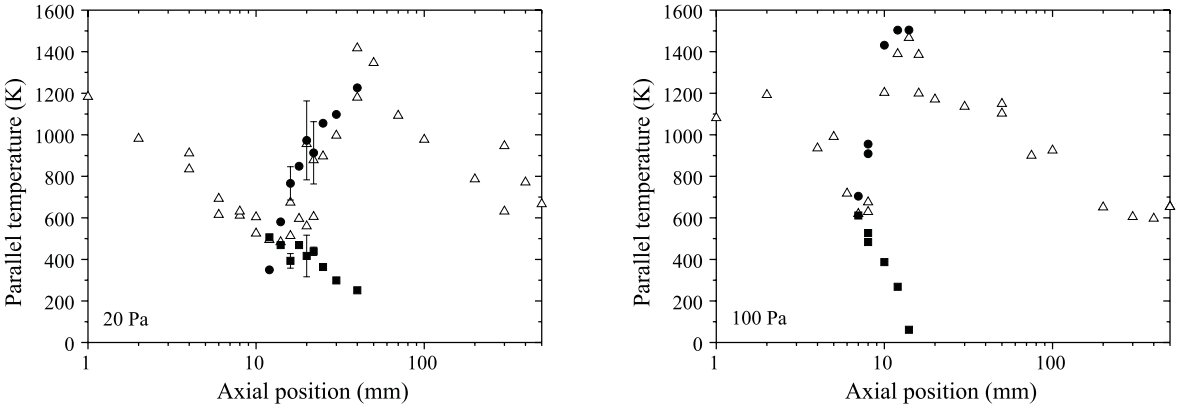

Fig. 8.5: Axial profile of the H atom parallel temperature (open triangle) at 20 Pa (left) and at 100 Pa (right). Throughout the shock wave an average temperature is determined from the temperature of the two Gaussian components of the distribution function (see Eq. 8.3). The temperature of both the fast (solid square) and the slow (solid circle) component of the VDF are also shown in the shock region.

8.5 Theoretical velocity profile in the shock region: Mott-Smith approach

The H atom average velocity measured throughout the stationary shock wave along the plasma jet centerline can be compared with a theoretical model based on a bimodal approximation of the velocity distribution function. Under the assumption that the VDF is the sum of a cold and a warm component, the density profile as well as the corresponding velocity profile of the flowing fluid can be calculated as shown by Mott-Smith [13] and Glansdorff [14]. The centerline velocity is given by

$$w(\tilde{z}) = \frac{w_2(1 + e^{4\tilde{z}/L})}{(w_2/w_1) + e^{4\tilde{z}/L}}, \tag{8.4}$$

where $\tilde{z} = z - z_0$, z_0 being the center of the shock wave (point of inflection), w_1 and w_2 are the velocity ahead of and behind the shock respectively, and L is the shock thickness defined as

$$L = (w_1 - w_2) \left.\frac{dz}{dw}\right|_{\max}, \tag{8.5}$$

according to the Prandtl formalism [26]. We found that L= 16.8 mm and 9.7 mm at 20 Pa and 100 Pa respectively. At 100 Pa, $L_{\mathrm{Hydro}} = 2$ mm (see Eq. 2.28), $L_{\mathrm{MS}} = 5$ mm [13], and $L_{\mathrm{Two-Fluids}} \approx 6$ mm [14]. In both cases L is underestimated, however, in comparison with a hydrodynamic calculation, models based on the solution of the Boltzmann equation provide a value closer to the real one. The velocity can also be expressed as a function

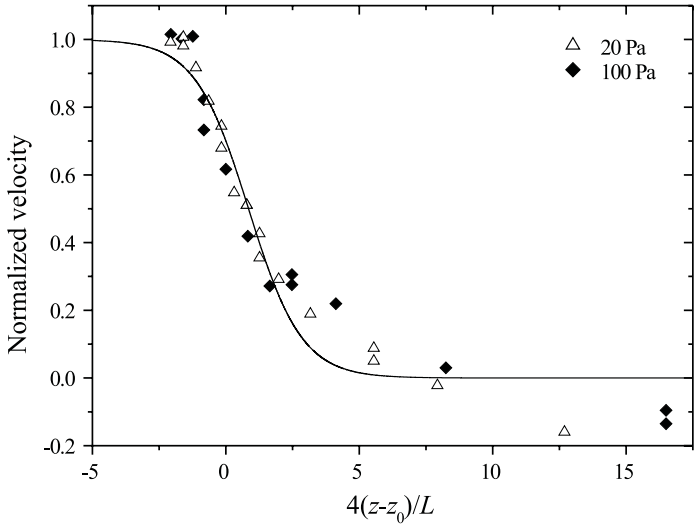

Fig. 8.6: Normalized H atom velocity (see Eq. 8.6) profile within the stationary shock wave of an expanding hydrogen plasma at 20 Pa (open triangle) and at 100 Pa (solid diamond) background pressure. The parameter z_0 corresponds to the center of the shock wave and L is the shock thickness. The solid line represents the calculated normalized velocity profile under the assumption of a bimodal distribution function based on the theory developed by Mott-Smith [13] and Glansdorff [14].

of the Mach number M ahead of the shock front and the adiabatic exponent γ using the Rankine-Hugoniot relations. In order to make the results independent of the conditions, one can define a normalized velocity in the following way

$$\tilde{w}(\tilde{z}) = \frac{w(\tilde{z}) - w_2}{w_1 - w_2}. \tag{8.6}$$

When the measured (normalized) velocity is to be compared with the theoretical (normalized) velocity given by Eq. 8.4 (Eq. 8.6) a scaling length S needs to be introduced to take into account the shift in position between the inflection point of the density curve and the velocity curve. The parameter S is given by

$$S = \frac{L}{4} \ln \frac{w_2}{w_1}. \tag{8.7}$$

The comparison between experiments and calculations is shown in Fig. 8.6. As can be seen from the graph, the agreement is relatively good at the beginning of the shock wave even if the normalized velocity profile measured at 100 Pa deviates slightly from the predictions. However, in the final part of the shock region, a significant deviation is observed. This

effect has already been reported in literature in the case of on-axis density profiles measured in neutral gas shock waves [2, 6, 7]. It arises from the fact that the model developed by Mott-Smith is a one-dimensional (1D) normal shock wave model which does not account for scattering effects. Such effects, related to the invasion of the supersonic jet by the background gas, occurs for a 2D shock wave when the flow enters the rarefied regime [23], i.e. when the Knudsen number Kn is large. It has indeed been observed that at high background pressure the agreement between experimental data and the Mott-Smith model is good and it deteriorates at low pressure. The Knudsen number ahead of a shock wave is the ratio of the mean free path for momentum exchange to the shock thickness. It reads

$$Kn = \frac{1}{n_{H_2}\sigma_{H-H_2}L}. \tag{8.8}$$

The temperature dependent momentum exchange cross-section σ_{H-H_2} is taken from literature [27] and the H_2 density has been measured by means of CARS [28]. Under our conditions, $Kn = 0.7$ at 20 Pa and $Kn = 0.2$ at 100 Pa ahead of the shock wave meaning that the latter is formed in a transition flow regime. Surprisingly, the H atom velocity profile measured at $p_{\text{back}} = 20$ Pa and the one measured at $p_{\text{back}} = 100$ Pa exhibit a similar behavior in the final part of the shock wave, as can be seen in Fig. 8.6, in contradiction with measurements reported in literature. The two normalized velocity profiles deviate in approximately the same way from the theoretical calculation. In other words there is no clear influence of the background pressure. This remarkable fact is a consequence of the non-conservation of both the H atom forward flux and the H atom momentum throughout the stationary shock wave of the plasma jet [15, 16, 22]. In that case the Mott-Smith approach used to calculate the average velocity is not valid since it is based on the Rankine-Hugoniot relations. A theoretical calculation of the H atom velocity profile within the normal shock wave would therefore require a 2D model capable of accounting for a decoupling between the H atom fluid and the H_2 molecule fluid induced by H atom surface-recombination processes.

8.6 Conclusions

The specific ground-state hydrogen atom shock wave pattern formed in a weakly ionized hydrogen plasma jet can serve as a test case to validate predictions of kinetic models based on the Boltzmann equation used to study the behavior of the velocity distribution function and the fluid macroscopic properties within a shock wave. The two-photon absorption laser induced fluorescence spectroscopy is well adapted to extract local information about ground-state atoms at a microscopic scale, both in a gas and in a plasma environment. Using this diagnostic tool one can provide large datasets to support theoretical studies devoted to the shock wave properties. Such data are also of relevance in order to better understand the shock wave formation at low background pressure, i.e. in a rarefied flow regime, and the related invasion of the shock region by the residual gas particles, which is of interest in various fields like astrophysics and plasma-assisted chemistry.

Acknowledgments

The authors would like to acknowledge fruitful discussion with Prof. M.C.M. van de Sanden. The authors greatly appreciate the skillful technical assistance of M.J.F. van de Sande, A.B.M. Hüsken, and H.M.M. de Jong. This work is part of the research program of the Netherlands Foundation for Fundamental Research on Matter (FOM). It is financially supported by the Netherlands Organization for Scientific Research (NWO) as well as the Euratom foundation.

References

[1] Y.B. Zel'dovich and Y.P Raizer, *Physics of Shock Waves and High Temperature Hydrodynamic Phenomena*, Academic Press, New York, Vol. 1-2 (1966).

[2] A. Ramos, B. Maté, G. Tejeda, J.M. Fernández, and S. Montero, *Phys. Rev. E* **62**, 4940 (2000).

[3] F.J. Uribe, R.M. Velasco, L.S. García-Colín, and E. Díaz-Herrera, *Phys. Rev. E* **62**, 6648 (2000).

[4] S. Takata, K. Aoki, and C. Cergignani, *Phys. Fluids* **12**, 2116 (2000).

[5] C. Cercignani, A. Frezzotti, and P. Grosfils, *Phys. Fluids* **11**, 2757 (1999).

[6] H. Alsmeyer, *J. Fluid. Mech.* **74**, 497 (1976).

[7] F. Robben and L. Talbot, *Phys. Fluids* **9**, 653 (1966).

[8] J. Panda and R.G. Seasholtz, *Phys. Fluids* **11**, 3761 (1999).

[9] P.L. Eggins and D.A. Jackson, *J. Phys. D: Appl. Phys* **7**, 1894 (1974).

[10] M.C.M. van de Sanden, R. van den Bercken, and D.C. Schram, *Plasma Sources Sci. Technol.* **3**, 511 (1994).

[11] G. Pham-Van-Diep, D.A. Erwin, and E.P. Muntz, *Science* **245**, 624 (1989).

[12] D.A. Erwin, G. Pham-Van-Diep, and E.P. Muntz, *Phys. Fluids* **3**, 697 (1991).

[13] H.M. Mott-Smith, *Phys. Rev.* **82**, 885 (1951).

[14] P. Glansdorff, *Phys. Fluids* **5**, 371 (1962).

[15] S. Mazouffre, P.J.W. Vankan, R. Engeln, and D.C. Schram, accepted for publication in *Phys. Plasmas*.

[16] S. Mazouffre, M.G.H. Boogaarts, J.A.M. van der Mullen, and D.C. Schram, *Phys. Rev. Lett* **84**, 2622 (2000).

[17] U. Czarnetzki, K. Miyazaki, T. Kajiwara, K. Muraoka, M. Maeda, and H.F. Döbele, *J. Opt. Soc. Am. B.* **11**, 2155 (1994).

[18] H.W.P. van der Heijden, M.G.H. Boogaarts, S. Mazouffre, J.A.M. van der Mullen, and D.C. Schram, *Phys. Rev. E* **61**, 4402 (2000).

[19] S. Mazouffre, M.G.H. Boogaarts, R. Engeln, J.A.M. van der Mullen, and D.C. Schram, *Proceedings of Laser-Aided Plasma Diagnostics* **9**, California, U.S.A., 320 (1999).

[20] R. Resnick, *Introduction to Special Relativity*, John-Wiley & Sons, New York (1968).

[21] G.M.W. Kroesen, D.C. Schram, and J.C.M. de Haas, *Plasma Chem. Plasma Process.* **10**, 551 (1990).

[22] S. Mazouffre, R. Engeln, M.G.H. Boogaarts, J.A.M. van der Mullen, and D.C. Schram, *Proceedings of Thermal Plasma Processing* **6**, Strasbourg, France (2000).

[23] E.P. Muntz, B.B. Hamel, and B.L. Maguire, *AIAA J.* **8**, 1651 (1970).

[24] R. Campargue, *J. Chem. Phys* **52**, 1795 (1970).

[25] *Atomic and Molecular Beam Methods*, edited by G. Scoles, Oxford University, New York (1988).

[26] C. Muckenfuss, *Phys. Fluids* **3**, 320 (1960).

[27] A. Phelps, *J. Phys. Chem. Ref. Data* **19**, 653 (1996).

[28] R.F.G. Meulenbroeks, R.A.H. Engeln, J.A.M. van der Mullen, and D.C. Schram, *Phys. Rev. E* **53**, 5207 (1996).

Chapter 9

General Conclusion

Since all sections of this manuscript, which can be regarded as individual stories, have their own conclusion, we will attempt in this general conclusion to give an overview of the main outcomes of the last four years of fundamental research on expanding plasmas. This chapter should therefore be seen as the counterpart of section 1.5 where the main objectives of this work are presented in the form of a series of questions. The actual view on the transport phenomena in intermediate scale plasma expansions will be presented and discussed in the light of our findings. In doing so, we will also point to experimental facts that still remain unclear or unexplained, and we will also present new problems that emerged from that work. In order to open the way in the near future to experiments which, as we hope, will contribute to confirm our present view.

Inert neutrals: validity of the gas expansion picture

The Rayleigh scattering measurements of the Ar and H_2 density profile along the jet axis in respectively Ar-H_2 and pure H_2 expanding plasmas confirm the idea that the expansion of inert neutrals can be described as a normal gas expansion [1,2]. The data also show that the inert particle properties such as the density, the velocity and the temperature can be well approximated using an hydrodynamic approach even in a rarefied flow regime. In the supersonic domain the set of simplified equations governing a steady isentropic flow can be used. Across the normal shock front the observed different compression stages are predicted by models based on the Navier-Stokes equation. Laser induced fluorescence measurements reveal that the supersonic plasma expansion is however not adiabatic, i.e. the adiabatic exponent γ is less than the expected value (1.3-1.4 instead of $\frac{5}{3}$ for an atomic gas). It is well established that the presence of charged particles leads to a low γ [3]. However, with H_2 seeding, the ionization degree of the plasma is relatively low, and the explanation must be found elsewhere. The low value of γ may be caused by the relatively high heat conductivity at the higher plasma temperature. As a consequence energy can be supplied from the source and the downstream part of the zone of silence into the supersonic domain.

Atomic radicals: influence of surface chemistry

Contrary to neutrals, hydrogen radicals exhibit a deviation from the classical expansion picture. As shown in this thesis, the transport properties of H atoms are very peculiar. For instance, there is no density jump across the shock front whereas the axial velocity drops, that corresponds to a non conservation of the H atom forward flux. Another remarkable property is that in the core of the jet the H atom fluid is decoupled from the main gas fluid, and the decoupling is already apparent at the plasma source exit. This is imaged for instance in the fact that in an Ar-H_2 plasma the H atom velocity is higher than the Ar atom velocity (see, for example, chapter 6). This anomalous transport of hydrogen radicals is a direct consequence of the interaction between the plasma and adjacent surfaces. It is clearly demonstrated that under certain circumstances, that are discussed below, surface chemistry can strongly influence the plasma flow properties by way of recombination processes.

The recombination of H atoms at the vessel walls to form molecular hydrogen is an efficient process under our conditions. A large surface is available, the loss (or recombination) probability Γ on stainless steel is high for H ($\Gamma_{ss} \approx 0.2$) and the residence time inside the vacuum chamber is long ($\tau_{\rm res} \approx 1$ s). This favorable combination of experimental conditions results in the creation of a large density gradient for H atoms between the jet and its surrounding (indeed H atom are almost absent in the background). In turn those gradients force H atoms to diffuse out of the plasma jet, even in the supersonic domain, and subsequently they are decoupled from the inert neutral fluid. The outward diffusion of H atoms makes possible an energy exchange between the interior of the jet and the outside, that explains the low value of γ. Moreover, it is shown that even if the mass of the radical is close to or identical to the mass of the carrier gas (H in H_2 and D in H_2 experiments), the losses of radicals can not be avoided. As a consequence only a small fraction of the H radicals produced in the source is available in the downstream region, creating a net loss of chemical potential.
One can wonder whether the anomalous radical transport is a very general phenomenon, or if it mainly concerns H atom in view of its small mass. In an unmagnetized plasma jet, we demonstrated that the outward losses solely depend on the thermal velocity, on Γ, on $\tau_{\rm res}$, and on the momentum exchange cross-section. At the present moment, we have even more experimental evidences that support the idea of a general process. Some TALIF experiments have been performed on N_2 and Ar-N_2 plasma jets [4]. It is found that N atoms are better confined inside the jet (in comparison with H at identical pressure); nevertheless losses of N radicals are present [4]. Previous observations originate from a low Γ for N atoms [5] ($\Gamma_{\rm ss} \approx 0.001$) combined with a relatively low thermal speed.

Source strength and confinement

A point of concern is also the relatively low dissociation degree measured at the source exit: about 2 % and 7 % for a H_2 and Ar-H_2 plasma respectively (when calculated on axis). Indeed a high dissociation degree is expected in the arc channel in the case of hydrogen at a 1 eV electron temperature. This striking fact was already envisaged from earlier CARS and depolarization Rayleigh scattering experiments [6], however such a low fraction of H atoms was not expected. As we will see, the poor plasma source strength can be explained when involving plasma surface interactions. Once again, this is especially of interest for H atoms, because the loss probability on a Cu surface (the material the arc nozzle is made of) is close to unity. As described in chapter 7, since the arc root attached at the nozzle entrance, only a small amount of energy is supplied in the nozzle, and recombination mechanisms are favored. The H atoms are therefore also lost in the source nozzle via

$$\mathrm{H} + \mathrm{H}_{\rm wall} \rightarrow \mathrm{H}_2^{v,J}. \qquad (1)$$

The association of H atoms on metallic surfaces is known to generate vibrationally excited H_2 molecules [7]. Yet no significant amount of vibrationally excited H_2 molecules has been detected by CARS, neither in the jet nor in the background [6]. This is not in contradiction with aforementioned explanation; excited H_2 molecules can be deactivated

through collisions with particles (high density in the arc) and with the wall as well (very efficient process). They can also be involved in other reactions (see below). The situation needs further clarification, especially due to the fact that CARS measurements could not be performed at the arc outlet. In the case of a pure hydrogen plasma, the measured low fraction of H atom may be linked with the observed loss of ionization, i.e. the absence of visible radiation, through the reactions

$$H_2^{v,J} + H^+ \rightarrow H_2^+ + H \quad \text{and} \quad H_2^+ + e \rightarrow H^* + H. \tag{2}$$

Subsequently the excited H atom emits light before leaving the arc. This process can also explain the presence of negative ions, formed by dissociative attachment of electrons on $H_2^{v,J}$ molecules, observed directly at high background pressure.
In the light of our observations we can propose a solution to increase the source strength and to improve the radical confinement inside the plasma jet, in order to obtain a high radical density in the downstream region. As regards the source, a good solution is to supply energy in the nozzle by driving the current outside the arc by means of an external anode. Another possibility is to vary the nozzle geometry in such way that H atoms only "see" a small surface (see appendix of chapter 6) and to play with the nozzle material (the requirements are a low Γ and a high thermal conductivity). To confine the H radicals one may use a magnetic field! The external anode configuration can certainly provide a relatively high amount of ions; using an applied axial magnetic field B such as the Hall parameter $H_e >> 1$, the electrons are magnetically confined. Because of charge neutrality restraint, the ions get also confined, and it may become more difficult for H atoms to leave the rotating plasma jet. The confinement may be enhanced because of the efficient charge exchange process between a proton and H: $k \approx 10^{-14}$ m^3 s^{-1} at 1 eV [8]. Such a confinement method is however not easy to achieve. Indeed, a strong magnetic field is required to magnetize the high electron(ion) density necessary to confine H by momentum exchange: $B \approx 1$ T for $n_e = 10^{21}$ m^{-3}.

Charged particles as transient species

To a large extent, charged particles dominate the chemistry in a plasma environment. Charge exchange between an ion and a molecule may be an important step in the formation of a new molecule or a radical. For instance, the reaction

$$Ar^+ + H_2 \rightarrow ArH^+ + H \tag{3}$$

is exothermic for ground-state H_2 by nature. Dissociative recombination of molecular ions is also an important process in chemistry (extremely fast reaction). Atoms and molecules can also be excited, ionized or even dissociated by electron impact. The transport of charged particles therefore deserves some attention. In retrospect, they can be considered as transient species in the sense that they are also efficiently consumed at walls. Plasma-surface interactions may accordingly influence the transport of ions in a (unmagnetized) plasma jet. Ions recombine at conducting surfaces to form neutrals; as a consequence

density gradients between the jet and its surrounding are created. The transport of ions is however more complex than the transport of neutral radicals. It is affected by electric fields and friction with electrons. Note that these two influences can be replaced by ∇p_e in the electron momentum balance. It also depends on the Debye length[1] and on the charge exchange processes. Departure from the classical expansion behavior may be expected especially in the case where the Debye length is large (low ionization degree) and where the charge exchange process is non resonant.

Departure from TE within a shock wave

Another interesting characteristic of a plasma expansion is the departure from thermodynamic equilibrium (TE) within the stationary compression shock wave. The local velocity distribution function (VDF) of H and Ar atoms is measured by Doppler-shifted LIF. All VDF exhibit significant deviation from the Gaussian form, i.e. the equilibrium profile, both in the barrel shock wave and in the normal shock front. Such a behavior is however expected since a shock wave is a transition zone through which a supersonic flow has to adapt the local subsonic conditions. To work in a rarefied flow regime makes it easier to observe. The VDF can be well approximated by two Gaussian components, i.e. a bimodal approximation is valid. One component (fast and cold component) corresponds to the zone of silence conditions, i.e. it reassembles particles of the jet that have not yet collided with particles standing in the shock region. The other component (slow and warm component) corresponds to the conditions in the shock region, i.e. it represents particles that have already experienced at least one collision. Across a shock wave, population is gradually transferred from the fast to the slow component and the macroscopic properties of the two Gaussian components vary.
No third component, the so-called scattered component, has been observed [9]. The explanation lies mainly in the fact that our bimodal approximation differs from the Mott-Smith (MS) model [10]. In the MS approach, the fast component corresponds to the conditions upstream of the normal shock wave and the slow component corresponds to the downstream conditions. In other words, in the MS model, the properties of the two Gaussian components are linked to the supersonic and subsonic conditions. Only the content of the two distributions vary through the shock wave. The existence of a third component with intermediate properties then results from a blending between the supersonic and the subsonic distributions.

Mixing with the background gas and recirculation pattern

The departure from TE results from collisions between particles of the jet and particles of the background. In other words, a shock wave is formed due to the invasion of the supersonic domain by the background gas. A question that still remains concerns the formation

[1] The Debye length is the distance over which spontaneous charge separation takes place owing to thermal motion. Thus it defines the average distance over which an electric field may exist in the plasma.

of the shock wave at low pressure: is the shock created by invasion from the Mach disk region (case in hydrodynamic regime) or is the invasion from the side also important or even dominant? As shown in the appendices, the invasion and the mixing with background gas does exist. The Ar atom VDF measured in the barrel shock of an Ar-H_2 plasma reveals that Ar atoms re-enter the jet. Seeding D_2 molecules in the background while burning a H_2 plasma, D atoms are found in the supersonic domain. The invasion process depends of course on the pressure, i.e. on the ratio of mean free path and shock dimension.
Mixing effects in the shock wave are very important for chemistry. In the supersonic zone, a high flux is available, combined with a high particle kinetic energy ($E_c \approx 2$ eV for Ar). Therefore the remaining question is the magnitude of the radial inward flux. At this moment it is still difficult to precisely quantify the invasion but some experiments could clarify the situation. For example, one can look at the invasion of an argon jet by Kr atoms using TALIF. Probing molecules by LIF in H_2-D_2 mixtures is also an interesting possibility (see [10] and appendix 2). The latter can also be used to establish at which location atoms are produced via

$$H(D) + D_2(H_2) \rightarrow HD + D(H). \quad (4)$$

Mixing between the plasma jet and the background gas is closely linked with the recirculation pattern which arises from the long residence time in the vessel: vortices in which particles are "trapped" are formed around the jet [11,12]. Recirculation plays an important role in transport phenomena. It offers several opportunities for particles present in the background (injected, created at the wall, or coming from the jet) to interact with the plasma jet.

Towards plasma-surface interaction study

As pointed out in this work the interactions between plasma and surface have a large impact on both the transport properties and the source features with consequences on the chemistry. It thus appears to be of prime interest to study in more details those processes in the near future. To end this general conclusion, we here propose a series of investigations which would help in the understanding of plasma chemistry as a whole.
The study of the loss probability Γ as a function of the temperature is especially of interest since $T_{wall} \neq T_{source} \neq T_{substrate}$. Another important issue is the variation of Γ with the flux impinging onto the surface. The determination of the reaction product, including the state and the energy distribution, is important from a fundamental point of view to learn about the dynamics of recombination mechanisms in realistic conditions (so far experiments in UHV condition and well defined clean surfaces). For instance the vibrational distribution, in the electronic ground-state, of O_2 and H_2 molecules generated at a wall can be probed by means of LIF. It goes without saying that excited molecules play an important role in chemistry. Undoubtedly, the subject of formation of molecules on surfaces (CO, NH_3, H_2O to name a few) is very promising. On a fundamental perspective of course (e.g. production of molecules in interstellar medium), but also to investigate the possibility of using a surface as a catalyst to favor the production of a desired molecule.

References

[1] M.C.M. van de Sanden, R. van den Bercken, and D.C Schram, *Plasma Sources Sci. Technol.* **3**, 501 (1994).

[2] R.F.G. Meulenbroeks, R.A.H. Engeln, M.N.A. Beurskens, R.M.J. Paffen, M.C.M. van de Sanden, J.A.M. van der Mullen, and D.C. Schram, *Plasma Sources Sci. Technol.* **4**, 74 (1995).

[3] K.T.A.L. Burm, W.J. Goedheer, and D.C. Schram, *Phys. Plasmas* **6**, 2622 (1999).

[4] I. Bakker, *Properties of an Expanding Thermal Nitrogen Plasma*, internal report VDF/NT 01-06, Eindhoven University of Technology, The Netherlands (2001).

[5] S.F. Adams and T.A. Miller, *Plasma Sources Sci. Technol.* **9**, 248 (2000); H. Singh, J.W. Coburn, and D. Graves, *J. Appl. Phys.* **88**, 3748 (2000).

[6] R.F.G. Meulenbroeks, R.A.H. Engeln, J.A.M. van der Mullen, and D.C. Schram, *Phys. Rev. E* **53**, 5207 (1996).

[7] R.I. Hall, I. Cadez, M. Landau, F. Pichou, and C. Schermann, *Phys. Rev. Lett.* **60**, 337 (1988); C.T. Rettnwe and D.J. Auerbach, *J. Chem. Phys.* **104**, 2732 (1996).

[8] R.K. Janev, W.D. Langer, K. Evans,Jr., and D.E. Post,Jr, *Elementary Processes in Hydrogen-Helium Plasmas*, Springer-Verlag, Berlin (1987).

[9] A. Ramos, B. Maté, G. Tejeda, J.M. Fernández, and S. Montero, *Phys. Rev. E* **62**, 4940 (2000).

[10] S. Mazouffre, P. Vankan, I. Bakker, R. Engeln, and D.C. Schram, *Proceedings of Laser-Aided Plasma Diagnostics* **10**, Fukuoka, Japan (2001).

[11] R.F.G. Meulenbroeks, D.C. Schram, M.C.M. van de Sande, and J.A.M. van der Mullen, *Phys. Rev. Lett.* **76**, 1840 (1996).

[12] W.M.M. Kessels, A. Leroux, M.G.H. Boogaarts, J.P.M. Hoefnagels, M.C.M. van de Sanden, and D.C. Schram, *J. Vac. Sci. Technol. A* **19**, 467 (2001).

Appendix A

Invasion of a supersonic jet by the background gas particles

The rarefaction process of a free jet flow and the subsequent invasion of the zone of silence by the background gas particles is a well-known problem. It has been already studied in the late sixties and in the early seventies, both theoretically [1, 2] and experimentally by mass spectrometric measurements [3]. It has been shown that the invasion is mass dependent in favor of the light species, and that this effect can be used for the separation of mixtures of gases and isotopes [3, 4]. On a technological point of view, it may have other interesting applications especially in the field of plasma assisted chemistry. Supersonic plasma jets are used for instance for the fast deposition of thin layers. In that case, an efficient mixing between the precursor gas injected at the jet periphery and the plasma jet particles is of crucial importance. Collisions in the shock region with supersonically flowing particles ($E \approx 4$ eV for Ar in a cascaded arc plasma) may enhance the reactions and thus speed up the deposition process. On a fundamental point of view, the invasion effect concerns the formation of a shock wave at low background pressure. Its influence on the velocity distribution function (VDF), and the related appearance of a scattered component, is also of particular interest.

In all studies, the zone of silence, or the stationary shock wave depending on Kn, is invaded by a species only present in the ambient gas surrounding the jet and not already in the jet. That naturally facilitates experiments like flux measurements since it is easy to distinguish between the different fluid components. The measurements performed in an expanding argon plasma jet (see chapter 3) on the Ar atom VDF by Doppler-shifted laser induced fluorescence reveal that in the rarefied regime Ar atoms from the ambient gas cross the barrel shock wave and penetrate the shock region.

In Fig. A.1 the Ar atom radial VDF (determined in a direction perpendicular to the jet axis) measured at $z = 50$ mm, i.e. in the shock region, is shown for $r = 0$ mm (on the jet centerline) and for $r = 22$ mm (in the barrel shock wave). In the two cases a strong deviation from thermodynamic equilibrium (TE) is observed. The VDF can nevertheless be decomposed into two Gaussian components, a high perpendicular temperature one, the *warm* component, and a low perpendicular temperature one, the *cold* component.

On the jet centerline, the cold component reassembles Ar atoms from the jet that have not

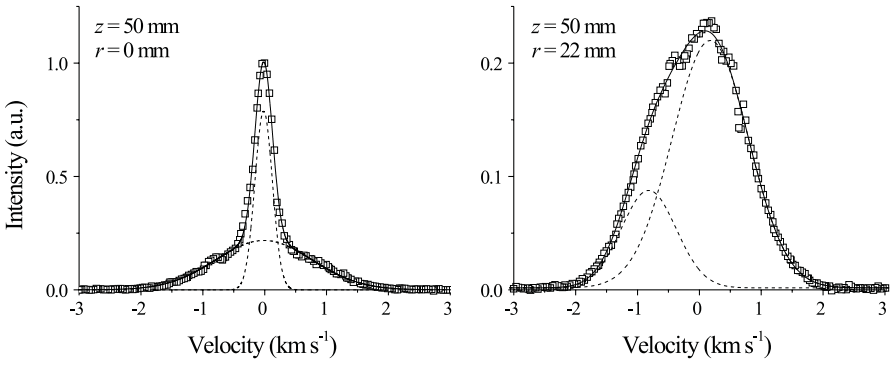

Fig. A.1: Radial Ar VDF recorded at 20 Pa at $z = 50$ mm and at $r = 0$ mm (left) and $r = 22$ mm (right). Also shown is the result of a fit using a bimodal approximation as well as the two individual Gaussian components.

yet experience any collisions with the particles located in the shock wave. The temperature of that group is low due to the quasi-adiabatic cooling process during the supersonic expansion phase. The warm component corresponds to Ar atoms that originate from the plasma jet vicinity. Those atoms collide in the barrel shock wave with Ar atoms from the jet. The resulting energy exchange leads to an increase in the radial velocity spread and therefore to a rise in temperature. On the jet axis the average radial velocity is zero for both component as expected in view of the cylindrical symmetry of the expansion. Such a non-Gaussian Ar velocity profile, constituted of two equilibrium components of which both the origin and the properties can be perfectly defined, is a proof in favor of the invasion of the stationary shock wave by Ar atoms from the background gas. Indeed at 20 Pa the mean free path ahead of the shock front is in the order of the jet radius, the shock structure is diffuse and therefore the probability that particles enter the jet is relatively high.

In the barrel shock wave, the two velocity groups exhibit an opposite mean velocity. The velocity of the cold component is positive (for $r < 0$), i.e. the flow of Ar atom belonging to that group is directed outward, whereas the mean velocity of the warm component is negative, i.e. the Ar atoms move towards the jet core. The temperature of the jet particles increases, in comparison with the situation $r = 0$ mm, because of multiple collisions.

In Fig. A.2 the mean velocity as well as the temperature of the two Gaussian components of the Ar atom radial VDF are shown as a function of the radial position at $z = 50$ mm and at 20 Pa background pressure. For the cold component the maximum radial velocity is reached at $z = 20$ mm which defines the beginning of the barrel shock wave ($M = 1.7$ at that location). Behind this limit the velocity decreases and the temperature increases as a consequence of collisions with the background gas. The barrel shock ends around $z = 40$ mm ($M = 1$). Ar atoms situated in the surroundings of the jet enter the latter with a radial velocity of about 250 m s^{-1}. The temperature of this Ar atom group starts to change significantly solely for $r < 20$ mm, i.e. inside the jet, due to the numerous collisions,

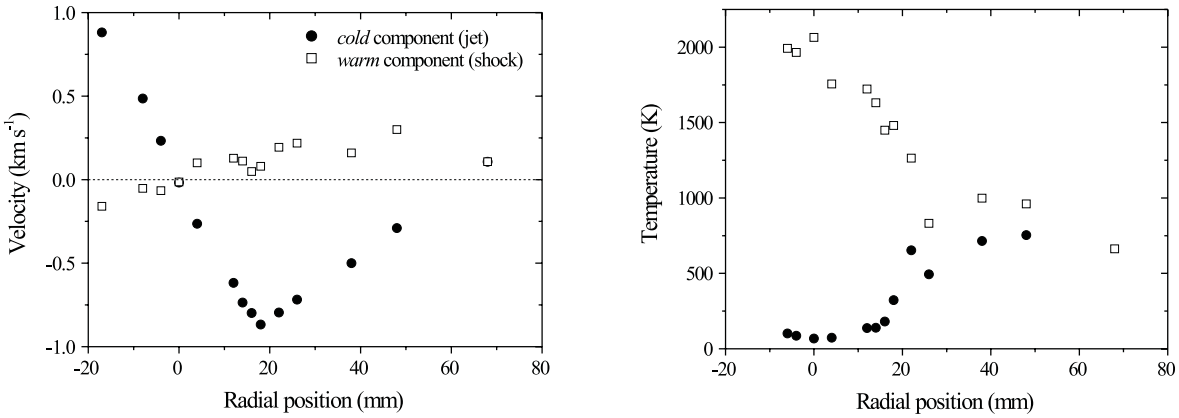

Fig. A.2: Ar radial VDF Gaussian component mean velocity (left) and temperature (right) as a function of the distance form the jet axis measured at $z = 50$ mm and 20 Pa.

and the maximum is reached at the jet center.
When moving towards the jet axis, the contents of the VDF decreases as can be seen in Fig. A.1, that means only a small fraction of the particles located in the jet vicinity can reach the interior of the jet. This effect is naturally pressure dependent: for instance it is observed that at 100 Pa hardly any particles from the outside reach the jet centerline in the shock wave region.
We demonstrated that the invasion of the supersonic domain of an expanding jet always exists at low pressure. This means that it does not only concern a category of particles different from the one that composes the flow [5]. Unfortunately the ground-state Ar flow[1] entering the shock wave from the side can not be determined from our data set since we are probing metastable Ar atoms. Neither can be at the moment the Ar flux that originates from the downstream region of the shock wave. Such information would be valuable to study the formation of a shock wave at low pressure, therefore we may have to consider in the near future the local detection of Ar atoms.

[1] J.B. Fenn and J.B. Anderson, *Proceedings Rarefied Gas Dynamics* **2**, edited by J.H. de Leeuw, Academic Press, New York (1966).
[2] E.P. Muntz, B.B. Hamel, and B.L. Maguire, *AIAA J.* **8**, 1651 (1970).
[3] R. Campargue, *J. Chem. Phys.* **52**, 1795 (1970).
[4] J.W. Brook and V.S. Calia, *J. Energy* **4**, 199 (1980) and refences herein.
[5] see also S. Mazouffre, M.G.H. Boogaarts, J.A.M. van der Mullen, and D.C. Schram, in *Heat and Mass Transfer under Plasma Conditions*, edited by P. Fauchais, J. van der Mullen, J. Heberlein, ANYAS, Vol. **891**, 348 (1999), for the invasion of a supersonic Ar jet by H and H_2.

[1] The ambient gas is mainly composed of ground-state Ar atoms, $n_{Ar}/n_{Ar*} \approx 10^4$ in the supersonic jet vicinity at 20 Pa, and therefore the shock wave is mostly formed by collision with those atoms

Appendix B

Recirculation and downstream chemistry

Due to the large residence time inside the vacuum chamber ($\tau_{\text{res}} \approx 1$ s at 20 Pa) recirculation cells are formed around the plasma jet [1]. The created flow pattern allows for background particles to mix and react with the jet particles, mainly at the boundary of the supersonic domain and in the subsonic flow zone when $Kn < 0.2$. This recycling process is believed to play an important role in the plasma chemistry and kinetics downstream of the shock wave, e.g. in the formation of stable molecules or molecular fragments. In order to obtain a better insight on the recirculation process, D_2 is injected in the vessel while creating a hydrogen plasma in an arc, and one of the reaction products, D atoms in that case, is locally probed. This work is an extension of the work by Meulenbroeks *et al* in which HD molecules density and temperature are measured by CARS when burning the arc on a H_2-D_2 mixture [2]. The settings are: 0.4 slm D_2, 3.5 slm H_2, standard arc conditions. Deuterium atoms are produced mainly via the following reaction [2]

$$H + D_2 \rightarrow HD + D \qquad k = 3 \times 10^{-19}\ \text{m}^3\,\text{s}^{-1}. \tag{B.1}$$

The local D density is measured by TALIF spectroscopy. In figure B.1 the D atom radial density profile measured at $z = 30$ mm at 20 Pa, i.e. shock region, is shown. The maximum D density is observed at the jet boundary (see Fig. 7.6). Atomic deuterium is also found inside the jet, meaning that D atoms or/and D_2 molecules invade the shock wave. In figure B.2 the D atom density profiles measured along the jet axis for two background pressures are shown. First, the D density depends on the background pressure. Second, the plasma jet supersonic domain is invaded (see Fig. 7.2). Third, the D_2 dissociation degree is extremely low: $\alpha \approx 10^{-4}$ in the subsonic domain at 20 Pa. Finally, at 100 Pa, the profile exhibits a maximum around $z = 200$ mm. These experimental data reveal that the ambient gas indeed mix with the plasma flow and that molecules injected in the background can actively participate in the chemistry.
A point of concern is the production of D atoms. Measurements support the idea of local production. In the jet vicinity, the D density decreases when the H density decreases while the D_2 density remains approximately constant. Moreover, the 100 Pa axial profile can be explained as follows: ahead of the Mach disk only few D_2 molecules have already entered the jet, whereas behind the shock wave D_2 fully mix with the jet; the D_2 density therefore

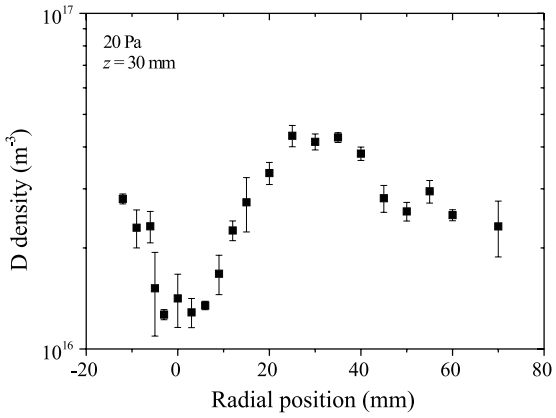

Fig. B.1: D atom radial density profile at $z = 30$ mm and 20 Pa, when D_2 is seeded in the background.

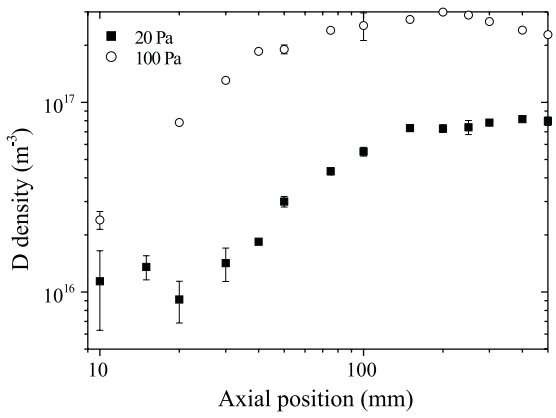

Fig. B.2: D atom density profile along the jet axis at 2 different pressures for D_2 vessel injection.

increases at the beginning of the subsonic region and subsequently more and more D atoms are produced since the H atom density decreases only slowly; at some point however losses of D atoms get larger than production that leads to a decrease of the D density.
Assuming that the main loss mechanism for deuterium atoms is diffusion, the local D density can be estimated by

$$n_D = k\, n_H\, n_{D_2}\, \tau \qquad \text{with} \qquad \tau = \frac{\Lambda^2}{D} \approx \frac{3\Lambda_0^2}{\lambda v_{\rm th}} + \frac{(2-\gamma)R}{\gamma v_{\rm th}}, \tag{B.2}$$

where τ is the diffusion time [3], Λ_0 the diffusion length, λ the elastic collision mean free path, v_{th} the thermal speed, R the vessel radius, and γ the wall-loss probability. As an example n_D is calculated on axis at $z = 100$ mm and at 20 Pa. Using Eqs. B.1 and B.2 with $\gamma = 0.1$, and $n_{D_2} \approx 2 \times 10^{20}$ m^{-3} from CARS measurements, one finds $\tau = 4$ ms and $n_D \approx 10^{19}$ m^{-3} which is more than two orders of magnitude higher than the measured value. The discrepancy may arise from an erroneous γ or from the fact that the reaction between D and H_2 is not taken into account. This simple estimation however reveals that the problem of D atom, or associated HD molecule, production as well as the issue of invasion of the supersonic domain by D_2, can only be solved by measuring the local D_2 density, using two-photon LIF spectroscopy for instance.

[1] W.M.M. Kessels, A. Leroux, M.G.H. Boogaarts, J.P.M. Hoefnagels, M.C.M. van de Sanden, and D.C. Schram, *J. Vac. Sci. Technol. A* **19**, 467 (2001).
[2] R.F.G. Meulenbroeks, D.C. Schram, M.C.M. van de Sanden, and J.A.M. van der Mullen, *Phys. Rev. Lett.* **76**, 1840 (1996).
[3] P.J. Chantry, *J. Appl. Phys.* **62**, 1141 (1987).

Summary

The expansion of a plasma from a hot and dense source to a low pressure environment is a general physical phenomenon which concerns a large variety of objects such as supernovae, solar flares, laser spots, and free jets produced from thermal plasma sources.

Over the last decade, the transport of charged particles as well as ground-state atoms and molecules has been extensively studied in laboratory scale plasma expansions. It has been shown that, to a large extent, the flow characteristics of ions and electrons and inert atoms and molecules could be interpreted in terms of a quasi-adiabatic supersonic expansion of a gas into a vacuum. In other words, the theory of the free jet flow developed in the field of gas dynamics could be well applied in the case of a plasma expansion, only minor corrections being necessary to account for field and current generation, and for the relatively high plasma temperature (departure from adiabatic flow).

However, at this point, questions remained about the transport properties of atomic radicals, i.e. reactive neutral atoms such as H, N, C, in a supersonic plasma flow. This thesis is mainly concerned with the study of transport mechanisms of ground-state hydrogen atoms in the expansion of thermal plasmas generated by a cascaded arc from Ar-H_2 and He-H_2 gas mixtures, and from H_2 gas. A clear understanding of transport phenomena in free plasma jets containing hydrogen are of prime importance since H atoms play a key role in plasma assisted surface modification processes (deposition of thin films, etching of microstructures) as well as in the field of controlled nuclear fusion. The local macroscopic properties of the H fluid (density, temperature, velocity) are determined by means of Two-photon Absorption Laser Induced Fluorescence spectroscopy. The properties of Ar atoms are measured by LIF (with a cw source) and UV Rayleigh scattering, and the behavior of H_2 molecules is probed by UV Rayleigh scattering.

We found that the transport of atomic radicals can not be described using the classical free jet flow picture. Contrary to inert particles, hydrogen radicals recombine on a surface (the reactor walls) to form stable hydrogen molecules. This recombination process induces huge density gradients between the plasma jet and its surrounding which in turn force the radicals to diffuse out of the jet. It is demonstrated for the first time that, under specific circumstances (high wall-loss probability and large residence time) surface-chemistry can play a key role in the transport mechanisms of reactive particles.

The evolution of both the H and Ar atom velocity distribution function in the course of the plasma flow, especially in the stationary compression shock wave where a strong departure from thermodynamic equilibrium occurs, is also investigated, as well as the invasion of the supersonic domain of the jet by the residual background gas. We found that in a rarefied flow regime a bimodal approach can well describe the measured velocity distribution function in the shock region. However, the two-component model of the velocity distribution proposed in this thesis differs from the Mott-Smith approximation that explains the absence of a third component, the so-called scattered component.

Stéphane Mazouffre, June 2001.

Acknowledgments

It will be obvious that the research undertaken over the last four years, which forms the subject of this thesis, is the result of teamwork, and not the work of a single person, however determined. I wish, then, to thank all those who have contributed, in whatever degree, to the realization of this mamuscript.

I would like to thank first of all Daan Schram, my supervisor, for the confidence he has shown in me and for the freedom of opinion to which he has accustomed me. His overwhelming energy and his endless enthusiasm, although sometimes difficult to match even for someone of my young age, have allowed me to make fast progress both professionally and personally. I will never forget the hundreds of hours we spent talking about physics, of course, but also just about life. And in 20 years' time, I will be telling my children for the twentieth time how proud I am to have studied all those years ago under such a great man....

Thanks to Joost van der Mullen for his ever cheerful but efficient supervision during the first year of my thesis. I am sorry about the article that never was, and I sincerely hope that someone will finish that study very soon. Et pourquoi pas ?

I must also thank the calmest person I have ever had the opportunity of meeting, a certain Maarten Boogaarts. I could not have wished for a better person to introduce me to experimental spectroscopy. And we did finally manage to write that article!

Many thanks to Richard Engeln, a.k.a. The Boss, my co-supervisor, for almost three years spent working together with never a cross word. I am glad and proud to have been his first Ph.D. student; I could not have wished for better. I will never forget the few days we spent together in Limoges (you will have to give the snails another chance). As for those 170 pages, I suggest we buy two bottles And by the way, is it CARS or LIF?

Now is the time to thank Prof. Frieder Döbele and Prof. Nader Sadeghi for having shared their great experience of laser spectroscopy with me. I also want to thank them, together with Prof. M. E. H. van Dongen, for their constructive criticism after reading the first draft of my thesis.

Of course, many thanks to everyone at the ETP group, and especially to Marco and Maikel for having put up with me for four years in the same office (sorry for all the swearing, but is it that surprising coming from a Frenchman?!); to Jeanne, our secretary, for having helped me with all those wonderful forms; to Bertus, Herman, Ries and Jo, for having helped me solve countless technical problems in computing, optics or mechanics; to Richard van de Sanden for having taught me to stand up for my point of view come what may; and finally to Edouard and Karine for the wonderful times in French.

Thank you to the residents of Cassandraplein 41, the most minimalist apartment I know of. Thank you to Colin for these years of flat-sharing. It took us a while to get settled in to each other, but it was worth it in the end. Sorry for having contributed to the ruining of your accent. Zeez French! Wee weel never get zem to speek ze Eengleesh proper. Oh, and thank you for the widescreen TV, which was much better for playing Doom... Thanks

Acknowledgments (continued)

to Tarik for the wild year we spent together (only my bank account thought it wasn't that wild). Trix, Kix, Niks... Succes! Since you left we have got hold of a comfortable couch. No more evenings slouched on a mattress wearing a pizza box as a sun visor. Carole, even though your stay was relatively brief, it allowed us to get the apartment straight. And nothing has changed since you left. We have kept up the good habits you got us into.
A big thank you to the IPM people for the months I spent in their company in that wonderful house. I particularly want to thank one of them: my friend Peter. I know we will never forget the first time we shook hands in that narrow corridor a few days after my arrival in the Netherlands. Fate was smiling on us that day. Good luck with your thesis. I know everything will work out. With a trainer like me, you should be prepared for anything!! I also want to thank all the Thales members, and especially Ivo, as I have made him suffer a bit recently, for having accepted me at some of their special parties. The wine was good that night; we should have done it again.
Thank you to everyone at the Laser- und Plasmaphysik group at Essen University in Germany for four very pleasant months I spent at their faculty, where I was able to have a go at photon generation in the VUV, but also in the wonderful region of the Ruhrgebiet. Thanks to Frieder Döbele, Uwe Czarnetzki, Thomas and Claudia, Norbert, Michael, Peter, Timo, Kari and Anne.
Thanks to Philippe Supiot and Corinne Foissac of Lille University for having initiated me into nitrogen plasmas. Sorry to Corinne for the lack of sleep and for the imposed diet. I will always be in your debt. Thank you to Gerrit Kroesen and Gerjan for the few days we spent in New York. It was a good idea to choose a hotel on Broadway after all. Thanks to Armelle Vardelle, Jean Desmaison and Jean-Pierre Lecompte at the ENSI at Limoges for having enabled me to teach a few classes at my alma mater, and for having advised me on my future career. Thanks also to Lisette for having designed the cover for my thesis. I think it is really stylish, and just what I wanted.
Finally, I want to thank with all my heart the people who mean more than anything else to me, and who, despite being hundreds of kilometers away, have still had to suffer my endless tales about plasma physics. Your help has been precious; never doubt that for a second. A thousand thanks, then, to my Mum, to Raymond, Marie-Thérèse, Clément, my godfather Serge, Giselle, my godmother Simone, Sylvian, my Laquaire grandparents, Aimée and Christian. After the family come my friends, who are so dear to me. Thank you Grégorie, Jean and Emmanuelle, David and Manuella, Alexandre and Valérie, Olivier, Sophie and JB, Charles, Michel, Daniel, Christophe, Jeff and Sonia, Anne, Alexandrine, Estelle, Gael and Fabien.
Bedankt, Thanks, Danke, Merci.

List of publications

- *Transport of neutral atomic hydrogen in a supersonic plasma jet.*
  S. Mazouffre, M.G.H. Boogaarts, J.A.M. van der Mullen, and D.C. Schram,
  Heat and Mass transfer under Plasma Conditions, edited by P. Fauchais, J.A.M. van der Mullen, and J. Heberlein, ANYAS, Vol. 891, 348 (1999).

- *Anomalous atomic hydrogen shock wave pattern in a supersonic plasma jet.*
  S. Mazouffre, M.G.H. Boogaarts, J.A.M van der Mullen, and D.C. Schram,
  Phys. Rev. Lett. **84**, 2622 (2000).

- *A time-resolved experimental and computational study of two-photon LIF in a hydrogen plasma.*
  H.W.P. van der Heijden, M.G.H. Boogaarts, S. Mazouffre, J.A.M van der Mullen, and D.C. Schram,
  Phys. Rev. E **61**, 4402 (2000).

- *The physics of plasma expansions.*
  D.C. Schram, S. Mazouffre, R. Engeln, and M.C.M. van de Sanden,
  Atomic and Molecular Beams, edited by R. Campargue, Springer, NY, 209 (2001).

- *Density and temperature of N atoms in the afterglow of a microwave discharge measured by a two-photon laser induced fluorescence technique.*
  S. Mazouffre, C. Foissac, P. Supiot, P. Vankan, R. Engeln, D.C. Schram, and N. Sadeghi,
  Plasma Sources Sci. Technol. **10**, 168 (2001).

- *Transport of ground-state hydrogen atoms in a plasma expansion.*
  S. Mazouffre, M.G.H. Boogaarts, I. Bakker, P. Vankan, R. Engeln, and D.C. Schram,
  Phys. Rev. E **64**, 016411 (2001).

- *Influence of surface chemistry on the transport of H atoms in a supersonic hydrogen plasma jet.*
  S. Mazouffre, P. Vankan, R. Engeln, and D.C. Schram,
  Phys. Plasmas **8**, 3824 (2001).

- *Flow dynamics and invasion by background gas of a supersonically expanding thermal plasma.*
  R. Engeln, S. Mazouffre, P. Vankan, D.C. Schram, and N. Sadeghi,
  accepted for publication in Plasma Sources Sci. Technol. (2001)

List of publications (continued)

- *Behavior of the H atom velocity distribution function within the shock wave of a hydrogen plasma jet.*
  S. Mazouffre, P. Vankan, R. Engeln, and D.C. Schram,
  accepted for publication in Phys. Rev. E. (2001)

- *Plasma expansion: fundamentals and applications*
  R. Engeln, S. Mazouffre, P. Vankan, I. Bakker, and D.C. Schram,
  Proceedings of the International Conference on Phenomena in Ionized Gases XXV,
  to be published in Plasma Sources Sci. Technol.

- *Quantitative two-photon LIF measurements of atomic hydrogen densities, temperatures, and velocities in an expanding thermal plasma.*
  M.G.H. Boogaarts, S. Mazouffre, H.W.P. van der Heijden, P. Vankan, J.A.M. van der Mullen, and D.C. Schram,
  submitted for publication in Rev. Sci. Instrum.

- *Wall-association processes in expanding thermal hydrogen plasmas.*
  S. Mazouffre, P. Vankan, W.M.M. Kessels, R. Engeln, M.C.M. van de Sanden, and D.C. Schram,
  submitted for publication in IEEE Trans. Plasma Sci.

- *TALIF performed on expanding nitrogen plasmas.*
  S. Mazouffre, I. Bakker, R. Engeln, P. Vankan, and D.C. Schram,
  in preparation.

Stellingen

behorende bij het proefschrift

Transport Phenomena in Plasma Expansions Containing Hydrogen

A Laser Spectroscopic Study

door

Stéphane Mazouffre

I

Wall-association processes can strongly influence the transport mechanisms of radicals in plasma expansions.

Dit proefschrift

II

Within the stationary shock wave of a plasma expansion the atom velocity distribution function can be decomposed into two Gaussians. One component corresponds to the unhampered supersonic conditions. The other component originates in collision events.

Dit proefschrift

III

In a rarefied flow regime, the shock region and the supersonic domain of an expanding plasma are invaded by background gas particles.

Dit proefschrift

IV

Liberté. Égalité. Fraternité.
After more than four years spent in The Netherlands, I discovered that the country of individual freedom was not the one I thought of.

V

To love someone today is to take the risk of loving someone else tomorrow.

VI

Imagination creates dreams. Science destroys them by confronting us with reality.

VII

"Anticipatory plagiarism occurs when someone steals your original idea and publishes it a hundred years before you were born."

Robert Merton

VIII

The existence is ruled by free will, not by determinism.

"My life was running out, I knew not through what breach."
Samuel Beckett, Molloy.

IX

The only difference between Religion and Science is that Science does account for observational facts.

X

Controlled nuclear fusion could certainly be achieved if no reactor walls would be needed.

XI

Fortunately life is not always straightforward.